

ANALYSIS AND DESIGN OF THE MECHANICAL SYSTEMS
ONBOARD A MICROSATELLITE IN LOW-EARTH ORBIT:
AN ASSESSMENT STUDY

by

Dylan Raymond Solomon

A thesis submitted in partial fulfillment
of the requirements for the degree

of

Master of Science

in

Mechanical Engineering

MONTANA STATE UNIVERSITY
Bozeman, Montana

December, 2005

©COPYRIGHT

by

Dylan Raymond Solomon

2005

All Rights Reserved

APPROVAL

of a thesis submitted by

Dylan Raymond Solomon

This thesis has been read by each member of the thesis committee and has been found to be satisfactory regarding content, English usage, format, citations, bibliographic style, and consistency, and is ready for submission to the College of Graduate Studies.

Dr. David M. Klumpar and Dr. Vic Cundy

Approved for the Department of Mechanical Engineering

Dr. Christopher Jenkins

Approved for the Division of Graduate Education

Dr. Joseph J. Fedock

STATEMENT OF PERMISSION TO USE

In presenting this thesis in partial fulfillment of the requirements for a master's degree at Montana State University, I agree that the library shall make it available to borrowers under rules of the Library.

If I have indicated my intention to copyright this thesis by including a copyright notice page, copying is allowable for scholarly purposes, consistent with "fair use" as prescribed in the U.S. Copyright Law. Requests for permission for extended quotation from or reproduction of this thesis in whole or in parts may be granted only by the copyright holder.

Dylan Raymond Solomon

December, 2005

ACKNOWLEDGEMENTS

I would like to thank the Space Science and Engineering Laboratory (SSEL), the College of Engineering at Montana State University, and MontanaTech in Butte for providing research assistantship and collaboration for enabling this research. Thanks to Dr. Dave Klumpar for his advice, guidance and opportunity to explore the space sciences. Thanks to industry partners, Tether's Unlimited Inc. and Ecliptic Enterprises for their influences on the mission. A special thanks to Danny Jacobs and the satellite design team for an enjoyable and highly educational exploration of small satellite technology and operations.

TABLE OF CONTENTS

LIST OF TABLES	ix
LIST OF FIGURES	x
NOMENCLATURE	xiii
ABSTRACT	xvi
1. INTRODUCTION	1
Space Science and Engineering Laboratory	1
Statement of Problem	1
CubeSat and P-Pod	2
RocketPod™	6
Tethers Unlimited Incorporated.....	7
BarnacleSat, a Picosatellite.....	8
ICDs and Spacecraft Configuration.....	9
2. MISSION	13
BarnacleSat CONOPS	14
Subsystem Development and Systems Engineering.....	16
Structure.....	16
Command and Data Handling (C&DH)	17
Power	18
Communications	19
GPS Payload	20
Tether Deployer	21
Ground Station.....	22
3. BACKGROUND	23
Orbital Debris	23
Tether Payload and Electrodynamic Drag.....	25
Gravity Gradient	27
Launch Vehicle Environment.....	28
Role of the Structure	28
Harmonic Vibrations and Steady-State Acceleration	30
Launch Configuration	32
Load Factors.....	33
Random Vibrations.....	33
Acoustic Loads.....	35
Thermal Environment.....	37

TABLE OF CONTENTS CONTINUED

Orbital Parameters and Geometry.....	38
Beta Angle	42
Incident Radiation.....	44
Electromagnetic Spectrum.....	45
Shortwave Radiation.....	46
Longwave Radiation.....	47
Direct Solar.....	48
Albedo.....	49
Planetary Emissions.....	49
Thermal Control Techniques.....	50
Heat Transfer Theory.....	53
Conduction.....	53
Contact Resistance.....	54
Convection.....	55
Radiation.....	56
Transient Conduction.....	57
Analytical Solution Techniques.....	58
Finite Element Method.....	59
Finite Difference Method.....	61
4. MECHANICAL DESIGN.....	64
Structure Subsystem.....	64
Requirements.....	64
Satellite Design.....	67
Primary Structure.....	67
Secondary Structure.....	71
Tertiary Structure.....	75
Modularity.....	78
Manufacturing.....	81
Mass and Material Properties.....	81
Thermal Subsystem.....	85
Requirements.....	85
Control Strategy.....	87
Tether Payload.....	90
Parametric Orbits.....	93
Beta Angle.....	98
5. STRUCTURAL ANALYSIS.....	100
Requirements and Verification Criteria.....	101
Preliminary Static Analysis.....	103
Maximum Inertial Load.....	103

TABLE OF CONTENTS CONTINUED

Simplified Static Model	106
Failure Modes	108
Buckling	108
Bending	111
Bearing Stresses and Mechanical Fasteners	114
Dynamic Analysis	115
Harmonic Vibrations	116
Power Spectral Density	119
Acoustic Vibrations	122
Finite Element Analysis	125
COSMOS	125
Convergence	127
Loading Conditions and Boundary Conditions	127
Launch Rails	128
Flat Plate	131
Tabs	133
Preliminary Results	135
The Satellite	136
Baseplate	136
Sides	139
Tophat	142
Tether Bracket	144
Battery Bracket	146
Results and Conclusions	147
 6. THERMAL ANALYSIS	 150
Objective	150
Orbit Profile	151
BSat Thermal Control	153
Steady-State Analysis	154
Effective Optical Properties	156
Steady-State Results	156
Transient Analysis	158
Lumped Capacitance	159
Transient Results	162
Finite Difference Analysis	165
SINDA	166
Battery Consideration	169
Calorimeter Experiment	170
Physical Thermal Model	175
Parametric Orbits	176
Incident Flux	181

TABLE OF CONTENTS CONTINUED

Transient Temperatures	184
Thermal Stress	203
Results and Conclusions	207
7. RESULTS, CONCLUSIONS, and FUTURE WORK.....	211
Structure.....	211
Thermal.....	215
APPENDICES	222
APPENDIX A Engineering Drawings.....	223
APPENDIX B Mass Budget.....	258
APPENDIX C Fastener Diagram	260
APPENDIX D RocketPod™ Spring Force	262
APPENDIX E Structure Analytical Worksheet	266
APPENDIX F Structural Harmonic Response	276
APPENDIX G Vibroacoustic Response.....	281
APPENDIX H Safety Factors and Error Convergence	289
APPENDIX I Fabrication Costs	295
APPENDIX J Simplified Geometry	297
APPENDIX K Effective Optical Properties	308
APPENDIX L MATLAB Lumped Capacitance Code.....	318
APPENDIX M Absorbed Flux	323
APPENDIX N Calorimeter Experiment.....	327

LIST OF TABLES

Table	Page
3-1: Load Factors and Frequency Data of Delta II	32
3-2: Acceleration Spectral Density for Delta II	37
3-3: Solar Flux and Albedo Heat Loads	49
3-4: Orbit Average Earth IR	50
3-5: Surface Finish Properties (<i>Data supplied from Gilmore, 2002</i>).....	52
4-1: 3M Scotch-Weld Epoxy Data.....	71
4-2: BSat Material Properties.....	82
4-3: BSat Thermal Subsystem Requirements	86
4-4: BSat Subsystem Energy Generation.....	87
4-5: Thermophysical Properties of Shroud	92
5-1: BSat Maximum Compressive Strength	108
5-2: BSat Buckling Loads.....	110
5-3: BSat Bending Stresses.....	113
5-4: Fastener Strength and Bearing Stresses.....	115
5-5: BSat Natural Frequencies	118
5-6: Theoretical vs. FEM Natural Frequencies.....	118
5-7: Acoustic Response Results.....	124
5-8: Preliminary Static Results	136
6-1: Environmental Radiation.....	152
6-2: Optical Property Data	154
6-3: Lumped Capacitance Results	164
6-4: BSat's Secondary Battery	169
6-5: Calorimetry Results	171
6-6: BSat Temperature Extremes.....	204
6-7: Solar Panel Thermal Stress Results.....	204

LIST OF FIGURES

Figure	Page
1-1: Stanford's OPAL Satellite	3
1-2: P-Pod and Standard CubeSat.....	3
1-3: Launch Vehicle Metric Cost Comparison	5
1-4: Delta II Miniskirt Structure	6
1-5: Ecliptic's RocketPod	7
1-6: TUI's Hoytether™	8
1-7: P-Pod ICD	10
1-8: RocketPod ICD_1	11
1-9: RocketPod ICD_2.....	12
2-1: BarnacleSat Mission Timeline	14
2-2: BarnacleSat deployed from Delta II upper stage.....	15
2-3: BSat Primary Structure (EDU).....	17
2-4: 5V Regulator, Test Board.....	18
2-5: Chipcon CC1000 Dev. Board.....	20
2-6: Surrey GPS Receiver.....	21
2-7: Tether Deployer Next to BSat EDU	21
2-8: MSU Yagi-Antenna.....	22
3-1: Catalog of Orbital Debris	24
3-2: Orbital Debris as Observed from GEO	25
3-3: EDT Concept.....	26
3-4: Hoytether	26
3-5: BSat Gradient Force	28
3-6: Axial Acceleration Profile for Ariane LV	30
3-7: Axial Acceleration at MECO for Delta II	31
3-10: Vibration Types.....	34
3-11: Power Spectral Density	35
3-12: Delta II SPL Curve	36
3-13: ASD Curve for Delta II	37
3-14: Satellite Thermal Environment.....	38
3-15: Geometry of an Ellipse & Orbital Parameters.....	39
3-16: Orbital Parameters.....	41
3-17: Orbit Beta Angle	42
3-18: Sample of Orbit Beta Angle	44
3-19: Depiction of Eclipse Fraction vs. β and Altitude	44
3-20: The Planck Distribution.....	47
3-21: Delineation of the Electromagnetic Spectrum.....	48
3-22: Radiation Energy Balance	52
3-23: Contact Resistance.....	55
3-24: Tetrahedral Element	59
3-25: Element Equations in Matrix Form	61

LIST OF FIGURES CONTINUED

Figure	Page
3-26: FDM Formulation.....	62
4-1: Tether Specifications.....	66
4-2: Structure Requirements.....	66
4-3: BSat End-rail Details.....	69
4-4: BSat EDU Structure.....	70
4-5: BSat Solar Panel Assembly.....	72
4-8: BSat Battery Bracket (x2).....	76
4-9: BSat Antenna Cups.....	77
4-10: JED 22 pin Connector by JST and Solar Panel Right-Angle Pin Header.....	79
4-12: Typical Stress-Strain Curve for Aluminum.....	83
4-13: Mass Budget.....	84
4-14: BSat Center of Mass.....	84
4-15: Thermal Block Diagram.....	86
4-16: BSat Cross Section.....	89
4-17: BSat Thermal Resistance Depiction.....	90
4-18: BSat Tether Shroud.....	92
4-19: BSat STK Simulation of Access Times for one 24 hour period.....	94
4-20: BSat Average Access Time vs. Inclination and Altitude for 2006.....	95
4-21: BSat Total Access Time vs. Inclination and Altitude for 2006.....	96
4-22: BSat Sun vs Elipse Times for Parametric Orbit.....	97
4-23: BSat Beta Angle Precession during 2006.....	99
5-1: BSat and RocketPod Fit-Check.....	100
5-2: BSat Worst-Case Loading Orientation.....	103
5-3: RocketPod™ Deployment Sequence.....	104
5-4: Ejection Capabilities of RocketPod™.....	106
5-5: Simplified BSat Model.....	107
5-6: Column Buckling.....	109
5-7: Cantilever Beam.....	111
5-8: Bearing Stresses.....	114
5-9: Primary Structure 1 st Mode, Harmonic Response.....	117
5-10: FEM Boundary Conditions for the Baseplate and FR4 Board.....	119
5-11: Idealized System with a SDOF.....	120
5-13: Stress/Strain Diagram.....	125
5-14: BSat Physical Boundary Conditions and Inertia Load.....	126
5-16: Launch Rail in Bending.....	130
5-17: Beam Bending, FEA vs. Analytic.....	130
5-20: Stress Distribution of Single Tab.....	134
5-21: Tab FOS and Deformed Shape.....	135
5-22: BSat Baseplate Loading Conditions.....	137
5-23: Baseplate as a Simply Supported Beam.....	138

LIST OF FIGURES CONTINUED

Figure	Page
5-24: Baseplate Bending Curve	139
5-25: Buckling of BSat Side	140
5-26: Quasi-Static Loading of Sides	141
5-27: Tophat Loading	143
5-28: Tophat Stress Distribution.....	143
5-29: Tether Bracket Bearing Stresses.....	144
5-30: Tether Bracket Quasi-Static Load	145
5-31: Battery Bracket Stress Distribution	146
6-1: BSat's Passive Attitude	152
6-2: Orbit Beta Angle.....	152
6-3: Beta Angle and Flux Load.....	153
6-4: Simplified Geometric Model.....	155
6-5: Steady-State Temperature Results.....	157
6-6: Equivalent Sphere.....	158
6-7: Biot Number vs. Temperature and Emissivity	160
6-8: Lumped Capacitance GUI	162
6-9: Parametric Transient Temperatures; Hot-Case	163
6-10: Parametric Transient Temperatures; Cold-Case.....	164
6-11: Thermal Desktop Sphere	167
6-12: Sphere Comparison with Q_{gen}	168
6-13: Sphere Comparison without Q_{gen}	168
6-14: Calorimeter Apparatus.....	170
6-15: Battery Experiment.....	172
6-16: Battery Temperature at Optimal Current.....	173
6-17: Battery Temperature vs. Voltage State.....	174
6-18: BSat SINDA Model.....	176
6-19: Total Absorbed Flux, $\beta=0^\circ$	177
6-20: Total Absorbed Flux, $\beta=68.4^\circ$	178
6-21: Total Absorbed Flux, $\beta=90^\circ$	179
6-22: Parametric Beta Angles	181
6-23: Direct Incidence, $\beta=0^\circ$	182
6-24: Direct Incidence, $\beta=68.4^\circ$	182
6-25: Direct Incidence, $\beta=90^\circ$	183
6-26: Direct Incidence, $\beta=90^\circ$, fast-spin.....	184
6-27: BSat Solar Absorptivity Verification	185

NOMENCLATURE

<i>ASD</i>	-	Acceleration Spectral Density [g^2/Hz]
<i>AU</i>	-	Atomic Unit
<i>c</i>	-	Speed of light = 2.998 E8 m/s
<i>C&DH</i>	-	Command and Data Handling
<i>DARPA</i>	-	Defense Advanced Research Projects Agency
<i>E</i>	-	emissive flux [W/m^2]
<i>EDT</i>	-	Electrodynamic Tether
<i>ELV</i>	-	Expendable Launch Vehicle
<i>EPS</i>	-	Electric Power Subsystem
<i>FEA</i>	-	Finite Element Analysis
<i>g</i>	-	Earth's gravity at sea level = 9.81 m/s^2
<i>GEVS</i>	-	General Environmental Verification Specifications
<i>h</i>	-	Convection coefficient [$\text{W}/\text{m}^2\cdot\text{K}$]
<i>Hz</i>	-	Frequency [rad/s]
<i>ICD</i>	-	Interface Control Document
<i>IR</i>	-	Infrared
<i>k</i>	-	Thermal conductivity [$\text{W}/\text{m}\cdot\text{K}$]
<i>LEO</i>	-	Low Earth Orbit
<i>LV</i>	-	Launch Vehicle
<i>MECO</i>	-	Main Engine Cut-Off
<i>NODPO</i>	-	NASA Orbital Debris Program Office

NOMENCLATURE CONTINUED

<i>OPAL</i>	-	Orbiting Automated Picosat Launcher
<i>PCB</i>	-	Printed Circuit Board
<i>PPD</i>	-	Payload Planners Guide
<i>P-Pod</i>	-	Poly Picosatellite Orbital Deployer
<i>PSD</i>	-	Power Spectral Density [g^2/Hz]
<i>Q</i>	-	Energy [W]
<i>q''</i>	-	Heat flux [W/m^2]
<i>R''_{t,c}</i>	-	Contact resistance [$\text{m}^2 \cdot \text{K}/\text{W}$]
<i>RF</i>	-	Radio Frequency
<i>rms</i>	-	Root Mean Square
<i>SPL</i>	-	Sound Pressure Level [dB]
<i>SSEL</i>	-	Space Science and Engineering Laboratory
<i>T</i>	-	Temperature [K]
<i>TCS</i>	-	Thermal Control Subsystem
<i>TUI</i>	-	Tethers Unlimited Inc
<i>α</i>	-	solar absorptivity
<i>β</i>	-	Beta Angle [°]
<i>ϵ</i>	-	IR emissivity
<i>σ</i>	-	Stefan-Boltzman constant = $5.67 \text{ E-}8 \text{ W}/\text{m}^2 \cdot \text{K}$
<i>ρ</i>	-	Material Density [kg/m^3]
<i>C_p</i>	-	Specific Heat [$\text{J}/\text{kg} \cdot \text{K}$]

NOMENCLATURE CONTINUED

<i>C</i>	-	Heat Capacity [J]
<i>SINDA</i>	-	S ystems I mproved N umerical D ifferencing A nalyzer
<i>FDM</i>	-	F inite D ifference M ethod
<i>EDU</i>	-	E ngineering D esign U nit
COTS	-	C ommercial O ff- T he- S helf

ABSTRACT

A study of the mechanical systems contributing to the design and performance of a picosatellite's mission in low-Earth orbit (LEO) was performed through design and analysis. The unique architecture of this satellite stems from a form factor established by the internationally recognized CubeSat Program. This CubeSat-Plus architecture limits the satellite's size to be no larger than a 10 x 10 x 15 cm *cube* with an overall mass not exceeding 2 kg. This satellite would then be launch into LEO and conduct on-orbit GPS measurements while remaining tethered to the second stage booster of a Boeing Delta II Launch Vehicle (LV). To ensure the structural integrity of the satellite, Finite Element Analysis (FEA) was conducted on all primary, secondary, and tertiary structural constituents to determine the maximum stresses experienced by the satellite during launch, deployment, and while in orbit around Earth. All space deliverable platforms must be designed in strength to satisfy a predetermined standard as set forth by the LV provider. Theoretical characterization of the dynamic environment coupled with the equation of motion, and static failure modes were the primary constituents of this assessment study. Consequential data sets piloted the assessment criterion and a means of implementing conclusive remarks. The design of this satellite will reveal evidence of system level design philosophies that were required given the extremely small form factor. The satellite's on-orbit thermal environment was quantified and characterized using finite difference techniques and solar simulation software. The extremely dynamic behavior of a LEO satellite required a fundamental understanding of both long wave and shortwave thermal radiation along with creative strategies to ensure on-orbit thermal stability for the satellite's electrical components. Thermal Desktop was employed to develop an accurate thermal model by which to assess incident radiation, conductive and radiative heat management, and temperature-dependent mechanical responses of the satellite's structure and working systems. Conclusions from both the design efforts and model analyses show that this picosatellite is both sufficiently strong to survive the expected launch loads, and provides a thermally stable environment for the components housed within its interior.

1. INTRODUCTION

Space Science and Engineering Laboratory

Montana State University's Space Science and Engineering Laboratory (SSEL) is an academic research center within which students are given responsibility for the design and fabrication of a variety of high altitude and spaceborne platforms. Students are involved with every aspect of the satellite's design, fabrication, testing, and operations. Each project brings together a team of students from a variety of disciplines to apply their academic knowledge to the fabrication of real-life, high altitude experimental platforms. SSEL was started under the auspices of the Department of Physics at MSU in November, 2000. Its initial satellite project conformed to the CubeSat standard that had been conceived by Stanford and California Polytechnic State (Cal Poly) Universities. SSEL offers a practical space education program where students develop the necessary skills and experience needed to succeed in the Aerospace industry [CubeSat, 2005].

Statement of Problem

A multidisciplinary team of student engineers and scientists was formed in the fall of 2004 with the purpose of preparing a flight-capable picosatellite for launch into LEO. For the program's expedited fruition the mechanical constituents of the satellite were designed, fabricated, and analyzed in a one year period. The structural subsystem was assessed based on the inherent stresses associated with launch loads, and the on-orbit thermal environment. These stresses were a result of a variety of static and dynamic load

environments and the natural temperature gradient that exists. A stable structure is defined to appropriately house all pertinent subsystems, protect onboard systems from the space environment, meet the thermal expansion criteria and dimensional specifications of the deployment device, and provide a means of integrating all electronics and payload packages. The Thermal Control System (TCS) of the spacecraft was designed to maintain all payload and subsystem components within predetermined temperature ranges. To evaluate possible TCS strategies extensive radiative and conductive modeling was performed for a variety of possible transient orbital parameters. Distinction between sunlit and eclipse periods is highly dependent upon the spacecraft's orbit and once defined, provides a valid data set by which to assess on orbit thermal stability of the spacecraft.

This thesis focuses on the mechanical systems that support this mission and will discuss the design and analyses conducted to ensure on-orbit mission success. Prior to an in depth discussion the remaining material in this chapter will educate the reader on programmatic and mission level topics which are responsible for this satellite program and by which requirements were defined.

CubeSat and P-Pod

The CubeSat standard grew out of Stanford University's OPAL¹ microsatellite mission in February of 2000. The objective of this mission was to demonstrate the feasibility of a new payload platform for testing and performing on-orbit space experiments in the nano and picosatellite architectures; <100 kg and <1 kg, respectively.

¹ Orbiting Automated Picosat Launcher

OPAL, as seen in Figure 1-1, deployed six picosatellites weighing less than 1 kg and measuring approximately 10 x 7.5 x 2.5 cm. With the success of the OPAL mission a new standard in spacecraft design was introduced to the satellite community under the premise that supporting science missions and performing new ones is attainable by reducing the spacecraft's size by orders of magnitude [Heidt; et al., 2000]. This attempt was first envisioned by the DARPA² funded OPAL mission and shows cognizance among leading industry partners on the growing concern of the high cost associated with most traditional space missions. The CubeSat Program and the P-Pod³ of Figure 1-2 have been recognized as a solution to this concern, and is formulated under the trend in satellites to do more for less cost.

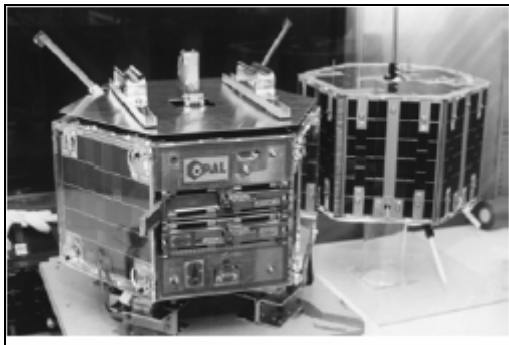


Figure 1-1: Stanford's OPAL Satellite

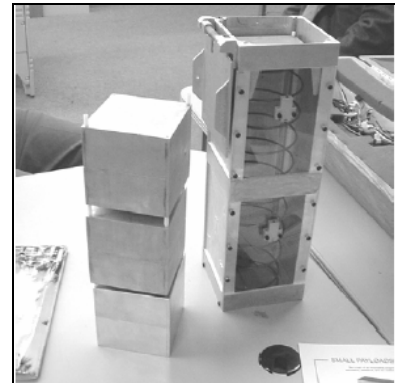


Figure 1-2: P-Pod and Standard CubeSat

Individual CubeSat development teams have been formed at over 40 universities, high schools, and private firms around the world. The CubeSat Program has been growing in popularity and practicality; in large part due to the advances in electronics' capabilities, power consumption, and size. Decreasing the overall size of the spacecraft

² Defense Advanced Research Projects Agency

³ Poly Picosatellite Orbital Deployer

directly reduces the mission and launch costs, and provides opportunities for academic institutions to be involved in the entire spacecraft design processes: conceptualization, design, build, test, launch, operate, and communication with an *in-situ* orbiting platform.

Stanford University collaborated with Cal Poly of San Luis Obispo to develop the P-Pod seen in Figure 1-12, a standardized deployment mechanism for the CubeSat. Efforts began in 1999 with the intent of making this standard available to the academic-based CubeSat market; and in June of 2003, five university satellites were successfully launched into orbit using this standard; the P-Pod and the 10 cm cube of the CubeSat. The existence of the P-Pod allows students to devote their efforts to the satellite's actual design and construction while not having to worry about its deployment; this in essence, reduces the mission's order of complexity.

The 2003 launch and the launch of 15 CubeSats currently scheduled for March, 2006 are two launch opportunities made available by Kosmotras on the converted Russian SS-18 Dnepr LV [Heidt; et al., 2000]. There are no current launches scheduled for P-Pods and CubeSats within the U.S.A, but efforts are ongoing with Boeing and Lockheed Martin and other launch providers to provide a domestic launch opportunity within the financial budgets of the program participants.

Access to space has and will continue to be a formidable obstacle for space experimental platforms. The financial burden to the academic participants is the cost and integration of the satellite with the LV and not the actual fabrication of the satellite. The costs per kilogram for a variety of LV configurations are seen in Figure 1-3. Comparing launch vehicle costs begins by first understanding that launch vehicles are rather

incomparable. A Dnepr, for example, costs far less than a Delta II, but it is also a much smaller vehicle. Differences in vehicle size can mask more important cost differences caused by vehicle design, nation of manufacture, and other factors [Futron, 2002]. Therefore, the comparative strategy of Figure 1-3 is the result of a metric study that compares launch vehicles' cost-effectiveness and design against a normalized cost. In other words, the dollar amount seen below is not the cost to the payload customer, but instead purely a means of evaluating launch vehicles. For a university CubeSat it does show a dramatic cost advantage with the Dnepr launch vehicle. For the actual cost of a Dnepr hosted picosatellite, Tom Bleier⁴ states that the budget of a single cube is approximated at \$50K and that the launch per kilogram for the Russian Eurokot is \$30K-50K. [Bleier; et al., 2000]

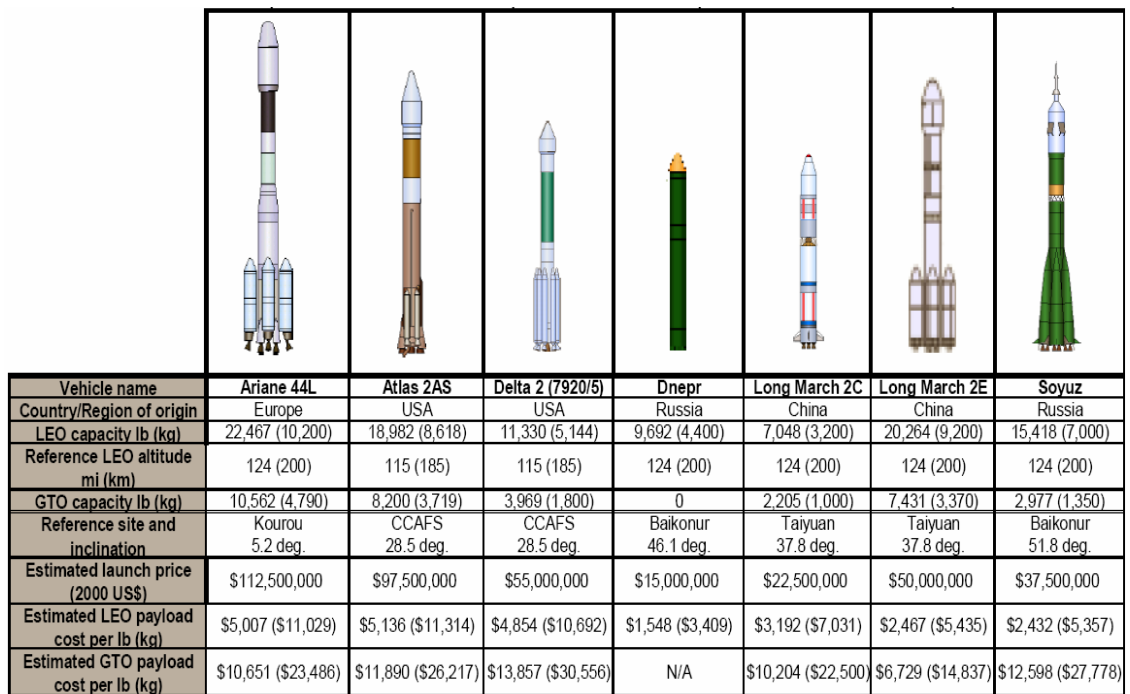


Figure 1-3: Launch Vehicle Metric Cost Comparison (Reproduced from Futron, 2002)

⁴ From experience with QuakeSat, a triple CubeSat

RocketPod™

Leading the effort in establishing domestic launch opportunities for CubeSat-type spacecraft is Ecliptic Enterprise Incorporated (Ecliptic)⁵ of CA, USA. Ecliptic developed the RocketPod™ deployment mechanism which is designed to mount on the LV's exterior, similar to their RocketCam product. They believe strongly that a qualified RocketPod™ will increase the frequency of CubeSat launch opportunities and extend them to include an abundance of domestic-based launches. The current configuration of Figure 1-4 reveals that the first RocketPod™ flight will include four units, each pair accompanied by a RocketCam. The RocketPod is undergoing qualification testing solely for Boeing's Delta II LV where it will ride into space onboard a GPS satellite insertion mission. This information will be referred to frequently as this discussion progresses. The RocketPod prototype is shown in Figure 1-5.

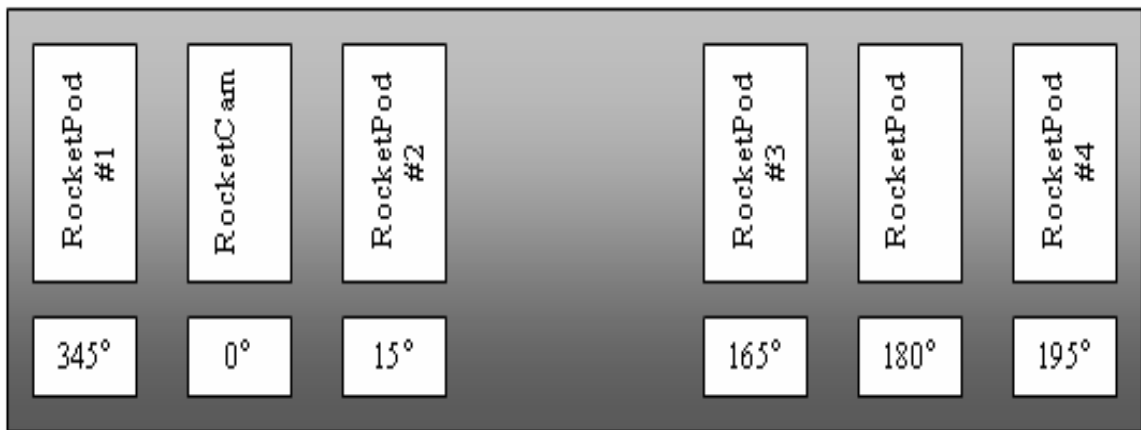


Figure 1-4: Delta II Miniskirt Structure

⁵ Outfitting Boeing and Lockheed Martin LVs w/ RocketCams since 1997

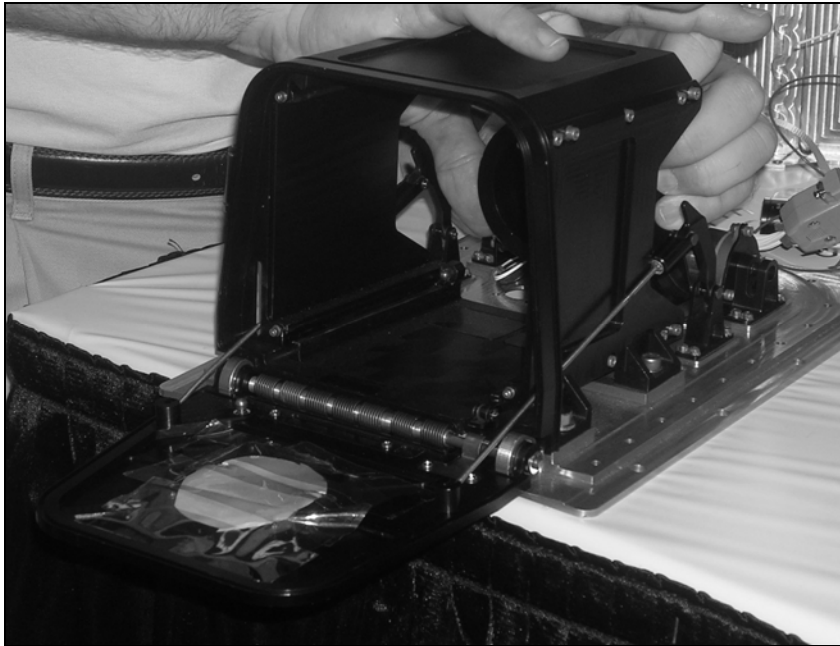


Figure 1-5: Ecliptic's RocketPod

Tethers Unlimited Incorporated

Tethers Unlimited, Inc. (TUI) is a small research and development company that has formally expressed interest in the picosatellite launch as a test platform. TUI specializes in advanced space technologies with the development of products based upon space tether technologies. Similar to academic interest, TUI is beginning to equip university-based CubeSat with tether payloads because of their low space access costs. TUI's technology is centered on their long-life, damage resistant tether system for extended-duration, high-value, and crew-rate missions [TUI, 2005]. Their tether, the *Hoytether*TM, is composed of multiple strands to provide redundant load paths for the expected micrometeorite impacts; thus, ensuring longevity of the tether system. This construction is seen in Figure 1-6.

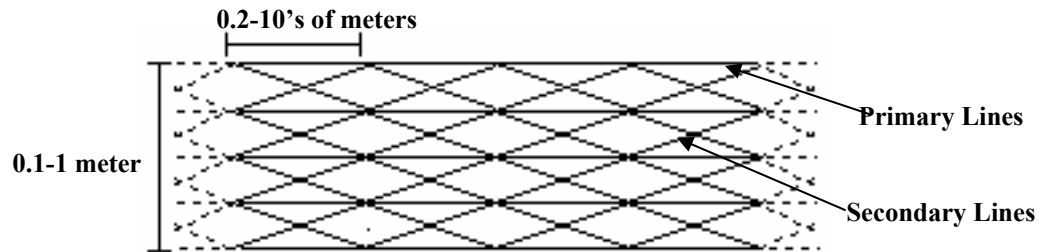


Figure 1-6: TUI's Hoytether™ (Reproduced from *tethers.com*)

BarnacleSat, a Picosatellite

In the wake of the RocketPod™ development, SSEL began conceptualizing the BarnacleSat (BSat) mission in the fall of 2004, and by December, a Tethers Unlimited Inc. (TUI) payload was identified. BSat is a technology demonstration mission with primary objectives of verifying RocketPod™ ejection and quantifying the performance of an electrodynamic tether (EDT) in LEO. In collaboration with TUI and Ecliptic Enterprises, the BSat mission is currently supported by the Montana NASA Space Grant Consortium (MSGC), whose mission requirements are defined by the aforementioned entities.

In addition to preparing a deployable payload for the RocketPod™'s first flight, BSat will also accommodate a TUI tether payload to demonstrate the utility of a one-kilometer tether. The form factor for BSat is the CubeSat Plus architecture which is similar to the CubeSat form. This architecture was advantageous as it provided the additional volume required for the tether to significantly increase the deorbit rate of the spent Delta II upper stage. Whereas nominally the RocketPod™ would be ejecting a free flying satellite, here the tether will connect the deployed spacecraft to the spent orbital booster. BSat's primary mission goal will be to increase the natural-orbital decay rate of the booster

following the completion of its primary mission. The design of BSat is governed by the following requirements:

1. Monitor the increase orbital decay rate of the booster;
2. Obtain *in-situ* GPS position data to gain insight on the deployment dynamics of a TUI deployer system;
3. Verify the survivability of a TUI EDT and the variety of COTS⁶ subsystem components in LEO.

ICDs and Spacecraft Configuration

The CubeSat Plus architecture offers approximately 30% more interior volume than its predecessor by increasing the 10 cm standard to approximate 14.5 cm in height; the 10 cm x 10 cm footprint remains unchanged. With this added height, the satellite will house a 1 km tether and all avionics within its interior. ICDs⁷ for both the RocketPod™ and P-Pod define the physical size of the spacecraft and are included here as they will be referred to frequently. Figure 1-7 is the P-Pod ICD and Figures 1-8 & 1-9 are the RocketPod ICDs. In this case the RocketPod™ design is meant to include the P-Pod requirements; this ensures that CubeSats remain compatible with the RocketPod™. It was the responsibility of the mechanical engineer to interpret these ICDs and design a structure that would properly interface with the deployer.

⁶ COTS: Commercial Of The Shelf

⁷ ICD: Interface Control Document

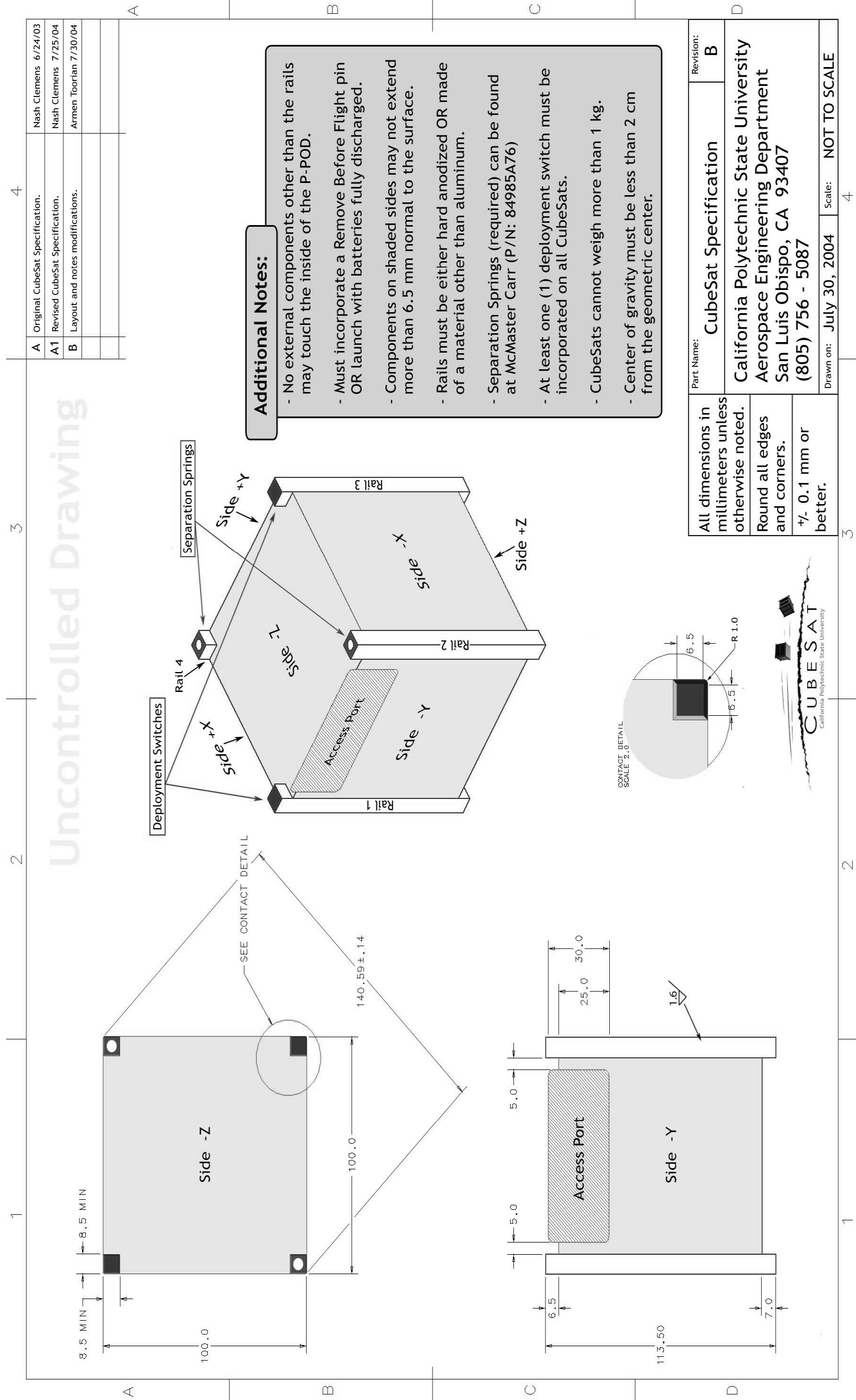


Figure 1-7: P-Pod ICD

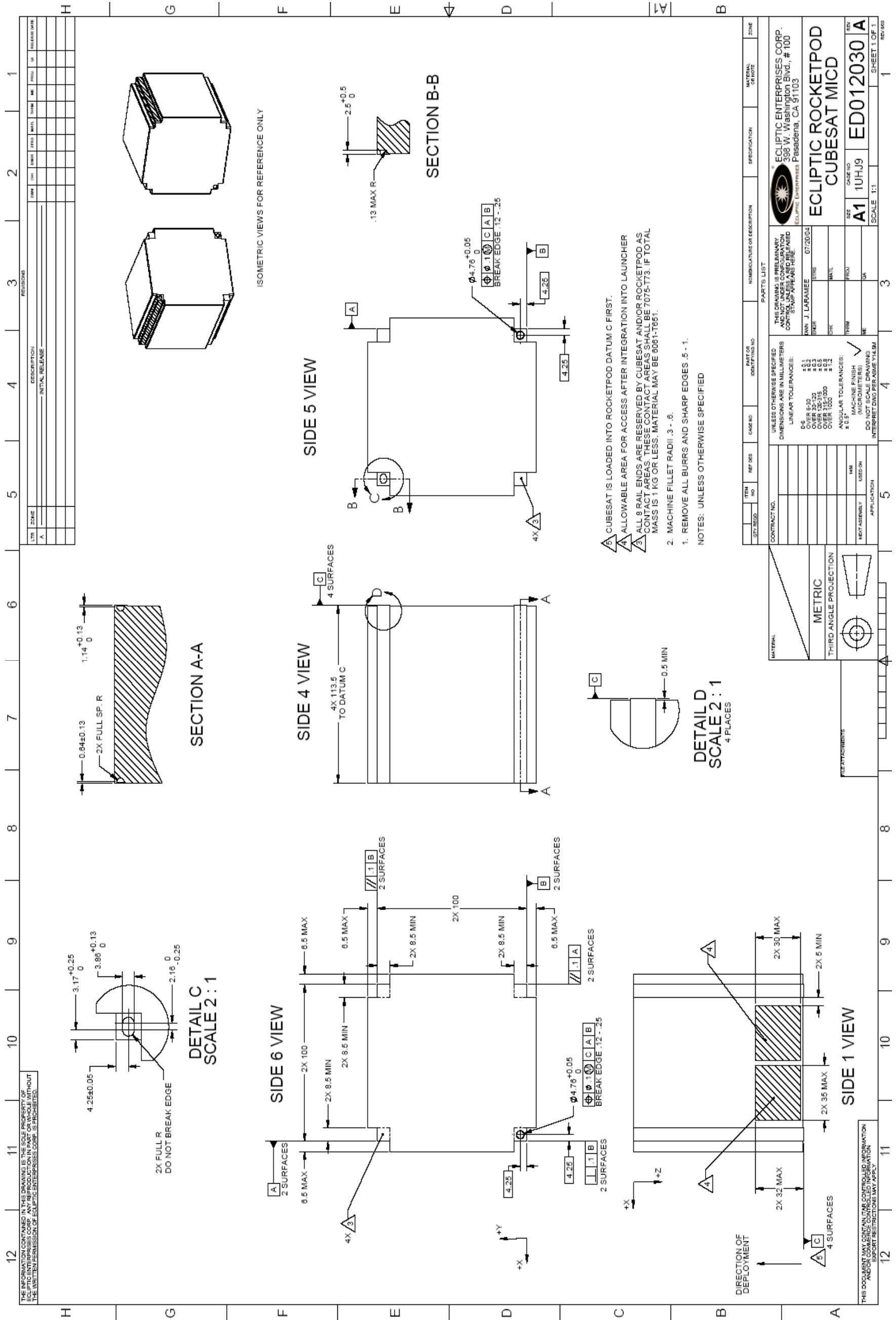


Figure 1-8: RocketPod ICD_1

2. MISSION

The BSat mission will fly as a Class-D secondary payload ejected from the RocketPod™ deployer. The RocketPod™ will remain externally attached to the orbit insertion stage of an ELV⁸, and await command for BSat deployment only after the completion of the booster's primary mission. The separation speed of BSat is tunable between the limits of 1 m/s – 3 m/s prior to launch: to satisfy the mission requirements it is anticipated that a slower ejection velocity will be chosen to aid in achieving the highest resolution of GPS data possible. Position and velocity data will then be recorded *in-situ* by BSat as a 1 km long conductive tether is unfurled. The study of the dynamics of gossamer structures in space is a complex problem that has been extensively studied; however, these studies could greatly benefit from space flight data, as adequate ground simulation is not possible. The secondary objective of the BSat mission will make use of the GPS data to validate tether-simulation packages such as TUI's TetherSim™. [Voronka; et al., 2005]

Phase 1 of this mission encompasses the successful deployment of BSat, which ends with the tether unwound to its full length and gravity-gradient stabilized. This period is mission critical and will require high-resolution monitoring of the satellite's onboard GPS receiver. The time scale on which gravity-gradient stabilization will occur is not predefined and will only be determined once the data has been retrieved and analyzed. As a result of this uncertainty, Phase 1 is currently defined to last ten days (upon deployment). Phase II then consists of the remaining 170 days where discretionary GPS

⁸ Expendable Launch Vehicle

data will be recorded in low resolution while the booster's ephemeris is monitored via radar on Earth. During the deployment and unfurling stage of the mission (Phase 1) high resolution GPS data will be recorded, stored, and relayed to SSEL's ground station. Phase 2 will have lower resolution GPS data acquisition and telemetry monitoring of the spacecraft's health; the booster's ephemeris will be monitored on Earth via radar. For BSat's mission timeline refer to Figure 2-1.

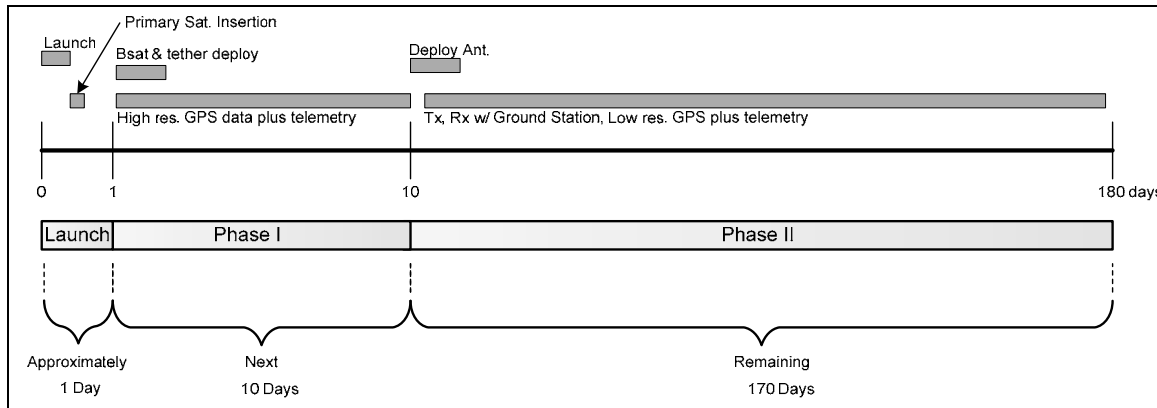


Figure 2-1: BarnacleSat Mission Timeline

BarnacleSat CONOPS

The concept of operations (CONOPS) for the BSat experiment is currently based on philosophies of the Terminator™ demonstrator mission along with heritage from the successful XSS-10 Mission⁹.

1. RocketPod™ will attach to a Delta II ELV as a secondary payload with BarnacleSat stowed within;
2. Once the second stage separates from the primary satellite RocketPod™ will await command to initiate the deployment of BSat;

⁹ XSS-10: Jan 30, 2003; Delta 7925-9.5 ELV primary launch of a GPS satellite. Secondary payload that was launch from the booster after completion of the ELV's primary mission, 800 km orbit, 40° inclination

3. After a period of time sufficient to ensure that the booster is oriented in a manner that will deploy the tether toward the preferred direction, a command will activate the RocketPod™'s separation mechanism to eject BSat. The initial ejection momentum will be sufficient to pull the tether out of the deployer to its full 1 km length. Passive braking will be used to halt the deployment in a gradual manner to prevent rebound of BSat, see Figure 2-2;
4. Phase I is the time-sensitive, absolutely critical period that will define mission success. This period is currently defined to last 10 days beginning on deployment and encompassing the acquisition and onboard storage of high-resolution spatial and velocity measurements;
5. BarnacleSat's communication antennas will be deployed on completion of Phase I so that chances of entanglement with the tether are at a minimum;
6. Phase II begins with the antenna deployment and will encompass the remaining orbital mission lifetime up to 170 days. During this period BSat will transmit data at least once per day to the SSEL ground station. While continuing to monitor telemetry and GPS data at discretionary rates, data from both phases will be downloaded and processed.



Figure 2-2: BarnacleSat deployed from Delta II upper stage

Subsystem Development and Systems Engineering

Detailed progress on BSat has been made and prototype construction and subsystem development is under way. The primary challenges in the satellite design have been to reduce the volume of spacecraft support systems within a bus that is only 30% larger than a standard CubeSat to accommodate a payload volume approaching 70% of the total spacecraft volume. An overview of some of the subsystems of note follows.

Structure. The RocketPod™ ICD dictates the physical structure of BSat so that the two entities will interface properly. Along with requirements from the ICD, the structure must withstand the specific g-loads, acoustic and vibrational loads, and the thermal environment of space. The chassis of BSat consists of both machined 6061 and 7075 aluminum sides fastened together with countersunk machine screws; refer to Figure 2-3. Launch rails are provided in the satellite to successfully interface with the RocketPod™. A tether shroud bracket that interfaces the tether payload within the confines of BSat's interior has been fabricated. Aluminum solar panels have been designed for securing solar cells to BSat's exterior. The estimated mass of the chassis is 670 grams while the satellite's overall mass cannot exceed 2 kg. The antenna deployment mechanism will consist of a Delrin® housing where the antenna is attached, curled up and kept in place by a nylon line wrapped around a resistor. Current will be sent through the resistor causing it to heat the line, and the antenna to unfurl. Three printed circuit boards are intended to carry the BSat subsystems: a C&DH board, a Power board, and a

Communications board. The GPS payload, batteries, and antennas will be mounted directly to the chassis.

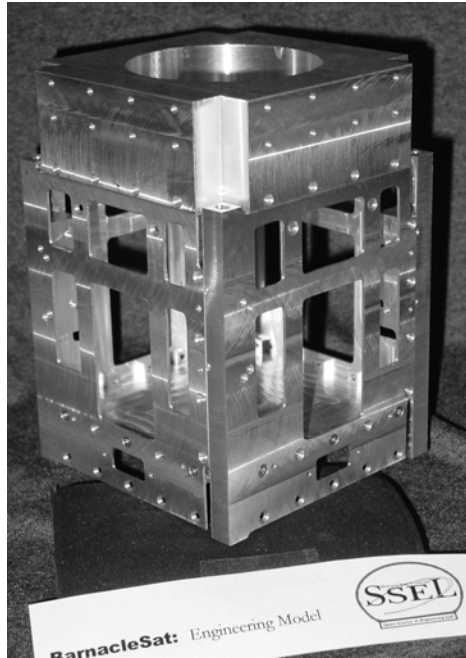


Figure 2-3: BSat Primary Structure (EDU)

Command and Data Handling (C&DH). The C&DH subsystem will control most of the internal electronics: communications uplink (Rx) and downlink (Tx), and organizing payload and telemetry data for transfer to the ground station [Obland; et al., 2001]. The choice of processors was driven primarily by SSEL's MEROPE mission heritage, power usage, processing speed, and adequate interfaces. The Motorola MC68HC812A4 (HC12) microcontroller is the centerpiece of the C&DH board and was chosen for its speed, processing power, 8 channel, 8-bit A/D, watchdog timer, 1k RAM, 4k programming space, external memory mapping, two sets of serial interfaces, and multiple interrupts for both software and hardware. Also mounted to the C&DH board is a 1 GB flash chip for data storage and additional A/D converters for capturing housekeeping and telemetry

data. The C&DH subsystem team is currently reevaluating the choice of microcontrollers as Motorola's new X-series supplements the HC12 with a more compatible 3.3 V model.

Power. The power subsystem consists of two 3.6 V Lithium Ion cells for energy storage, diode protected double-junction solar cells, and a 5 V and 3 V regulator; the prototype of which is seen in Figure 2-4. The double-junction solar cells from Spectrolab measure 3.1 x 7 cm and are 21.5% efficient. [Spectrolab] Solar cells will be mounted to all four sides of the satellite in such a manner that three sides will have four cells in two strings, and the fourth side will have a string of two cells. The solar cells will provide 4.0 V at a nominal 2.14 watts. The duty cycle budget reveals that the power system is required to generate a maximum 50 watt-hrs of energy per day.

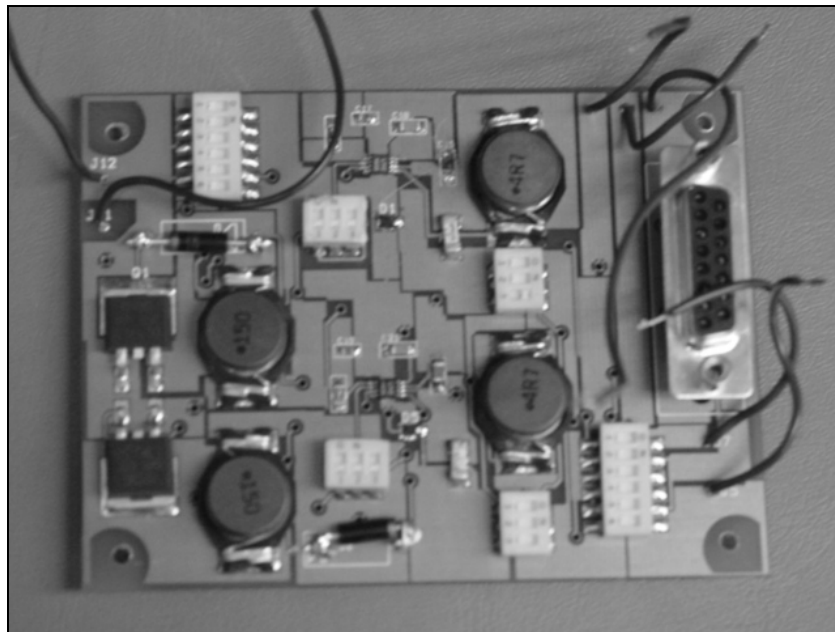


Figure 2-4: 5V Regulator, Test Board

Communications. The communications subsystem hardware consists of a Chipcon CC1000, an RF Micro Devices, RF 5110G amplifier, and an Alpha Incorporated, AW002R2-12 TR switch. Following in the footsteps of the MEROPE Mission the communications system onboard the satellite will be programmed to Tx and Rx at 437 MHz. These decisions were based upon characteristics of SSEL's ground station and to minimize the amount of work required to prepare the ground station for the BSat Mission. Thus, the CC1000 Transceiver will serve as both the RF receiver and transmitter onboard the satellite. The CC1000 has many favorable features, some of which are listed here: low power, programmable between 300-1000 MHz, 3.3V bus, built-in FSK modulation and Manchester encoding, and 9600 KBaud with an average current consumption of 9.3 mA. The major dilemma with a radio-on-a-chip is the limitations on the output power. A subsystem requirement defines a minimum output power of 1W for Tx which means that the amplifier would need to perform at a maximum 30 dBm of gain. The antenna consists of a half-wave dipole with two separate elements on opposing sides of the spacecraft. A single dipole antenna will be tuned to the 2 m transmissions while the 3rd harmonic will remain sufficient for reception. The Chipcon development board has been obtained and can be seen in Figure 2-5.

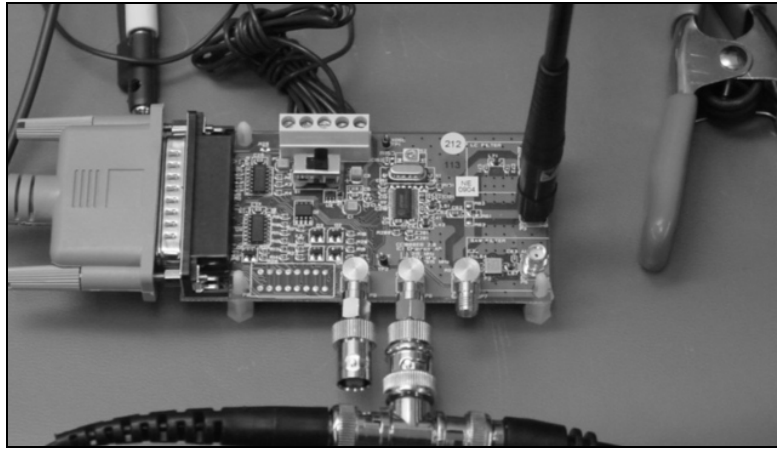


Figure 2-5: Chipcon CC1000 Dev. Board

GPS Payload. The essence of the BSat Mission as well as one of the most challenging aspects is the selection of a GPS receiver. A GPS unit is required within BSat to record position and velocity data in order to verify the performance of the tethered-satellite deployment. The necessity of removing the velocity and altitude restrictions on COTS GPS receivers has been found to be far too expensive for CubeSat-type applications. As currently identified, the Surrey Satellite Technology LTF SGR-05 GPS receiver (see Figure 2-6) is the preferred choice due to its micro-satellite form factor; however, the \$15K price tag has made it difficult for SSEL to acquire.

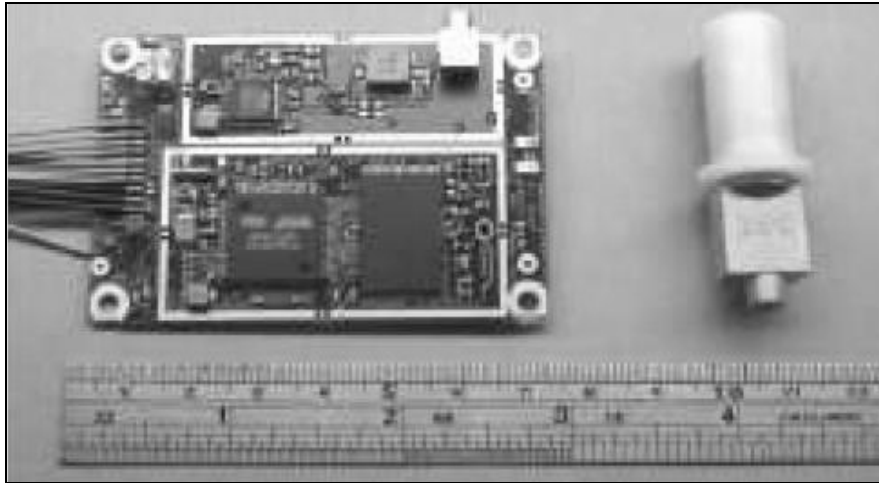


Figure 2-6: Surrey GPS Receiver

Tether Deployer. Under the MAST Mission TUI has developed a tether deployment system that is useful in micro-satellite applications. The deployment mechanism and tether shroud will be supplied by TUI and integrated into BSat as a single unit. Figure 2-7 shows the tether shroud next to the BSat EDU.



Figure 2-7: Tether Deployer Next to BSat EDU

Ground Station. Communication with BSat will be done through a preexisting ground station located on the MSU campus. This same station will also be responsible for ground-satellite communications between two other SSEL satellites: MEROPE and Maia. The ground station is made up of three main components. An Icom IC-910H satellite radio (transceiver), a LabJack U12 interface to control the rotors on the roof, and a computer with satellite tracking software, Nova for Windows, are used to control the movement of the antenna array and to also handle communication and information from the satellite. The antenna array, seen in Figure 2-8, has two yagi-style antennas tuned to the 70 cm and 2 m bands. The 70 cm antenna will be used as the transmission antenna and the 2 m antenna will be used as the receiving antenna.



Figure 2-8: MSU Yagi-Antenna

3. BACKGROUND

This section contains an overview of the orbital debris concern, the physics of a tether as a solution, the inherent concerns of the launch vehicle interface, the on-orbit thermal environment and the role of heat transfer, thermal control techniques, and the analytical strategies for assessing the mechanical characteristics of the spacecraft.

Orbital Debris

The motivation behind this technology demonstration is twofold; to demonstrate new space-technologies for the picosatellite class of spacecraft, and to demonstrate a conscious experimental effort in regards to the growing orbital debris problem. The population of man-made orbital debris is growing rapidly, dominating the meteoroid environment in all but the micrometer size range [Voronka, 2005]. The NASA Orbital Debris Program Office (NODPO) states that collision with orbital debris is a hazard of growing concern as historically accepted practices and procedures have allowed man-made objects to accumulate in orbit. As a result the NODPO has taken steps to mitigate this concern with several mandates; e.g. requiring the depletion of onboard energy sources after the completion of the mission, and limiting the orbit lifetime after mission completion to 25 years [NSS 1740.14, 1995]. To meet this requirement many satellites and other orbital platforms maneuver into a disposal orbit trajectory.

The USSTRATCOM Space Surveillance Network [2004] estimates that of the 9,233 objects that are large enough to trace, 2,927 are satellite payloads, and 6,306 are classed as rocket bodies and debris; this is presented graphically in Figure 3-1 and Figure 3-2.

Conventional techniques for performing deorbiting maneuvers have required missions to factor into their mass budget, a particular amount of reserve propellant. Propellant not only takes up significant volume but is also comparatively heavy. This leads into the unique role of a conductive tether and the physics that suggests a possible new way of deorbiting a spacecraft or rocket body.

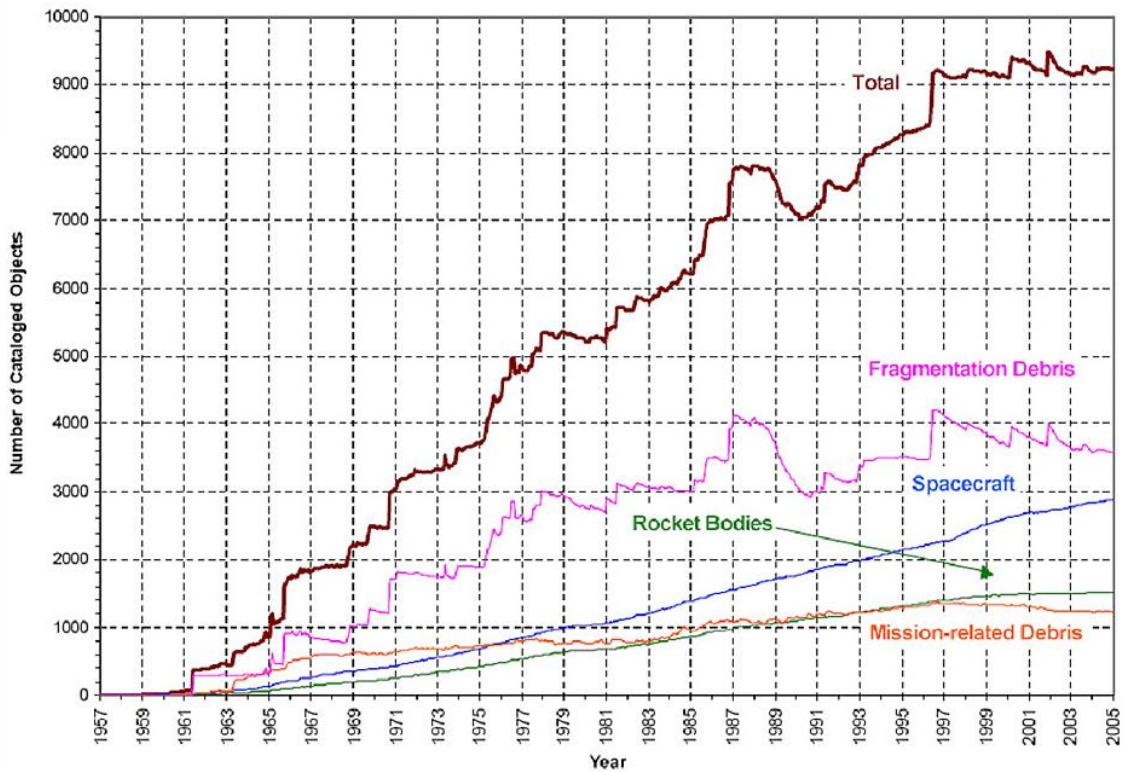


Figure 3-1: Catalog of Orbital Debris (Reproduced from the *ODQN*¹⁰, 2005)

¹⁰Orbital Debris Quarterly News

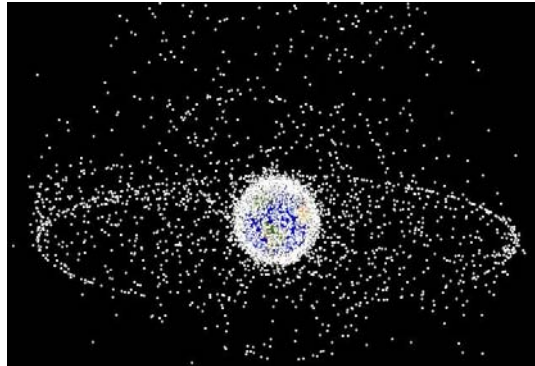


Figure 3-2: Orbital Debris as Observed from GEO (*Reproduced from ODQN, 2005*)

Tether Payload and Electrodynamic Drag

An electrically conductive tether providing electrodynamic drag is thought to be a cost-effective substitute for the propellant consuming rocket motors. Studies of an electrodynamic tether have also shown significant mass savings compared to conventional rocket-based deorbit systems. Moreover, because it uses passive electrodynamic drag to achieve deorbit, it can deorbit the spacecraft even if the host has lost power and control functions [Forward and Hoyt, 1998].

A tether constructed from a conductive, gossamer medium will provide an electrical interaction between the tether itself and the ambient plasma. The electrodynamic interaction at orbital speeds traveling transversely to Earth's magnetic field will induce current flow; similar to an electric motor. This current will interact with Earth's magnetic field to generate a Lorentz $\mathbf{J} \times \mathbf{B}$ force on the tether as seen in Figure 3-3. This is the very essence and physics behind an EDT. The kinetic energy of the spacecraft will begin to degenerate at the expense of heat generated by the current flowing through the ohmic resistance of the tether. Consequently, the orbital energy of the spacecraft will

decay, causing it to deorbit far more rapidly than it would naturally [Forward and Hoyt, 1998].

The tether payload onboard BSat is a proprietary product of TUI made of a mixture of Aracon and Spectra materials. A 1 km tether will be stowed within the spacecraft and wound inside of a composite shroud. The composite is made of carbon fibers with an epoxy resin which was injected via a vacuum mold to ensure out-gassing compliance. This information will be elaborated on as it plays a significant role in the thermal characteristics of the satellite. As seen in Figure 3-4, the tether is of Hoytether™ construction by which individual strands are braided together in an open-net structure that provides redundant load paths and protects against single point failure in the event of micrometeorite impact. In order to electrically insulate the spacecraft from the tether and to prevent the RF¹¹ antennas from electrical shorts, a short section of the tether nearest the satellite will be constructed of nonconductive materials.

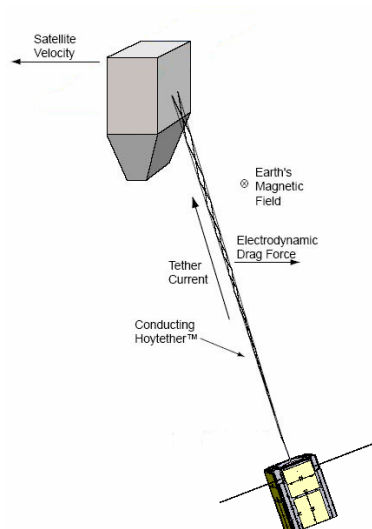


Figure 3-3: EDT Concept (*Reproduced from Forward and Hoyt, 1998*)

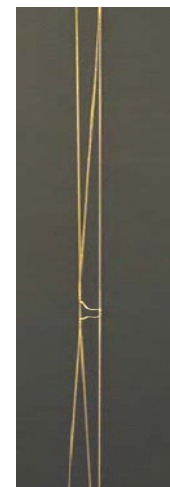


Figure 3-4: Hoytether with 2 primary and 1 secondary lines

¹¹ Radio Frequency

Gravity Gradient

The subject of gravity gradient stabilization was introduced in the mission description and is an important characteristic that defines the orientation/location of BSat's RF antennas. In the absence of a physical attitude system onboard BSat, the electrodynamic and atmospheric drag associated with a conductive tether will provide an inherent attitude system. This is best understood by the implementation of force-balance equations, but will be omitted here as this thesis focuses on the spacecraft's mechanical systems and not the physics of a tether.

In the absence of resultant forces in the form of atmospheric or electrodynamic drag, a nonconductive tether would be coincident with the local vertical. However, with the implementation of a conductive tether, the inherent electrodynamic drag causes the equilibrium position of the tether's center of mass to lag at an angle, α , in the orbit plane. The shear mass of BSat attached at the end of tether will experience a gradient force, F_{GB} , which is the resultant of a combined gravity and centrifugal gradient. The magnitude of this gradient force would then depend on BSat's radial distance from the booster's center of gravity. As shown in Figure 3-5, this force acts in the vertical direction along the radius vector of BSat towards nadir¹². For this reason BSat's dipole RF antenna will be oriented perpendicular to this direction; thus, optimizing the radiation pattern of a dipole antenna.

¹² Nadir – Direction towards center of Earth

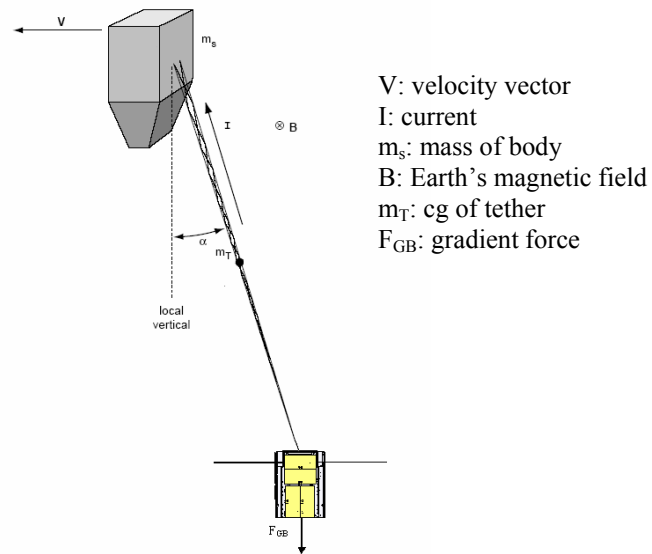


Figure 3-5: BSat Gradient Force (Reproduced from Forward and Hoyt, 1998)

Launch Vehicle Environment

Role of the Structure

The performance of a spacecraft's structure is commonly divided into several areas of interest: environments on Earth, those during launch, and those while on-orbit. These environments drive the design requirements of the spacecraft's structure; it is the responsibility of the structural designer to ensure survivability and functionality of both structural and nonstructural components in response to these environments. In addition to supporting all of the spacecraft's subsystems, the structure must also exhibit external features to ensure attachment to the LV and accommodate ordinance-activated separation [Wertz and Larson, 1999]. As discussed previously, the packaging of BSat is defined by Figure 1-7 through Figure 1-9 such that by complying with these specifications, BSat will adequately interface with the deployer and the LV. BSat's pointing accuracy and position stability have been defined by the EDT payload; its inherent attitude response to

the electromagnetic phenomenon is strongly dependent upon the gravity gradient force, which in return defines BSat's on-orbit performance. It is of common industry knowledge that the most critical structural requirements and dynamic envelope¹³ are defined by the selected launch vehicle; in the case of BSat, the Delta II and RocketPod™, respectively. As BSat was designed to meet the LV requirements, it is thought that the spacecraft offers a robust design to all Earth-based¹⁴, induced environments. The GEVS¹⁵ initiates this by stating: “...*the design and verification of payloads shall not be burdened by transportation and handling environments that exceed stresses expected during launch* [Baumann, 1996].” It is in this section that those load-causing events will be addressed and will focus on what Sarafin [1995] describes as the most complex load-causing environment, launch.

As the launch vehicle contractor, Boeing offers the *Delta II Payload Planner's Guide* (PPG) to payload customers who intend to use their launch vehicle for access to space. This document describes the launch environment and details extensively the requirements for a satellite payload's rigidity, and response to inertial loads caused by transient and steady-state accelerations. A spacecraft's fundamental frequency¹⁶ typically defines its rigidity and response to forces from both engine oscillations and aerodynamic sources [Wertz and Larson, 1999]. Steady-state acceleration introduces quasi-static loads on the spacecraft and is defined as an evenly distributed, uniformly induced load; these loads

¹³ dynamic envelope- space allocation

¹⁴ handling on the ground

¹⁵ **General Environmental Verification Specifications**

¹⁶ lowest natural frequency corresponding to first mode of vibration

induce harmonic vibrations. Transient loads or dynamic loads are associated with engine thrusts and sound pressure which induce random vibration of the structure.

Harmonic Vibrations and Steady-State Acceleration

Beginning with lift-off the booster engines introduce a quasi-static load on the spacecraft in the form of axial acceleration that gradually increases until the boosters deplete the stored propellant. As seen in Figure 3-6 this event can occur several times during launch depending upon the LV configuration. The challenge here is to identify the events that are critical, then to predict the induced loads. For the Delta II, as seen in Figure 3-7, it is extremely clear that at MECO the spacecraft will experience its maximum acceleration. Because the primary payload has yet to be identified this value is inferred to be the maximum of 8 g's.

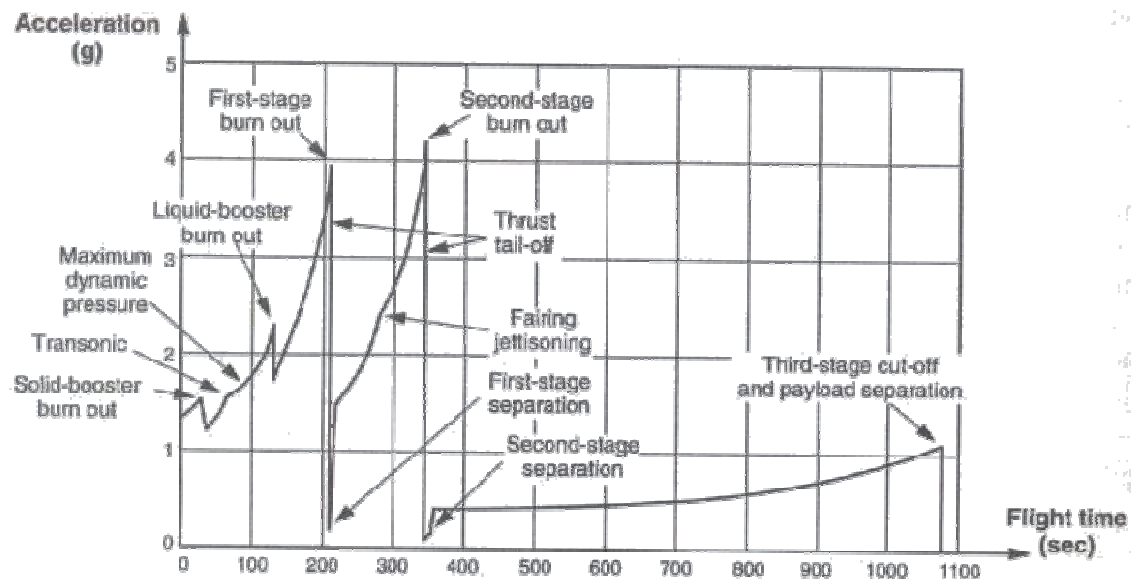


Figure 3-6: Axial Acceleration Profile for Ariane LV

(Reproduced from Sarafin, 1995)

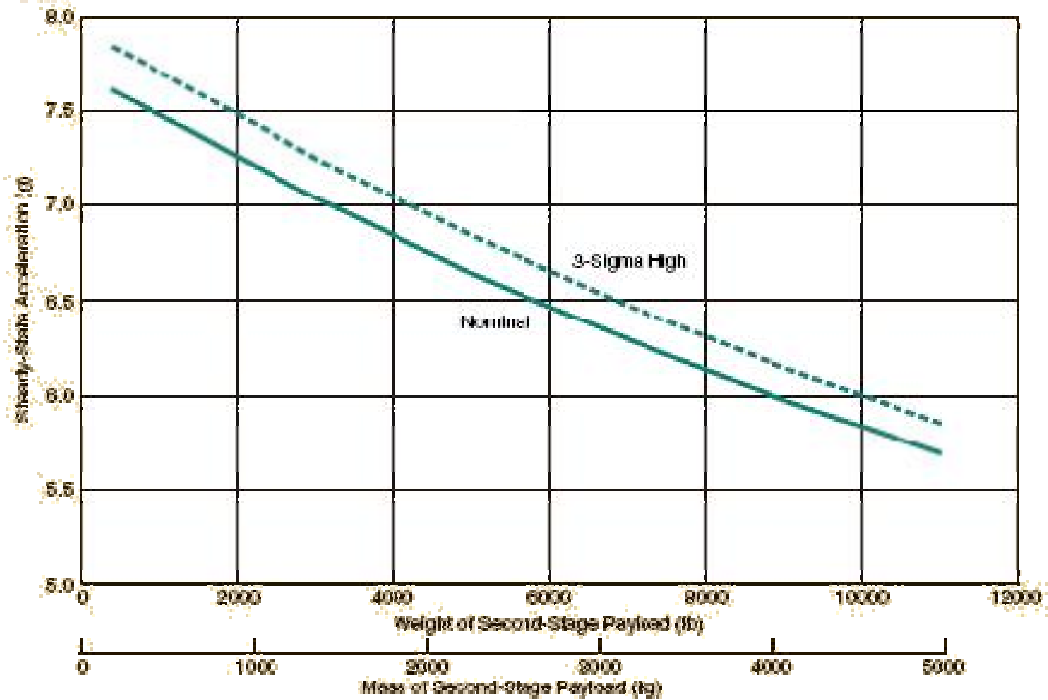


Figure 3-7: Axial Acceleration at MECO for Delta II (Reproduced from Delta II PPD, 2000)

To utilize these load factors as an analytical tool the PPD also states that the spacecraft's fundamental axial and lateral frequencies must exceed 35Hz and 15Hz, respectively. These values are tailored to avoid the LV's natural frequencies for two important reasons: to ensure that the spacecraft will experience much lower loads, and to protect the LV's control system from the adverse effects of coupling the responses of both the spacecraft and the LV. Under these conditions the spacecraft experiences an external force from the LV and responds by vibrating, known as a forced vibration. *"If the frequency of the external force [LV] coincides with one of the natural frequencies of the system [spacecraft], a condition known as resonance occurs, and the system undergoes dangerously large oscillations"* [Rao, 1995]. Table 3-1 below is information

taken directly from the PPD and is the foundation for the analytical routines used to assess the structure's stability during launch.

Table 3-1: Load Factors and Frequency Data of Delta II

LV	Load Factors (g's)						Min. Fundamental Frequency (Hz)	
	Lift-off		Max. Airloads		Stage I/II Events			
	Axial	Lateral	Axial	Lateral	Axial	Lateral	Axial	Lateral
Delta (all series)	+0.2 -2.2	±2.0	—	—	-5.7 -6.0	—	35	15

Launch Configuration

The typical launch vehicle consists of a series of stages, each associated with a critical event and each associated with a unique influence on the stowed payload. These loads are categorized as either quasi-steady¹⁷ or transient. As depicted in Figure 3-6 from above, the variation arises when a booster is steadily consuming its stored propellant where upon depletion, the stage separates from the LV and the engines from the next stage ignite. This approach maintains efficiency by incrementally shedding unnecessary mass [Sarafin, 1995]. Staging events occur any time a rocket engine ignites or shuts down exposing the payload to a transient force; in the interim, the payload experiences static loading. Figure 3-8 depicts the stages of a Delta II.

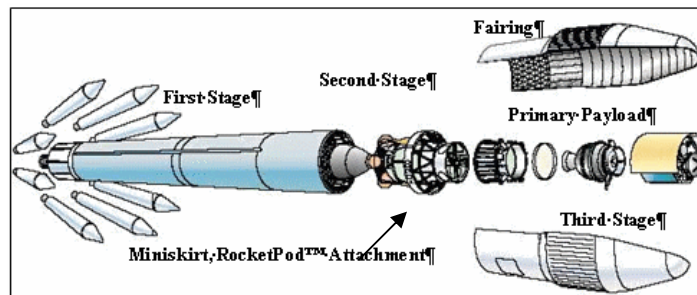


Figure 3-8: Configuration of a Delta II Launch Vehicle (*Reproduced from Delta II PPG; 2000*)

¹⁷ quasi steady – relatively steady-state

Load Factors

It is common industry practice to specify load factors in quantifying the loading environment during launch. Load factors are multiples of Earth's gravitational acceleration (g's) at sea level and they are provided to the payload customer in the PPD. An example of a load factor representing an inertial force is seen in Figure 3-9. A load factor represents the inertia force acting the spacecraft and distinction is made between the axial and lateral directions.

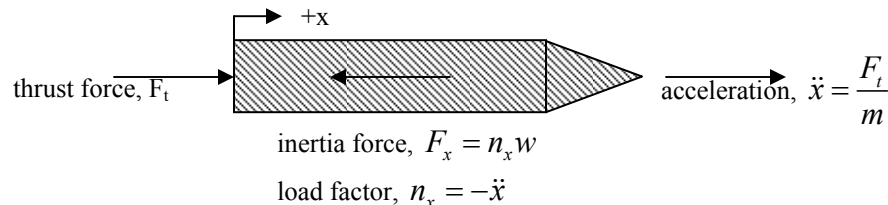


Figure 3-9: Load Factor Depiction (Reproduced from Sarafin, 1995)

Random Vibrations

Load factors which quantify quasi-steady accelerations are termed *deterministic loads* simply because they offer information as a function of time. With the introduction of random vibrations the value of a deterministic load becomes inappropriate in discussion because random vibrations are both a function of time and location. Termed *nondeterministic* or *probabilistic*, the value of the excitation cannot be predicted; however, it is possible to estimate the average or rms¹⁸ values of the excitation. Both load types are depicted in Figure 3-10.

¹⁸ root mean square

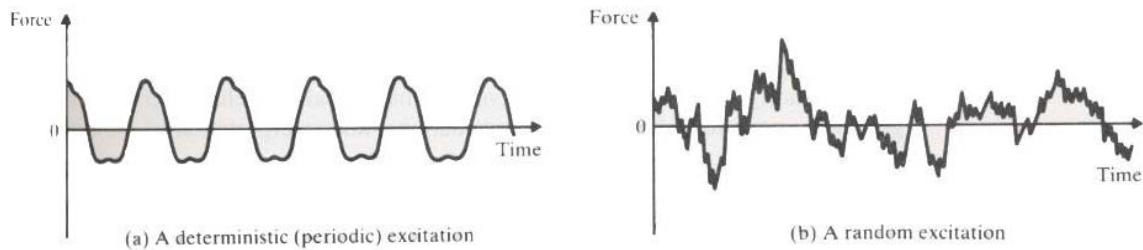


Figure 3-10: Vibration Types (*Reproduced from Rao, 1995*)

The major source of random vibrations on a spacecraft is the acoustic noise generated from the LV engines. Acoustic loads are introduced to the spacecraft by aerodynamic turbulence when the LV passes through the transonic¹⁹ portion of its flight where it is assumed that these loads exhibit some statistical regularity. These types of loads are statistically estimated and are assumed to have a Gaussian distribution, which determines the percentage of time the vibration is within certain limits [Wertz and Larson, 1999].

To examine the frequency content and quantify the magnitude of a random process the PPD publishes *power spectral density* (PSD) data for predefined frequency ranges. “The term “power” is a generic term that can represent acceleration, velocity, displacement, force, strain, etc... [Sarafin, 1995].” In other words, to quantify the response to random accelerations, knowledge of the mean-square acceleration is determined at specific frequencies. The PSD at frequency f , is obtained by taking the derivative of the acceleration function and dividing by a selected frequency band. The resultant is the magnitude of the vibrational power within a frequency band whose center is f . PSD is commonly expressed in units of g^2/Hz ; where upon taking the square root of

¹⁹ transonic – speed of sound barrier

the area under the PSD curve, the rms acceleration due to the random event is obtain.

Figure 3-11 below depicts a typical PSD curve plotted on log-log paper.

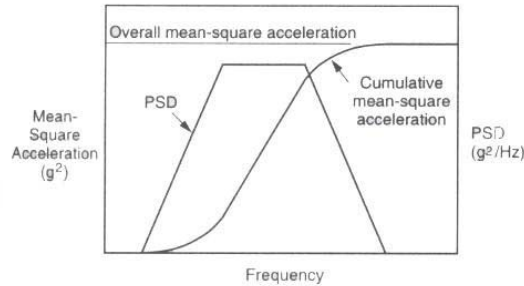


Figure 3-11: Power Spectral Density (Reproduced from Sarafin, 1995)

Acoustic Loads

The acoustic environment is a function of both the launch vehicle and launch pad configurations. It is presented in terms of the sound pressure level (SPL) and depicts the combination of sound-energy which is reflected from the launch pad and the aerodynamic smoothness of the launch vehicle. Acoustic excitation is rapidly time-varying and includes waves with many different frequencies; as a result, the spacecraft structure will have a *vibroacoustic response*. Relative to the random vibration discussion, the SPL is representative of the rms pressure within a particular frequency band and is expressed in units of decibels, dB. Figure 3-12 expresses the Delta II acoustic data as it is presented to payload customers. To put this data in a form which is useful for determining a structure's response, the SPL data is manipulated with Equations 3.1 and 3.2 to yield acceleration spectral density, [g²/Hz].

$$P(f) = \sqrt{\frac{1}{T} \int_0^T p(f, t)^2 dt} \quad (3.1)$$

$$SPL(f) = 20 \log \frac{P(f)}{P_{ref}} \quad (3.2)$$

The rms pressure $P(f)$ is obtained by the integration of the pressure at time t within a selected frequency band and evaluated over the specified time domain. For clarification a decibel (dB) is the logarithm of the ratio between $P(f)$ and the reference pressure P_{ref} , typically set at 2.0×10^{-5} Pa [Sarafin, 1995].

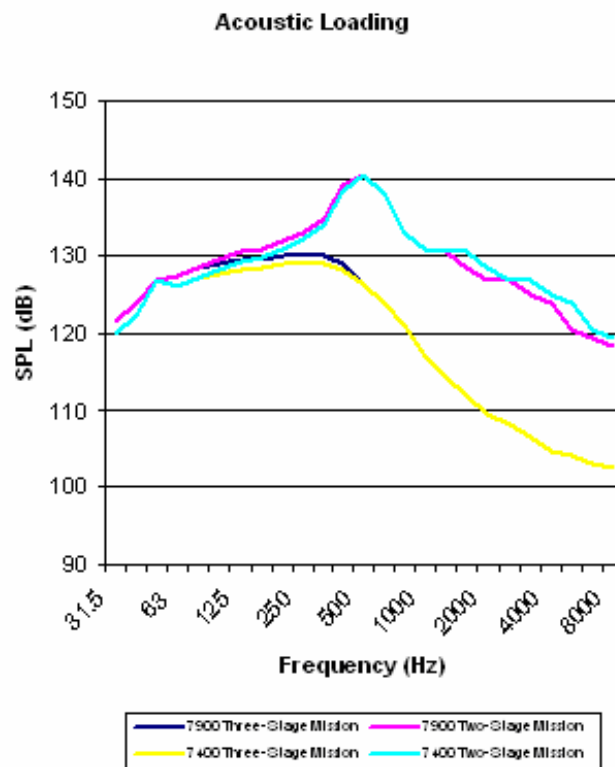


Figure 3-12: Delta II SPL Curve

SPLs are plotted at the center frequencies of one-third octave bands, on a log scale, over the range of 20 to 10,000Hz. The structural constituents most susceptible to acoustic loads are typically light in weight and large in surface area. For BSat, particular

attention focused on the PCBs²⁰ which fit this description and are intended to mount perpendicular to the axial acceleration. Table 3-2 and Figure 3-13 below present the data of random vibrations for the Delta II LV.

Table 3-2: Acceleration Spectral Density for Delta II

FREQ(Hz)	ASD(G ² /Hz)	dB	OCT	dB/OCT	AREA	Grms
20.00	0.0016	*	*	*	*	*
300.00	0.0600	15.74	3.91	4.03	7.68	2.77
700.00	0.0600	0.00	1.22	0.00	31.68	5.63
2000.00	0.0210	-4.56	1.51	-3.01	75.78	8.70

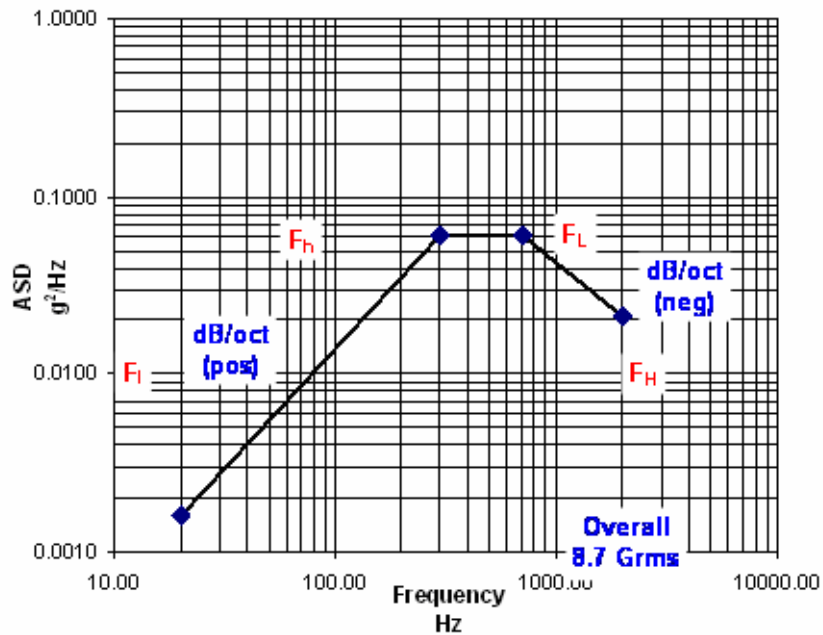


Figure 3-13: ASD Curve for Delta II

Thermal Environment

Spacecraft thermal control is a process of energy management in which environmental heating plays a major role [Gilmore, 2002]. As illustrated in Figure 3-14

²⁰ Printed Circuit Boards

there exist three unique forms of environmental heating: direct sunlight, IR²¹ radiation from Earth, and sunlight reflected off Earth²². The depiction below expresses the environment that BSat will be subjected and a basis by which the thermal environment was investigated to determine the most appropriate thermal control technique.

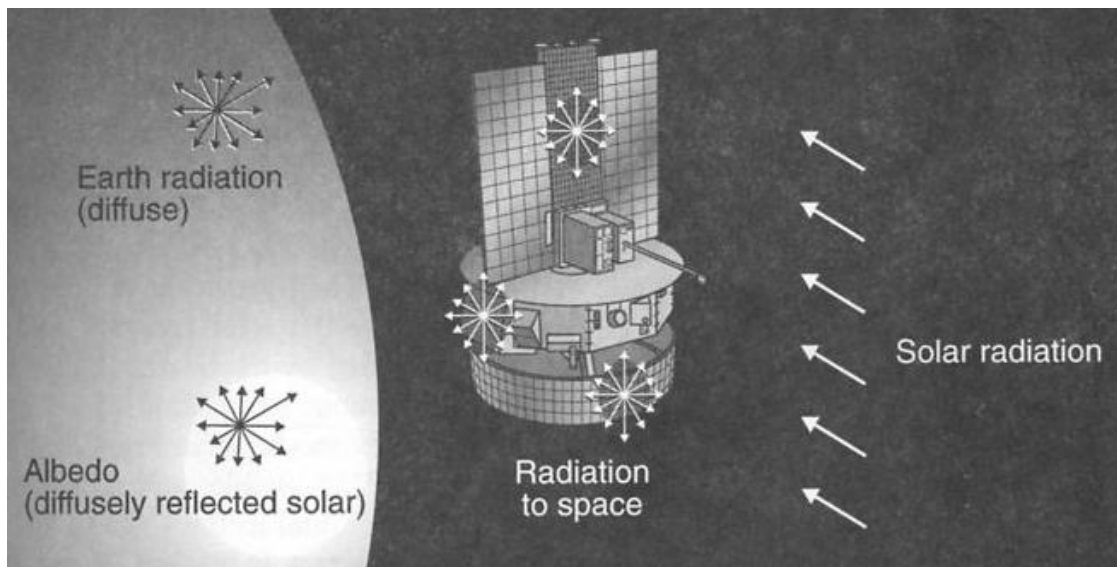


Figure 3-14: Satellite Thermal Environment (*Reproduced from Wertz and Larson, 1999*)

Orbital Parameters and Geometry

Prior to the discussion of the orbital thermal environment it is essential to address some of the key features that influence an Earth-orbiting satellite. Most fundamental and certainly most influential were the discoveries of Johannes Kepler who in 1605, published that the orbit of each planet is an ellipse, with the Sun at one focus. This statement, which was later mathematically verified by Isaac Newton, not only applies for celestial bodies, but also to a satellite's orbit with Earth at one focus. There are many

²¹ IR - infrared

²² Reflected sunlight off Earth is called albedo

ancillary equations which support Kepler's discoveries; however, most geometrically relevant are the key parameters presented in Figure 3-15. The eccentricity of the ellipse is equal to c/a and is a measure of the deviation of the ellipse from a circle. As in the case of BSat and most low-earth orbiting satellites, the orbital geometry is circular²³.

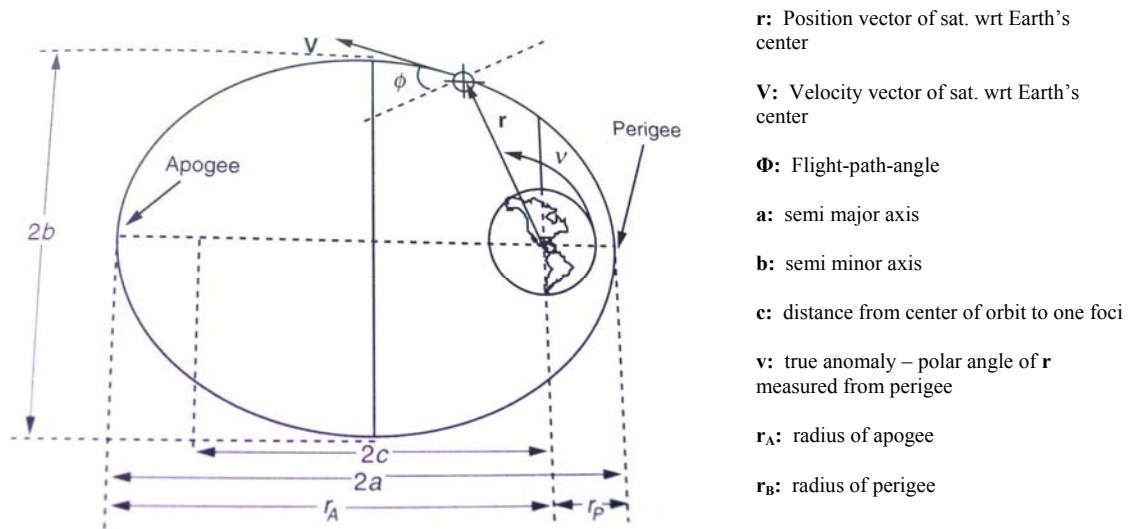


Figure 3-15: Geometry of an Ellipse & Orbital Parameters
 (Reproduced from Wertz and Larson, 1999)

In addition, there is significant amount of information which can be inferred from Figure 3-15 that is relevant to a satellite's thermal environment. In many incidences, planets are considered satellites whose orbit center is the Sun. Describing the thermal environment of an Earth-orbiting satellite requires defining Earth's position in its orbit relative to the Sun. Astronomical characterization of Earth will be discussed here as it inherently influences the environment of a satellite.

²³ circle – an ellipse with eccentricity equal to zero

In a given year, Earth processes around the Sun to complete one full orbit. Earth's orbit around the Sun is elliptical meaning that the intensity of the sunlight reaching Earth varies depending on Earth's distance from the Sun. At summer solstice, Earth has entered its apogee portion of its orbit and the intensity of the Sun is at a minimum. At perigee or winter solstice, Earth is closest to the Sun and experiences its greatest solar intensity. Aside from this position vector characterization, it is known that Earth rotates once every 24 hours about its spin axis which is inclined 23.4 degrees with respect to the ecliptic²⁴. Given that the relative distance between the Earth and Sun is so much greater than the distance between a LEO satellite and Earth, the solar intensity at Earth is correlated, or equal to that incident on the satellite. Concurrently, the amount of time a satellite spends in the Sun is highly dependent upon the satellite's apparent position with respect to Earth. This orbital parameter is defined by the satellite's inclination and is the measure of the angle between the orbit plane and Earth's equator. Figure 3-16 emphasizes the orbital parameters which are commonly used in the analysis of environmental heating. The lines of ascending and descending nodes are the points in the orbit at which the satellite crosses Earth's equator while traveling from south to north and conversely from north to south, respectively.

²⁴ ecliptic – plane of the sun as view from Earth's center

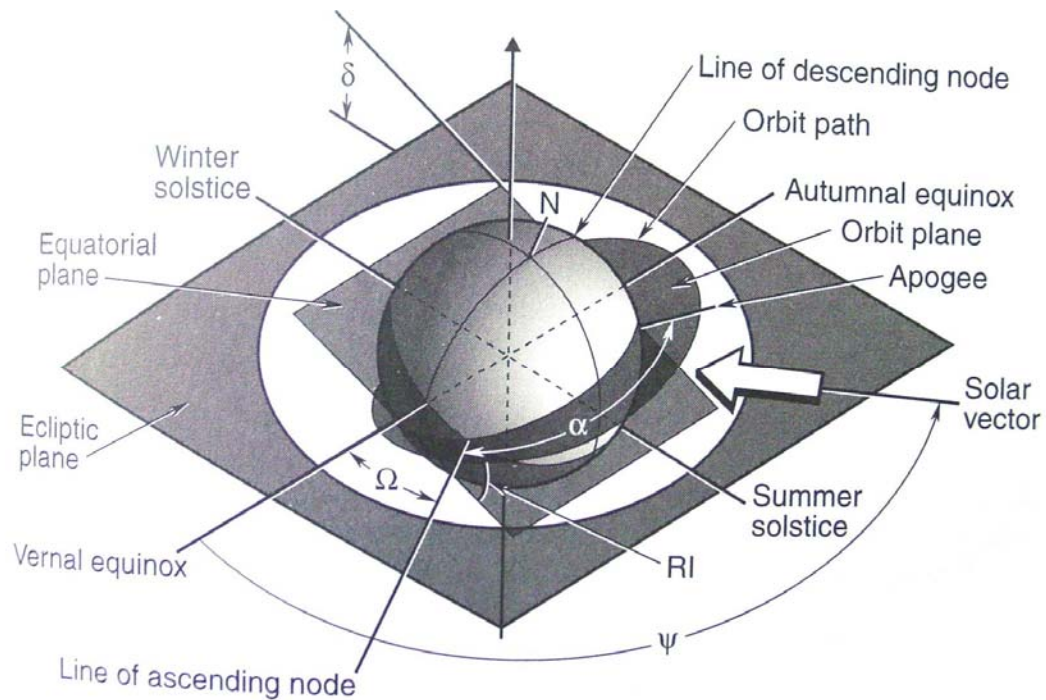


Figure 3-16: Orbital Parameters (Reproduced from Gilmore, 2002)

In discussion a satellite's altitude is frequently measured as the distance between the satellite's orbit and the surface of Earth; however, when defining a satellite's orbital period, this distance is measured from the center of Earth to the satellite's orbit and is quantified by the following equation:

$$P = 2\pi \left(\frac{a^3}{\mu} \right)^{1/2} \quad (3.3)$$

where P is the period, μ is the product of the universal gravitational constant and the mass of the Earth ($\mu_{\text{Earth}} = 3.98603\text{E}14 \text{ m}^3/\text{s}^2$), and a is the semi major axis of the orbit. While the orbital period of a satellite essentially remains constant over the life of the mission the eclipse fraction does not and is dependent upon the satellite's inclination.

Beta Angle

A satellite's inclination is a starting point for the investigation of another parameter of interest to the thermal analysts, the orbit beta angle (β). The orbit beta angle shown in Figure 3-17 is the angle measured between the orbit plane and the solar vector and can vary between ± 90 degrees. A satellite's eclipse fraction is dependent upon β and varies continuously because of orbit nodal regression and the change in the Sun's right ascension and declination over the year [Gilmore, 2002]. In other words, because the position of the sun progresses from vernal equinox²⁵ throughout the year and because its angular position above or below the equator changes, a satellite's exposure to the sun will also vary. Figure 3-17b illustrates a sun-synchronous, polar orbit in which the orbit circle is tangent to the disk of the Earth.

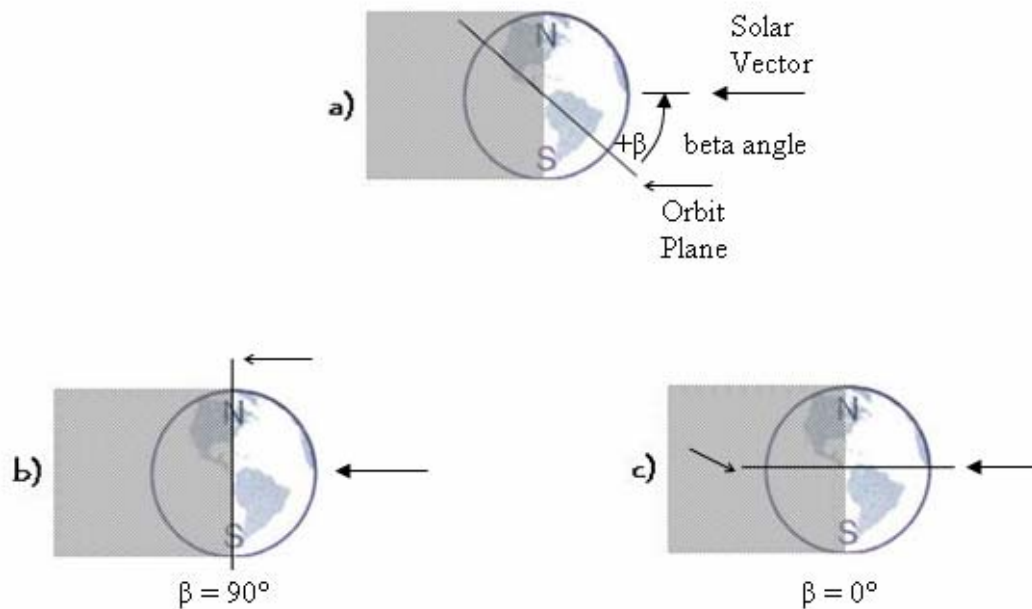


Figure 3-17: Orbit Beta Angle (Reproduced from Gilmore, 2002)

²⁵ first day of spring

In contrast Figure 3-17c illustrates an equatorial orbit in which the ecliptic is in the orbit plane signifying a maximum eclipse fraction. Throughout the year a satellite's beta angle will move slowly up and down the globe plot; thus, resulting in various eclipse fractions. Mathematically, the orbit beta angle is defined as:

$$\beta = \sin^{-1}(\cos \delta_s \sin RI \sin(\Omega - \Omega_s) + \sin \delta_s \cos RI) \quad (3.4)$$

where δ_s is the declination of the Sun, RI is the orbit inclination, Ω is the right ascension of the ascending node, and Ω_s is the right ascension of the Sun. The eclipse fraction of a circular orbit can then be calculated by the following relation:

$$f_E = \frac{1}{180^\circ} \cos^{-1} \left[\frac{(h^2 + 2Rh)^{1/2}}{(R+h) \cos \beta} \right] \quad (3.5)$$

where f_E is the eclipse fraction, R is Earth's radius (6378 km), h is the orbit altitude, and β is the orbit beta angle. The beta angle is the single most influential orbital parameter of interest to the thermal engineer since the eclipse time decreases with an increase in β . The beta angle can vary from 0 to a maximum that equals the orbit inclination plus the maximum declination (23.4 degrees) of the Sun [Gilmore, 2002]. Below are two figures; Figure 3-18 depicts the variation in orbit beta angle over the course of a year, and Figure 3-19 details the dependency of the eclipse fraction on β and altitude.

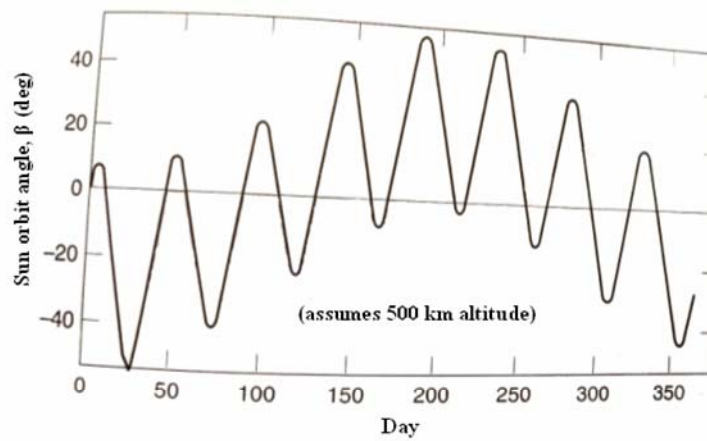


Figure 3-18: Sample of Orbit Beta Angle (*Reproduced from Lockheed Martin*)

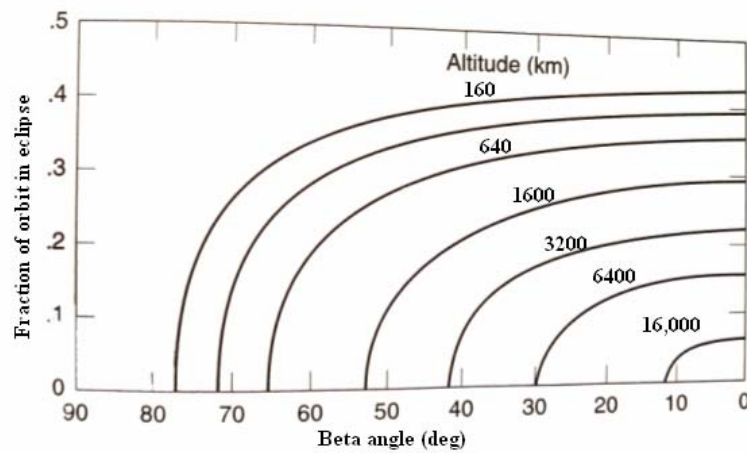


Figure 3-19: Depiction of Eclipse Fraction vs. β and Altitude (*Reproduced from Gilmore, 2002*)

Following common industry practices, the thermal analysis conducted on BSat can be summarized as a parametric study that was bounded by the limits of anticipated orbit beta angles.

Incident Radiation

As illustrated in Figure 3-14 the only significant sources of environmental heating are direct sunlight, Earth's albedo, and IR energy emitted by Earth. As alluded to earlier the

overall thermal control of a spacecraft is achieved by balancing the heat emitted by the body against these incident heat loads and the internal heat generated by the various subsystems. From the first law of thermodynamics the surface of a satellite must satisfy the conservation of energy and can be expressed as

$$Q_{sat} = Q_{solar} + Q_{albedo} + Q_{Earth} + Q_{gen} \quad (3.6)$$

where,

Q_{sat} = total energy input to satellite (energy that is available to change temperature)

Q_{solar} = solar absorption energy

Q_{albedo} = reflected solar energy from planet

Q_{planet} = emitted energy from Earth

Q_{gen} = internal heat generation from satellite components

The first three terms: Q_{solar} , Q_{albedo} , and Q_{planet} are radiation heat transfer modes while Q_{sat} represents the total energy balance for the surface of the satellite. When $Q_{sat} = 0$ the surface is in equilibrium with no heating or cooling occurring. When $Q_{sat} < 0$ the surface is cooling and when $Q_{sat} > 0$ the surface is warming. Each term in Equation 3.6 is presented in detail in the following discussion.

Electromagnetic Spectrum. Each of the radiation heat transfer modes represented on the right-hand-side of Equation 3.6 is a wavelength dependent quantity owing to a specific portion of the electromagnetic spectrum. As many thermal control techniques are based upon the quantization and knowledge of the electromagnetic spectrum, it is important to first address thermal radiation as the propagation of electromagnetic waves. Radiation is attributed to the standard wave properties of frequency ν and wavelength λ [Incropera and Dewitt, 1996]. For radiation propagation in a vacuum the two properties are related by:

$$\lambda = \frac{c}{\nu} \quad (3.7)$$

Where c is the speed of light in a vacuum: $c = 2.998E8$ m/s. At any temperature above absolute zero (0 °K), all matter continuously emits electromagnetic radiation and is referred to as blackbody²⁶ radiation. In actuality no surface is a perfect blackbody and the actual spectrum of emitted radiation is dependent on the surface characteristics of objects ranging from picosatellites such as BSat, to large objects such as the Earth or Sun.

Shortwave Radiation. Radiation from the Sun, referred to as *solar radiation*, is the primary source of energy exploited by satellites. The Sun emits radiation as approximately equivalent to the emission of a blackbody at 5800 °K. From the Planck distribution, shown in Figure 3-20, the spectral²⁷ emissive power of a blackbody at this temperature reaches a maximum in the visible spectrum (0.27-3.0 μm). Solar intensity is usually divided into three wavelength regions: 7 % ultraviolet (0.20-0.40 μm), 46 % visible (0.40-0.70 μm), and 47 % near IR (0.70-3.0 μm) [Wertz and Larson, 1999]. In addition to direct solar radiation a LEO spacecraft also experiences Earth's albedo. A planet's albedo is usually expressed as the fraction of incident sunlight that is reflected back to space; therefore, characterized as short-wave energy with wavelengths between 0.27 and 3.0 μm. Figure 3-20 depicts the temperature dependency of spectrum radiation.

²⁶ blackbody – energy distribution by wavelength is only a function of temperature

²⁷ spectral – wavelength dependent

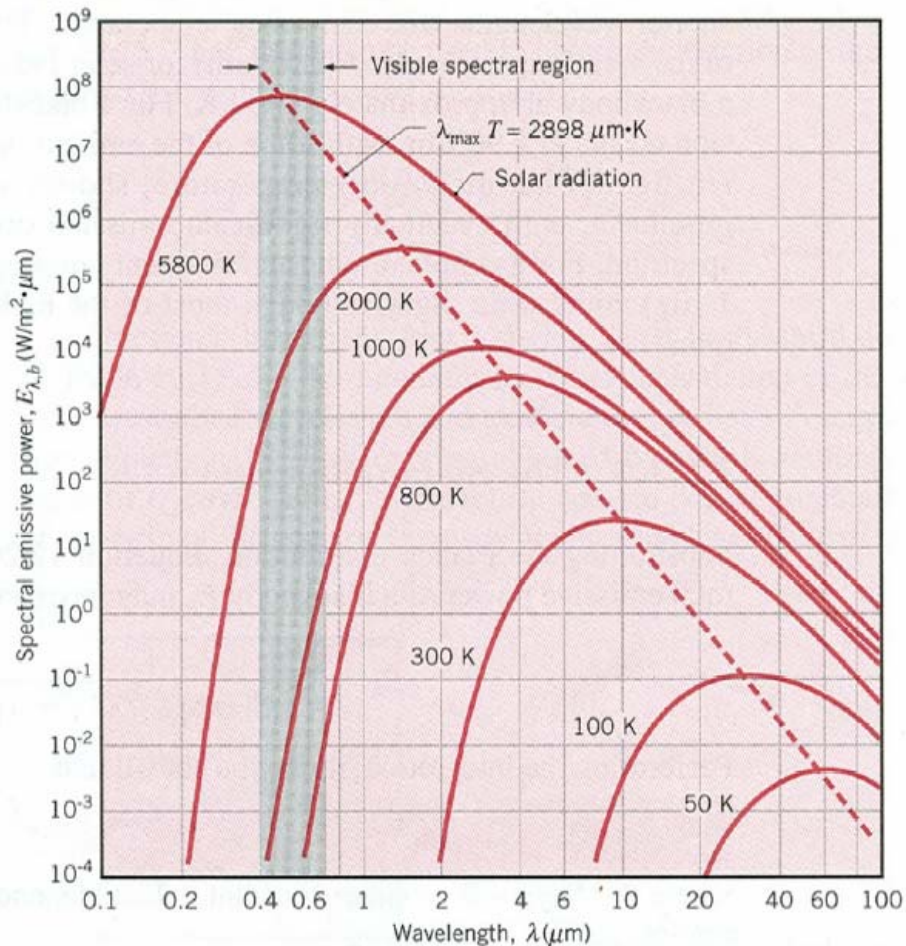


Figure 3-20: The Planck Distribution (*Reproduced from Incropera and Dewitt, 1996*)

Longwave Radiation. Longwave exchange deals with terrestrial radiation in the wavelengths of 1.0 to 100 μm [Sarafin, 1995]. Termed *planetary emissions*, all sunlight that is not reflected as albedo is absorbed by Earth and eventually re-emitted as IR energy or *blackbody radiation*. The IR energy emitted by Earth has an effective average temperature of 255 $^{\circ}\text{K}$ and is approximately of the same wavelengths as that emitted by a spacecraft; that is, of much longer wavelength than that of the Sun [Wertz and Larson, 1999]. Figure 3-21 subdivides the different forms of electromagnetic radiation.

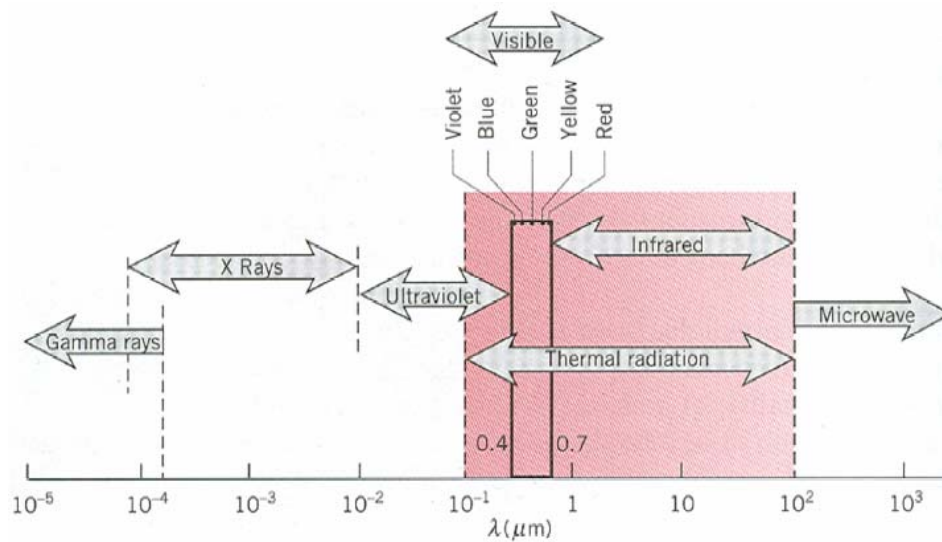


Figure 3-21: Delineation of the Electromagnetic Spectrum
(Reproduced from Incropera and Dewitt, 1996)

The Stefan-Boltzman law describes the amount of emission occurring from an object above 0°K as:

$$E = \varepsilon\sigma T^4 \quad (3.8)$$

where E is the emissive flux in $[\text{W}/\text{m}^2]$, σ is the Stefan-Boltzman constant ($\sigma = 5.67\text{E}-8 \text{ W}/\text{m}^2 \cdot \text{K}^4$), T [$^\circ\text{K}$] is the absolute temperature of the emitting object, and ε is the emissivity of the body [Incropera and Dewitt, 1996]. Equation 3.8 is obtained by integrating the Planck distribution (Figure 3-20) for a given temperature and shows that bodies of higher temperature emit radiation in shorter wavelengths than bodies of lower temperatures.

Direct Solar. The Sun is a very stable energy source which is constant to within a fraction of a percent over the 11-year solar cycle. However, because Earth's orbit is elliptical, the direct solar flux for Earth-orbiting spacecraft varies from $1322 \text{ W}/\text{m}^2$ at

summer solstice to 1414 W/m^2 at winter solstice [Gilmore, 2002]. For the thermal analysts it is customary to define the *solar constant* as 1367 W/m^2 which is the intensity of sunlight at Earth's mean distance from the Sun (1 AU²⁸).

Albedo. The fraction of incident sunlight that is reflected off Earth is referred to as albedo and it known to be highly variable. The amount of albedo incident on a spacecraft attenuates differently as the satellite travels over different portions of the globe. Usually, the reflectivity is greater over land than oceans and increases with orbit inclination and cloud coverage. Due to this variability the selection of the best albedo value has forced the industry to define a yearly orbit-average albedo value equal to 30 % of the solar flux. Presented below are the parametric values used in the thermal analysis of BSat, taken as worst-case.

Table 3-3: Solar Flux and Albedo Heat Loads

Identifier	Solar Flux (W/m^2)	Albedo (W/m^2)
Perigee (Earth)	1414	424
Apogee (Earth)	1322	397
Solar Constant	1367	410

Planetary Emissions. Planetary thermal emissions depend on the planet's surface temperature. This form of radiation is in the infrared band of the electromagnetic spectrum and for many reasons is a variable source of incoming heat at the spacecraft interface. In general the highest value of Earth-emitted IR occurs at lower inclinations

²⁸ Atomic Unit

and decreases with increasing latitude. Similar to albedo heat loads, Earth IR is a substantial source of environmental heating for a spacecraft in LEO. As the altitude of the spacecraft increases to 13,000 km the effect of Earth IR diminishes and is assumed negligible [Sarafin, 1995]. A satellite is in most circumstances, and in the case of BSat, usually warmer than Earth's effective temperature. From this, the theory of heat transfer and the second law of thermodynamics imply that the net heat transfer rate is directed from the satellite to Earth. For a steady-state analysis the worst-case hot and cold values were chosen to be 275 W/m^2 and 218 W/m^2 , respectively.

Table 3-4: Orbit Average Earth IR

Orbit Inclination (deg)	Beta-angle (deg)	Earth IR (W/m^2)	
		Min	Max
0-30	0	228	275
	90	228	275
30-60	0	218	275
	90	218	275
60-90	0	218	244
	90	218	244

Thermal Control Techniques

The thermal control subsystem is responsible for maintaining temperatures of key components within their acceptable limits. A thermal control system can be classified as either passive or active and is fundamentally based upon the physical characteristic that all external surfaces of a spacecraft are radiatively coupled to space. Passive thermal control utilizes radiators, thermal isolation, and surface coating to achieve thermal control. Active thermal control relies on heaters and other electric constituents to maintain desirable temperatures ranges. However, due to the limited power generation ($\sim 2 \text{ W}$) capabilities of a picosatellite such as BSat, active thermal control is not appropriate

for this particular architecture. Where mass and power are seriously limited under the CubeSat architecture, a passive system that requires neither power nor mechanical motion is preferred and is the standard control technique implemented within the CubeSat community.

The distinction of the spectral heat loads from above allows for the selection of thermal-control finishes that are very reflective in the solar spectrum but highly emissive to room temperature; this is the very essence of passive thermal control. The two primary surface properties of importance are the IR *emissivity*, ϵ , and the solar *absorptivity*, α . It is the role of the thermal analysts to select the appropriate surface finish which minimizes absorbed solar energy while allowing the emission of energy like an ideal blackbody. A thermal figure of merit for surface coatings is the ratio of short-wavelength absorptivity to long-wavelength emissivity, α/ϵ [Sarafin, 1995]. A surface with lower α/ϵ will be cooler than a surface with high α/ϵ because solar energy penetration is prevented.

To summarize, the radiation energy from the Sun has a much shorter wavelength than the IR energy emitted by Earth. This simply means that Earth IR loads incident on a body cannot be reflected away from a radiator surface with a passive technique because the same passive system would prevent the radiation of waste heat from BSat's electrical components. Figure 3-22 emphasizes that while it is trivial in selecting a surface coating that can protect the satellite from incident solar energy, that the same mechanism is difficult when balancing a satellite's emissions against the incident longwave radiation.

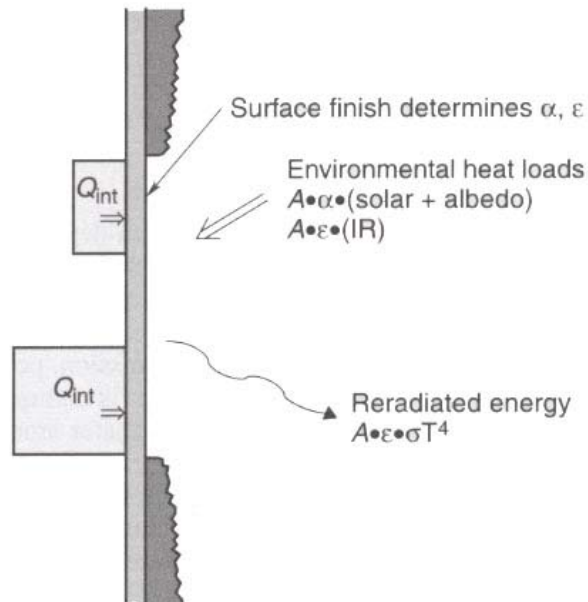


Figure 3-22: Radiation Energy Balance (*Reproduced from Gilmore, 2002*)

Thus, Earth IR presents a large energy input into the thermal system for the BSat mission in LEO. This is an inherent risk and was evaluated to determine the extent of this load and to what extremes thermal control was necessary. Table 3-5 is a summary of the surfaces finishes that were investigated for use on BSat. This table is also a result of literature reviews for thermal finishes used on the genre of satellites to which BSat belongs.

Table 3-5: Surface Finish Properties (*Data supplied from Gilmore, 2002*)

Surface Finish	Absorptivity (α)	Emissivity (ϵ)
Bare Aluminum	0.09	0.03
5-mil Silver Teflon	0.05	0.78
Anodized Aluminum	0.35	0.84
White Paint	0.15	0.6
Black Paint	0.86	0.86

The energy generation of a satellite is introduced by the subsystems which require electrical energy. Subsystem components, or hardware, never convert the entire energy

that powers them to the task it is meant to perform; therefore releasing heat as the by-product of operation. BSat's internal heat generation will be discussed in greater detail in chapter six.

Heat Transfer Theory

The discipline of heat transfer is often viewed as an extension of thermodynamics and is essentially concerned with temperature and the flow of heat. The first two laws of thermodynamics have already been cited as they are often employed in the discussion of heat transfer. However, at the molecular level where the energy exchange actually occurs, there exist the three modes of heat transfer: conduction, convection, and radiation. These three mechanisms facilitate the flow of heat and are processes that describe the energy exchange between bodies of different temperatures.

Conduction

Conduction is the motion of thermal energy across a medium due to a temperature gradient within the medium. It presents a means for thermal energy to be transferred through the spacecraft structure as well as the hardware itself. Conduction is a diffusive process meaning that the transfer of energy occurs at the molecular level and energy is exchanged from more energetic particles to the less energetic particles. For heat conduction, the rate by which this phenomenon occurs is known as Fourier's Law and is expressed in the following form for steady-state analysis

$$q'' = -k\nabla T = -k\left(i\frac{\partial T}{\partial x} + j\frac{\partial T}{\partial y} + k\frac{\partial T}{\partial z}\right) \quad (3.9)$$

where q'' is the heat flux [W/m^2], k [$\text{W}/\text{m}^2\cdot^\circ\text{K}$] is the thermal conductivity of the medium, T [$^\circ\text{K}$] is temperature, and ∇ is the three dimensional del operator indicating directional dependent heat flow [Incropera and Dewitt, 1996]. The important features to note here are that in many systems Equation 3.9 can be reduced to a one or two dimensional heat flow problem to simplify analysis. The thermophysical property, k , is a transport property which is tabulated for most common materials.

Contact Resistance

In the design of a spacecraft's thermal system, contact conductance defines that the interface between adjacent structural members is significantly lower than the conductance of the material itself. The existence of a finite contact resistance is primarily due to surface roughness effects or *asperities* which significantly constrict the heat transfer to regions where the actual contact is made. Thermal contact resistance, $R_{t,c}''$, per unit area of interface is defined as

$$R_{t,c}'' = \frac{T_A - T_B}{q''} \quad (3.10)$$

where $R_{t,c}''$ is the contact resistance [$\text{m}^2\cdot^\circ\text{K}/\text{W}$], T is temperature [$^\circ\text{K}$], and q'' is the heat flux directed perpendicular to the unit area [Incropera and Dewitt, 1996]. Figure 3-23 depicts the physics of thermal contact.

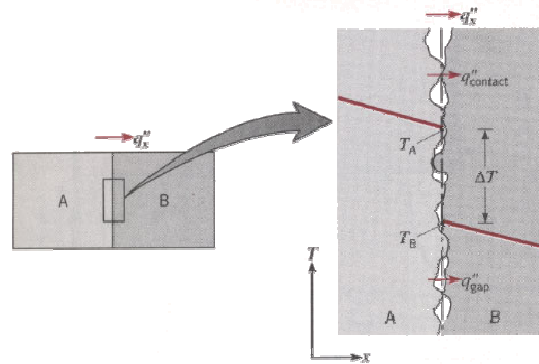


Figure 3-23: Contact Resistance (*Reproduced from Incropera and Dewitt, 1996*)

Convection

Convection is the mechanism which describes the heat transfer between a surface and a moving fluid. Convection is the phenomenon which describes the transfer of thermal energy due to the bulk motion of fluid particles interacting with a surface. In terrestrial applications convection is a significant contributor to the transport of thermal energy; however, in the vacuum of space convection is not an available heat transfer mechanism by which to facilitate the thermal needs of a spacecraft. Convective heat transfer is defined by Newton's Law of Cooling

$$q_{conv}'' = h\Delta T \quad (3.11)$$

where q_{conv}'' is the convective heat flux [W/m^2], h [$\text{W}/\text{m}^2 \cdot ^\circ\text{K}$] is the local convection coefficient, and ΔT is the temperature difference between the surface and the fluid [Incropera and Dewitt, 1996]. Because BSat exists in the absence of pressurized modules or fluid loops, the discussion of convective heat transfer will not be extended beyond this section.

Radiation

Thermal radiation as previously discussed is the heat transfer mechanism which entails the energy emission by matter which is at a finite temperature. While the transport of energy by conduction or convection requires the presence of a material medium, radiation does not; in fact radiation transfer occurs most efficiently in a vacuum [Incropera and Dewitt, 1996]. Recall Equation 3.8; the Stefan-Boltzmann law provides insight into the ideal blackbody and the deviation from this ideal radiator. Whereas a perfect blackbody emits and distributes energy as only a function of its surface temperature, any real surface is radiatively dependent upon the optical property of emissivity. Emissivity values range between zero and one and are a measure of how efficiently a surface emits energy relative to a blackbody.

Table 3-5 expresses the variety of surface properties investigated for the BSat mission. Consider Figure 3-22 which depicts a satellite's surface radiatively coupled to space. By applying the first law of thermodynamics, the steady-state energy balance applied at this surface is represented as:

$$Q_{in} - Q_{out} = 0$$

where: $Q_{in} = Q_{solar} + Q_{albedo} + Q_{IR} + Q_{gen}$ and $Q_{out} = Q_{radiator}$

thus: $Q_{in} = A\alpha q_{solar} + A\alpha q_{albedo} + A\epsilon q_{IR} + Q_{gen}$ and $Q_{out} = A\epsilon\sigma T^4$

By applying the last two expressions to the conservation of energy equation allows for the direct calculation of the surface temperature:

$$T = \left[\frac{A\alpha q_{solar} + A\alpha q_{albedo} + A\epsilon q_{IR} + Q_{gen}}{A\epsilon\sigma} \right]^{\frac{1}{4}}$$

where the flux terms were defined in Table 3-4. This is the fundamental approach to applications involving the radiatively coupled surface of a satellite. It is important to note the dependency of each component of the incident flux on the optical properties of absorptivity and emissivity. Parametric routines were employed for BSat to gain insight into the appropriate surface treatment necessary for maintaining the operational temperature constraints and the variable beta angle as seen in Figure 3-18.²⁹ The primary mechanisms of heat transfer in space both internally and externally to a spacecraft are the radiation and conduction exchanged between cavities, and the ability to radiate waste heat, respectively.

Transient Conduction

A major objective in a conduction analysis is to determine the temperature field in a medium resulting from conditions imposed on its boundaries [Incropera and Dewitt, 1996]. Once this distribution is known, the conduction heat flux at any point and at any time may be obtained. On a rate basis when it is necessary to know the temperature of a body at a particular moment in time, insight must first be gained on how fast a particular material reacts to thermal influences. This understanding is referred to as specific heat, C_p , and is seen in the energy storage term on the right hand side of Equation 3.12 of the non-steady energy equation. The energy generation term is presented as \dot{q} .

$$\frac{\partial}{\partial x} \left(k \frac{\partial T}{\partial x} \right) + \frac{\partial}{\partial y} \left(k \frac{\partial T}{\partial y} \right) + \frac{\partial}{\partial z} \left(k \frac{\partial T}{\partial z} \right) + \dot{q} = \rho C_p \frac{\partial T}{\partial t} \quad (3.12)$$

²⁹ A detailed discussion is presented in the thermal analysis chapter of this thesis.

This equation is the general form of the heat diffusion equation and provides the basic tool for heat conduction analysis. It is important to recognize that in the absence of time-dependent analysis the right hand side vanishes and the foregoing results are on a steady-state basis. However, for transient conduction the product of a material's specific heat and density, ρ , measures the ability of that material to store thermal energy. Specific heat represents the heat capacity per unit mass of a material and has units of [J/kg·°K]. A material's heat capacity, C , would then be defined as the amount of heat, [J], required to increase the temperature, [°K], of a material by one degree.

Analytical Solution Techniques

As this thesis entails the assessment of the mechanical systems onboard BSat, an introduction to the solution techniques that were employed will be discussed here. The mechanical systems onboard the satellite range from structural constituents which are inherently stressed during launch, to the thermal stability of the satellite which is extremely dynamic given the nature of a satellite in LEO. Both techniques discussed below are numerical methods which yield approximate values of unknowns at discrete number of points in the continuum. That is to say, when analytical solution techniques are complicated due to geometries and the mathematical solutions to governing equations are mathematically cumbersome or unattainable, numerical techniques are employed which ideally reduces the problem to a system of simultaneous algebraic equations. As customary in numerical routines, the process of modeling a body is conducted by

discretization; a method of dividing the body into an equivalent system of smaller bodies (finite elements) interconnected at points.

Finite Element Method

In the case of BSat, the solution for structural problems refers to determining the displacements at each node and the stresses within each element that encompass the structural body. These estimated stresses are then weighted against the strength of the material to produce a margin of safety. Under the assumption that BSat's loading environment is known, the objective of employing a finite element routine is to determine the resulting stresses and displacements. The first step is the discretization of the body into smaller finite elements with associated nodes. The shape of the element is often limited by the mesh-generation program used to discretize the body. The FEM package used for the structural analysis of BSat was COSMOSWorks and is limited to tetrahedral-shaped elements with four corner nodes, an example of which is depicted in Figure 3-24. Tetrahedral elements are acceptable in this application as the overall goal is to perform a three-dimensional stress analysis [Logan, 2000].

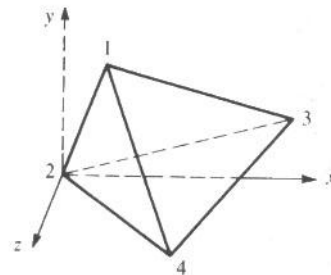


Figure 3-24: Tetrahedral Element (*Reproduced from Logan, 2000*)

The second step involves choosing the displacement function within each element as either a linear, quadratic or cubic polynomial. To satisfy compatibility, elements connected at a common node, along a common edge, or on a common surface must remain connected at that defining junction before and after the deformation takes place [Logan, 2000]. The displacement function is restricted in this sense and requires the known stress/strain properties for determining the behavior of one element to the next [Logan, 2000].

$$\varepsilon_x = \frac{du}{dx} \quad (3.13)$$

Equation 3.13 is the one-dimensional deformation equation which shows the relationship between strain, ε_x , and displacement, u . In addition to the relationship between strain and displacement, the constitutive law which relates stress to strain is necessary for deriving the equations for each finite element. Known as Hooke's Law, this constitutive law expresses that stress, σ_x , is proportional to strain, ε_x , by the modulus of elasticity, E , the material property.

$$\sigma_x = E\varepsilon_x \quad (3.14)$$

The next step is to derive the element stiffness matrix and equations which, based on the routines of COSMOSWorks, is accomplished using the work/energy method. [Logan, 2000] states that this method is much easier in applications for two and three dimensional elements and involves the principle of minimum potential energy and Castigliano's

theorem³⁰. The derivation of the element equations are in matrix form similar to Figure 3-25.

$$\begin{Bmatrix} f_1 \\ f_2 \\ f_3 \\ \vdots \\ f_n \end{Bmatrix} = \begin{bmatrix} k_{11} & k_{12} & k_{13} & \dots & k_{1n} \\ k_{21} & k_{22} & k_{23} & \dots & k_{2n} \\ k_{31} & k_{32} & k_{33} & \dots & k_{3n} \\ \vdots & & & & \vdots \\ k_{n1} & & & \dots & k_{nn} \end{bmatrix} \begin{Bmatrix} d_1 \\ d_2 \\ d_3 \\ \vdots \\ d_n \end{Bmatrix}$$

Figure 3-25: Element Equations in Matrix Form (*Reproduced from Logan, 2000*)

where $\{f\}$ is the vector of the element nodal forces, $\{k\}$ is the element stiffness matrix, and $\{d\}$ is the vector of unknown generalized displacements. Upon the application of appropriate boundary conditions to satisfy continuity and compatibility, these matrices transform into the global matrices by which displacements can be solved for using an elimination or iterative method. In its compact (matrix) form the global equation is written as $\{F\} = \{K\} \{d\}$ which represents a set of simultaneous algebraic equations.

As a final goal and with the aid of postprocessor computer programs, the results are analyzed and interpreted to provide the design. With BSat these techniques were employed using COSMOSWorks and revealed locations in the structure where large deformations and stresses occurred. The structural analysis chapter discusses these occurrences and the important role they played in making design/analysis decisions.

Finite Difference Method

A multidimensional temperature analysis is used for the same reasons numerical techniques are used in structural analysis. In this case, the best alternative is often one

³⁰ Provides a means for finding the deflections of structures from the strain energy

that uses the numerical technique referred to as the finite difference method (FDM). To reiterate an analytical solution allows for the determination of temperature at any point within a medium while a numerical method, such as FDM, enables the determination of the temperature at discrete points. Both FEM and FDM begin by subdividing the medium into a number of small regions; however, with FDM these subdivisions usually contain a reference point or node at its center whereupon each node represents a region over which the average temperature is assumed. No longer are tetrahedral elements the constituents of the mesh, but rather the selection of nodal points is often a matter of geometric convenience. Consider Figure 3-26; as in most cases with FDM it is geometrically convenient to construct rectangular or even square elements with centered nodes and edge nodes. Each node requires that energy is conserved and is designated by a numbering scheme that, for

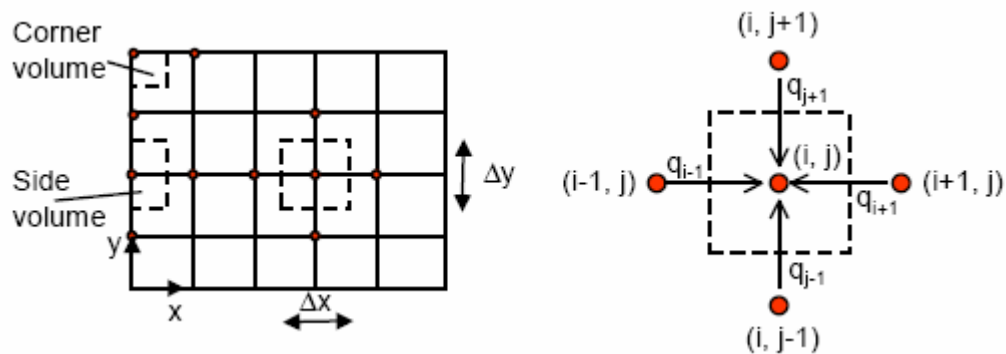


Figure 3-26: FDM Formulation (*Reproduced from Incropera and Dewitt, 1996*)

a two-dimensional system as seen above, takes the form shown on the right. The x and y locations are designated by the indices i and j , respectively.

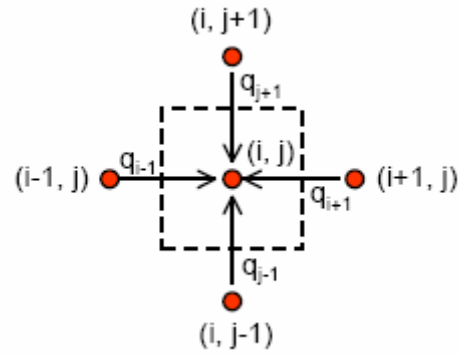
Applying energy balances to the control volume (i,j) about the node results in the finite-difference equation for that node. Notice that in this particular example steady-state conditions are applied and the system includes a heat generation term, \dot{q} .

$$q_{i-1}\Delta y + q_{j-1}\Delta x + q_{i+1}\Delta y - q_{j+1}\Delta x + \dot{q}\Delta x\Delta y = 0$$

where,

$$q_{i-1} = k \frac{T_{i-1,j} - T_{i,j}}{\Delta x} \quad q_{j-1} = k \frac{T_{i,j-1} - T_{i,j}}{\Delta y}$$

$$q_{i+1} = k \frac{T_{i+1,j} - T_{i,j}}{\Delta x} \quad q_{j+1} = k \frac{T_{i,j+1} - T_{i,j}}{\Delta y}$$



Hence, for the (i,j) node the differential heat equation, is reduced, implicitly, to an approximate algebraic equation. This development is the very essence of FDM. For BSat the FDM routine was employed through a SINDA³¹ postprocessor computer program. As will be discussed in greater detail later, a SINDA model was constructed of BSat to assess the on-orbit thermal environment to complete a parametric thermal study. SINDA is an industry standard, network style, thermal analysis program which numerically integrates the governing heat equations using the finite difference method. It is the thermal modeling software available at SSEL and is used performing transient and steady-state analysis involving radiation heat transfer and orbital parametric studies.

³¹ Systems Improved Numerical Differencing Analyzer

4. MECHANICAL DESIGN

The functional success of an orbiting platform³² is defined by a set of top-level requirements, that when applied, implicitly govern the design and performance of the foregoing subsystems. These requirements are intended to be absolute as they define mission success; however, with modification to the mission CONOPS or science objectives, exceptions are typically enacted. This reiterates the strength and formidability of the role that science plays on the mission architecture. This section is intended to deliver the requirements, architectures, and design of the mechanical subsystems onboard BSat.

Structure Subsystem

Requirements

The requirements which govern the physical design of the BSat structure are presented in terms of ICDs as seen in Figure 1-7 through Figure 1-9. This information defines the absolute size and shape of the satellite as it is intended to interface with the RocketPod™. These top level driving requirements are supplemented by operational requirements and derived requirements that support all of the satellite's subsystems: communications (*Comm*), command and data handling (*C&DH*), the electrical power system (*EPS*), and payloads. Significant insight has already been presented on the characteristics of these subsystems where it is now important to discuss how these subsystems coalesce. To begin, the structure is characterized by the following listed requirements:

³² orbiting platform – generic term to describe a satellite or spacecraft

1. BSat will have a remove-before-flight (*RBF*) pin access area located on a side face;
2. BSat will have a data port access area located on a side face;
3. BSat will have two kill-switches mounted on respective rail-ends;
4. 75% of the flat rail surface shall be available for rail contact inside the RocketPod™;
5. Secondary structures (i.e. solar panels) shall not exceed 6.5 mm in height (between rails) from the exterior surface;
6. BSat must adequately meet all RocketPod™ specifications;
7. BSat must be fabricated from materials with thermal expansion properties comparable to those of 6061-T6 and 7075-T73 aluminum;
8. The center of mass of BSat must remain within 2 cm of the geometric center;
9. BSat must not exceed 2 kg;
10. BSat's launch rails will have a surface finish that is hard anodized;
11. BSat must withstand 125% of launch loads.

Comparison of the conventional CubeSat specifications in Figure 1-7 with the RocketPod™ specifications in Figures 1-8 and 1-9 shows that many of the features have gone unchanged and that BSat's structural uniqueness is a result of evolution from a cubic design to one that is more rectangular in shape. That is to say that the BSat's primary structure was not designed around specifications outlined by the P-Pod, but instead by Ecliptic's RocketPod™. The structural design also has to accommodate a TUI tether payload with the dimensions shown in Figure 4-1. Figure 4-2 depicts the requirements of BSat's structure with distinction between exterior and interior interfaces.

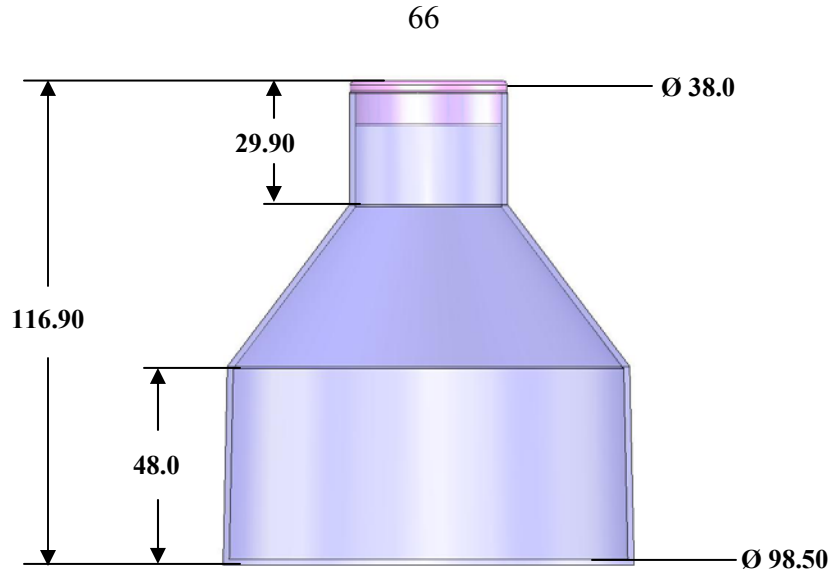


Figure 4-1: Tether Specifications
(All dimensions in mm)

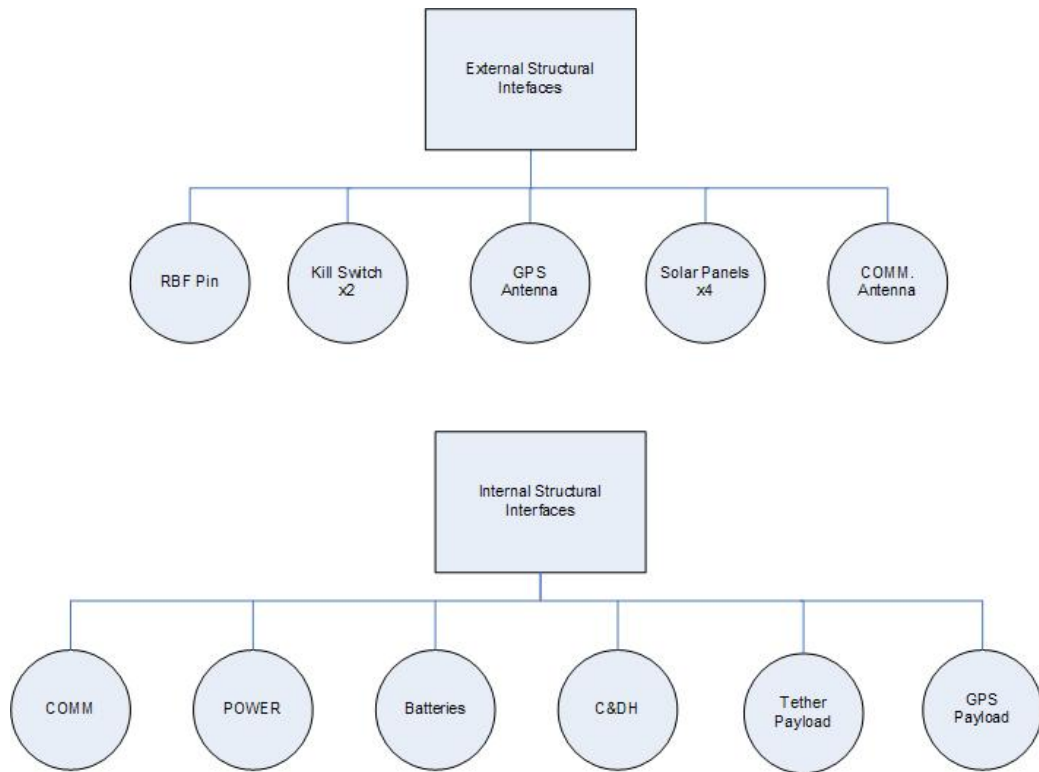


Figure 4-2: Structure Requirements

Under these constraints the structure has accordingly been subjected to a variety of iterations within the limits of its specifications and concept electronics. While the EDU model of Figure 2-3 has already materialized, the flight unit will be discussed here in the anticipation of its fabrication.

Satellite Design

The BSat flight unit satisfies all the dimensional specifications as previously identified in addition to providing an integration strategy for all electronics and payload packages. In the presence of many undetermined factors³³ the primary goal of the structural design was to ensure ease of manufacturability while providing a means to integrate the avionics and TUI tether assembly. To provide system-level deliverables the design considers foremost the size and shape of the tether assembly, and then followed closely by the geometries of MEROPE's space hardware. Utilizing MEROPE as heritage-technology is thought to produce a worst-case volume criterion for the electronics packages necessary to support the top-level requirements. Once determined these packages will be optimized and integrated into the structure as detailed in the following paragraphs. The engineering drawings are available in Appendix A.

Primary Structure. A satellite's primary structure is considered the backbone, or major load path, between the spacecraft's components and the launch vehicle [Sarafin, 1995]. The primary structure of BSat consists of six independent parts, that, when assembled provide a means of housing all the appropriate subsystems while simultaneously providing an effective framework in terms of stiffness and survivability to induced

³³ Undetermined factors imply that flight-avionics have yet to be manufactured.

frequencies, steady-state accelerations, and transient loading during launch. The primary structure is comprised of essentially three main components: a baseplate, a tophat, and four adjoining sides. Due to the unique geometry of the tether assembly, the adjoining sides were optimized to provide the greatest possible interior volume while providing a means of securely mounting a variety of PCBs. This was accomplished by means of solid modeling schemes using SolidWorks. The critical dimensions provided by Ecliptic were fulfilled to ensure proper integration of the satellite with the RocketPod™.

To compliment the ease of manufacturability, the design of the four sides is nearly identical with the exception of minor end-rail details seen in Figure 4-3. This is not to suggest that the fabrication is seamless; the extremely thin (~1 mm) features, or walls, required implementing tooling schemes to compliment the machining processes. The four sides will be the only constituents in contact with the RocketPod™ and for that reason they are fabricated from 7075-T6 aluminum.³⁴ Each side is equipped with strings of tapped holes for securing the tether bracket and for general assembly. To trivialize construction, all necessary fasteners are #2-56 in both the 100° flathead and socketcap styles. Figure 4-3 shows the variation of the four sides; sides labeled *A* and *B* are responsible for fixing all translations and rotations within

³⁴ If the absolute mass of BSat was not to exceed 1 kg, then 6061-T6 would be sufficient.

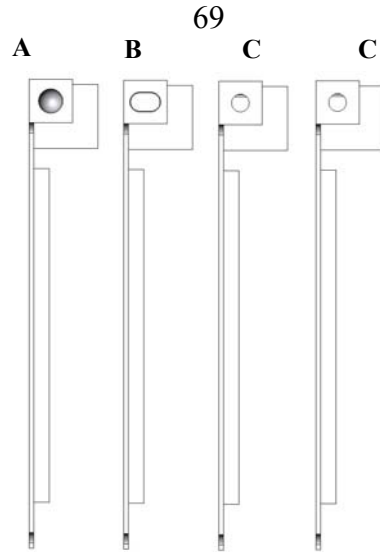


Figure 4-3: BSat End-rail Details

the RocketPod™, and side *C* (x2) includes a tapped hole on its rail-end for mounting a kill switch. The open-architecture of the sides is desirable for providing access during testing and to provide a means of routing wires between the subsystems. Panels equipped with solar cells will be mounted on the exterior and will protect the electronics from the harsh space environment.³⁵

The baseplate is simple in design yet shares the same 1 mm thickness as the adjoining sides. To alleviate some of the machining complexity of the sides, the baseplate is equipped with the tapped holes that are geometrically matched with the countersinks on the sides. This along with the tophat will serve to provide much of the torsional strength of BSat. It is common practice that a tapped hole must accommodate a thread depth at least equal to the diameter of the fastener. Therefore, the depth of these tapped holes is 3 mm and chosen to belong on the baseplate rather than the sides; an optimization that

³⁵ This infers radiation particles traveling thru the satellite.

allows greater PCB size and volume in the bottom portion of the satellite. To minimize excess mass, the baseplate is fabricated from 6061-T6 aluminum.

The tophat is the most unique feature of the BarnacleSat structure. Its uniqueness derives from the RocketPod™ ICD that calls for a cylindrical cavity to prevent straying of the spring mechanism from its preferred orientation. The tophat was designed with a series of tapped holes for the general assembly and for securing components stored within its volume (i.e. batteries and RF antennas). In addition to mounting the antennas, the tophat is also designed with access holes that allow the antennas to deploy out from the sides of the satellite. The additional volume made available with the tophat results in approximately 1/3 greater interior volume for housing the tether and satellite avionics. The tophat is fabricated from 6061-T6 aluminum. All six parts are shown in their EDU form in Figure 4-4.



Figure 4-4: BSat EDU Structure

Secondary Structure. The secondary structures of BSat include the four solar panels and the tether shroud bracket. All of these components are fabricated from 6061-T6 aluminum and are geometrically compliant with respect to the primary structure; i.e. the EDU model has physically shown the proper alignment of all fittings. There are two solar panel designs: three panels are identical and were designed to accommodate two strings³⁶ of cells. The fourth panel, which provides access to a serial connector and RBF pin, carries only one string of two solar cells. All four panels mount to the exterior of BSat via six #2-56 socketcap machine screws. It is intended that the pin header (discussed later) be secured with 3M Scotch-Weld DB125 A/B Epoxy on the back side of the panels; its mechanical properties are shown in Table 4-1.

Table 4-1: 3M Scotch-Weld Epoxy Data

	Tensile Strength [MPa]	Conductivity [W/m·°K]	CTE [μm/m/°C]	Cure Time [min]
DB125 Epoxy	22.8	.154	98	25

The pin header is then intended to pass through an opening in the sides to its mating pin header mounted on the power board. Each panel was designed with several daisy-chain thru holes³⁷ by which wires are routed to help alleviate any stresses that may develop at the solder connections. Bus bars are used where applicable. The channel cuts on the backside of the panels are intended to provide room for routing wires down to the pin header as seen in Figure 4-5 below.

³⁶ A solar cell string connects two cells in series.

³⁷ Daisy chain – Method of braiding wires within the panels so that the solder joints on the actual cells are not sacrificed.

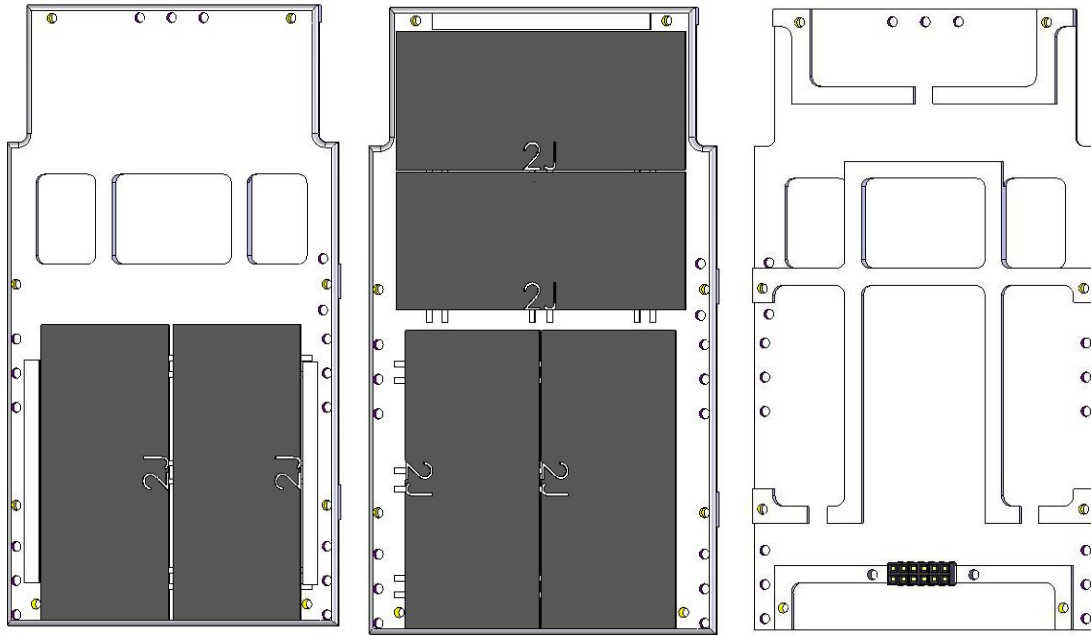


Figure 4-5: BSat Solar Panel Assembly (*yellow-fasteners, purple-daisy chain*)

Many CubeSat designs utilize ACCULAM™³⁸ as the solar panel substrate for mass savings; however, due to its epoxy/glass construction it is a thermal insulator. In fact compared to 6061-T6 aluminum, ACCULAM™ is three orders of magnitude more resistant to heat conductance. This is not desirable considering that solar cells are electrically more efficient at cooler temperatures [Gilmore, 2002]. BSat was designed with aluminum solar panels as a means of conducting heat away from its solar cells for optimal performance.

To prepare BSat's solar panels for integration into the general assembly the solar cells themselves were first adhered to the solar panels. This is a controlled process that required a class 10,000 clean environment to ensure that debris would not be embedded within the silicon adhesive. Preparing the silicon is another involved process that

³⁹ ACCULAM™ - distributed as G10/FR4 through McMaster-Carr.

required a vacuum pump for degassing entrapped air bubbles and a template for ensuring an even distribution of silicon on the panel; Figure 4-6 depicts these steps. Through experimentation it was determined that applying silicone within a footprint 80% the size of the solar cell produced an acceptable distribution of adhesive between the solar cell and solar panel. This experimentation was done using *dead-cells*, or *practice-cells* purchased from Spectrolab. The cells were adhered to translucent FR4 material and then visually inspected from the opposing side. This process also revealed the mass of the silicone necessary for adhering the solar cells.

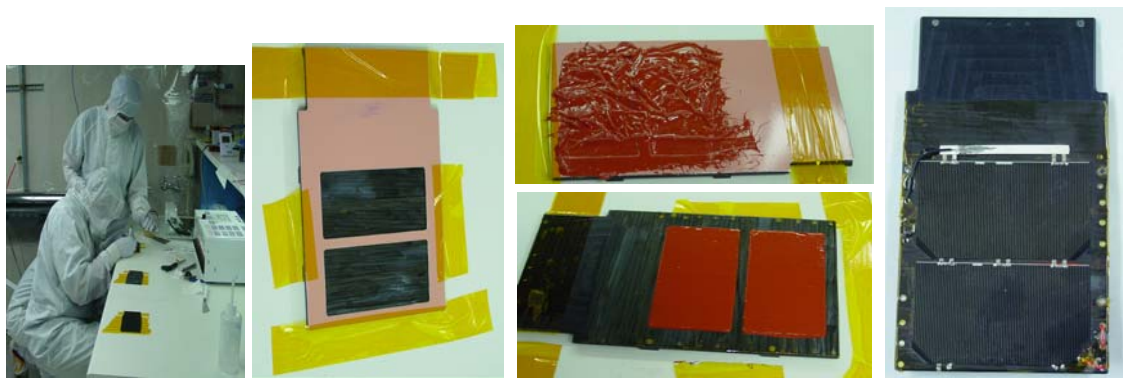


Figure 4-6: Clean Room Solar Cell Preparation

The remaining constituent of BSat's secondary structure is the tether-shroud bracket. The bracket was designed to interface properly with TUI's tether system (Figure 4-1) while providing tapped holes by which to mount, secure, and assemble all subsystems from its bottom surface. It is geometrically compliant in a manner consistent with the design of the primary structure and is fabricated from 6061-T6 aluminum as it remains interior to the satellite and thus will never be in direct contact with the deployer's launch rails. The concept electronics package of Figure 4-7 will mount to the tether-shroud

bracket via standoffs. The concept design is the result of optimizing the components belonging to MEROPE. The dimensions presented in Figure 4-7 are absolute values and were parameters given to the other subsystem design teams to ensure compatibility. The bracket is the most load-bearing element of the BSat structure and thus was designed with significant strength while simultaneously adding significant torsional strength to the satellite itself. The tether-shroud bracket is shown in Figure 4-7.

The tether-shroud bracket consists of diagonal cuts at the four corners (plus two small access ports) for any wires that are necessary to connect electronics mounted in the bottom to those mounted in the top portions of the satellite. There are four counter bore holes that accept M2.5 x 0.45 cap screws located at the four diagonal blocks for fastening the tether system, and eight counter bore holes on the bracket's bottom side by which to secure #2-56, 3/16" Hex x 3/8" (in length) male-female standoffs for integrating the electronics package.

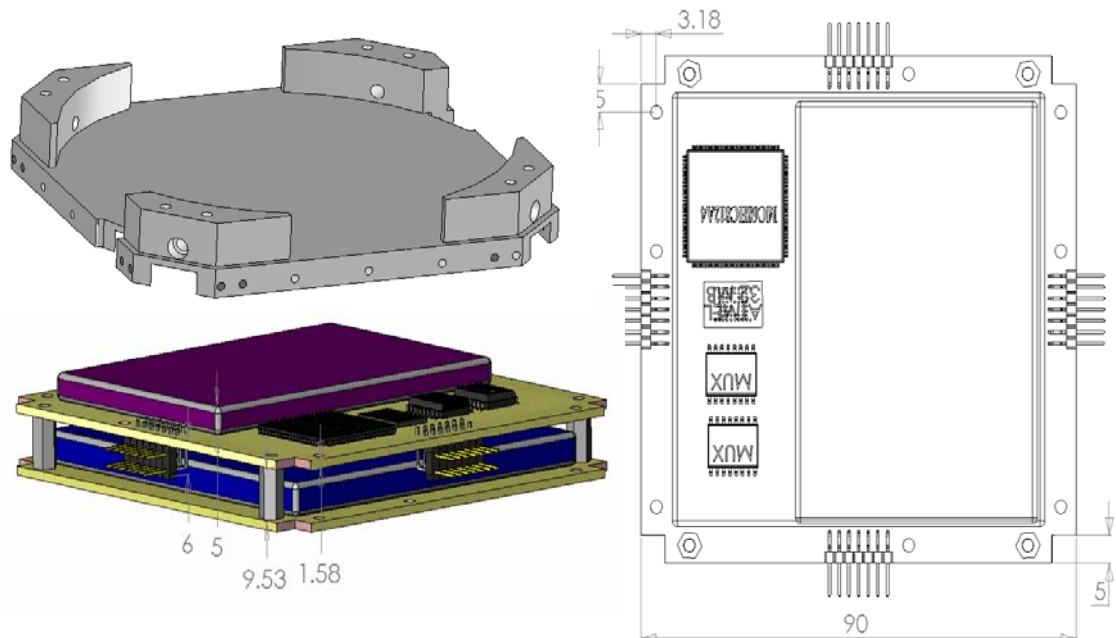


Figure 4-7: Concept Electronics Package and Tether Bracket (*dimensions in mm*)

Tertiary Structure. A spacecraft's tertiary structure system is defined as those structures interior to the spacecraft whose responsibility is to properly secure components and electrical hardware. Tertiary structures are often low in mass and custom products designed specifically to the configuration of the host spacecraft. These structures are most susceptible to acoustic loads and random vibrations as they are low in mass and often large in surface area [Sarafin, 1995]. The tertiary structures of BSat include both the battery brackets, RF antenna cups, and the PCBs. While the battery brackets are fabricated from malleable, aluminum 6061-T6 sheet metal, the antenna cups and PCBs are fabricated from Delrin®, and ACCULAM™, respectively; the mechanical properties of which are available in Table 4-2.

The BSat battery bracket of Figure 4-8 is intended to host a single 1950 mAh, Li-Ion, Rose Battery that measures approximately 10 x 34 x 53 mm. Two battery brackets and hence two batteries were designed to fit within the volume of the tophat and securely fastened with preexisting tapped holes of the tophat. To keep fabrication complexity at a minimum the battery bracket was designed not to require any machining; rather fabricated using a sheet metal bender. The orthogonal *bends* of the battery bracket are complimented by stress relieving notches to relieve the high stress concentrations associated with bending the metal. To obtain the radius on the bracket's mounting flanges, the bracket (w/ straight wings) is inserted into the tophat and bent into place by torquing a screw/nut combination prior to inserting the Helicoils³⁹ into the tophat. Once the wing conforms to the radial profile of the tophat, Helicoils are inserted and the

³⁹ Helicoil – although not mentioned until now, all tapped holes were drilled to fit Helicoil inserts to accommodate the stainless steel screw and aluminum mismatch.

brackets are secured into place from the assembly's interior. The bracket is slightly oversized to account for the expansion and contraction of the battery during charge and discharge, and will fit snugly within the bracket once the battery is wrapped in Kapton tape.

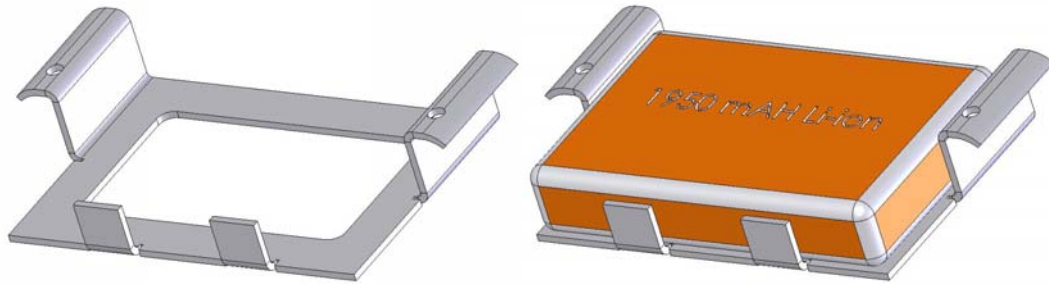


Figure 4-8: BSat Battery Bracket (x2)

The most profound⁴⁰ tertiary constituent of BSat is the antenna cups, or housing for the RF antennas. An effective and reliable antenna deployment system is vital for mission success and serves as the only method by which to retrieve the *in-situ* data collected by the GPS and telemetry data. From lessons-learned on the MEROPE architecture, a requirement was levied that the antenna system had to be deployed and undeployed without disassembling the satellite. The antenna cups presented shown in Figure 4-9 are the result of many iterations and design schemes which revolved around the fulfillment of this requirement.

⁴⁰ The word *profound* is used here to signify that BSat's RF antennas present a single-point failure of the satellite; therefore, they should be significantly tested to **guarantee** successful deployment.

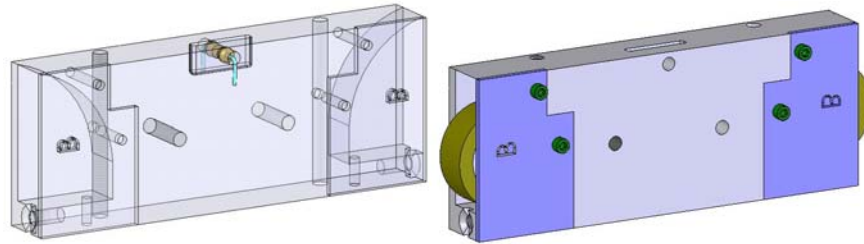


Figure 4-9: BSat Antenna Cups

The antenna housing, or cups, was designed to stow within the confines of the tophat and be secured through preexisting tapped holes belonging to the host structure. Raw Stanley® tape measure metal is used for the actual RF antenna where it is wound and held undeployed with a nylon line. The countersink-tapped holes on the posterior of the housing are accessible from the satellite's exterior and were incorporated as a means of securing the ends of the line. To ensure that the line would not be *pinched* the design also includes a notch in the countersink taps; thus, also providing a restricted path for the physical location of the line. It is important to note that this antenna design is not a stand-alone module because it requires design characteristics of the tophat to function properly. While the line is secured at one end, it is then routed along a notch in the tophat and wrapped around a resistor (located in the housing and accessed through the tophat) proceeding to the opposing side of the tophat and secured to the other countersink tap. For deployment, current is applied to the resistor causing it to heat and burn the line; thus, allowing the RF antennas to unfurl.

The last of the tertiary structures is an ACCULAM™ serial port and RBF pin mount plate. This ACCULAM™ plate was designed for fabrication with an FR4 shear, high-density DB-15 punch, and a drill press. It is geometrically compliant with two mount holes of the sides and must be secured to side *c* which is fastened to side *b* (refer to

Figure 4-11). This may appear to be a trivial tertiary structure; however, it is necessary to meet the requirements governed by the ICDs.

Modularity

Due to the extended mass allocation (2 kg) with the *CubeSat Plus*, a modular approach to BSat's structural was a design philosophy intended to simplify general assembly. The electronics package mounted beneath the tether bracket is fundamental to this approach as two, or possibly three subsystems⁴¹ will be mated together. Consequently, this electronics package in its current form exists as a conceptual model. To provide serial communications and electrical power between the two PCBs a *JED 22 pin*⁴² connector has been specified. The *JED 22 pin* utilizes a polarized shrouded header which prevents misalignment and provides rigid mating between the plug and receptacle; ensuring high reliability during vibration and shock [JST, 2003]. The spacing between the two PCBs and hence the length of the aluminum standoffs are then a function of this connector's height (7 mm).

Figure 4-10 depicts the electronics package as intended for flight. This *module* still needs to interface electrically with the electronics mounted in the upper segment of the satellite. As the shroud system presents a real estate *barrier* between the upper and lower

⁴¹ consuming two PCBs

⁴² distributed by JST Ltd. of the U.K.

portions of the satellite, it is unavoidable that wires will have to provide the interface mechanism. However, with ownership of the physical EDU subsystems, and a certain degree of logistical planning, the quantity of wires can be minimized.

Figure 4-10 also illustrates how the solar panels become *modular* by implementing an entirely different connector. This connector is a *MOD IV Receptacle Assembly* rated at 2 Amps and is thought to be sufficient for this application. The panel-side of the receptacle will be attached to the panel with the *DB125 Epoxy*.

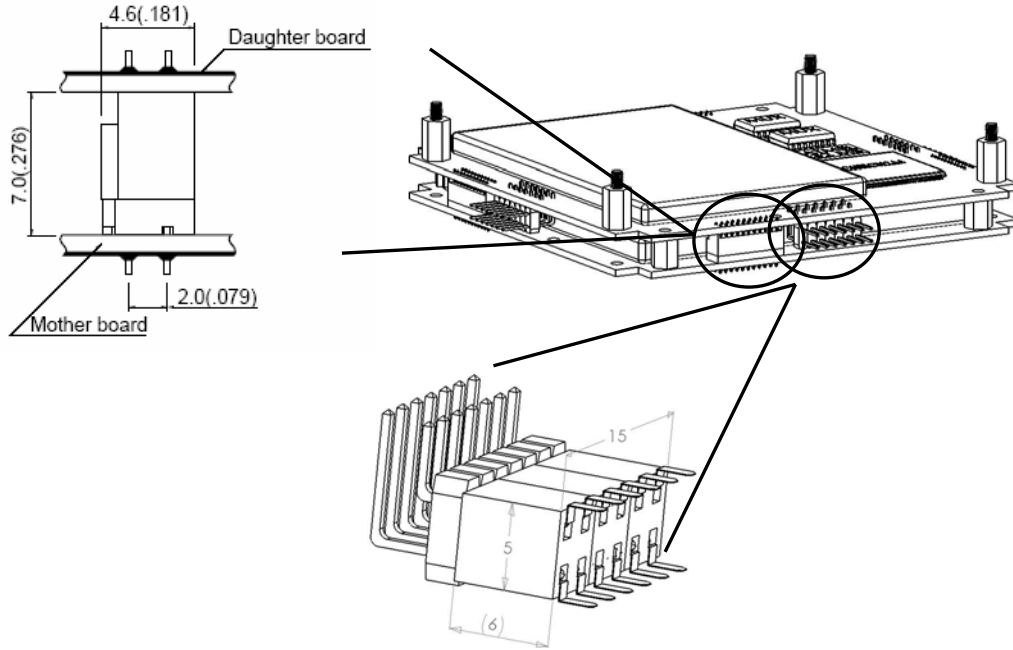


Figure 4-10: JED 22 pin Connector by JST and Solar Panel Right-Angle Pin Header
(Used to interface the two PCBs below the tether)

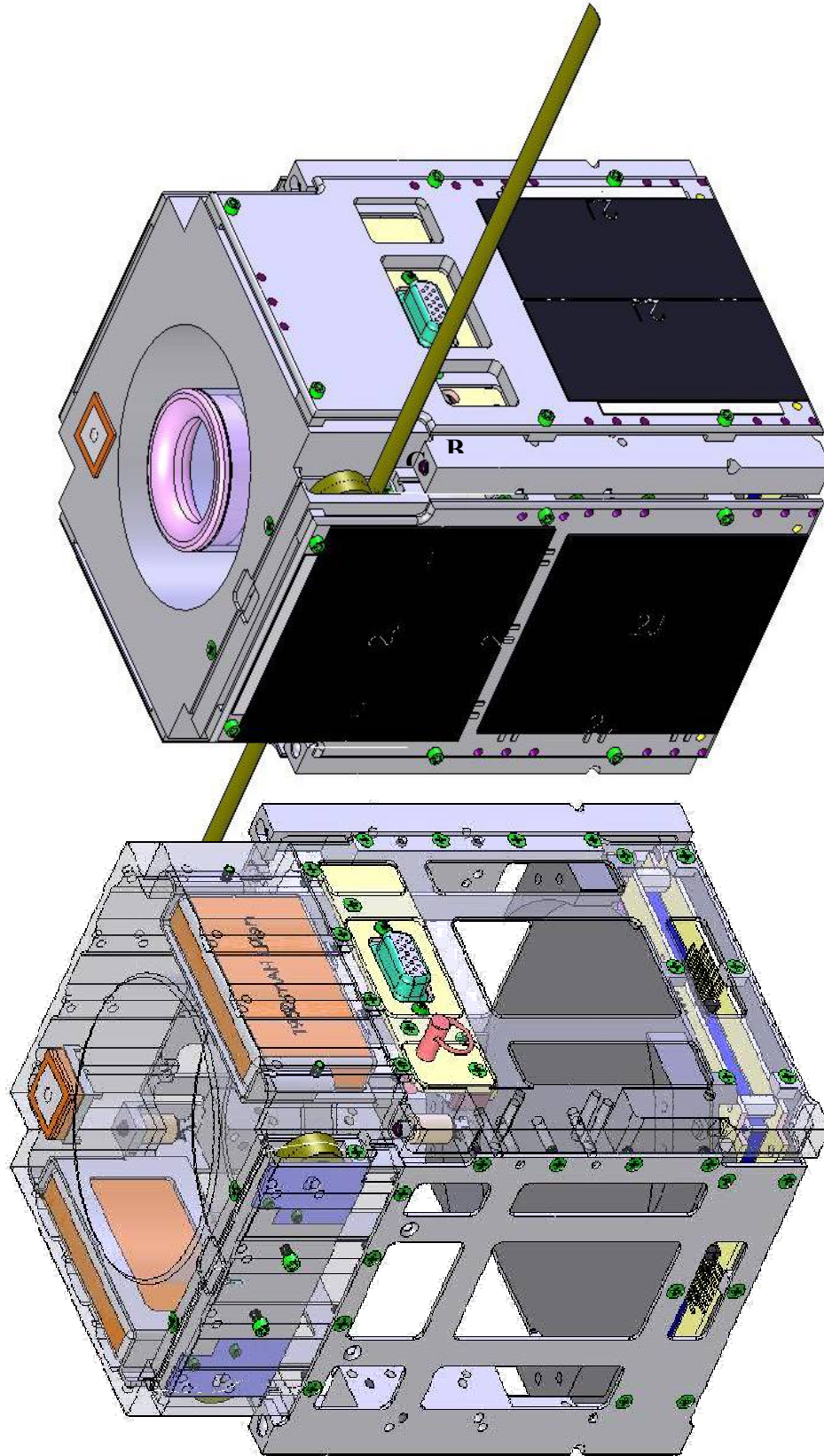


Figure 4-1-1: BSat Tertiary Structures and Deployed Antenna Configurations

The remaining modular designs include both the RF antenna housing and the solar panels. The antenna housing is modular in the sense that it interfaces independently with the primary structure, that both ends of the dipole are stored in the same housing, and the necessity of a single coaxial cable to signify RF connection.

A *modular* architecture clearly has significant advantages in the picosatellite class of spacecraft. With a payload that nearly consumes 70% of the interior volume, the BSat design presented above is the result of many trade studies and iterations focusing on this need while simultaneously concerning itself with manufacturing complexity, and the abundance of requirements. Further characterization will be possible once the subsystems have matured and are available to practice assembly procedures.

Manufacturing

The structural elements were manufactured at the *RAVE Technical Development Center* through an educational alliance with Montana Tech, Butte. The engineering drawings of Appendix A proved to be an effective means of communication. The parts were then fabricated with conventional milling techniques to supplement the educational requirement. From knowledge attributed to this experience, the BSat structural design is robust, much easier to assemble than many of its predecessors, and offers a baseline for a new generation of picosatellites as BSat is the first *CubeSat Plus* satellite being developed for the RocketPod™ deployer.

Mass and Material Properties

The structural analysis of BSat with respect to the aforementioned load environments is dependent upon the mechanical properties of both 6061-T6 and 7075-T6 aluminum, Delrin®, and Acculam™. Table 4-2 lists the relevant properties used throughout this mechanical assessment.

Table 4-2: BSat Material Properties

Material	Young's Modulus [GPa]	Density [kg/m ³]	Poisson's Ratio	Tensile Strength [MPa]	Conductivity [W/m·°K]	Specific Heat [J/kg·°K]	CTE [μm/m/°C]
6061-T6	68.9	2700	.33	276	167	896	23.6
7075-T6	71.7	2810	.33	503	130	960	23.6
Delrin®	2.9	1420	.25	62	.208	814	68
Acculam™	18.6 16.5	1800	0.22-0.38	310 262	.288	NA	9.9 11.9

The stress-strain diagram of Figure 4-12 is a characteristic of a particular material and conveys important information about the mechanical properties and type of behavior [Gere, 2001]. As will be discussed later, the margin of safety for BSat is evaluated relative to the materials' yield strength. This guarantees that all structural loading will remain within the elastic limit and will avoid undesirable strain hardening⁴³. As many parts are structurally unique, the stiffness and strength of one particular specimen is dependent upon its cross-sectional area, length, and material composition. When stresses develop under an applied load the molecular structure of the specimen is altered and heavily dependent upon its *elastic modulus*⁴⁴. The elastic limit of a material is defined by its *proportional limit*, or yield stress, and means that the material will return to its original shape without any permanent deformations.

⁴³ strain hardening – changes in a materials crystalline structure

⁴⁴ also called *Young's Modulus*

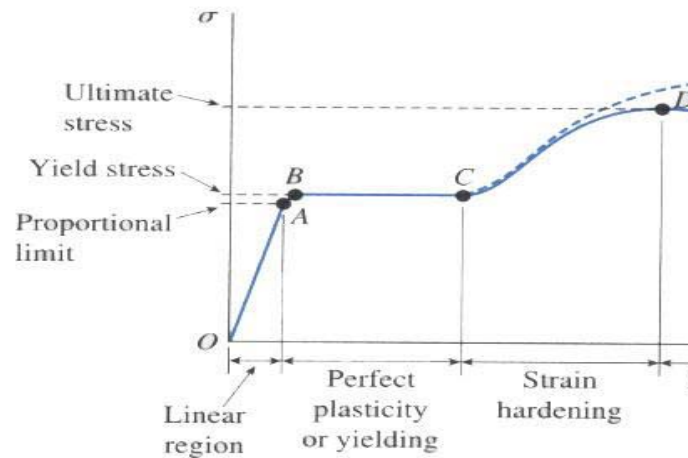


Figure 4-12: Typical Stress-Strain Curve for Aluminum
(Reproduced from Sarafin, 1995)

The mass budget is presented in its entirety in Appendix B. Figure 4-13 is the summary of the CBE⁴⁵ of BSat. This pie chart neglects the mass of the physical subsystem boards and is based on an absolute mass limit of 2 kg; thus, the *remaining* category is the current mass margin excluding the subsystem boards. Figure 4-14 depicts the center of mass comparison between an electronics package that is 0 grams versus 500 grams. By parametric evaluation it is evident that any mass within the limits of 0-500 grams will satisfy the requirement set forth by the ICDs where the center of mass must remain within 2 cm of the geometric center of the satellite. With a 0 gram electronics package the center of mass is (73, 49, 49) relative to the coordinate system seen in the figure. The center of mass of the satellite for a 500 gram electronics package is (55, 49, 49) with respect to the same coordinate system. Seeing that BSat measures

⁴⁵ Current Best Estimate

approximately 146 x 100 x 100 mm, the deviation from the geometric center is 1.4 mm and 18 mm, respectively.⁴⁶

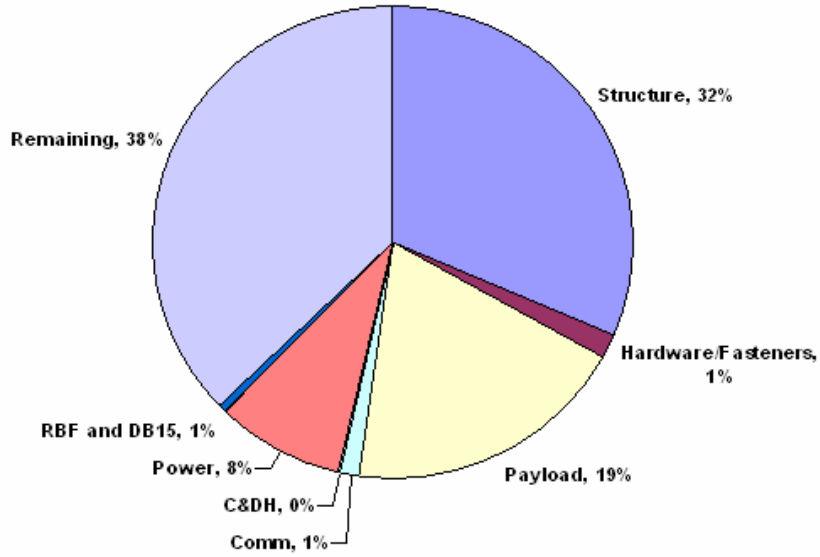


Figure 4-13: Mass Budget

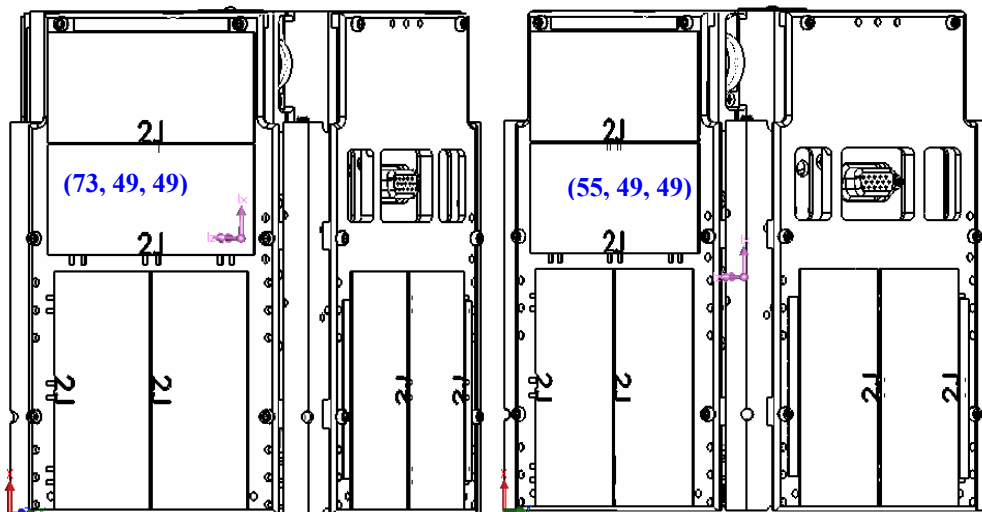


Figure 4-14: BSat Center of Mass (*L: 0 gram electronics package, R: 500 gram electronics package*)

⁴⁶ This is evaluated with respect to the net offset from the geometric center of the satellite.

Thermal Subsystem

Requirements

The Thermal Control System (*TCS*) onboard BSat is responsible for maintaining all payload and subsystem components within predetermined temperature ranges. The system has addressed each phase of the mission as it pertains to the overall mission requirements while simultaneously addressing all orbital environments that BSat will experience. BSat's TCS uses passive techniques to control onboard temperatures and has been parametrically evaluated for several on-orbit thermal environments.

Thermal control is critical to ensuring the performance and survival of BSat and its payload equipment. The design of the TCS began with the development of requirements and constraints; guidelines that control the iterative nature of this process that are governed by the operational and survival temperature limits of all pertinent subsystems. Exceeding survival limits generally causes permanent hardware damage, while exceeding operational limits is typically only detrimental while the temperature is out of range.

Table 4-3 shows the critical temperature limits that have been identified for each subsystem. To ascertain the level of thermal control needed to satisfy these requirements the following analytical methods have been conducted: a steady-state energy balance, a transient orbital analysis, and modeling in SINDA-based finite difference numerical solver; the block diagram of Figure 4-15 depicts the constituents of the thermal analysis.

Table 4-3: BSat Thermal Subsystem Requirements

	Operating	Survival
C&DH Board	-40 to 85	-55 to 150
COMM Board	-40 to 85	-55 to 150
GPS Payload	-20 to 50	-20 to 50
Power Board	-40 to 85	-55 to 150
Solar Cells	-55 to 85	-80 to 150
Batteries	0 to 35	-20 to 45

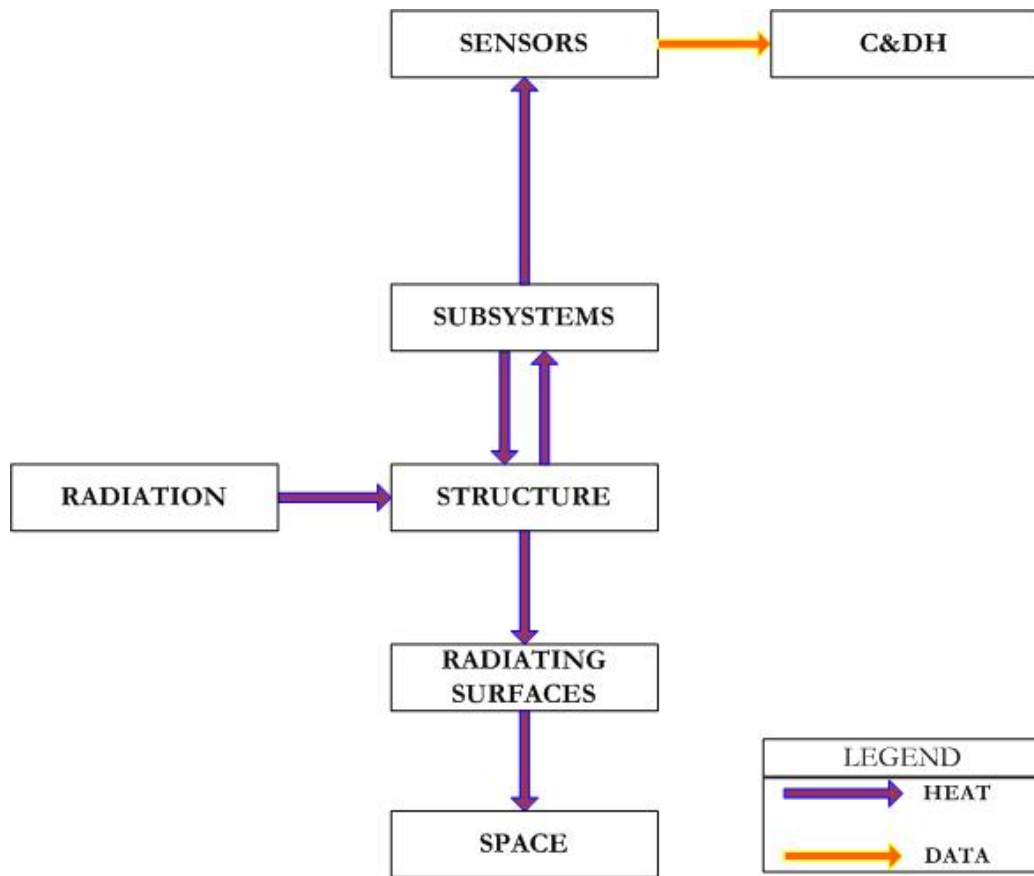


Figure 4-15: Thermal Block Diagram

Control Strategy

As mentioned above, the subsystems require specific temperature conditions to ensure reliable performance. The reliability of electrical components is often defined by a common industrial temperature standard of -40 to 85 °C. Components that are purchased as complete systems, or COTS, often have dissimilar standards; thus, requiring specific attention when addressing a favorable thermal environment. By inspection of Table 4-3, components such as the GPS payload and the batteries require distinct thermal attention because of their unique temperature ranges. To perform an energy balance on the surface of BSat the generation terms of Table 4-4 were considered possible heat input terms to the control volume.

Table 4-4: BSat Subsystem Energy Generation

Component	Energy (W)
C&DH	0.3
COMM_Tx	2.0
COMM_Rx	0.1
GPS	0.2
Power	0.6

The most distinct quantity from this table corresponds to operations during the satellite's communication with SSEL's ground station. To provide the 1 Watt output power necessary to facilitate the satellite's transmissions, an amplifier capable of 30 dB of gain has been specified and is responsible for the discrepancy between transmission (T_x) and reception (R_x).⁴⁷ However, the duty cycle of these operations are minimal when compared to the duration of any particular orbit; for instance, a 600 km, 40° inclination orbit has a maximum communications window with SSEL's ground station of 14

⁴⁷ The necessity of the 1 Watt output power is a result of performing a link analysis

minutes. During the remaining 94 minutes the satellite communications subsystem will be in standby to conserve power. To provide bounds for this parametric evaluation the shaded values from Table 4-4 were assumed negligible and the limits on the internal energy generation were defined as 0 Watts for the cold-case and 3 Watts for the hot-case; concurrently, both cases are also highly dependent upon the optical properties of BSat's exterior surface. With these limits identified, insight from the steady-state thermal analysis reveals that grouping components based upon their thermal needs provides the best thermal control solution.

The strategic placement of subsystems is not only a function of the satellite's thermal needs, but also on the physical layout of all components stored within BSat's interior. Figure 4-16 shows a cross-sectional view of the envisioned BSat flight unit. The architecture visually depicts a tether payload consuming approximately 70% of the interior volume with the remaining 30% dedicated towards all supporting systems. It is obvious from this figure that not all the systems can indeed fit into the volume designated below the tether assembly. Grouping the three subsystems on two boards (EPS, C&DH, and Comm) and as seen in Figure 4-16 is thought to be an effective passive thermal control technique. First, all three components have similar thermal requirements and comparative duty cycles. Secondly, when all three boards are active they will generate minimal heat. This heat has been included in the 10°C analysis uncertainty margin [Wertz and Larson, 1999].

Neither of the commercially purchased components, the GPS receiver and batteries, fit into the space below the tether shroud. This is an acceptable tailoring considering that

both of these COTS components have distinct thermal needs. Thermal cooling has been identified as a negligible concern for BSat; whereas, thermal heating has been identified on at least the secondary⁴⁸ batteries. This concern stems from the inherently consistent and substantial eclipse periods for low-inclination orbits. However, as will be demonstrated in the thermal analysis chapter, the batteries radiate significant amount of heat during discharge (a characteristic that occurs during eclipse). This is heat that will remain within the battery's control volume as the batteries will be completely encapsulated in Kapton tape.

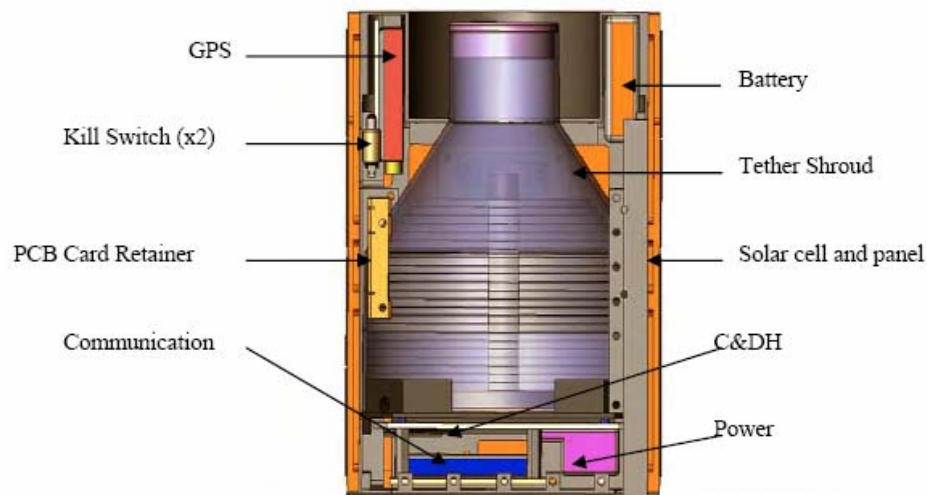


Figure 4-16: BSat Cross Section

In summary BSat's passive system has been developed parametrically to reflect the contributions and characteristics of the various electronics, the evaluation of suitable surface finishes, and variations in the anticipated on-orbit thermal environments. An active TCS is inappropriate under the CubeSat architecture as it uncouthly requires electrical power, is heavier, and requires a complex control system.

⁴⁸ secondary batteries are rechargeable whereas primary batteries are not

Tether Payload

The tether payload is a major contributor to the transient temperature environment of the satellite. The tether system in itself is comprised of two entities: a tether deployment device and a carbon-fiber, composite shroud. This payload acts as a large thermal mass that retains heat and helps keep the temperatures more steady. It is important to recognize here that the satellite will never reach a true steady-state temperature because of the constantly changing environment. Consider BSat in the absence of its tether payload; with its thin-walled construction, the satellite would react more quickly to the temperature swings. This is a result of the walls effective capability of radiating heat away weighted against its ability to conduct heat through its medium; less resistance to heat flow. Therefore, during the hot and cold transients the satellite would respond much more dramatically to changes in its environment as the incident fluxes would simply *flow* thru the satellite. With the tether present and BSat in eclipse, the shroud will be slowly radiating, or releasing, its stored energy during times when the exterior surfaces become cooler than the interior of the satellite.

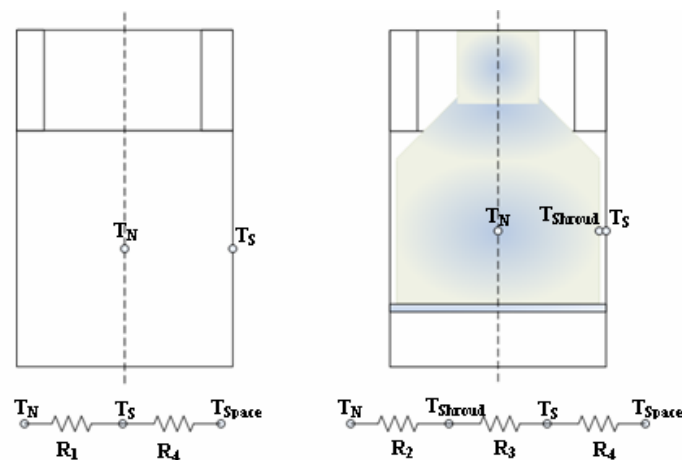


Figure 4-17: BSat Thermal Resistance Depiction (*L: w/o payload, R: w/ payload*)

Figure 4-17 depicts the additional resistance associated with the tether payload. It should also be noted that the surface properties of the tether shroud are expected to behave much differently than those associated with aluminum side walls. Furthermore, the thermal resistance and heat capacity of the tether shroud is much lower than that of the aluminum sides. The effective conductivity of the shroud depends greatly on the fiber orientation and shear volume of fiber to epoxy composition; for this particular composite, the *rule of mixtures* and the *Halpin-Tsai approximation* were employed to determine the thermophysical properties of the shroud [Barbero, 1999]. While the *rule of mixtures* applies to all other thermophysical properties, the *Halpin-Tsai* equations were used to determine the shroud's directional dependent thermal conductivity:

$$k_1 = k_f V_f + k_m V_m \quad (4.1)$$

$$k_2 = k_m \left[\frac{1 + \xi \eta V_f}{1 - \eta V_f} \right] \quad (4.2)$$

where,

$$\eta = \frac{\frac{k_f}{k_m} - 1}{\frac{k_f}{k_m} + \xi} \quad (4.3)$$

$$\xi = \log^{-1} \sqrt{3} \log \frac{a}{b} \quad (4.4)$$

Thermal conductivity in the longitudinal direction, k_1 , is defined by the *rule of mixtures* (Equation 4.1), and in the transverse direction, k_2 , by Equation 4.2. For the situation in which the fibers are circular, the aspect ratio, $\frac{a}{b} = 1$, and $\xi = 1$ [Barbero, 1999]. This is

an assumed characteristic of the tether shroud construction. The remaining thermophysical properties used in the SINDA model were obtained through the *rule of mixtures* assuming the fiber volume, V_f , is 40% and the matrix volume, V_m , is the remaining 60%. Table 4-5 addresses these values.

Table 4-5: Thermophysical Properties of Shroud

Specific Heat [J/kg·°K]	Density [kg/m ³]	Conductivity [W/m·°K]
1054	1530	$k_1 = 1.34$ $k_2 = 0.42$

The specific heat of the tether composite is significantly higher than that of the aluminum structure, which implies that it takes more energy to change the temperature of the payload by one degree. This also implies that the heat loss of the shroud will be at a much slower rate than its surrounding structure. By inspection of TUI's EDU tether system it is extremely clear how the tether shroud was fabricated; a mandrel on the inside to lay-up the pre-impregnated carbon fiber, and a Teflon bag on the exterior to create a vacuum during the curing period. This process results in a tether shroud that is highly reflective and smooth on the inside and dimensionally inconsistent and dull on the outside. Refer to Figure 4-18 below.

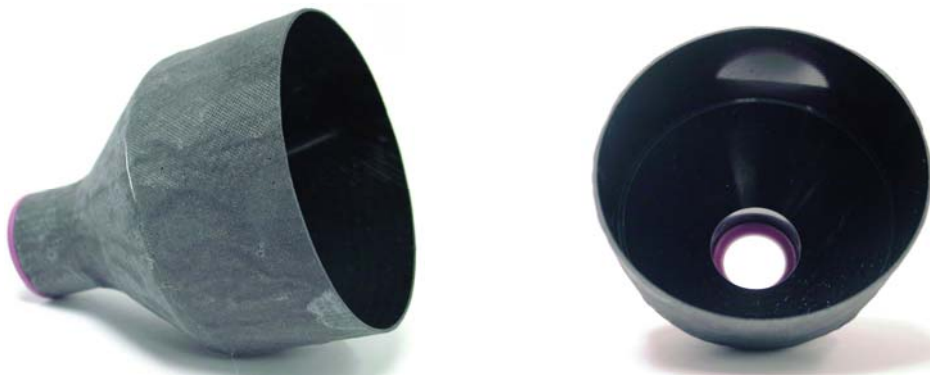


Figure 4-18: BSat Tether Shroud

This suggests that the inside surfaces of the shroud form a cavity whose inner surface is isothermal. When in eclipse the exterior surfaces of the satellite will each see an equal amount of Earth IR and the 4°K temperature of space.⁴⁹ This will cause heat to flow from the interior of the satellite directed outward. As radiation is the only means for this to occur, the surface of the material will emit electromagnetic energy according to the Stefan-Boltzmann law. Simultaneously, the inside of the shroud serves nearly as a *blackbody* simply by the presence of the small aperture, or tether exit hole. Radiation inside of the shroud will be reflected many times before emerging. Hence it is almost entirely absorbed by the cavity, and blackbody behavior is approximated. Considering that the interior is highly reflective, the radiation field in the cavity, which is a cumulative effect of emission and reflection from the cavity surface, is absorbed by the shroud and emitted out as a function of its temperature. These effects will be discussed in the thermal analysis section.

Parametric Orbits

In the absence of a RocketPod™ flight manifest, the orbit parameters of this first flight are baselined on the XSS-10 mission which flew piggy-back on a Delta II GPS orbit-insertion mission.⁵⁰ It is the vision of Ecliptic Enterprises that owing to the frequency of Delta II launches, in particular GPS satellite insertion missions, the Delta II LV will host the RocketPod™'s first flight to space. From a thermal analysis standpoint, this validates the need to perform a parametric study given a range of plausible orbits. To

⁴⁹ The satellite will be spinning at a constant rate.

⁵⁰ Recall the autonomous inspection satellite that orbited a 2nd stage booster at 800 km and 40° inclination after injecting a GPS satellite.

begin, research was conducted and revealed that GPS insertion missions occurred at altitudes ranging from 600 km to 800 km and that the inclination was generally between 35° and 50° . To extend this further, and for completeness, the orbits that were considered plausible for BSat included those between the altitudes of 600-800 km and inclinations ranging from 0 - 90° . The beta angle should be considered when considering inclination angles. To investigate these orbits further the software, STK, was used to parametrically obtain information about BSat's orbit relative to SSEL's ground station at MSU. The issue here is to investigate the plethora of orbits against both the needs of satellite communications and the influences on BSat's thermal stability. Through STK the access windows with SSEL's ground station were obtained in addition to the relative change in eclipse fractions. The results of the simulation reveal that BSat's orbit should be biased towards an altitude above 700 km and an inclination ranging from 40° to 65° (Figure 4-20 and Figure 4-21). This gives substantial time-windows for satellite communications and offers consistent eclipse periods over the life of the BSat mission. The numbers within the bars of Figure 4-20 and 4-21 are the average access times and the number of access opportunities with SSEL's ground station for 2006.

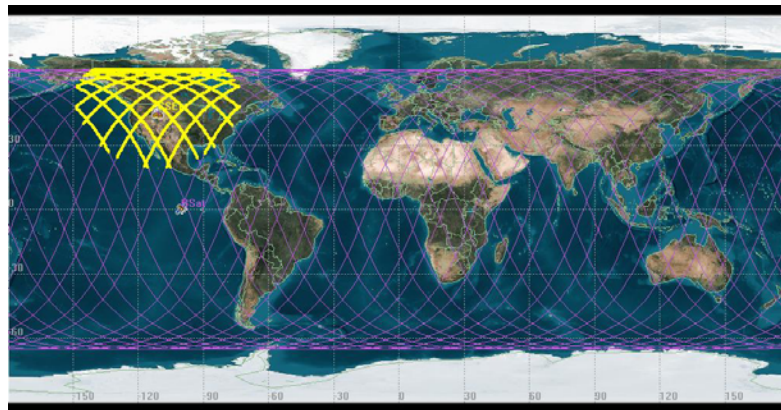


Figure 4-19: BSat STK Simulation of Access Times for one 24 hour period

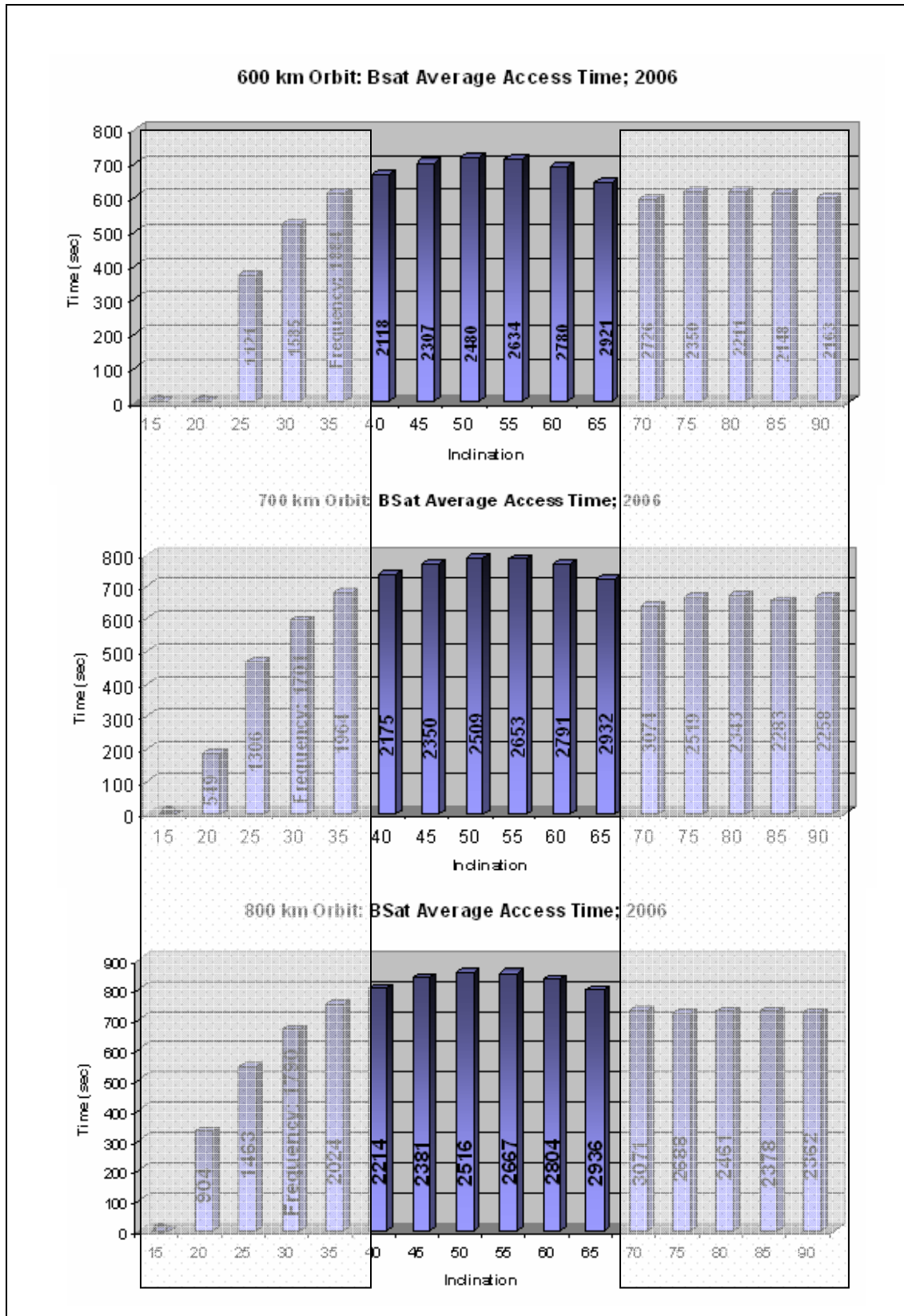


Figure 4-20: BSat Average Access Time vs. Inclination and Altitude for 2006

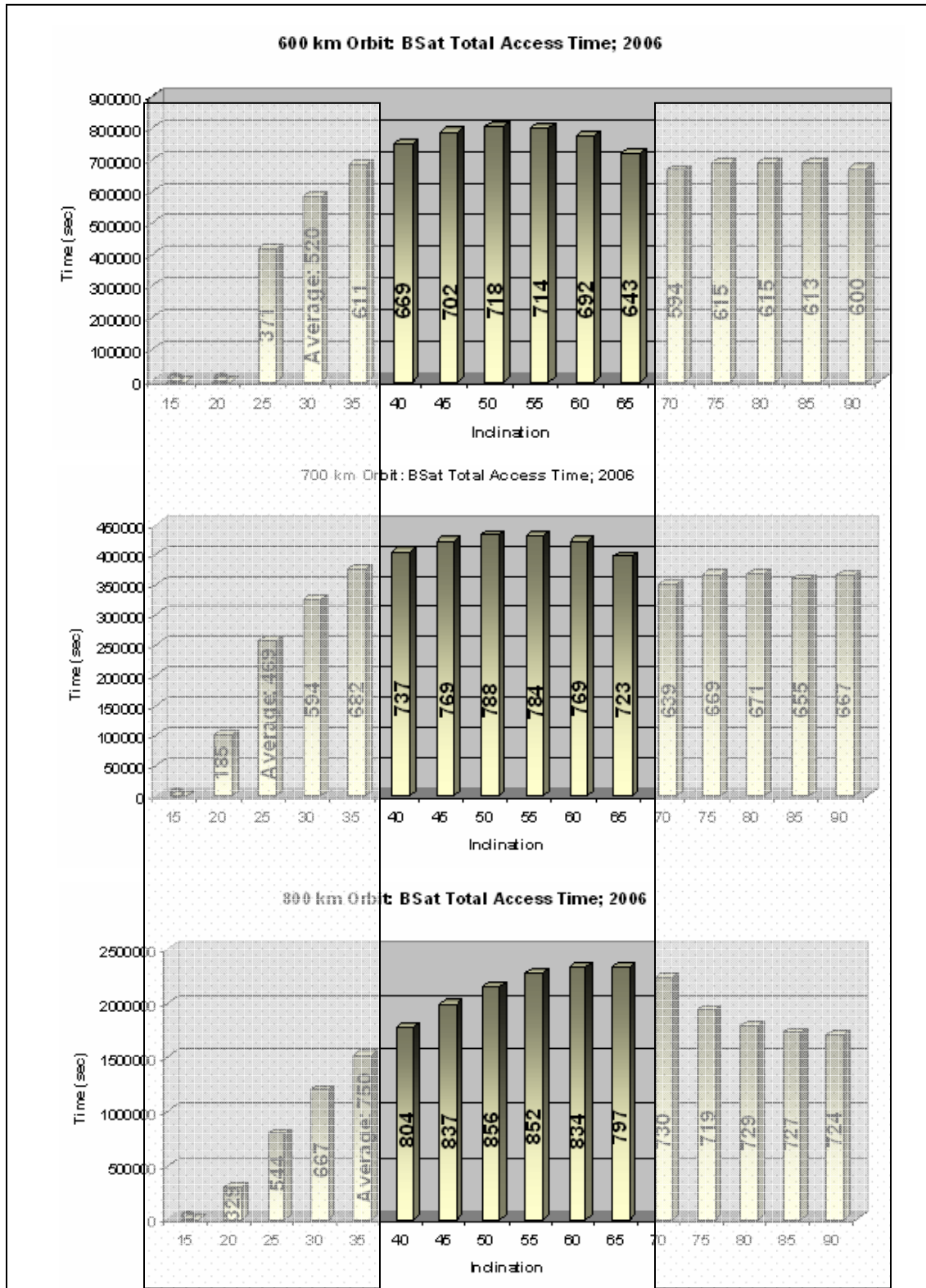


Figure 4-21: BSat Total Access Time vs. Inclination and Altitude for 2006

Figure 4-22 below shows how insignificantly the eclipse time changes relative to BSat's altitude: from 600 km to 800 km the change in eclipse decreases 2% and 3% for the two inclination extremes, respectively.

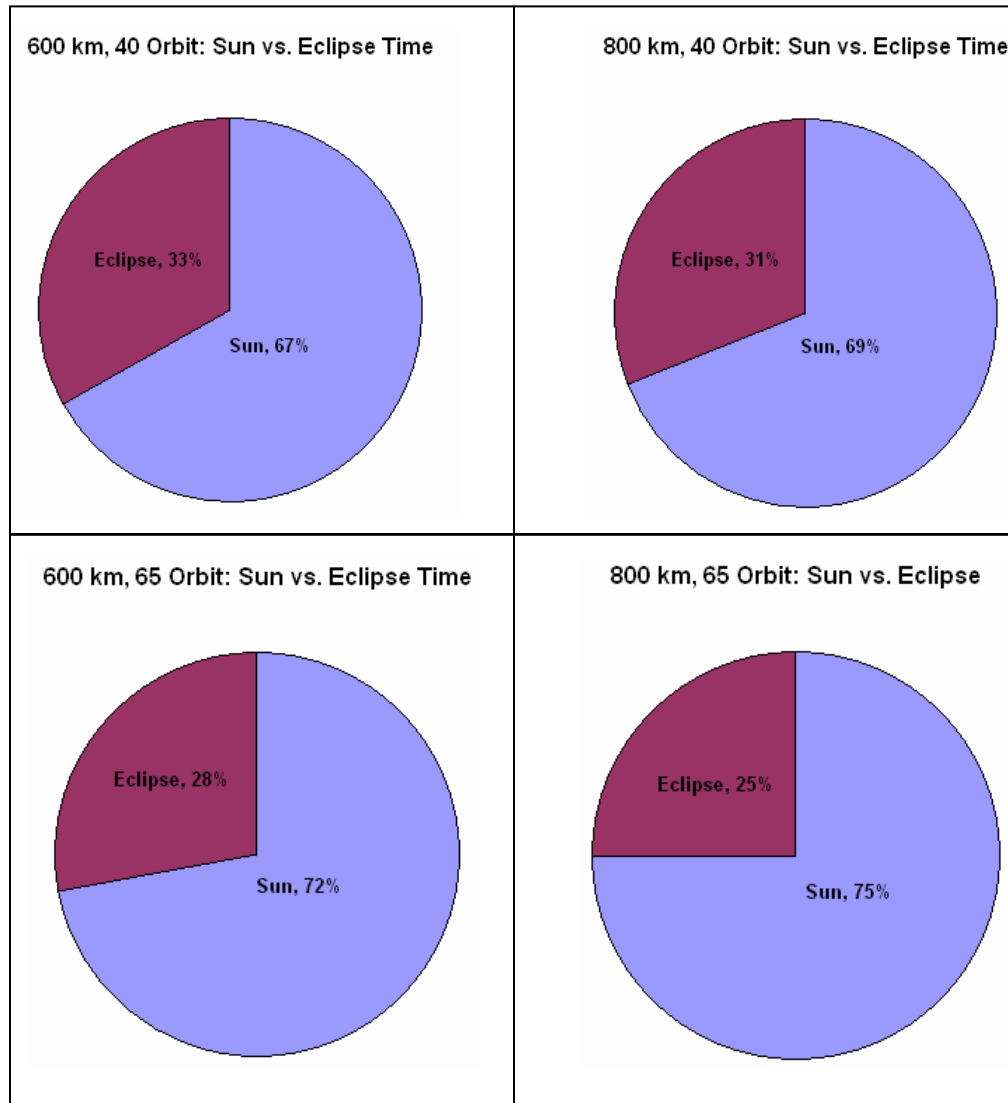


Figure 4-22: BSat Sun vs. Eclipse Times for Parametric Orbit

Beta Angle

The range set forth on the orbit's inclination has limited effect on the satellite's apparent beta angle. As eluded to in a previous discussion, the satellite's beta angle is never constant due to the precession of Earth around the Sun in a given year. From a thermal standpoint the beta angle can vary from 0° to 90° ; however, the maximum angle decreases when the correct inclination can be determined. As in the case of BSat with a range of acceptable orbit inclinations, the thermal analysis includes the maximum range of beta angles; an inclination of 65° and the Earth's tilt is approximated at 90° .⁵¹ Figure 4-23 is the result of another STK simulation that shows the precession of BSat's beta angle over the course of a year. As Figure 4-22 expresses the total percentage of sun-exposure, Figure 4-23 depicts the cyclical behavior of the beta angle and hence the eclipse fraction. To provide an accurate thermal assessment of BSat it was important to consider, parametrically, all the beta angles between 0° and 90° . This will ensure that the proper thermal control can be implemented when an orbit has been specified. Figure 4-23 shows that the altitude of BSat has little effect on its apparent beta angle.

⁵¹ Earth's tilt axis is 23.4° ; 90° because this is thermal parameter extrema.

Beta Angle Procession for 2006; for 65 deg. inclination orbit

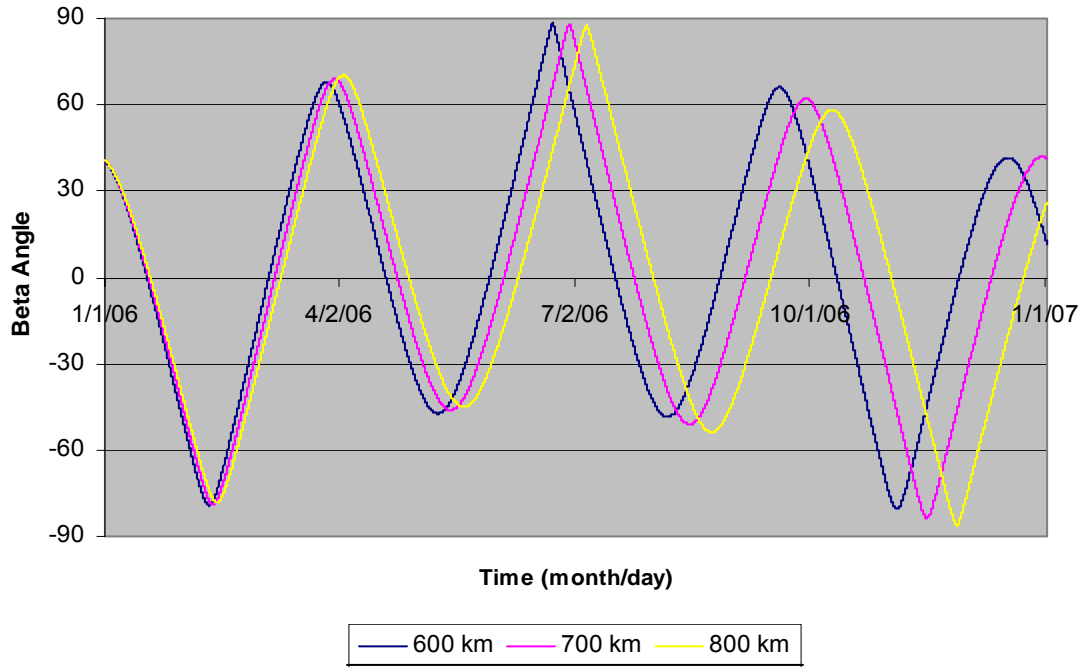


Figure 4-23: BSat Beta Angle Procession during 2006

5. STRUCTURAL ANALYSIS

BSat was conceptualized in September of 2004 under the auspices of SSEL, and quickly transformed into a student initiative to design and prepare a new genre of picosatellites of the CubeSat Plus architecture. BSat is the first generation of satellites designed for use in the RocketPod™. This section will address its structural stability. At the *Small Satellite Conference* in August, 2005, the EDU model was successfully fit-checked with Ecliptic's RocketPod™, see Figure 5-1. This was a milestone of the BSat Project and verified the integrity of all engineering drawings presented in the appendix.

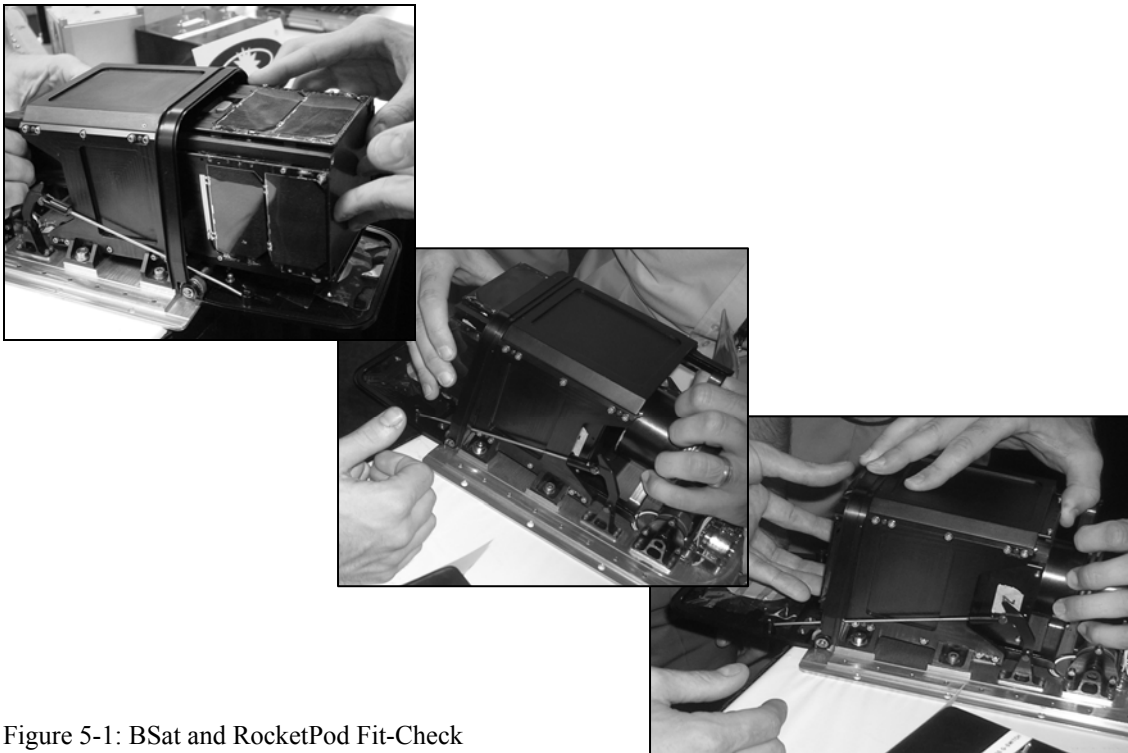


Figure 5-1: BSat and RocketPod Fit-Check

This chapter begins with a discussion of the requirements that drive the analytical assessment and continues on to exploit the standardization of methodologies used to assess BSat's structural design. There are many phases during the lifetime of a satellite in which it is called upon to withstand static loads; during manufacturing, transportation, and mostly during launch. However, [Sarafin, 1995] goes on to say that no structure is perfectly reliable; there are always unexpected scenarios, or loads, which may jeopardized the integrity of the spacecraft's structure. To counteract this, the design of a structure is always designed towards a higher standard. This standard then defines the measure of how much additional strength a structure has above a specified criteria.

As is the case with virtually all CubeSat structures, BSat's structure is mostly limited by the conventional milling techniques used to fabricate it. This suggests that under the constricted mass allowance of 2 kg, the structural members are generally well-suited to withstand any degree of loading within this range. BSat's measure of safety under a given load scenario is significantly large. The structure of BSat was designed for utilizing conventional milling techniques and with the inherent advantage of repeatable and reliable surface finishes.

Requirements and Verification Criteria

The requirements governing the design of BSat were discussed in chapter three and are summarized here. The satellite was subjected to these requirements several times during its iterative development; thus, ensuring a proficient EDU. Each part was

subjected to, and evaluated based on this common standard. This is the method used to determine BSat's integrity:

1. The structure (at the component level) had to withstand a maximum static and dynamic load of 8.0 g;
2. All components had to have fundamental frequencies greater than 35 Hz in both the axial and lateral directions;
3. The satellite had to withstand the random vibrations induced from a 140 dB sound-pressure wave (acoustics);

These are most likely sources of environmental loading and represent the baseline for BSat's analytical assessment. To reduce the probability of structural failure, the inertial loads on BSat were then multiplied by a 1.25 *factor of safety*; thus, imposing an inertial load factor of 10 g. The *factor of safety* is a multiplier for a limit load, in this case the material's yield strength, and is used to decrease the chance of failure. Then to address the suitability of a particular structure, the *margin of safety* reveals how much additional strength a structure has above the following criteria:

$$MS = \frac{\text{Allowable Stress}}{\text{Design Stress}} - 1 \quad (5.1)$$

where the design stress includes the factor of safety. A structure meets its criteria for strength analysis if its margin of safety is greater than or equal to zero [Sarafin, 1995].

For BSat this value was set at two.

Preliminary Static Analysis

Maximum Inertial Load

The perceived highest load BSat will encounter occurs during the launch sequences and is shown in Figure 5-2. The inertial load applied to the satellite is 10 g, which is a value equal to 125% of expected launch loads. Because the RocketPod™ is parallel to the direction of maximum acceleration during launch, this load acts through the satellite's center of gravity, which is centered within the satellite.

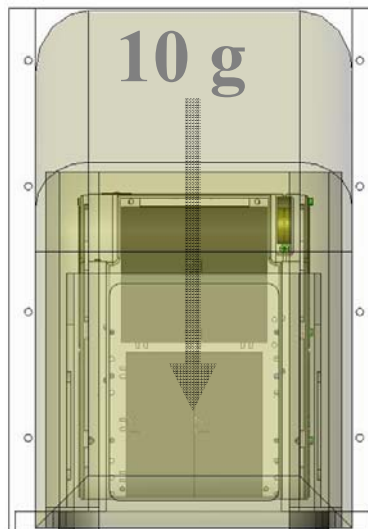


Figure 5-2: BSat Worst-Case Loading Orientation
(*L: axial direction, R: lateral direction*)

During the launch sequence BSat will have to support its own mass of 2 kg along with an inertial load ten times that of Earth's gravity. This inertial load is equivalent to a force of 196.2 N and occurs in the axial direction as seen in Figure 5-2. While BSat is stored within the RocketPod™, a deployment spring is held undeployed via a triggering mechanism that is activated by the door's position. This means that the spring force

created by its compression is retained by the system, and not induced on the satellite. However, in the situation of worst-case, it was assumed that a failure occurred on the release mechanism and the BSat was responsible for bearing the spring force. Figure 5-3 depicts the RocketPod™ spring mechanism.

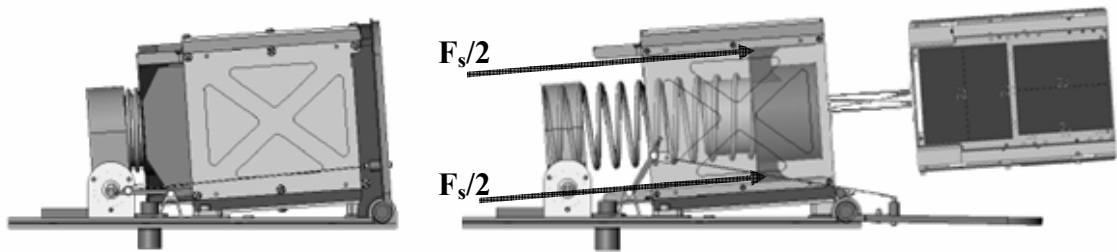


Figure 5-3: RocketPod™ Deployment Sequence (*Reproduced from Ecliptic Publishing, 2005*)

The spring force was obtained through knowledge of the ejection velocities versus the satellite's mass; at 0.6 kg, 1.0 kg, and 2.0 kg the ejection velocity was 2.6 m/s, 2.0 m/s, and 1.4 m/s, respectively. This is extended a little further here to include an expression for BSat's ejection velocity upon determining its final mass. This will also produce the satellite's actual ejection rate and will be useful for determining the final duty cycle and resolution of the GPS data. To begin, consider the spring in its compressed position; the work performed on the spring creates a potential that is stored until the spring is released. This *potential energy* transmits through the system and causes the satellite to move, or have *kinetic energy*:

$$K_{sat} = \frac{1}{2} m_{sat} v_{sat}^2 \quad (5.2)$$

$$U_{spring} = \frac{1}{2} kx^2 \quad (5.3)$$

where K_{sat} , m_{sat} , and v_{sat} are the kinetic energy of the satellite, its mass, and known velocity, respectively. Equation 5.3 is the expression for the potential energy, U_{spring} , spring constant, k , and linear displacement, x . The *Work Energy Theorem* states that in the absence of nonconservative forces, the conservation of energy takes on the following form:

$$\frac{1}{2}m_{sat}v_{sat}^2 = \frac{1}{2}kx^2 \quad (5.4)$$

which shows that the kinetic energy of the mass traveling at a known velocity was created exclusively by the stored energy within the spring prior to separation. By putting this equation in terms of m_{sat} and v_{sat} and utilizing the conditions as stated previously, the constant, C_1 is obtained. The equation for velocity as a function of mass is then:

$$v_{sat} = \frac{C_1}{\sqrt{m_{sat}}} \quad (5.5)$$

where constant, C_1 , was found to be $2 \text{ [kg}^{0.5}\text{m/s]}^{52}$. Figure 5-4 is a graphical comparison of the satellite's mass to the ejection capabilities of the RocketPod™. The distance, x , which the spring compresses is verified by Eclipse to be approximately 100 mm; this ensures that the spring-plunger pushes the satellite completely out of the RocketPod™ enclosure. Using this value in Equation 5.4 reveals a spring force equal to 40 N. See Appendix C.1 for the detailed worksheet.

⁵² The units on this constant are correct and repeated here: $\text{kg}^{0.5}\text{m/s}$; unit-analysis reveals this.

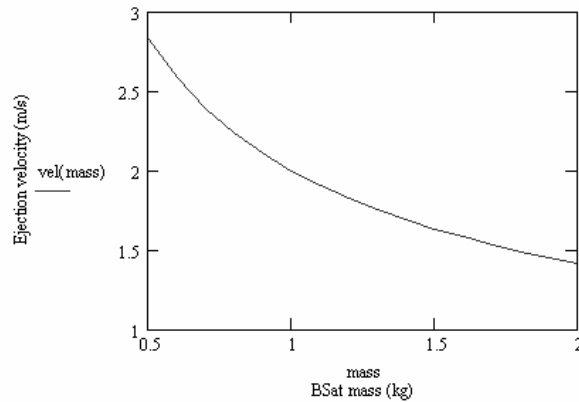


Figure 5-4: Ejection Capabilities of RocketPod™

This force is added to the inertial load for BSat in its axial direction and is assumed to be evenly distributed between the two launch rails which interface with the spring plunger. While the maximum lateral load remains at 196.2 N, the maximum axial load is now 236.2 N.

Simplified Static Model

To perform first-order static estimates of the satellite in response to these loads, a simplified model of BSat was created to determine areas where mass could be minimized. This simplified model as seen in Figure 5-5 depicts a generic CubeSat Plus form-factor consisting of four columns, (8.5 x 8.5 x 113.5) mm, four rectangular plates (83 x 145 x 1) mm, and two square plates (100 x 100 x 1) mm. The launch rails, or columns, are intended to be the only regions of the satellite in contact with the RocketPod™, and for this reason the entire axial load will occur in them. The spring plunger only contacts two rail ends which are positioned diagonally from each other.

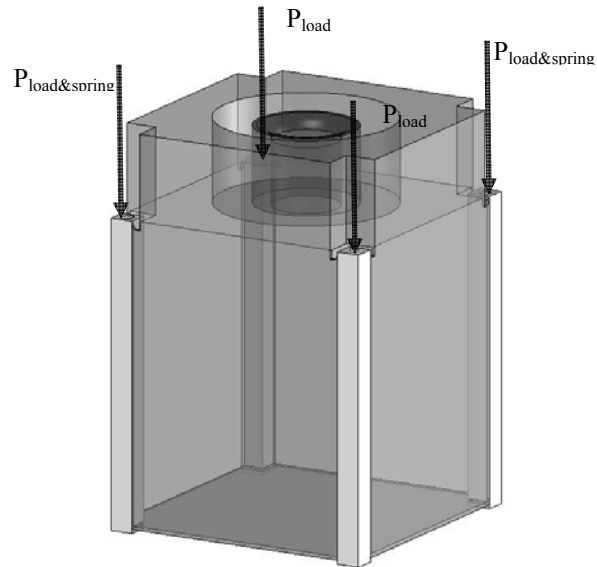


Figure 5-5: Simplified BSat Model

Assuming BSat is evenly loaded with the 10 g inertial force, and that the spring force is equally applying a load to the diagonal launch rails, do the loading conditions of Figure 5-5 become valid. The maximum axial load takes on two forms:

$$P_{load\&spring} = \frac{m_{sat}FS}{4} + P_{spring} \quad (5.6)$$

$$P_{load} = \frac{m_{sat}FS}{4} \quad (5.7)$$

where $P_{load\&spring}$ is the maximum axial load, FS is the factor of safety (10g's), and P_{spring} is the spring force; thus, the maximum compressive load acting on the rail is approximately 89 N. Concurrently, because the spring-plunger only occurs axially, the lateral loading is equivalent to P_{load} , which is approximately 49.0 N. For the maximum compressive strength in the side plates, it is assumed that the maximum load occurs due to failure of the spring-release mechanism entirely; causing the spring force to be

transmitted through the plunger itself and not the portions in contact with the end rails. This load was determined to be approximately 59 N. Table 5-1 is a summary of the detailed analysis performed in Appendix C.2.

Table 5-1: BSat Maximum Compressive Strength

	σ_{MAX} [MPa]	margin of safety	
Launch Rail	1.232	223 407	Al-6061 Al-7075
Side Panels	1.1	256 468	Al-6061 Al-7075

Table 5-1 shows that under the given loading conditions that each member is well within an acceptable margin of safety. As in the case of BSat, this information was used to understand the severity of BSat's stress-state during the launch phase of its mission. For both components, the worst-case or maximum loading occurs with the failure of the spring mechanism in which case, the launch rail and side walls are independently responsible for carrying the entire load of the satellite plus the added spring force.

Failure Modes

Because the largest stresses in the structure are sufficiently less than the yield strength of either type of aluminum, it is assumed that the most likely cause of failure will be either buckling or bending; both are discussed below.

Buckling

The failure of a structural column is typically attributed to an axial compressive load that generates lateral deflections; a phenomenon referred to as *buckling*. This implies that

the *buckling load* is a compressive load at which the column becomes unstable. Consider the axially loaded column of Figure 5-6.

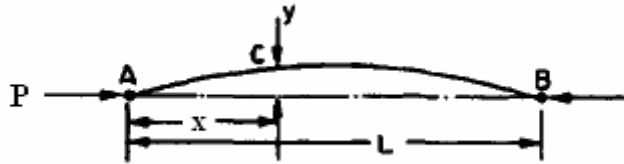


Figure 5-6: Column Buckling

The second order differential equation that defines the deflection curvature of a beam is represented by the following relationship:

$$\frac{d^2 y}{dx^2} = \frac{M}{EI} \quad (5.8)$$

where y is the lateral deflection in the y -direction, M is the bending moment, and EI is the flexural rigidity for bending in the xy plane. Recognizing that the bending moment is equivalent to the product of the load, $(-P)$, and the lateral deflection, Equation 5.8 is put into the following form which represents the buckling load of a column.

$$EI \frac{d^2 y}{dx^2} + Py = 0 \quad (5.9)$$

This equation should be recognizable as the differential equation that describes simple harmonic motion. It has a solution of the form:

$$y = C_1 \sin kx + C_2 \cos kx \quad (5.10)$$

$$\text{where, } k = \sqrt{\frac{P}{EI}}$$

where C_1 and C_2 are constants of integration that are evaluated from the end conditions of the column. For the simply-supported beam of Figure 5-6, the end conditions state that the deflections are zero at $x = 0$ and $x = L$. This gives $C_1 = 0$ and the nontrivial solution for the critical buckling load as:

$$P = P_{cr} = \frac{n^2 \pi^2 EI}{L^2} \quad (5.11)$$

where n is any positive integer denoting the *buckling mode shape*. The fundamental case, and the value that gives the lowest critical load is by setting $n = 1$. Any value higher than one is generally of no interest because the column buckles when the axial load is reached. To account for the end-condition effects, L^2 becomes L_{eff}^2 , the column's *effective length*; for simple support $L_{eff} = L$.⁵³ Finding the critical load for the column allows one to obtain the corresponding stress by dividing the load by the cross-sectional area.

$$\sigma_{cr} = \frac{P_{cr}}{A} = \frac{\pi^2 EI}{AL_{eff}^2} \quad (5.12)$$

This analysis routine was performed for BSat and is commonly known as elastic buckling analysis. It is valid here because the stresses present in BSat are below the materials' proportional limit. For BSat, the estimated critical buckling loads are presented in Table 5-2, and detailed in Appendix C.2.

Table 5-2: BSat Buckling Loads

	Critical Buckling Stress [MPa]	margin of safety
Launch Rail	318 Al-6061	258 Al-6061
	331 Al-7075	268 Al-7075
Side Panels	41 Al-6061	39 Al-6061
	43 Al-7075	40 Al-7075

⁵³ The reader is referred to [Gere, 2001] for a list of L_{eff} for the various end conditions.

The interesting note here is that the calculated buckling stress for the launch rail made of 6061-T6 is greater than the material's yield strength; however, not so for a launch rail made of 7075-T6. This suggests that with the predefined column height (113.5 mm), 6061 launch rails would yield in compression prior to yielding due to buckling. To ensure a sound-structure, the four aluminum sides and hence the launch rails were specified to be fabricated from 7075-T6 stock. The margins of safety show that these simplified parts are extremely well-suited to the defined loading environment.

Bending

When a beam with a straight longitudinal axis is loaded by a lateral force, the axis is deformed into the *deflection curve* of the beam. Consider the two-dimensional beam of Figure 5-7 which is exposed to a distributed load, p .

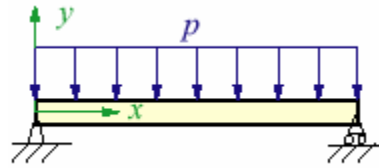


Figure 5-7: Cantilever Beam

The *Euler-Bernoulli* theory describes the elastic bending of the beam and is expressed by the following relation:

$$\frac{d^2}{dx^2} \left[EI \frac{d^2 w}{dx^2} \right] = p \quad (5.13)$$

$$EI \frac{d^4 w}{dx^4} = p \quad (5.14)$$

where p is the distributed loading, and w is the out-of-plane displacement of the beam. For an isotropic material with constant cross section, Equation 5.13 is simplified to Equation 5.14. In order to relate the pressure loading to the beam's out-of-plane deflection, and subsequently the associated bending stress, the equilibrium relations between the bending moment, M , the shear force V , and the intensity of the distributed load are presented below:

$$\frac{dV}{dx} = -p \quad (5.15)$$

$$\frac{dM}{dx} = V \quad (5.16)$$

where by combining these latter two equations to eliminate V , Equation 5.8 is revealed. In order to obtain Equation 5.14 from Equation 5.8 the constitutive equation relating stress to strain, known as *Hooke's Law*, is applied:

$$\sigma_x = E\varepsilon_x \quad (5.17)$$

where E is Young's Modulus and is the proportionality constant between stress, σ , and strain, ε . By applying the expression for the resultant moment ($dM = -\sigma_x y dA$), and through a series mathematical simplifications, the expression for the bending stress of a prismatic beam is established:

$$\sigma_x = \frac{-My}{I} \quad (5.18)$$

where M is the bending moment, y is the distance from the neutral axis, and I is the area moment of inertia of the beam. This equation is called the *flexure formula* and shows

that the stresses are directly proportional to the bending moment and inversely proportional to the moment of inertia of the cross section.

This linear-elastic analysis was performed on BSat's simplified structure under the predefined loading conditions. Table 5-3 presents the bending stresses and corresponding margin of safety for the simplified BSat model.

Table 5-3: BSat Bending Stresses

	BendingStress [MPa]	margin of safety
launch rail	6.8	41 Al-6061 74 Al-7075
Side Panel w/ uniform normal load	1.3	220 Al-6061 402 Al-7075
Side Panel w/ uniform normal and compression	.81	338 Al-6061 612 Al-7075
Baseplate	.761	363 Al-6061 661 Al-7075

To arrive at the information presented in Table 5-3, and as seen in Appendix C.2, scenarios of worst-case were defined for both the simplified launch rail and the side panel. As the launch rail is the only member of the BSat structure in contact with the deployer, the induced loads are a maximum because it contains the inertial load of the entire satellite. The side panels and baseplate do not interface with the deployer and are only subjected to the inertial load caused by the constituent's mass. The third entry in Table 5-3 expresses a side panel which is experiencing uniform lateral loading combined with a failure of the spring mechanism. In this case, the side panel is simultaneously being axially compressed on its short edges and subject to bending in its lateral direction. For all cases the margin of safety is high and reveals that removing material or changing

geometries will decrease the margin of safety; structural integrity will still be well within margin of safety design limitations.

Bearing Stresses and Mechanical Fasteners

The final two failure modes investigated for BSat were on its fasteners and the *tabs* in which they thread into. As the possible failure mode will be in shear, the worst-case condition was imposed onto a single fastener and represents a load equivalent to 196 N. Dividing by the fasteners cross-sectional area the stress is obtained. It is typical in the design of a spacecraft to minimize the number of single-point failures; for this reason and for the purposes of assembly, the applied load will be distributed amongst *redundant load paths* and the shear stress will always be lower than the aforementioned value.

A bearing failure is the result of a fastener's contact forces acting on the surface of the fitting resulting in permanent deformation. Consider Figure 5-8 in which a fastener is in single shear.

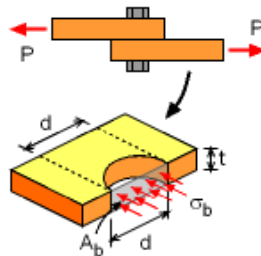


Figure 5-8: Bearing Stresses

As the load is applied, contact stresses or bearing stresses develop in the sections of the bars which are in contact with the fastener; similarly, the two bars attempt to shear the bolt. Contact stresses are often assumed to be uniformly distributed in which the *average bearing stress*, σ_b , is obtained by dividing the total bearing force, P , by the bearing area,

A_b. Failures in mechanically fastened joints are typically hard to predict because the loads often distribute unevenly and stress concentrations develop. To counteract this difficulty, Sarafin [1995] states that a *fitting factor* of 1.15 should be used to account for uncertainties. The fitting factor is simply multiplied into the bearing force and takes on the value of 226 N. Table 5-4 shows the results of this analysis.

Table 5-4: Fastener Strength and Bearing Stresses

	Stress [MPa]	margin of safety
#2-56 SS fastener	shear: 52.2	6
Tab	bearing: 34.4	8 Al-6061 15 Al-7075
Tab	shear tearout: 11.6	24 Al-6061 43 Al-7075

These results show that the tabs of the baseplate and tophat, could be specified with smaller dimensions. However, considering that there exists redundant load paths amongst all fittings and fasteners, the limitation here is sourced by conventionally milling techniques. That is to say that under any predicted loading, the design of BSat is not limited in strength, but instead by feasibility in cost and fabrication.

Dynamic Analysis

The dynamic loading conditions have been discussed previously and correspond to three main analysis groups: harmonic, random, and acoustic. These conditions induce vibrations within the structure and require attention to assess the structure's ability to provide a suitable environment for the subsystems. The majority of this analysis was performed using the FEM software COSMOS.

Harmonic Vibrations

Determining the response of a structure due to time-varying sinusoidal loads is a requirement to ensure that the natural frequency of the structure remains uncoupled to the LV. The natural frequencies for all of BSat's constituents were determined using COSMOS; whereupon simple geometries like flat plates, were compared against theoretical plate theory. The equation that defines the fundamental frequency of a rectangular plate with both pinned and fixed end conditions is:

$$\omega = \sqrt{\frac{D}{\rho t} \left(\frac{\pi}{2} \right) \left[\left(\frac{m}{a} \right)^2 + \left(\frac{n}{b} \right)^2 \right]} \quad (5.19)$$

where D is the plate's bending stiffness and is determined by: $D = Et^3/(12-\nu^2)$. The other parameters include are the material's elastic modulus, E , poissons ratio, ν , and density, ρ . The geometric parameters are the plate's thickness, length, and width represented by t , a , b , respectively. The variables m and n are positive integers signifying the mode of vibration. These are typically both set to one because this amounts to the lowest vibration mode and hence the structure's fundamental frequency.

While Appendix C.3 encompasses all the structures' fundamental frequencies, Figure 5-9 below depicts the harmonic response of BSat's four adjoining sides. It is important to note that a structure's natural frequency is solely dependent upon its mass and stiffness and that a single-degree-of-freedom (SDOF) system will always vibrate at the same frequency regardless of amplitude. In other words, the stiffness of an assembled structure is compounded by all of its constituents. Figure 5-9 shows the discretization implementation and the boundary conditions that were imposed. These boundary conditions (designated by the green arrows) were defined as fixed and were implemented

to represent the stiffness added by the inclusion of the tophat, baseplate, and tether bracket.

Model name: Assem1
 Study name: frequency
 Plot type: Frequency Plot1
 Mode Shape : 1 Value = 955.18 Hz
 Deformation scale: 0.000669214

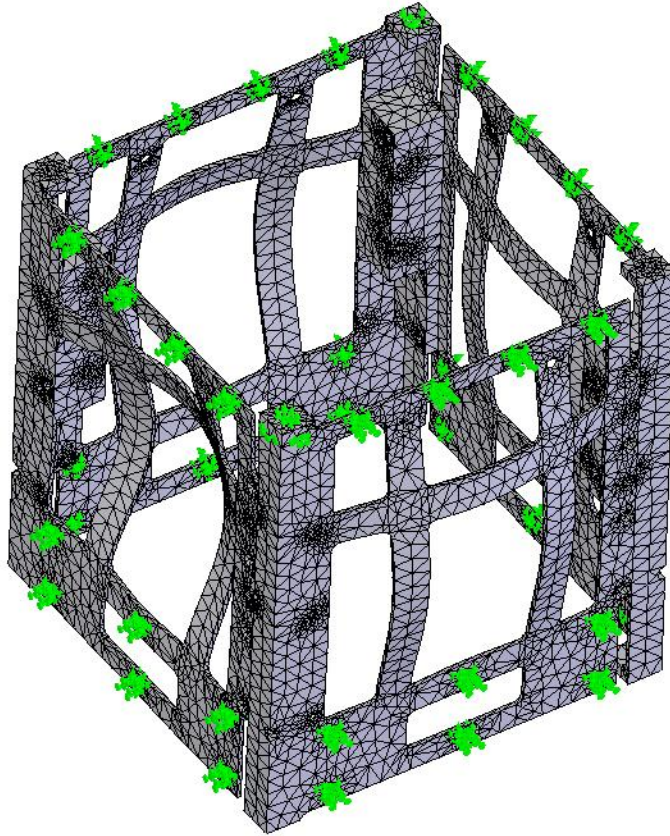


Figure 5-9: Primary Structure 1st Mode, Harmonic Response

This result verifies that indeed the BSat structure satisfies the 35 Hz minimum requirement. As an aside, with the 100 Hz requirement for human missions, the BSat structure would also accommodate a ride onboard the STS.⁵⁴ Appendix C.3 includes the first six mode values for all of BSat's structural parts; whereas, the first-mode natural frequency for each part is summarized in Table 5-5.

⁵⁴ Space Transportation System; i.e. space shuttle

Table 5-5: BSat Natural Frequencies

Part	Natural Frequency
Baseplate	495
Tophat	1595
Sides	388
Tether Bracket	1400
Solar Panels	2000
Battery Bracket	790
SRL. MNT. PLT	1440
FR4s	418

The two *true* flat plates of BSat are the baseplate and the FR4 boards shown in Figure 5-10. Thus for these two elements using Equation 5.19, it is possible to compare a true theoretical solution with the FEM results. While both components measured 98 x 98 mm square, the thicknesses were 1.0 mm and 1.57 mm for the baseplate and FR4, respectively. The results are presented in Table 5-6.

Table 5-6: Theoretical vs. FEM Natural Frequencies

	FEM N. Frequency	Theo. N. Frequency	% error
Baseplate	495	486	2%
FR4	418	435	4%

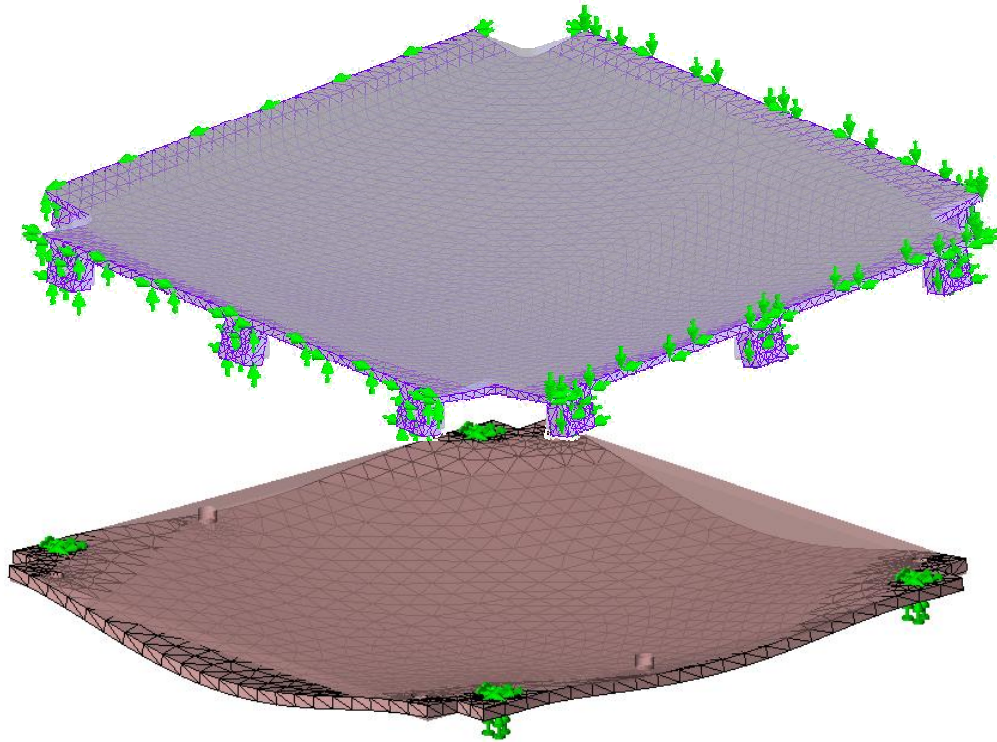


Figure 5-10: FEM Boundary Conditions for the Baseplate and FR4 Board

The discrepancies in the values of Table 5-6 is thought to be a result of the different boundary conditions (BCs). The FEM result for the FR4 board is 4% different than the theoretical; however, keep in mind that the FEM modeled was solved with different BCs. Whereas in the top figure, the baseplate is literally constrained in a manner consistent with the simply support stipulation of Equation 5.19, the bottom figure depicts the FR4 board suspended as it is intended for flight, with standoffs.

Power Spectral Density

For the random vibration environment it is impossible to predict a force-time history of the applied loads. It is therefore necessary to employ a frequency-domain method to

characterize a structure's response to random vibrations; this generates a power spectral density (PSD) function which is a function of the frequency content squared, divided by the bandwidth over that frequency. The term *power* is a generic term that can represent acceleration, velocity or displacement. The frequency content represents the vibrational power in a signal in terms of acceleration-squared. Therefore, the results of a PSD curve are presented in units of $[g^2/Hz]$.

For the purpose of this analysis the response of the plate will be treated as a SDOF system. Consider Figure 5-11, this is an example of a linear system in which the spring force is proportional to displacement and the damping force is proportional to velocity.

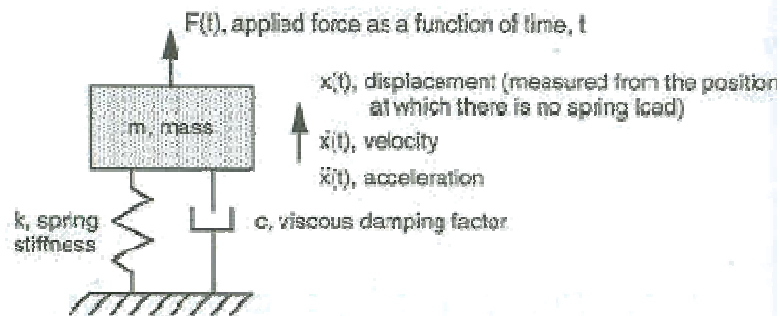


Figure 5-11: Idealized System with a SDOF (Reproduced from Sarafin, 1995)

The objective here is to determine the PSD response in terms of the random excitation; the first step is to start with the equation of motion as presented below:

$$m\ddot{x} + c\dot{x} + kx = F(t) \quad (5.20)$$

where m is the mass, c is the viscous damping factor, k is the spring stiffness, and $F(t)$ is the forcing function⁵⁵, and x , \dot{x} , \ddot{x} are displacement, velocity, and acceleration, respectively. From this form of the equation of motion it is clear that the $m\ddot{x}$ term is the

⁵⁵ Forcing Function – describes how applied forces vary with time or frequency.

inertia force, the $c\dot{x}$ term is the damping force, and the kx is the spring force. By putting Equation 5.20 in a form that represents the systems *damping ratio*, $\zeta=c/c_c$, and natural frequency, $c_c=2m\omega_n$, the following form of the equation of motion is obtained.

$$\ddot{x} + 4\zeta\pi f_n \dot{x} + (2\pi f_n)^2 x = \frac{F(t)}{m} \quad (5.21)$$

where the natural circular frequency, $\omega_n = (k/m)^{1/2}$, and the natural frequency, $f_n = \omega_n / 2\pi$. The solution to Equation 5.21 is then determined by implementing the frequency response approach. To aid in this solution and to mathematically define the PSD, the Fourier transform for frequency response is substituted for the transient function $x(t)$:

$$X(f) = \int_{f_n=-\infty}^{\infty} x(t)e^{j2\pi ft} dt \quad (5.22)$$

where $X(f)$ is the transformed variable for $x(t)$, and $j = \sqrt{-1}$. By substituting the appropriate derivatives of Equation 5.22 into Equation 5.21 the equation of motion *transforms* into an algebraic expression:

$$\ddot{X}(f) = H(f)\ddot{U}(f) \quad (5.23)$$

where $\ddot{X}(f)$ is the output Fourier transform, $\ddot{U}(f)$ is the input Fourier transform, and $H(f)$ is the transfer function that relates the input and output Fourier transforms:

$$H(f) = \frac{-(f/f_n)^2}{[1-(f/f_n)^2] + j2\zeta(f/f_n)} \quad (5.24)$$

where f is frequency, f_n is the system's natural frequency, and ζ is the damping ratio. To work in terms of the structures response to a random excitation it is necessary to obtain the rms acceleration:

$$\ddot{x}_{rms}(f) = |H(f)|^2 W_{\ddot{x}}(f) \quad (5.25)$$

where \ddot{x}_{rms} is the response acceleration spectral density, and $W_{\ddot{x}}(f)$ is the input acceleration PSD; for the acoustic analysis addressed in the next section, $W_{\ddot{x}}(f) = W_p(f)$ and represents the pressure power spectral density of the acoustic waves. The pressure spectral density is then the ratio of rms pressure at frequency, f , over the frequency band, $\Delta f(f)$, corresponding to the frequency.

Acoustic Vibrations

Acoustics induce sound-pressure waves causing a structure to have a *vibroacoustic response*. Because acoustics include waves with many different frequencies, they cause structures to vibrate randomly. It is a physical reality that BSat will be exposed to probabilistic loading; however, this environment has been quantified statistically and was shown in Figure 3-12 in terms of an SPL curve.

To perform analysis on a structure's response to acoustic loading, the PSD function was employed to perform this frequency-domain analysis. The structures that respond the most are light in weight and large in surface area; for BSat, these structures include the baseplate and FR4 boards. The vibroacoustic analysis for the BSat structure was simplified for the simple case of a flat plate with fixed boundary conditions. This analysis was performed in MATLAB using a modified methodology outlined by Sarafin and can be found in Appendix C.4. The results of this analysis are represented by Figure 5-12.

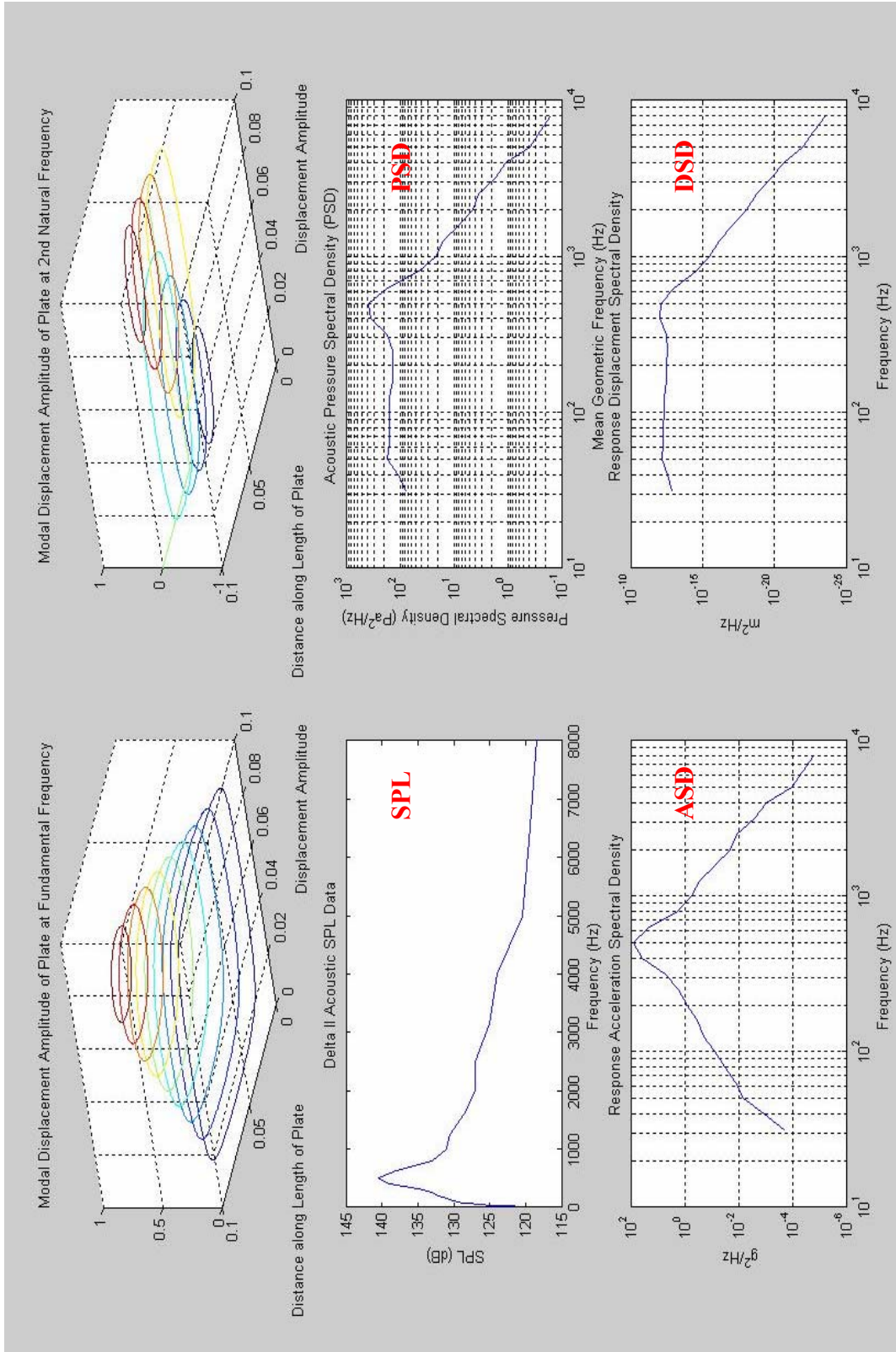


Figure 5-12: MATLAB Output of a Flat Plate's Response to Acoustics

While the graph labeled SPL^{56} is information supplied by the PPD, the PSD^{57} graph is a result of applying equations which correlate the sound pressure level to the rms pressure distribution. To obtain the ASD^{58} graph, the Fourier transform was applied to the equation of motion that resulted in an algebraic expression which related the pressure distribution function to the plate's acceleration response. The final DSD^{59} plot was then obtained by applying Parseval's Theorem and Miles Equation to obtain the displacement response. These mathematical steps are evident in the MATLAB code of Appendix C.4. The method employed here is valid exclusively for small deflections where it was necessary to guarantee that the rms displacement was not greater than half the plate's thickness. For BSat's baseplate and FR4 board the results are detailed below.

Table 5-7: Acoustic Response Results

	Thickness [m]	\ddot{x}_{rms} [g's]	Displacement [m]
Baseplate	.001	129	1.772e-5
FR4	.0015748	131	1.86e-5

Table 5-7 indicates that indeed the small-deflection method is valid for BSat's baseplate and FR4 boards. The maximum rms acceleration and displacement occur at the natural frequency. Figure 5-12 shows this for the baseplate as all the *peaks* can be read to occur around 500 Hz, the baseplate's natural frequency.

⁵⁶ Sound Pressure Level

⁵⁷ Pressure Spectral Density

⁵⁸ Acceleration Spectral Density

⁵⁹ Displacement Spectral Density

Finite Element Analysis

The finite element method is a numerical tool used in industry to solve a wide range of engineering problems. In the case of BSat, finite element analysis (FEA) was used to estimate the stresses endured by the satellite in a variety of different load scenarios. The program COSMOS was used here due to its availability in the SSEL, and because it is a computational module to the lab's preexisting SolidWorks modeling package.

COSMOS

The FEA software suite, COSMOS, is an extension of SolidWorks and was the FEA package chosen to perform BSat's numerical stress analysis. It is widely accepted as a linear static solver and it is well-suited in the application of BSat because it is not design-acceptable for the satellite structure to encroach on its yield strength. Figure 5-13 was presented previously, but here it is presented with the linear threshold superimposed upon it.

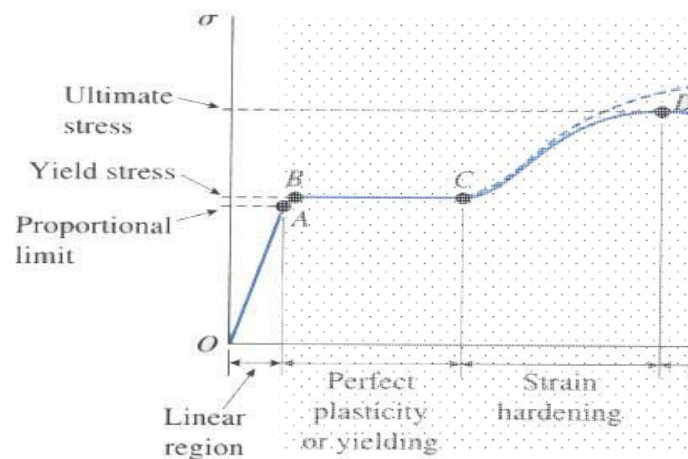


Figure 5-13: Stress/Strain Diagram

For the response of a structure to be linear the mechanical behavior must obey Hooke's Law:

$$\sigma = E \varepsilon \quad (5.26)$$

where stress, σ , is proportional to strain, ε , by the proportionality constant, E , known as Young's Modulus. This equation states that the elemental forces are linearly proportional to elemental deformations, and that when the loading is removed, that the material returns to its original, undeformed shape. This occurs within the elastic region of the material whereas in the plastic region, the material begins to develop permanent deformations.

COSMOS also includes a nonlinear solver, a linear buckling analysis tool, solvers for both steady-state and transient heat conduction, and a vibration solver. As the harmonic vibration data was already presented, this section discusses the linear-static analysis performed on BSat. Through the aid of the computer, this allows for the inclusion of the complex geometries and was solved in a manner the reflected BSat stowed within the RocketPod™ as intended for launch. Figure 5-14 shows these boundary conditions.

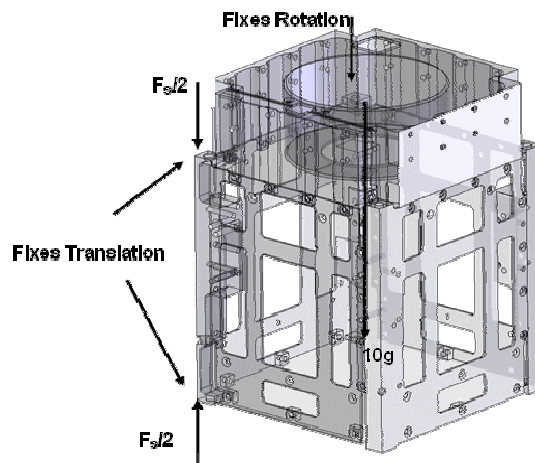


Figure 5-14: BSat Physical Boundary Conditions and Inertia Load

Convergence

To verify the results obtained from the numerical FEM software, COSMOS, it is first important to discuss the numerical routines' *convergence criterion*. The convergence criterion employed though COSMOS is based on the strain-energy approach for iterating strains; thus, giving an accurate estimate of the developed stresses. COSMOS begins a numerical routine by first calculating the displacements at all the nodes and then proceeds to calculate the strains followed by the stresses, independently. The stresses are calculated at strategic locations within the element known as Gauss points whereupon the elemental stress values at a common node are average to yield the nodal stress value. The displacement field obtained by FEM is continuous in order to satisfy compatibility whereas the stress field is usually discontinuous; this is the essence of why FEM is an approximation. For an exact solution the elemental stress values should give an identical stress value at their common node; however, the nodal stress values are extrapolated by the element solutions. The variation in stresses at common nodes provides a measure for the accuracy of the solution based on strain energy principles. The convergence criterion for BSat's FEM solutions guarantees that the iterations will continue until the strains have changed by less than 0.8%.

Loading Conditions and Boundary Conditions

While the primary structure experiences the greatest loads during launch, every other part is also exposed to an inertial load while fulfilling its responsibility. This section explains all load bearing structures and the corresponding imposed boundary conditions. All the green arrows represent boundary conditions while all the magenta arrows are the

applied load. It is the intent that analyzing the satellite at the part level will be compounded at the system level; a satellite structure that is many times stronger than any of its individual components. As the satellite design was an iterative process, it is important to begin with the simplified geometries and move on to the more complex. The materials are consistent with the information presented earlier; the four sides are made of 7075-T6 aluminum while all others are of 6061-T6 aluminum.

Launch Rails

The launch rail was modeled as a column measuring 113.5 x 8.5 x 8.5 mm. It is these columns which experience the greatest loading because of its direct interface with the spring plunger. This launch rail was analyzed with both linear static and buckling solvers. Figure 5-15 shows the non-translational and non-rotational constraint imposed on the columns bottom face and the axially compressive load which is equal to 89 N. The left-most figure depicts the 3321 nodes and 1,782 tetrahedral elements. The center figure shows the stress distribution due to the compression load; the average stress value being 1.2 MPa. The right-most figure represents the linear buckling analysis conducted through COSMOS. The *load factor* seen in this depiction is an indication of the critical buckling load of the column. Recall that the analytical results revealed a critical buckling load of 23,900 N; the critical buckling load of the FEA is $261 \cdot 89 = 23,229$ N. These values compare favorably.

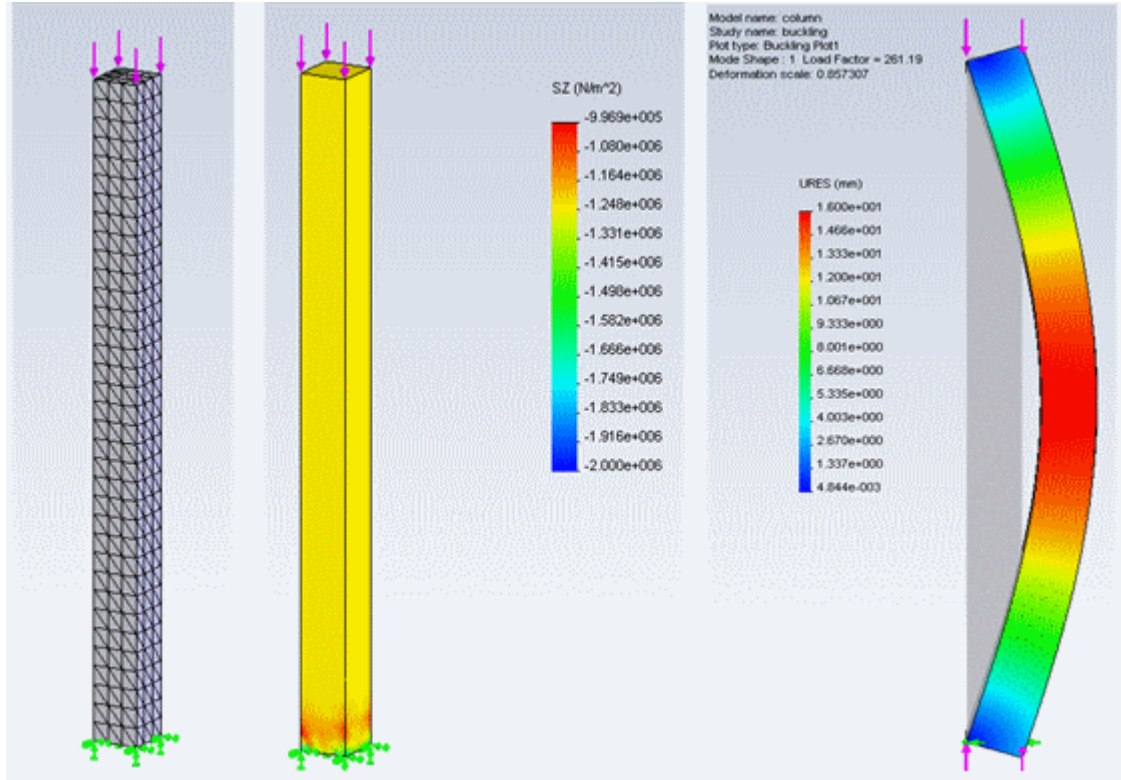


Figure 5-15: FEM Launch Rails

For the bending of the rail due to the 10g lateral load, Figure 5-16 shows the stress distribution of the FEA results. The undeformed rail is superimposed onto the deformed configuration to visually verify the application of boundary conditions. This lateral load is directed along a centerline of the rail and had a magnitude of 49 N; the force equivalent to a quarter of the satellite's inertial force.

The numerical results reveal an average stress value of 6.4 MPa occurring coincident with the rail's centerline. This is the *von Mises* stress which does not discriminate between compression and tension; it is defined by magnitude solely. Figure 5-17 compares the deflection curves of the analytical and numerical analyses. It is apparent that the FEA results are more conservative than the analytical routines. In this case, the

maximum deflection due to bending as a result of the 10 g lateral is predicted to be approximately 3×10^{-5} m.

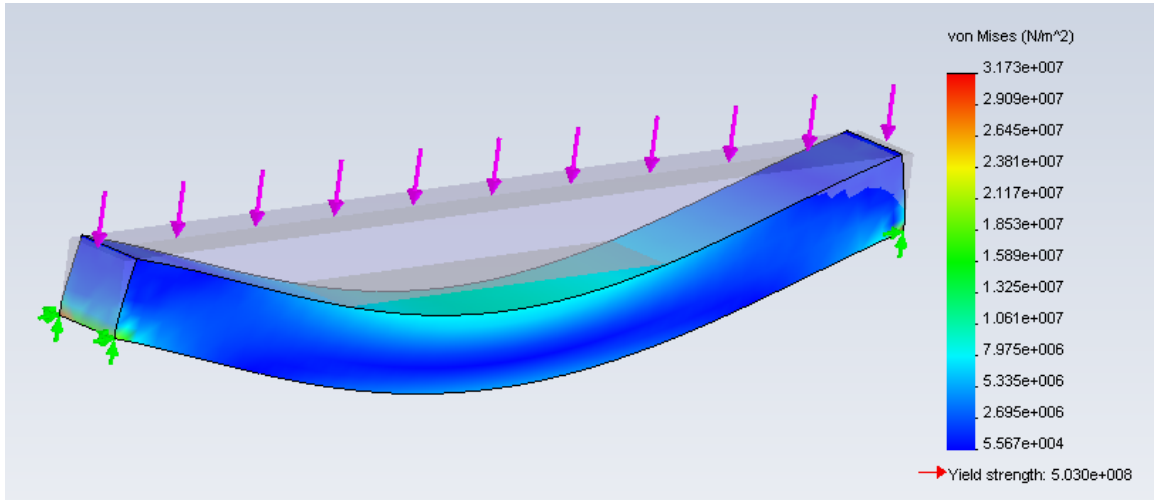


Figure 5-16: Launch Rail in Bending

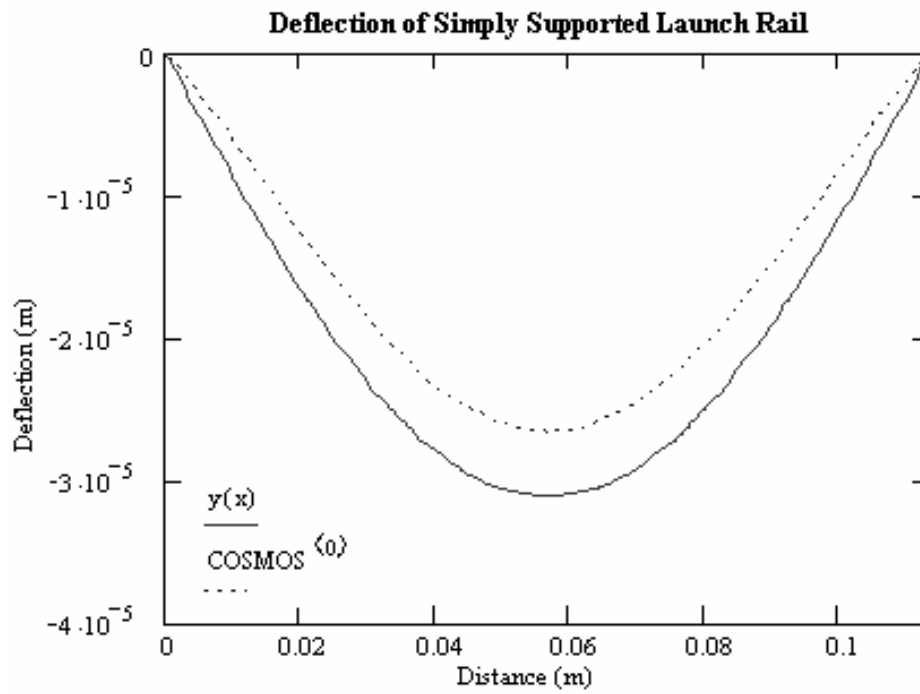


Figure 5-17: Beam Bending, FEA vs. Analytic

Flat Plate

The side panel was modeled as a flat plate measuring 113.5 x 83 x 1 mm. The side panel was investigated under a compressive load equaling 89 N, its corresponding buckling load, and a lateral pressure load equivalent to 276 Pa. The resulting stresses were then correlated to the analytical routines mentioned earlier. With this approach, the plate was analyzed with both the linear static and buckling solvers. Figure 5-18 shows the fixed constraint along a bottom face, and the compression load. The flat plate required a finer-mesh than its launch-rail counterpart and consisted of 11,980 nodes and 5,895 tetrahedral elements, as shown in the left hand panel of Figure 5-18.

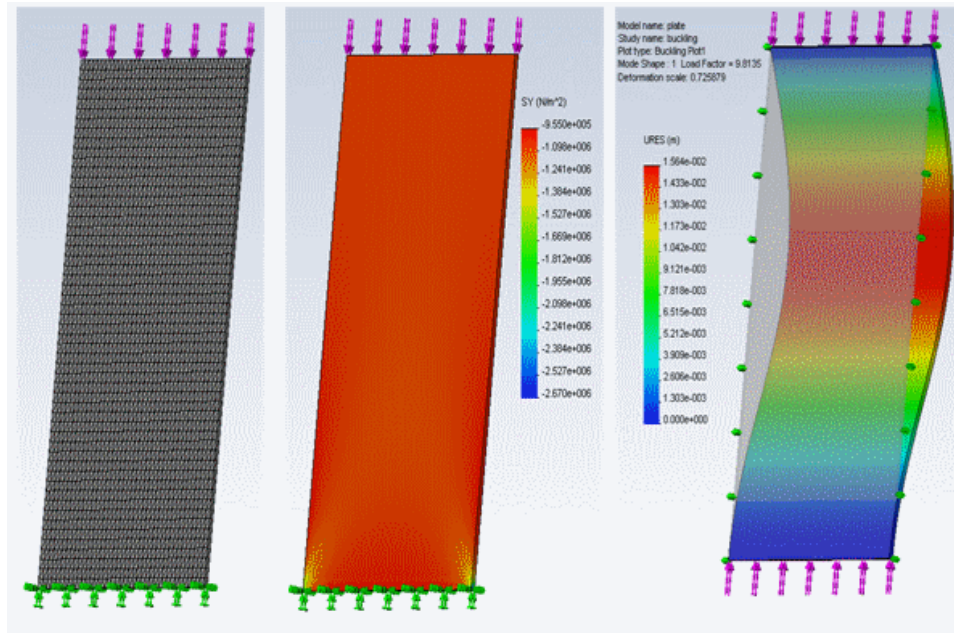


Figure 5-18: Flat Plate FEA Results

The center figure shows that the panel's average *van Mises* stress distribution due to the compressive load is 1.072 MPa. The right-most figure shows a critical buckling load equal to 873.4 N. As the yield strength of Al-6061-T6 is 275 MPa, these stress results are

sufficiently within the capabilities of the material. This load is significantly different than that obtained analytically; however, by including the same buckling coefficient as suggested by Young [1989], the critical buckling load for the panel is 3214 N; this value compares favorably with the analytical results.

The last failure mode investigated is the flat plate in bending. This occurs when the plate experiences its lateral-inertia load distributed evenly over the entire flat surface. If the deflection of the plate in response to this load becomes larger than half the thickness of the plate, the middle surface becomes appreciably strained and the stress in it cannot be ignored. This stress, called the *diaphragm stress*, enables the plate to carry part of the load as a diaphragm in direct tension. When this large deflection exists, the relations between load and stress are nonlinear. The side panels of BSat were first modeled as flat plates with a lateral pressure load equal to 276 Pa while three edges were simply supported and fourth fixed; refer to Appendix C.2 for more details. The FEM solution regarding this scenario is presented in Figure 5-19. The Van Mises stress at the plate's center is 0.6 MPa and the corresponding displacement is $6.5e-3$ mm. Since the plate retains its small-deflection characteristics, these results do not compare favorably with the analytical solutions and the plate does not develop diaphragm stresses. This condition is further restricted upon general assembly because both the exterior solar panels and the interior tether payload will prevent the side panels from deflecting substantially.

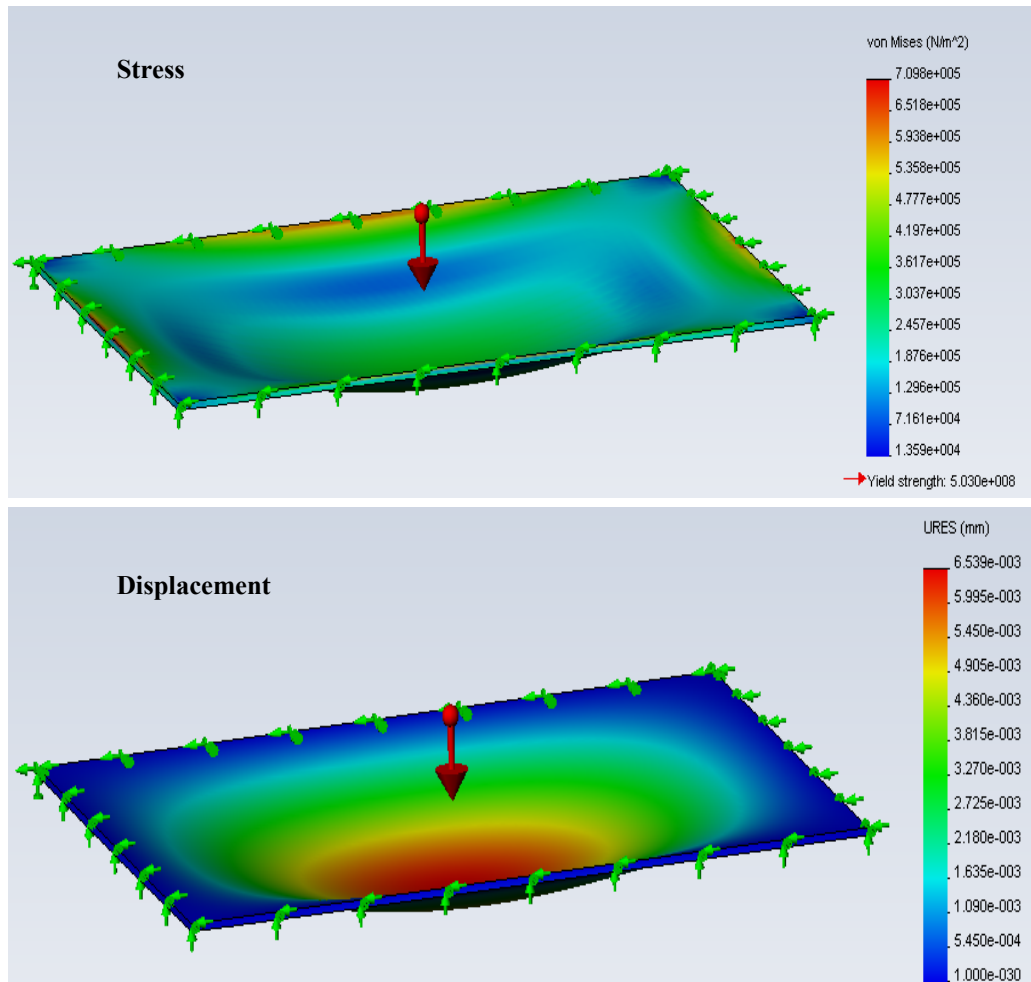


Figure 5-19: Side Panels In Bending

Tabs

BSat was designed with many *tabs* which are utilized as tapped holes for the fasteners. The tabs were optimized against both mass and structural stiffness as alluded to in the previous section. To ensure that these tabs were sufficient in both shear-tear out and in bearing, the entire inertial load of the satellite was imposed onto a single tab. The tabs of BSat measure 5 x 5 x 3 mm and all are specified to accommodate #2-56 Helicoil Inserts. They were loaded in bearing to 196 N while maintained fixed on the opposing

surface. Figure 5-20 depicts a single tab discretized to 2,932 nodes and 1,702 elements in the state of stress with the corresponding safety-factor distribution. Considering that all tabs have redundant load paths, the 196 N load represents the overall mass and a worst-case scenario for a single tab. Therefore, any loads less than 2 kg will produce even less probabilistic results.

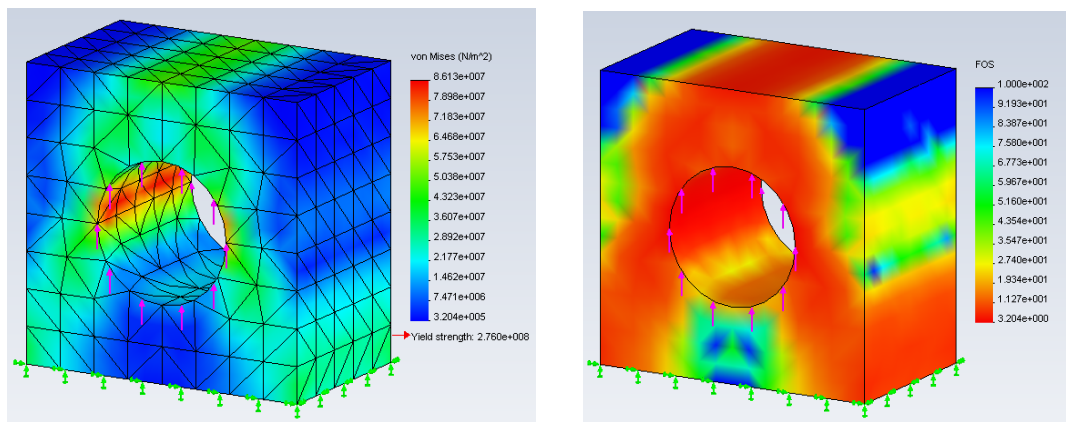


Figure 5-20: Stress Distribution of Single Tab

Comparing the results seen in Figure 5-20 with the two-dimensional analytical results reveals a discrepancy within the same order of magnitude as the analytical solution. However, this was expected considering the analytical bearing stresses only produce an average value whereas COSMOS produces elemental stress values based on the entity's geometry. The average FEM stress value on the *cylinder* was 35 MPa compared to 34.4 MPa. Failures in attachment fittings are often hard to predict because the loads are normally distributed unevenly among fasteners. Actual bearing stresses peak at the mating surfaces of the fittings; once the fitting begins to yield under the concentrated

stress, the load spreads more evenly through the holes. Comparing average FOS⁶⁰, analytical results show a value of 8 while the average from COSMOS is approximately 10. These two values compare favorably; however, even the case of minimum FOS of 3 as produced from COSMOS is still acceptable. To access this further, the same tab was analyzed based on the hoop stress criterion which assumes the hole is a thick-walled pressure vessel with an internal pressure equal to the same stress used above. In this case, the FOS was determined to be 5; this value closely resembles the minimum value as produced by COSMOS. Refer to Appendix C.2 for detailed documentation. Figure 5-21 shows the average FOS inferred from COSMOS along with the deformed shape to verify the application of boundary conditions and bearing load.

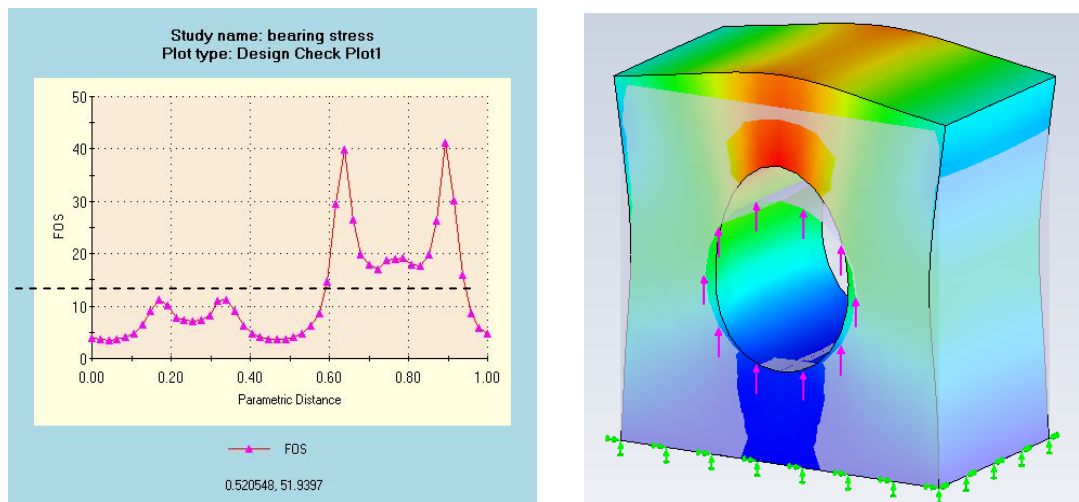


Figure 5-21: Tab FOS and Deformed Shape

Preliminary Results

This preliminary analysis has revealed a significant margin of safety and adequate survivability in terms of worst-case static loading and imposed failure modes. Table 5-8

⁶⁰ Factor of Safety

below is a comparison of analytical routines with the FEA results. In all cases the FEM solutions tend to be less conservative than the analytical solutions; however, the results are highly comparable. This information fundamentally validates the BSat structural design.

Table 5-8: Preliminary Static Results

	Compression Stress [MPa]			Buckling Load [N]			Bending [MPa]			Bearing Stress [MPa]		
	Analytic	FEM	% err.	Analytic	FEM	% err.	Analytic	FEM	% err.	Analytic	FEM	% err.
Launch Rail	1.232	1.2	3	23900	23229	3	6.797	6.4	6	NA		
Side Panel	1.073	1.072	1	3567	3214	10	.761	.7	8	NA		
Tabs	NA			NA			NA			34.4	35	2

The Satellite

The physical BSat structure is much more complex than the simplified components discussed previously. It is in this section that the physical parts will be scrutinized against the same conditions imposed earlier and any additional loading requirement that may accompany the individual part. The sides were modeled as Al-7075-T6 while all other parts were modeled as Al-6061-T6.

Baseplate

The baseplate was restrained by its tabs in a manner that reflected the flight configuration; thus, preventing all rotations and translations. It was then inertially loaded with a 10g acceleration factor and an additional 200 gram normal load to its plane surface. The ancillary load was included to provide margin for unexpected additions

(mass) that the baseplate may become responsible for. The red arrow in Figure 5-22 represents the application of 10g load factor.

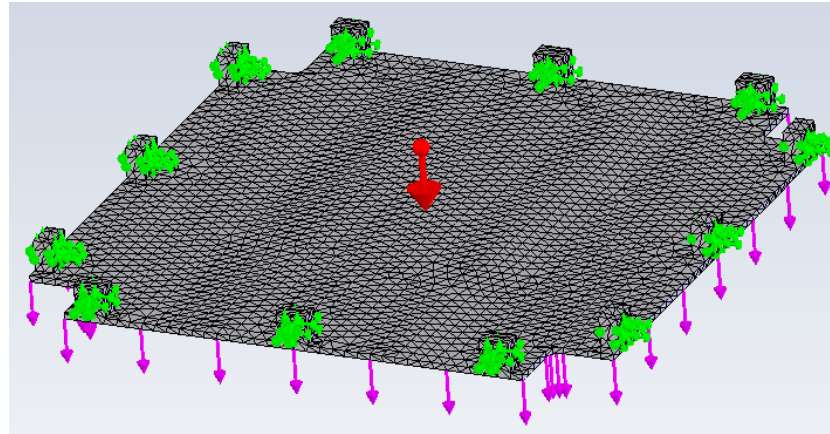


Figure 5-22: BSat Baseplate Loading Conditions

Considering that most components of the primary structure are 1 mm thick, a two-dimensional simply-supported beam was conceived that represents the physical cross-sectional area and length scales, see Appendix C.2. To present BSat's baseplate as a two-dimensional simply supported beam the two models had to exist under mutually exclusive boundary conditions. Simply supported beams are defined as pinned ended meaning that both the deflection and moment are zero. Usually the left end is restricted from translation while the opposite end has a SDOF; i.e. as the load is applied, the end stays on rollers and can travel horizontally. To apply this condition to the baseplate a non-translational boundary was imposed on the left end while the right end was fixed vertically and tangentially. Then to simulate a distributed load, a 10 N force was applied along the centerline of the baseplate (extending out perpendicular from the fixed end). Figure 5-23 shows this setup.

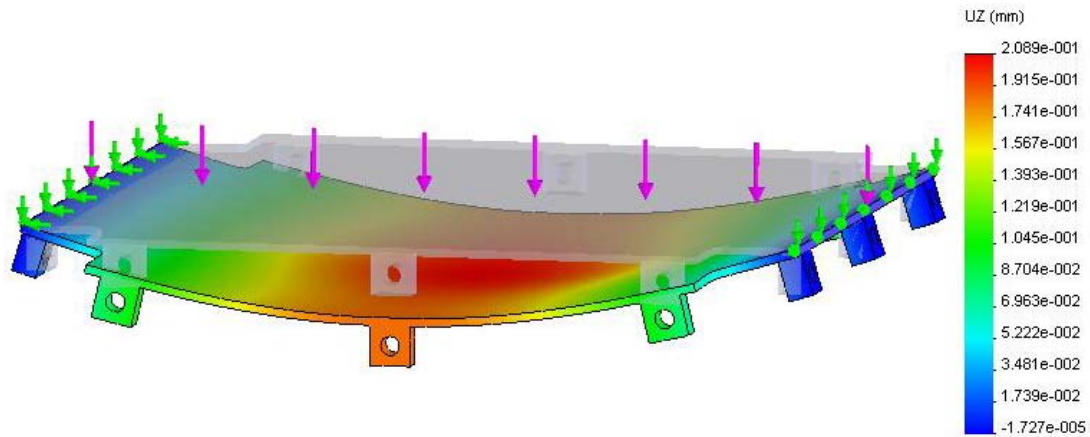


Figure 5-23: Baseplate as a Simply Supported Beam

The FEA results of this scenario shown in Figure 5-23 demonstrate that a maximum deflection occurs at the center of the baseplate and has a magnitude of approximately .209 mm. This is verified by analysis conducted on a two-dimensional simply supported beam as seen in Appendix C.2. The maximum deflection obtained analytically is .236 mm which is favorable when compared to the numerical result. Figure 5-24 is the comparison of the FEA deflection curve against a Fourier Series representation of a simply supported beam and Gere's displacement equation; in all cases the results compare favorably. However, the FEA result appears to show more stiffness in the structure which is true because of the baseplate's three-dimensional state.

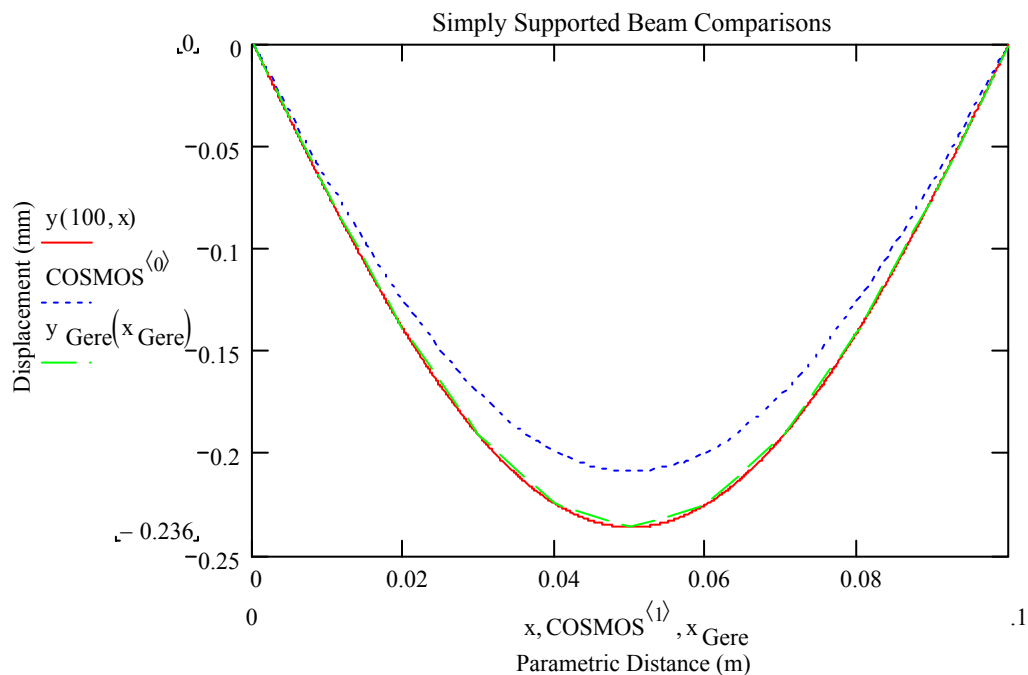


Figure 5-24: Baseplate Bending Curve

Sides

The final design of the four sides revolved around the combination of the launch rail and side panel. After completing a mass optimization, the sides loosely resembled the flat plate and column discussed previously. For this reason, failure analysis due to buckling and the 10g static response were reevaluated. The side was pinned at both ends via the two launch rail *cups* where an 89 N load was applied.

The spring force of the RocketPod™ is transferred directly to *side A* via two *cups* which are also used to fix translations while in the deployer. To fix the rotation, *side B* is equipped with a detail that also correlates to a fixture on the deployer. This side was discretized to 34,107 nodes and 17,203 elements. Figure 5-25 shows both the imposed

conditions and the critical buckling load. In this case, magnitude of the critical buckling was determined to be 6,230 N.

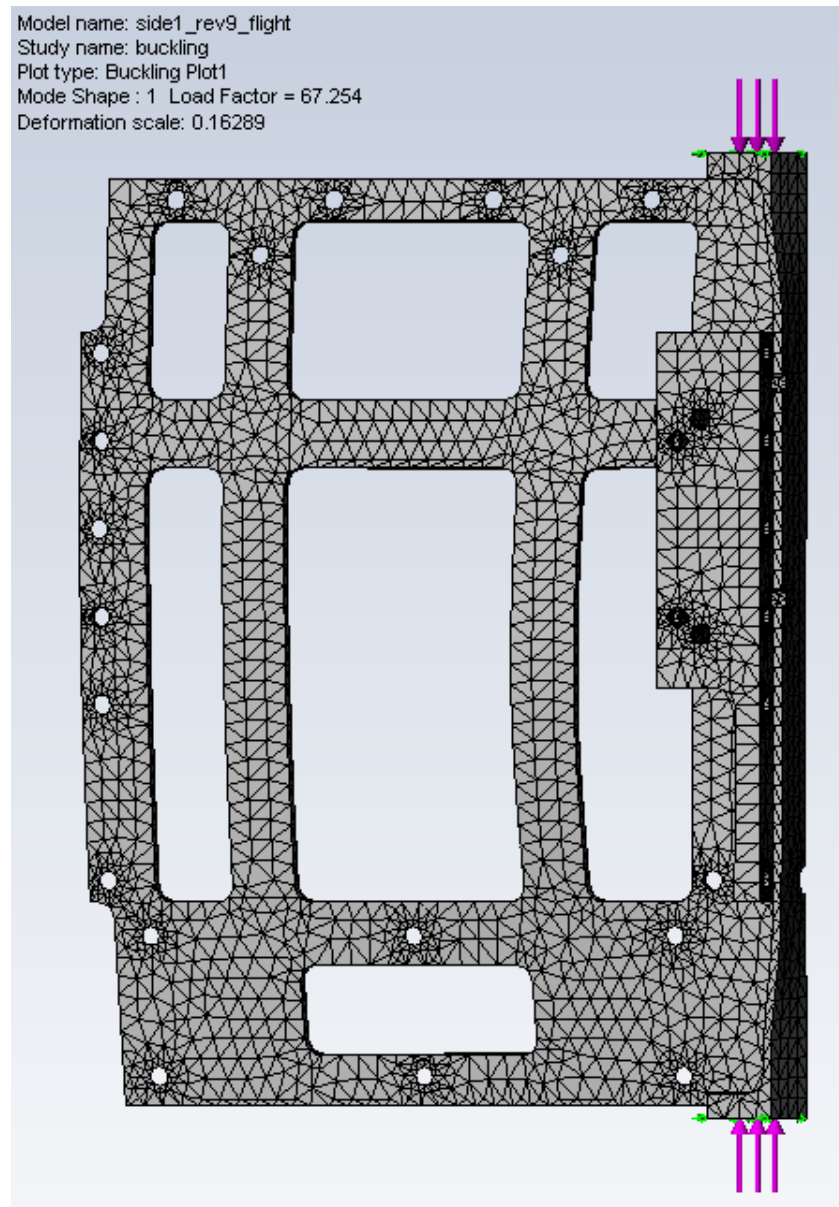


Figure 5-25: Buckling of BSat Side

For the 10g quasi-static load case, the sides were analyzed in concert to assess the stresses which developed in the 12 countersink holes which are intended to secure the

tether bracket. The load under investigation is the overall mass (2 kg) and the 10 g acceleration factor. This load is assumed to act at the spacecraft's center of mass and because the four adjoining sides are collectively burdened with this load, each side was defined to experience one-quarter of the total load, this load being 16.35 N applied at the countersink locations. Figure 5-26 shows the discretized assembly of the four adjoining sides.

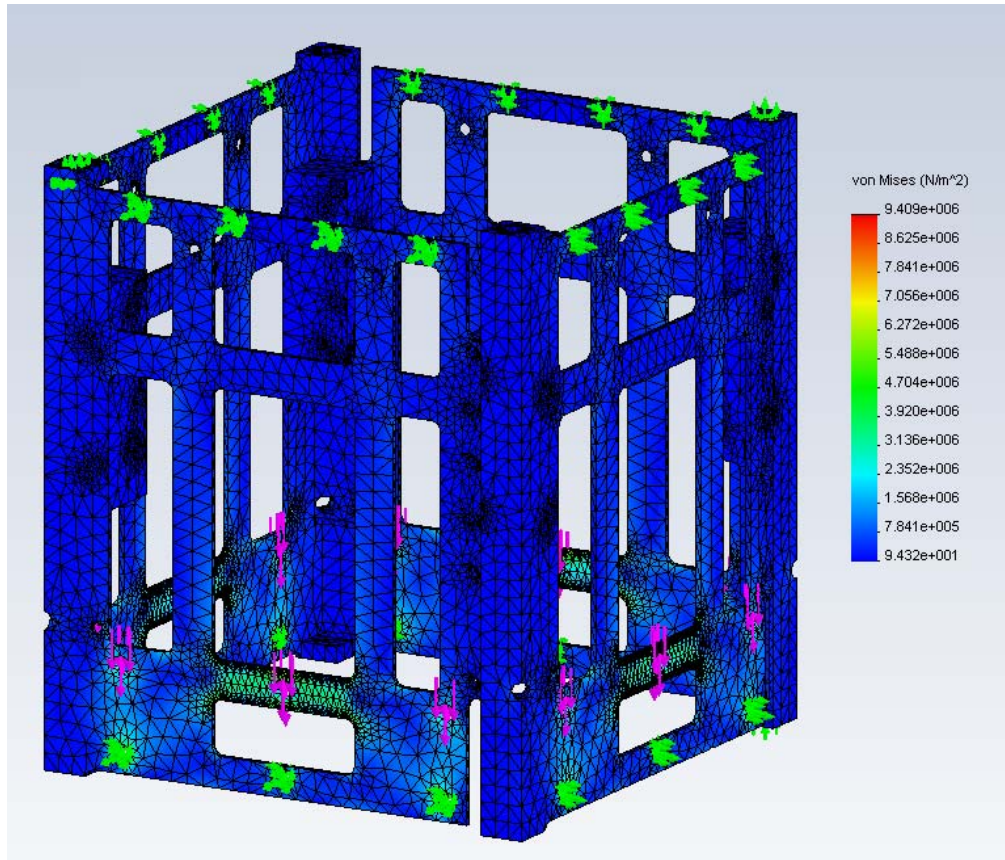


Figure 5-26: Quasi-Static Loading of Sides

The Von Mises stress distribution of Figure 5-25 reveals a maximum stress of 9.4 MPa occurring on the inner radii of the thru-cuts. However, the surface immediately surrounding the countersink is a greater concern because of shear-tear out effect. The

stress concentration in this region is approximated at 5.5 MPa resulting in a margin of safety of 53. It is clear that these loads are easily handled by the primary structure and that the greatest limitation in terms of the BSat structure was its manufacturing. With conventional milling techniques it is difficult to reduce that mass and hence the stiffness of the parts in terms of their thickness. Margin of safety and error plots are presented in Appendix C.5.

Tophat

The tophat was analyzed in bearing under the quasi-static loading of the battery assembly, antenna systems, and GPS payload; all components currently identified to reside within the tophat's interior. Also included was the 10g load factor associated with the acceleration during launch. The battery/bracket assembly has a combined mass of 55 grams, including the load factor this becomes a 5.4 N load. Although the RF antenna system is expected to induce a smaller load, this analysis assumes the same load as induced by the battery system; this is also because the antenna is still under development and the exact mass is currently unknown. The GPS patch is currently estimated at 20 grams; however, similar to the RF antennas its mass was assumed to be 55 grams. The GPS patch antenna with an approximated mass of 9 grams was also included in this analysis.⁶¹ The location of these components is depicted in Figure 5-27. Boundary conditions were setup such that the tophat was fixed; no translation or rotational deviation owing to its interface with the four adjoining sides. The bearing load was

⁶¹ This estimation was obtained from Nestor Voronka at TUI.

applied to the tapped holes as intended for flight with redundant load paths. No other loading is intended to affect the equilibrium of the tophat.

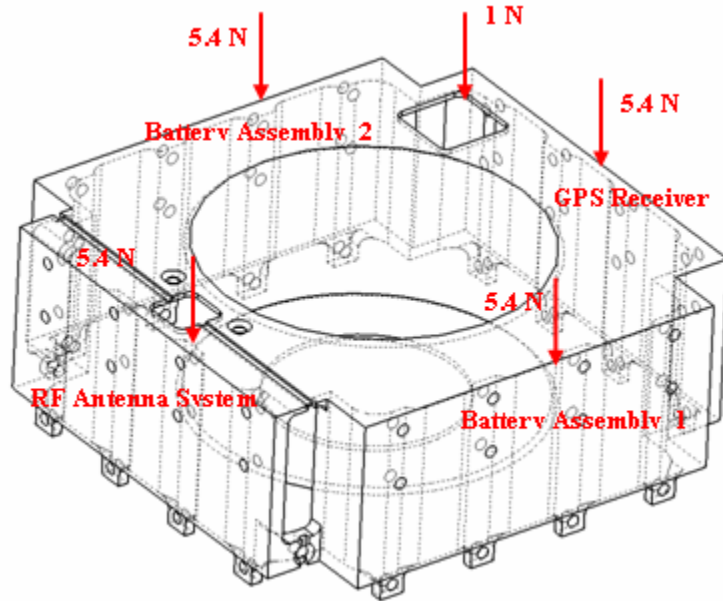


Figure 5-27: Tophat Loading

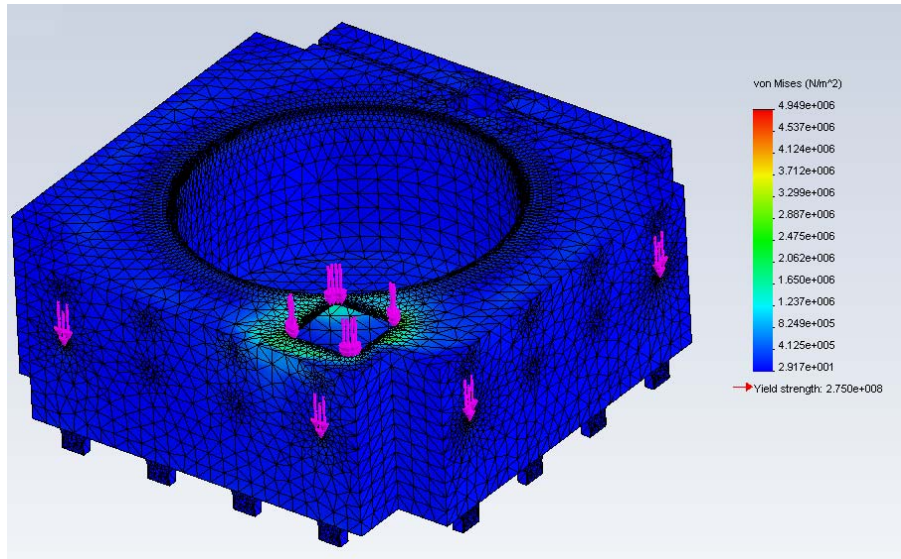


Figure 5-28: Tophat Stress Distribution

The bearing stresses that develop in the tophat from the batteries and antennas are well within the yield strength of Al-6061-T6. The corresponding minimum margin of safety was found to be 56. Both the margin of safety and error plots are available in Appendix C.5.

Tether Bracket

The tether bracket was first examined for strength of its mounting tabs under bearing load and the 10 g acceleration factor. This scenario corresponds to the tether unwound at its full length and the entire mass of the satellite pulling against the bracket's mounting tabs. Even though this scenario occurs after deployment (after launch) the 10 g load factor was included to assess the strength of the four mounting holes. The bracket was held fixed by the 12 mounting holes which correspond to bracket integration within the satellite, and then the bearing load of 196 N was applied to the four holes. The bracket was optimized with 31,147 tetrahedral elements and 59,593 nodes.

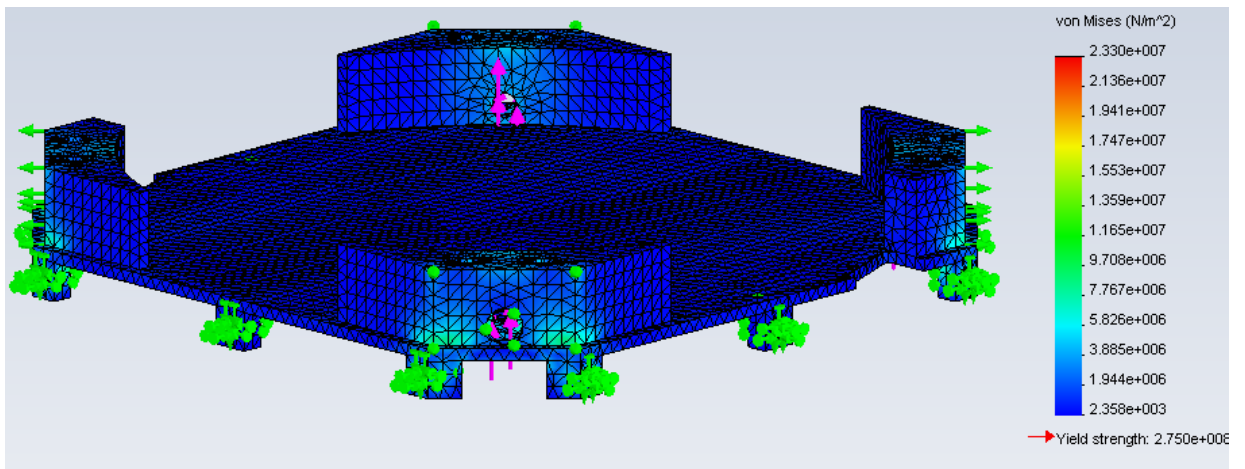


Figure 5-29: Tether Bracket Bearing Stresses

The stress distribution of the bracket in bearing is seen in Figure 5-28. The maximum stress occurs at an outlier element with a value of 23 MPa; however, the global-average stress value at the area of interest is approximately 9.7 MPa with a minimum margin of safety of 10. Both the margin of safety and error plots are available in Appendix C.5.

The quasi-static loading of the tether bracket is defined by the mass of the tether system being transmitted to the bracket, an assumed 500 gram electronics package pulling from the bottom, and the 10 g load factor. This scenario most closely resembles the loading environment during launch in which the bracket is responsible for, and experiences the greatest amount of loading. The acceleration factor was included in the force numbers such that the tether system pushed down upon the bracket at 27.5 N and the electronics package pulled away at approximately 50 N. Again, the bracket was restrained via the 12 tabs and forces applied in a manner that reflects the anticipated flight configuration.

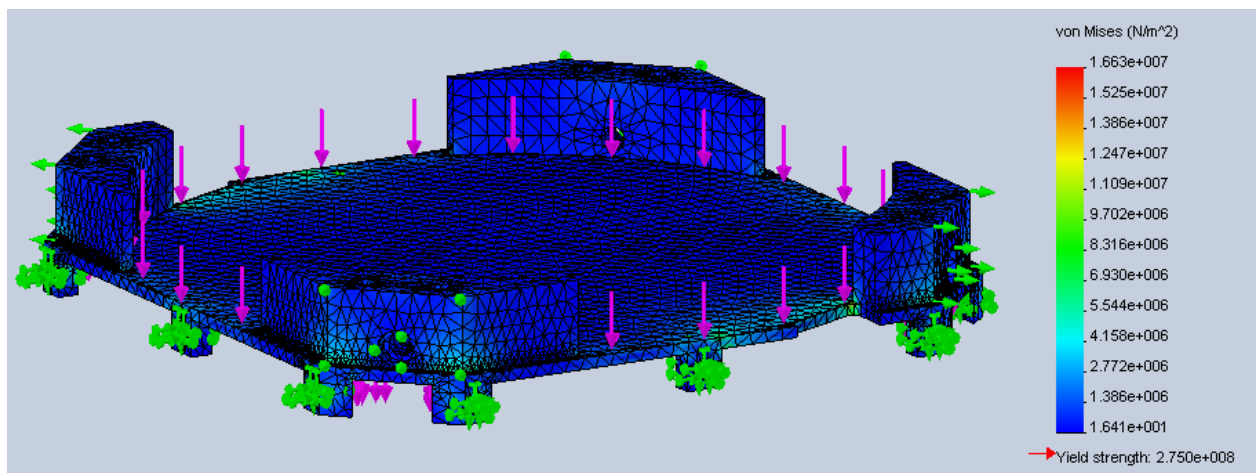


Figure 5-30: Tether Bracket Quasi-Static Load

The stress distribution reveals a maximum value of 17 MPa and a minimum margin of safety of 21. With a decrease in the conservative estimate of 500 grams, the electronics' mass will have less impact on the loads experienced by the bracket, causing an increase in the bracket's margin of safety.

Battery Bracket

The battery bracket while restraining the secondary battery during launch develops rather large stress concentrations. As the battery bracket is restraining a component which is 100 times its own mass (including acceleration factor), large stresses develop which ultimately result in low margins of safety. The two flanges that hold the mass of the battery were defined to experience a 5 N normal load while the two thru-holes and the back surface were restrained due to its interface with the tophat. Figure 5-31 depicts the discretized battery bracket along with the stress-relieving notches which were specified in its design.

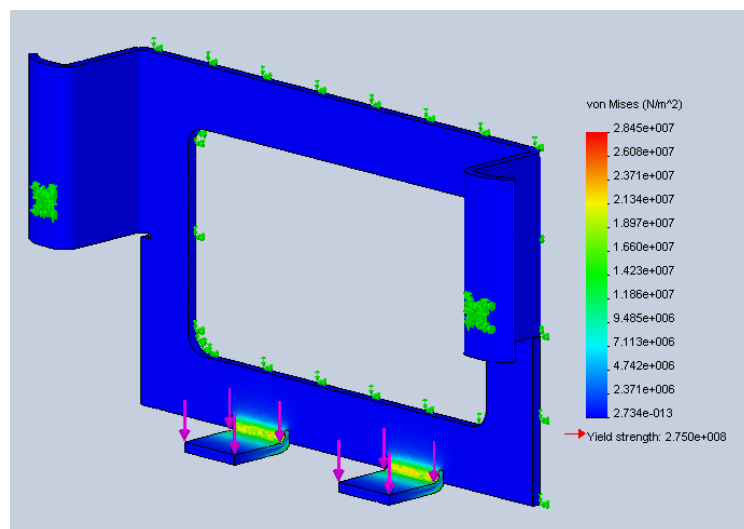


Figure 5-31: Battery Bracket Stress Distribution

The mesh was omitted from this figure because its resolution would visually conflict with the stress concentrations. By inspection the maximum stress approaches 24 MPa at the radius of the flanges and has a corresponding margin of safety equal to 10; both the margin of safety and error plots are provided in Appendix C.2. This survivability data is a conservative assessment of the flight configuration because the flanges will not exclusively hold the mass of the battery. For flight, the battery bracket will be encapsulated in Kapton tape for which the battery will fit *snuggly* within the bracket and the load will be distributed more evenly throughout the bracket. In both cases the battery bracket is suitable for the BSat launch environment.

Results and Conclusions

The above results lead to the following conclusions. To begin, it is quite clear that the limitations of the BSat structure are its manufacturability. In order to preserve reproducibility and ease of fabrication, the structure is sufficiently designed to accommodate BSat's launch environment. While all of the constituents of the satellite are low in mass, the stiffness of the structure included a 10 g acceleration factor. This margin was utilized in the material selection and number of bolted connections. To reiterate, the four sides were analyzed and are to be fabrication from Al-7075-T6 while all others are Al-6061-T6.

1. The harmonic vibrations of all structural members surpass the fundamental frequency requirement of 35 Hz in both the axial and lateral directions.

2. The simplified structure was analyzed dynamically for vibroacoustic response. Both the baseplate and FR4 board are sufficient in strength to accommodate the SPL levels of the Delta II LV. The dynamic analysis was simplified to that of the dynamics of a flat plate because of the highest surface area to mass ratio. This analysis was conducted under small-deflection theory in which both parts were verified not to deflect greater than half their thicknesses.
3. The acoustic vibrations appear to induce the most critical dynamic response. In this case, the maximum deflections at the center of the plate were observed to occur at the entities fundamental frequency. It is recommended that components mounted at the center of these plates be appropriately bonded and inspected after environmental testing.
4. Comparison of analytical and FEM solutions for the simplified geometry are within 10%, a value that is acceptable and builds confidence in the FEM solutions pertaining to the physical structure.
5. The physical structure was scrutinized against a strain-energy convergence criterion that systemically calculated the elemental stress values and their deviation from the corresponding nodal stress value. Plotted results are available in Appendix C.4. In most cases there existed outlier elements with large error values; therefore, they were omitted and attention was instead addressed to the critical stress areas.

6. The critical members of the structure under a static load are the battery brackets and tether bracket. The high stress concentrations are relatively localized where effort was made to resolve mesh conflicts and error convergence. In both cases the margin of safety is acceptable and is a conservative estimate.
7. The structure will not experience a high enough load during any phase of the mission to experience linear buckling of any components.
8. The induced stress by both the dynamic and static loading are well within the yield strength of Al-6061-T6 with acceptable margins of safety. However, to satisfy the RocketPod™ requirement the four sides which interface directly with the deployer must be fabricated from Al-7075-T6.
9. TUI has stated that a torsional spring will be incorporated into their deployment spool which is meant to gradually decrease the unwinding rate when the tether approaches its full length. For this reason, shock analysis was omitted from this investigation.
10. All structural parts are intended to be surface-treated upon fabrication. This treatment has been performed in-gratis by Sonju Inc. of Kalispell, MT. For masking instructions refer to the *orange notebook* documentation of the tether bracket.

6. THERMAL ANALYSIS

While in orbit BSat will experience a variety of conditions that characterize the space environment. This environment will affect the onboard subsystems' performance via a combination of internal heat generation and the external heat fluxes: direct solar, Earth albedo, and Earth IR. With respect to a LEO satellite, solar radiation is considered collimated outside Earth's atmosphere whereby Earth IR and subsequently its albedo are non-collimating. In other words, due to the large distance of the Sun from Earth, it is accurate to consider that the solar vector is in parallel rays by the time they interact with BSat. Due to the vacuum of space, heat energy is managed exclusively through conductive and radiative heat transfer mechanisms. This section aims to analyze BSat's thermal environment with respect to the satellite's temperature distributions. A parametric study was conducted on a range of possible orbits to ascertain the degree of thermal control implementation.

Objective

In addition to providing the temperature distributions through a spectrum of possible orbits, this section is intended to parametrically evaluate the thermal conditions of the satellite in accordance with the thermal requirements of its components. The notable temperature constraints are the onboard batteries and the control strategy that has been limited to passive techniques due to the limited electrical power generation. Stresses induced by thermal expansion were the final consideration here because it is thought that thermal stresses could affect the performance of the satellite structure. It is an advantage

that BSat is composed primarily of Al-6061-T6 and Al-7075-T6, which are known to exhibit the same thermal expansion characteristics; this implies that thermal expansion is not a structural concern, but that its associated stresses should be assessed.

Orbit Profile

The definitive orbit of BSat is dependent upon the primary payload on the LV. Therefore there is a need to conduct a parametric study on a range of possible orbits. While low Earth orbits are typically associated with high inclination angles achieve significant coverage of Earth's surface, BSat's inclination range has been limited between 40° and 90° ; those angles catering to the greatest access times with the ground station. The certainties currently identified for the BSat mission include its passive gravity gradient, nadir pointing baseplate, an altitude between 600 and 800 km, and a slow spin rate. Figure 6-1 (not to scale) shows the altitude range and spin axis of BSat.

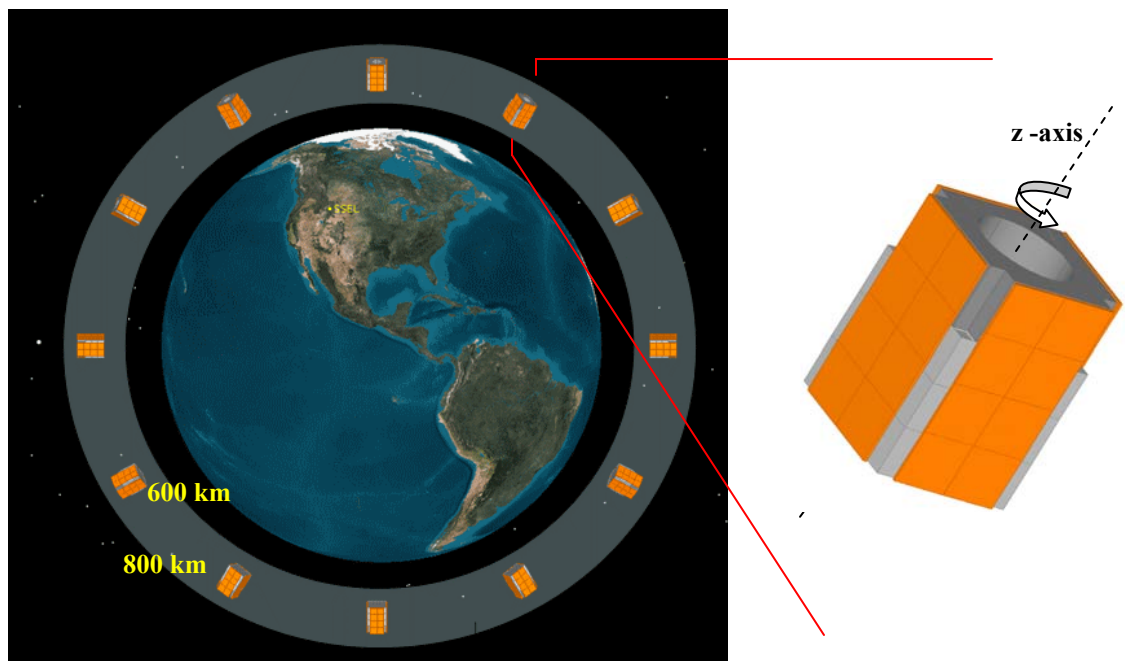


Figure 6-1: BSat's Passive Attitude

The beta angle is the primary factor when quantifying the intensity and duration of solar heating. The beta angle is an angular measurement between the satellite’s orbit plane and the solar vector. This ultimately determines the eclipse fraction, or duration the satellite is shadowed by Earth. The beta angle is independent of inclination or altitude. This angle processes throughout the year and can vary from 0° to 90°. For this reason it was necessary to parametrically include both extremes and an intermediate angle. Figure 6-2 is a depiction of the orbit beta angle.

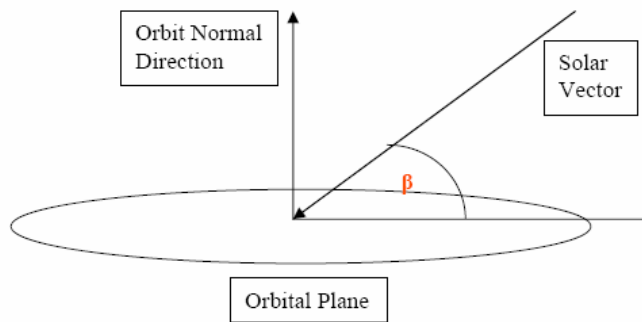


Figure 6-2: Orbit Beta Angle (Reproduced from Hansman, 2003)

This figure shows that the beta angle can vary from ±90°. Figure 6-3 shows that the three forms of environmental heating are also fundamentally influenced by the satellite’s orbit-beta angle. Table 6-1 lists the industry accepted, yearly-average heat fluxes, and Figure 6-3 shown below delineates the fluctuation of these values relative to the orbit beta angle.

Table 6-1: Environmental Radiation

	Minimum [W/m ²]	Maximum [W/m ²]
Solar	1322	1414
Albedo	397	424
Earth IR	218	275

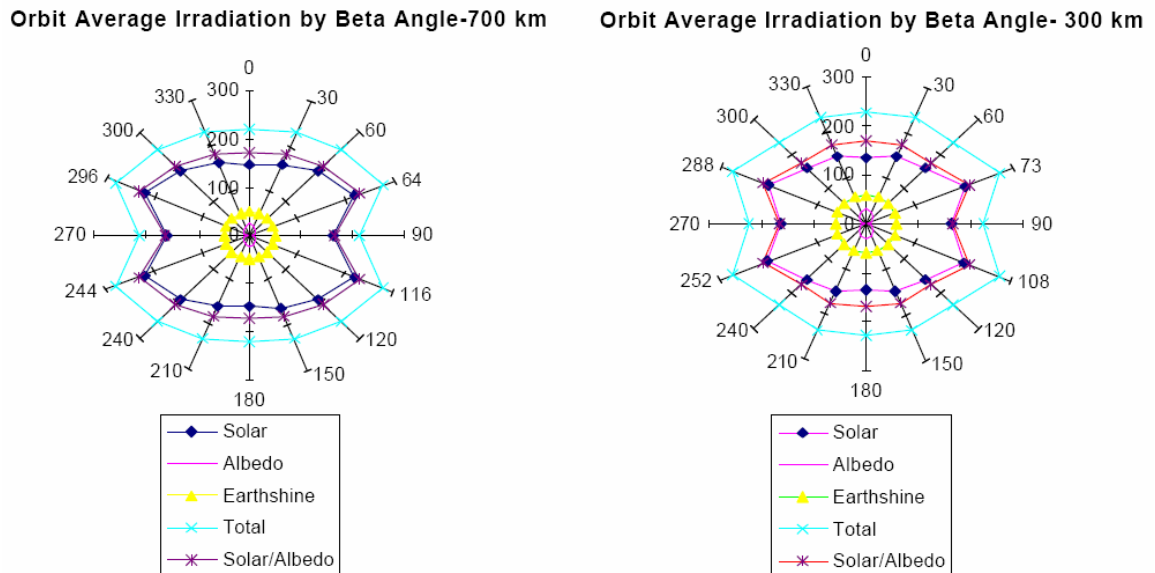


Figure 6-3: Beta Angle and Flux Load (*Reproduced from Duran, 1999*)

Although these plots were not generated to signify the intensity of the flux it does highlight the various important trends in a general LEO thermal environment. These trends are a physical phenomenon of Earth's glob plot rather than truly the beta angle; however, these flux loads are directly associated with the satellite's position around Earth. While albedo tends to increase with latitude, Earth IR tends to decrease. Figure 6-3 also signifies the strength of the solar load as compared to the two *planetary* forms which are significant when comparing orbit altitudes.

BSat Thermal Control

Due to the limited capability to generate electrical power, an active thermal control scheme has been determined unsuitable for the BSat mission. Therefore, thermal control is limited to passive techniques which are advantageous considering they require no

moving parts and no electrical power. Knowledge of prior satellite architectures⁶² builds confidence in this technique and has been determined appropriate for the BSat mission. For BSat, the role of thermal control coatings and thermal conductance at joints are exclusively responsible for controlling onboard temperatures. Coatings studied have been limited to those listed in the Table 6-2.

Table 6-2: Optical Property Data

Surface Finish	Absorptivity (α)	Emissivity (ϵ)
Bare Aluminum	0.09	0.03
5-mil Silver Teflon	0.05	0.78
Anodized Aluminum	0.35	0.84
White Paint	0.15	0.6
Black Paint	0.96	0.86
Black Anodized	0.86	0.86
Solar Cells	0.92	0.85

The interesting figure of merit is that a typical satellite (including BSat) is often optimized on the exterior in terms of allocated surface area for solar cells. This area then has a predefined alpha by epsilon ratio while the area surrounding the cells is determined by a selection process which revolves around the degree of thermal control.

Steady-State Analysis

Prior to the computational analysis with SINDA and Thermal Desktop, a steady-state analysis was conducted to reveal the effectiveness of the surface properties listed in Table 6-2. Recall Figure 4-20, in which the tether shroud is shown to consume nearly 70% of the interior volume. It also acts as a thermal barrier between some of the subsystems. For this portion of the analysis the shroud is assumed to present an adiabatic surface

⁶² particularly in the CubeSat class of satellites

which isolates the electronics mounted in the top portion of the satellite from those mounted below it. This is a logical assumption considering that the internal heat generation is significantly small and that the two cavities do not *thermally influence* each other. Also, for purposes of thermal analysis, all electrical energy allocated to a subsystem is assumed to be dissipated as heat (refer to Table 4-4). The geometry of the shroud's conical section was normalized against the overall volume and added, resulting in a simplified, yet effective model as seen in Figure 6-4. The construction of this model is detailed in Appendix D.1.

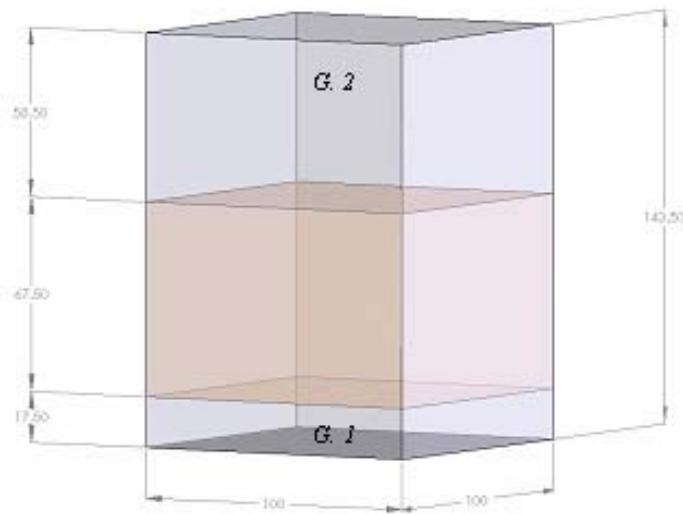


Figure 6-4: Simplified Geometric Model

In Figure 6-4, the beige area represents the tether volume while the remaining volumes, G1 and G2, represent the electronics. This simplification trivializes the projected area as seen by the radiation sources and is justified considering that the satellite will be spinning, allowing each surface to isothermally absorb and reject heat energy.

Effective Optical Properties

Any particular surface of BSat is composed of a variety of materials with a unique solar absorptivity and IR emissivity. This suggests that no surface in its entirety is solely defined by a single set of optical properties. For this reason a scheme was employed that averaged a surface's optical properties to obtain an effective optical property data set. For BSat, the four surfaces encompassing the sides are entirely occupied by four solar cells, two structural launch rail surfaces, and the remaining unoccupied surface area of the solar panels. The bottom and top surfaces are entirely thermal radiators as no solar cells will be mounted on these surfaces. Appendix D.2 presents the averaging scheme used to obtain effective optical properties.

Steady-State Results

The results of the steady-state analysis are seen in Figure 6-5. This comparison is a result of the internal power generation and the three forms of environmental heating. In both cases the extreme temperatures correspond to the worst-case conditions as mentioned in chapter four. Figure 6-5 was used to emphasize the role of surface finishes on BSat's in-situ temperatures. It is important to realize that these values cannot be taken as the actual temperatures of the satellite; rather they show the significance of passive thermal control strategies. More realistic temperatures result from a transient analysis accounting for the eclipse fraction and duration of sun exposure along with the heat capacitance of the satellite. The transient analysis will be discussed next.

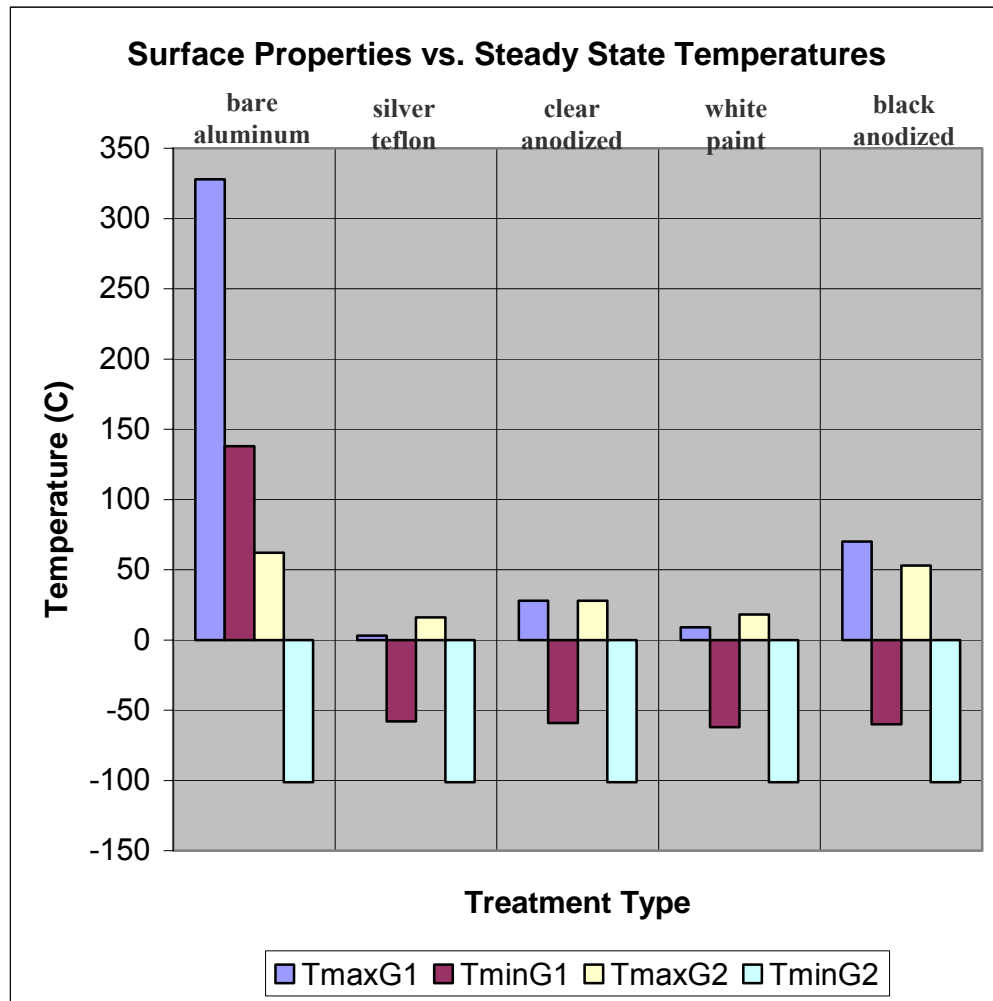


Figure 6-5: Steady-State Temperature Results

Figure 6-5 shows that while the incoming solar radiation is dominant over the satellite's ability to reject waste heat for the warm case, that the radiative ability of the satellite dominates the incoming Earth IR for the cold case. This is because the IR load is incident upon a single surface (i.e. the baseplate) while the radiative ability is defined by all remaining surfaces; a surface area which is significantly larger than the projected area. For all hot cases, the ability to reject waste heat is a function of the surface's emissivity value; in the case of bare aluminum, the satellite surfaces demonstrate high solar

absorptivity with minimal ability to reject waste heat, a figure of merit associated with a high alpha by epsilon ratio.

Transient Analysis

To begin the transient thermal analysis of BSat, an isothermal spherical model was generated that geometrically represented the physical dimensions. The use of a sphere to represent BSat is advantageous because it offers a constant projected area, or *view factor* while in orbit. The geometric equivalency was complemented by the predicted mass of the satellite and the corresponding specific heat. Figure 6-6 shows these models. The advantage here is that at any moment in time, the solar flux will be incident upon half of the sphere, or its cross-section, which is constant at any angle. The optical properties were then input from the list obtained from the effective optical property data.

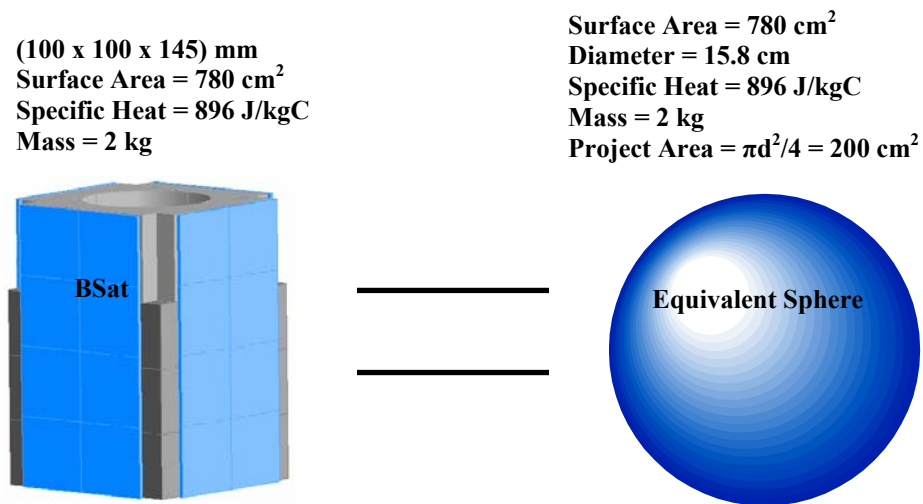


Figure 6-6: Equivalent Sphere

Lumped Capacitance

Prior to conducting the above transient analysis using the *lumped capacitance method* it was necessary to obtain the satellite's Biot number. Lumped capacitance is the method of choice in transient heat conduction and has proven to be an expedient method of analyzing an isothermal⁶³ body. The Biot number is the ratio of an object's ability to conduct heat to the rate at which heat can be transmitted into or out of the object's surface; more formally referred to as radiation. As lumped capacitance is often employed in convection heat transfer problems, it is appropriate here considering that the satellite is structured around a series of extremely thin, flat plates. This implies that the Biot number is dependent upon the material composition, size and construction [Duran, 1999]. In the case of radiation, the Biot number would then also depend on the heat transfer ability of the satellite. For the *spherical* BSat, the ratio of conductive resistance to radiative resistance is of the following form:

$$Bi = \frac{R_{cond}}{R_{rad}} = \frac{\left(\frac{L_c}{k}\right)}{\left[\frac{1}{\varepsilon\sigma(T_s + T_{surr})(T_s^2 + T_{surr}^2)}\right]} \quad (6.1)$$

where L_c is the characteristic length⁶⁴, k is the thermal conductivity, ε is the surface emissivity, A is the cross-sectional area, T_s is the sphere's surface temperature, and T_{surr} is the 4 °K temperature of space. Note that the Biot number depends on the surface temperature and the chosen emissivity value. To validate the lumped capacitance

⁶³ isothermal – no temperature gradient exhibited by body.

⁶⁴ for a sphere the characteristic length is equal to $r/3$

method, Equation 6.1 was solved for a variety of surface temperatures and emissivity values as seen Figure 6-7.

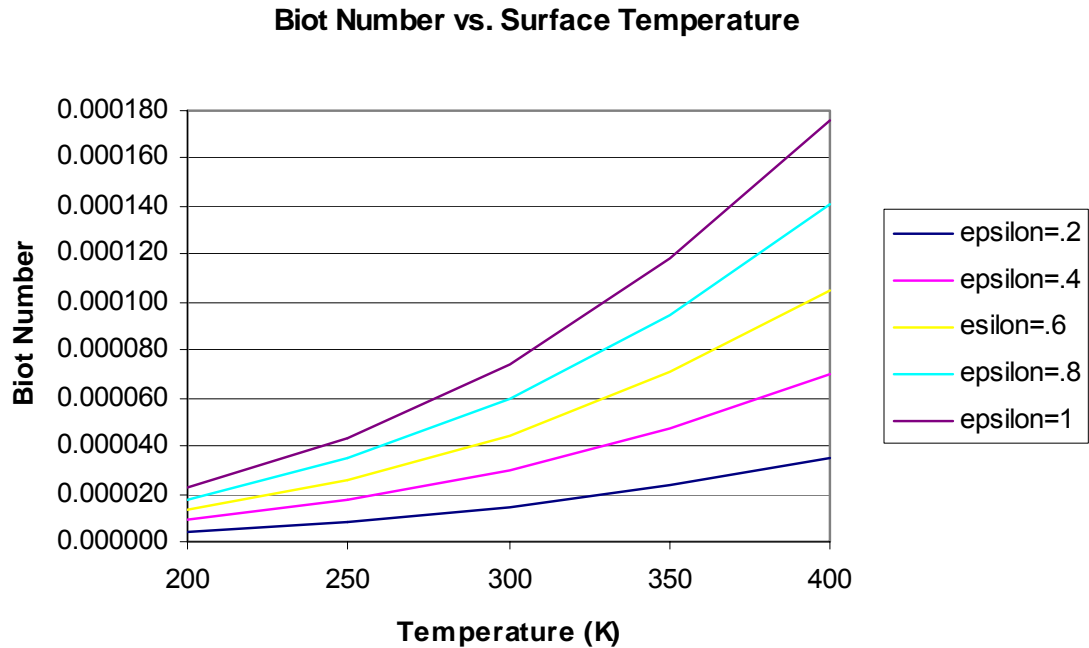


Figure 6-7: Biot Number vs. Temperature and Emissivity

The lumped capacitance method is considered appropriate for isothermal bodies if its Biot number is less than 0.1. Temperatures of the satellite were bounded by 200 °K and 400 °K as shown on the x-axis and emissive properties were varied from 0 to 1 as shown in the legend. Figure 6-7 shows that all parameters produce Biot numbers less than 0.1; results that strongly support the validity of the *bulk* temperature analysis.

In the pursuit of transient temperatures utilizing the lumped capacitance method it was first necessary to start with the conservation of energy:

$$\dot{E}_{in} + \dot{E}_{gen} - \dot{E}_{out} = \dot{E}_{st} \quad (6.2)$$

where the \dot{E} terms are representative of energy entering and exiting the spacecraft. These values coincide with the definitions of the Q terms presented in Equation 3.6 and are expressed in Watts. The energy storage term on the right-hand side represents the thermal mass of the satellite and is simply the change in energy storage due to an environmental temperature change. Energy storage, \dot{E}_{st} , is expressed by the following relation:

$$\dot{E}_{st} = \frac{dU_t}{dt} = \frac{d}{dt}(mC_p T) = \frac{(T_2 - T_1)}{\Delta t} mC_p \quad (6.3)$$

where m is the satellite's mass, C_p is the specific heat, and dT/dt is the change in temperature with respect to time. It is clear that \dot{E}_{st} is associated with the rate of change in the internal thermal energy. Taking this a step further produces an iterative equation that can be solved for temperature, T_2 :

$$T_2 = T_1 + \frac{(Q_{in} - Q_{out})\Delta t}{mC_p} \quad (6.4)$$

where,

$$Q_{in} = \alpha A_p q_{solar} + \alpha A_p q_{albedo} + \varepsilon A_p q_{Earth} + Q_{gen} \quad (6.5)$$

and

$$Q_{out} = \sigma \varepsilon SA T_s^4 \quad (6.6)$$

T_s and T_2 are equivalent, α and ε are the surface optical properties, q are the source fluxes listed in Table 6-1, Q_{gen} is the internal heat generation listed in Table 4-4, and A_p and SA are the cross-section and total surface areas, respectively.

Transient Results

The transient analysis was run for the orbit case in which the satellite's altitude is 800 km and an inclination of 45°. The periodic and eclipse fractions provided by Wertz and Larson state that for worst-case cold, the maximum eclipse time for a 100.87 minute orbit is 35.13 minutes. This means that for a satellite orbiting at 800 km, it will spend approximately 1/3 of its time per orbit in the shade. For the parametric evaluation of optical properties, a MATLAB GUI⁶⁵ was developed that allowed for quick changes in these parameters, and resulted in a graphical output. Its code is available in Appendix D.3. Figure 6-8 is a snapshot of the user-interface when running the lumped capacitance code. Notice that both the hot and cold worst-cases can be simulated with this GUI.

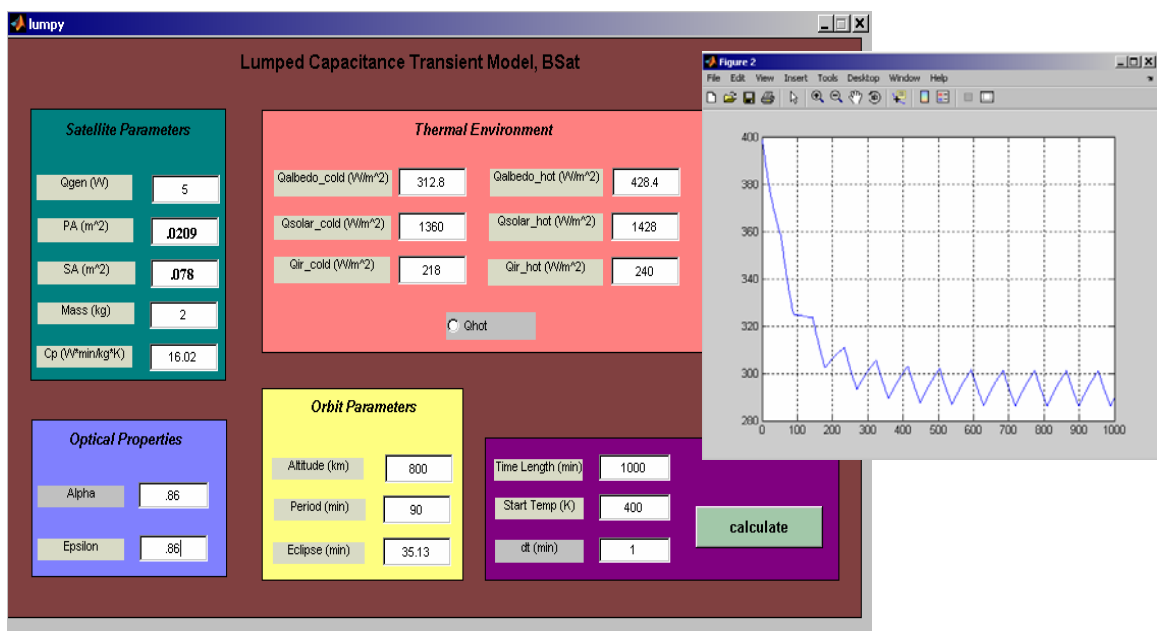


Figure 6-8: Lumped Capacitance GUI

⁶⁵ Graphical User Interface

The advantage of implementing bulk temperature analysis is that it readily produces results that are accurate and good first-order estimates. Wertz and Larson warn that a 10 °C analysis uncertainty margin should be included with this approach, which is implemented after analyzing Figure 6-9 and Figure 6-10 below. Figure 6-9 and 6-10 are parametric comparisons of BSat’s optical properties, where under the presumed orbit, black anodized or black paint should be used on the exterior of the satellite. This applies without including the solar cell properties which almost entirely consume the sides of BSat. The optical properties of the solar cells lie between the black paint and black anodized, thus temperatures can be inferred from Figure 6-9 and Figure 6-10.

HOT

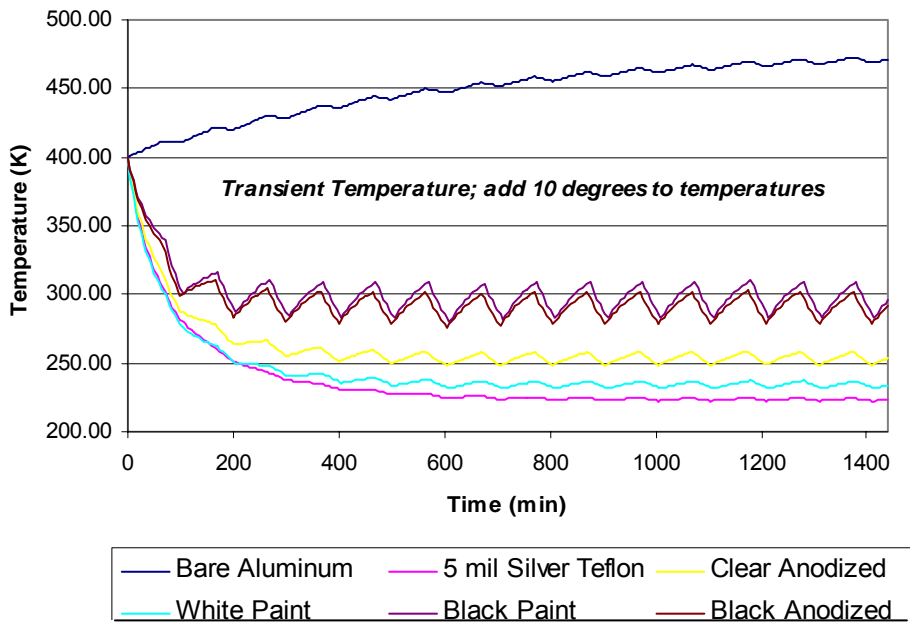


Figure 6-9: Parametric Transient Temperatures; Hot-Case

COLD

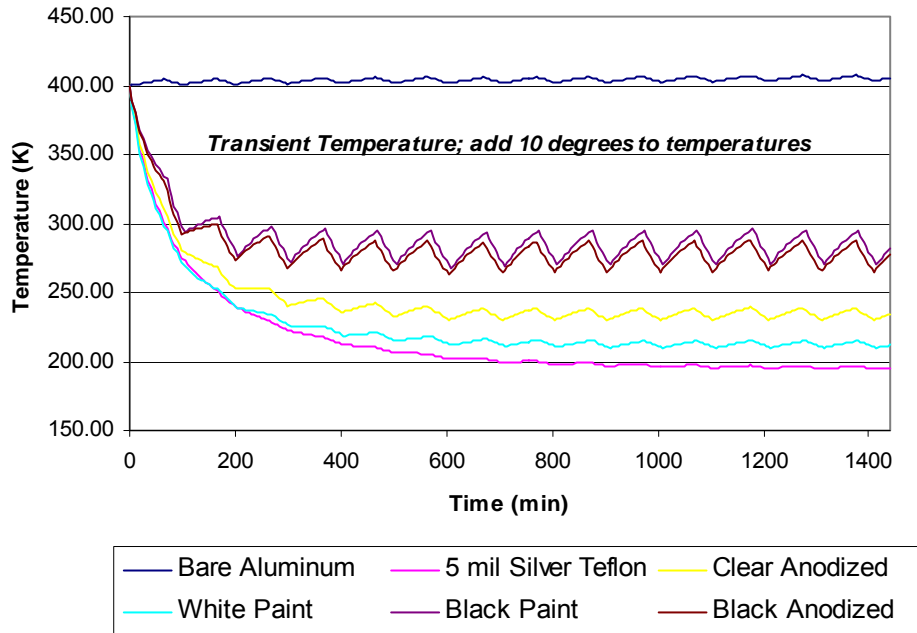


Figure 6-10: Parametric Transient Temperatures; Cold-Case

The temperatures presented in Figures 6-9 and 6-10 are not taken as absolute; accounting for the 10 °C uncertainty margin, the extreme values for all the properties corresponding to both the hot and cold cases is presented in Table 6-3.

Table 6-3: Lumped Capacitance Results

	α/ϵ ratio	Hot-Case		Cold-Case	
		T _{max} [°C]	T _{min} [°C]	T _{max} [°C]	T _{min} [°C]
Bare Aluminum	3.0	210	179	145	120
Silver Teflon	0.064	-38	-61	-66	-89
Clear Anodized	0.42	-4	-35	-24	-53
White Paint	0.25	-26	-52	-48	-73
Black Paint	1.12	47	0	33	-13
Black Anodized	1.0	40	-5	25	-18

This transient temperature analysis clearly demonstrates the difference between a solar reflector and solar absorber. While the bare aluminum with its high alpha by epsilon

ratio acts as the latter by absorbing solar energy while emitting only a small percentage of the IR energy, silver Teflon with a small ratio acts as the former by reflecting solar energy while absorbing and emitting IR energy. An alpha/epsilon ratio in the vicinity of unity appears to be the logical choice for BSat's surface treatment. This allows for the absorption of solar energy while simultaneously allowing the satellite to emit heat when it enters an eclipse. This is apparent in Figures 6-9 and 6-10 where the black paint and black anodized are defined with alpha by epsilon ratios close to unity; a ratio which allows the surfaces to react more drastically to the changes in the environment. As a figure of merit, thermal control finishes are affected in different ways by the exposure to the space environment. The typical trend is an increase in solar absorptivity with little effect on IR emissivity. This is why satellites are typically cold-biased at the beginning of their life and tend to heat-up as their missions progress. For BSat with its relatively short mission this temporal effect on solar absorptivity is negligible. Refer to Gilmore [2002] for further information on the degradation rates of common thermal control finishes.

Finite Difference Analysis

The finite differencing technique uses a discrete network of nodes and elements that represent the capacitance of the object. It is a numerical technique that integrates the governing equations to obtain temperatures. In the case of BSat, the finite difference method (FDM) was used to estimate the temperatures endured by the satellite under a

variety of orbital conditions. The software SINDA was used in conjunction with Thermal Desktop to acquire the satellite's temperatures for various orbits.

SINDA

SINDA is an industry standard, network style, thermal analysis program used to numerically integrate the governing equations using the FDM. SINDA is used in conjunction with Thermal Desktop which separates the numerical routines into two parts: a pre-processor and a library. Thermal Desktop makes use of property tables that can be accessed at any time during the assembly and analysis of the thermal model. This enables ease of modification of heat loads and allows for solving the model parametrically. In Thermal Desktop the model is constructed of elements that include nodes, plates and bricks. The model is then exposed to environmental boundary conditions and solved for temperatures using SINDA. In Thermal Desktop, the user also has the ability to input the satellite's orientation modes while in orbit.

To begin, a geometrically-equivalent sphere was modeled with SINDA as a basis of comparison. The sphere was modeled as a single node with a black anodized surface finish and was put in an 800 km, 45° inclination orbit. As was done with the lumped capacitance analysis, this node was defined to have an initial starting temperature of 400 °K. Figure 6-11 depicts the sphere in orbit with respect to Earth.

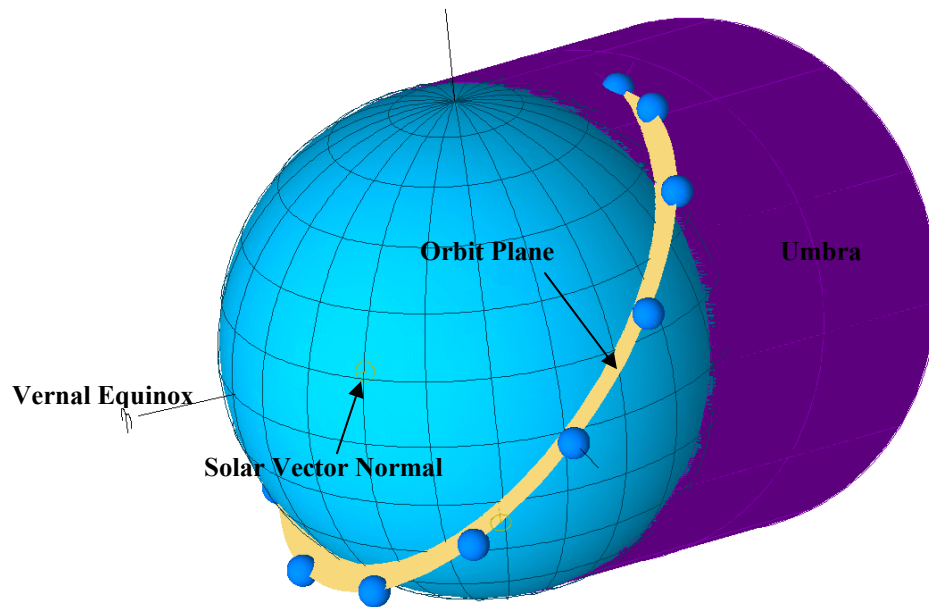


Figure 6-11: Thermal Desktop Sphere

The small sphere is the equivalent of BSat in many ways: specific heat, mass, surface properties, and orbital parameters. The temperature environment of this single node shows responses due to the different orbital positions. When in eclipse, the solar load vanishes and the satellite, or sphere, will lose heat to the space environment. When the object is exposed to the sun it undergoes environmental heating. With a spinning spacecraft particularly a picosatellite, uniform environmental heating and cooling is expected due to the validity of lumped capacitance and the orbit-average incidences of its surfaces. Figures 6-12 and 6-13 was a comparison of theoretical lumped capacitance against the transient results obtained by the simulation depicted in Figure 6-11.

**Sphere Comparison of Transient Temperature:
Q_{gen} = 3W, Black Anodized**

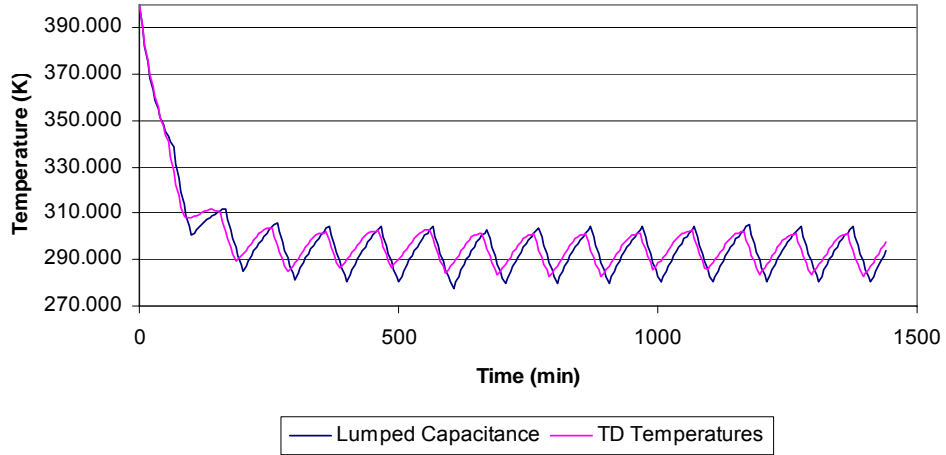


Figure 6-12: Sphere Comparison with Q_{gen}

**Sphere Comparison of Transient Temperature:
Q_{gen} = 0W, Black Anodized**

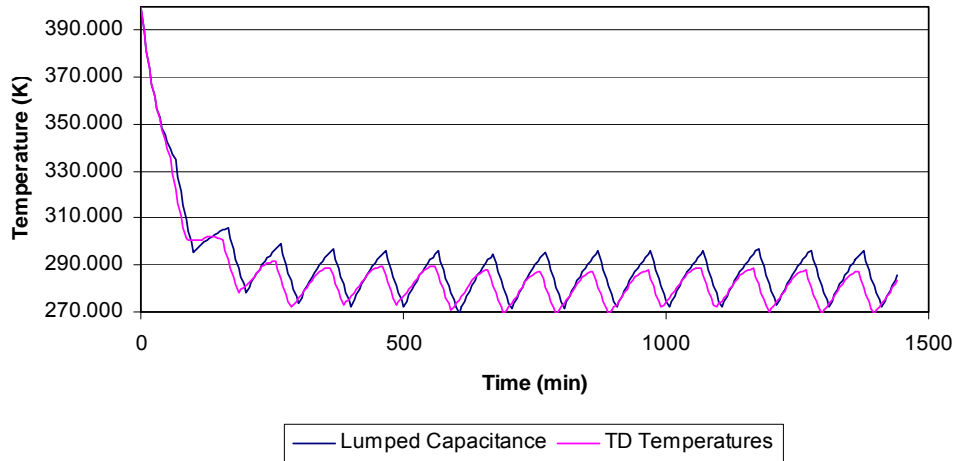


Figure 6-13: Sphere Comparison without Q_{gen}

The comparison shown in Figures 6-12 and 6-13 validate the theoretical lumped capacitance analysis of the equivalent sphere. The Thermal Desktop (TD) results appear to be slightly out of phase with respect to the theoretical; however, the order of

magnitude of the two data sets is complementary. These figures also show the significance of the internal heat generation term used in the energy balance. For no internal energy, the average of the theoretical and numerical data sets is 17 °C and 13 °C, respectively. With internal heat of 3 W, the theoretical and numerical averages are 25 °C and 26 °C, respectively. These numbers imply that that the SINDA numerical results are slightly more conservative exhibiting higher maximum temperatures and lower minimum temperatures.

Battery Consideration

To properly model BSat for simulation in SINDA it was important to first understand the behavioral characteristics of the secondary batteries. A battery is typically dense, resulting in a significant thermal-mass when considering the temperature environment of a satellite. To this end, the specific heat of the battery was determined through a calorimeter experiment. Obtaining a well understood thermal capacity of the battery has provided insight into what thermal control techniques are necessary for maintaining the battery within its appropriate temperature limits. For clarification, the absolute temperature requirements of this particular battery are listed in Table 6-4.

Table 6-4: BSat's Secondary Battery

Rose Lithium Ion Battery	
Nominal Voltage [V]	3.7
Capacity [mAh]	1950
Charge Temperature [°C]	0 to 45
Discharge Temperature [°C]	-10 to 60

Calorimeter Experiment

The calorimeter method is a standardized technique often employed to experimentally determine an object's specific heat. Calorimetry is a branch of thermodynamics that is the study of energy and heat flow. A calorimeter is an experimental device in which a chemical reaction (i.e. heat exchange) takes place. The apparatus was well-insulated to minimize the amount of heat allowed to enter or escape the test chamber to the surroundings; Figure 6-14 shows this apparatus. For a description of the set-up refer to Appendix D.5.



Figure 6-14: Calorimeter Apparatus

To empirically determine the specific heat of the Rose battery it was important to validate the assumption of a perfectly insulated apparatus, or in other words, to *calibrate* the calorimeter. To accomplish this, a material sample of known specific heat was first investigated prior to testing the battery. To verify the apparatus, the experiment was repeated with different initial temperatures and time durations. Scientists Dulong and Petit in 1818 collaborated to discover that the quantity of thermal capacity is constant in a

given object; therefore, changing the temperatures and time parameters should not reveal a different specific heat value for the same material.

The calorimeter utilizes the conservation of energy approach defined by the following set of equations:

$$q_{net} = 0 = q_{sample} + q_{water} + q_{calorimeter} \quad (6.7)$$

where,

$$q_{sample} = m_s C_{p_s} (T_f - T_{s_i})$$

$$q_{water} = m_w C_{p_w} (T_f - T_{w_i})$$

$$q_{cal} = C_{cal} (T_f - T_{cal_i})$$

where m is the mass of the respective constituent, C_p is the specific heat, and C_{cal} is the heat capacity of the calorimeter, which was obtained experimentally. For the detailed analysis refer to Appendix D.5; the results of this experiment are presented in Table 6-5.

Table 6-5: Calorimetry Results

Calorimetry Results	
Calorimeter Heat Capacity [J/K]	66
Battery Specific Heat [J/kgK]	973

The results of this work show that the thermal capacity of the battery is very similar to that of aluminum. This appears to be an appropriate value considering that the Lithium chemistry is known to be highly capacitive when compared to other battery chemistries. For the purposes of the BSat SINDA modal, the value presented in Table 6-5 will be used

when modeling batteries. As anticipated for flight and included in the thermal model, the battery will also be encapsulated in Kapton tape.

To understand the behavioral characteristics of the battery, an additional experiment was conducted using a power supply, electrical load, thermocouples, and a data logger. The battery was subjected to cyclical operation at various currents while concurrent temperatures were recorded. The data was then plotted to gain insight into the voltage versus temperature and current versus temperature for the battery. Five type-J thermocouples were integrated into the structure along with a battery, its associated bracket, and other related hardware items. The square hole where the GPS patch is mounted on the tophat served as an access area for routing wires. The thermocouple locations and the setup can be seen in Figure 6-15.

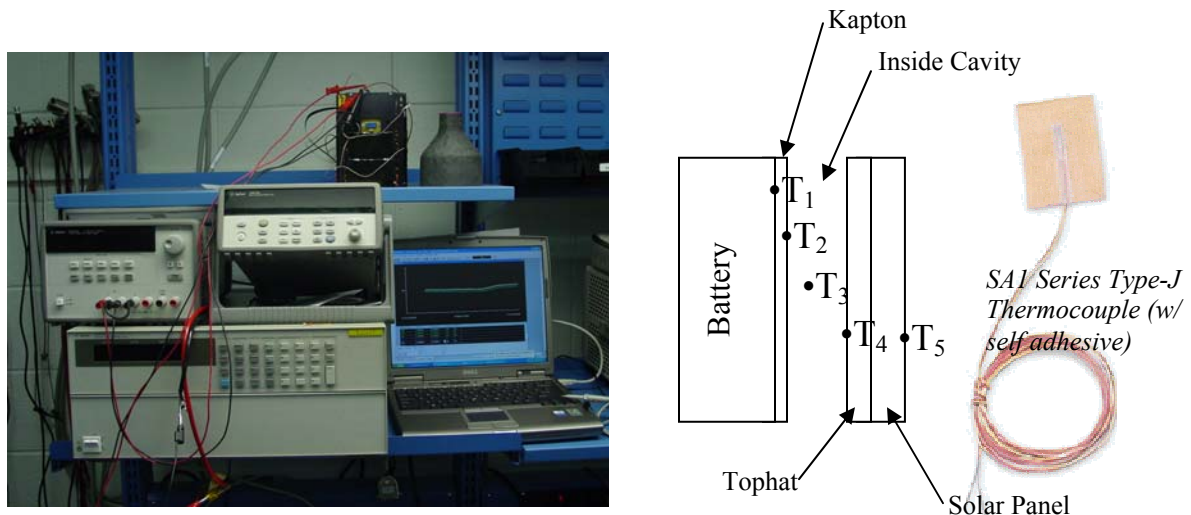


Figure 6-15: Battery Experiment

The thermocouples were arranged such that T_1 was placed on the surface of the battery, T_2 was placed outside a 1 mm layer of Kapton, the third, T_3 , was located in the cavity of the tophat, T_4 was adhered to the inside surface of the tophat, and T_5 was located on the

outside surface of the solar panel. The results are as follows for BSat's maximum current draw of 670 mA and nominal charge current of 140 mA. Figure 6-16 and 6-17 show the temperature state of the battery versus current and voltage, respectively.

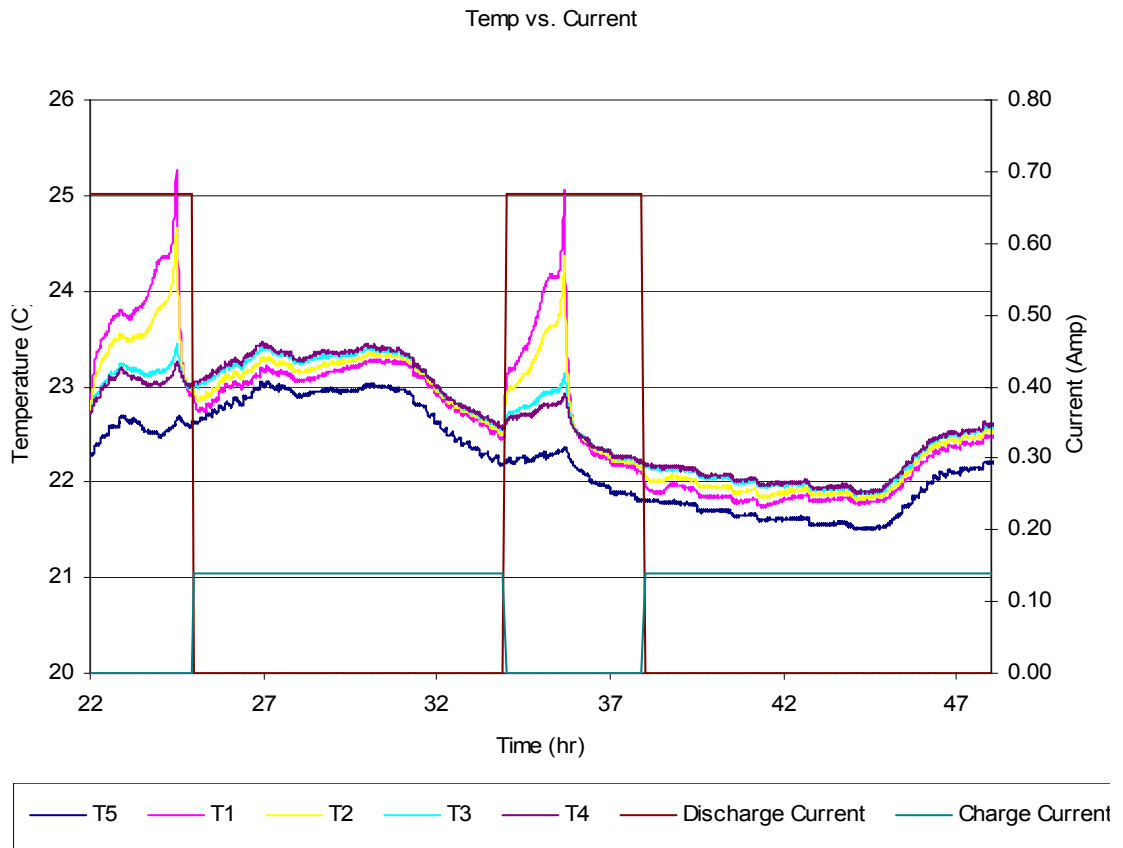


Figure 6-16: Battery Temperature at Optimal Current

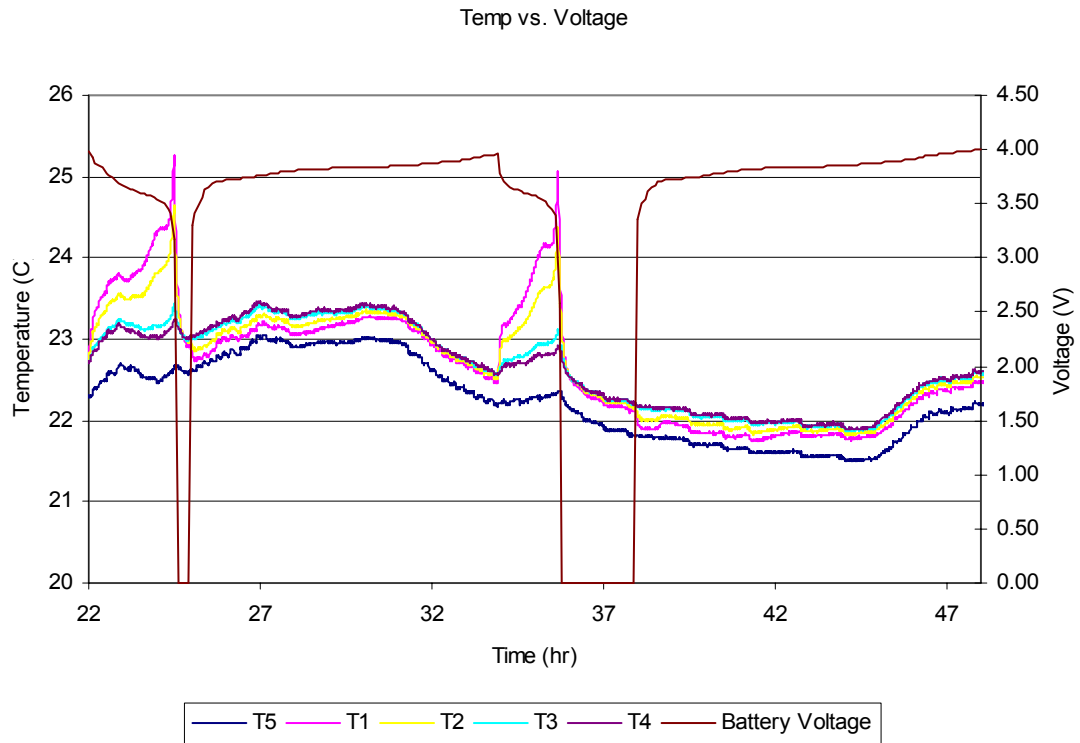


Figure 6-17: Battery Temperature vs. Voltage State

From this information it is extremely obvious that the Rose battery has a tendency to heat up while discharging at 670 mA, and to slightly heat during the final stages of a complete charge cycle; this is shown by the temperature rise on the right side of the plot. This information is useful to a point, but because the time scales are so much longer than any anticipated duty cycle, the temperature changes become relative. However, experimentally this data does bring light to many intrinsic characteristics of what to expect with in-situ temperature telemetry and the battery's corresponding state of charge. It is also clear that the thin layer of Kapton does insulate the battery from its surroundings and that the temperature on the outside of the solar panel, *T5*, is influenced significantly

by the convective conditions of the laboratory. The complete results are presented in Appendix D.5.

Physical Thermal Model

The objective of the SINDA model was to obtain temperature distributions across all the external surfaces of the BSat structure. The thermal model is geometrically equivalent to the physical model; however, simplifications were made to the details of the actual parts. The modeling strategy was to construct BSat using a series of flat plates and bricks; flat plates to represent the four adjoining sides, the baseplate, the tophat, and the tether bracket, and bricks for including the thermal mass of the launch rails. Thermal mass is important when considering the distributed temperatures of a system because they require energy to change temperature state and they store energy as a function of the surroundings. In the case of BSat, the launch rails, tether system, and the secondary batteries carry thermal inertia. These quantities will ultimately lower the average or bulk temperature of the satellite. As seen in Figure 6-18, the BSat SINDA model includes many of the temperature-manipulative features: four sides, a baseplate, a tophat, a tether bracket, a tether system, four solar panels, and two batteries which were wrapped in 1 mm of Kapton.

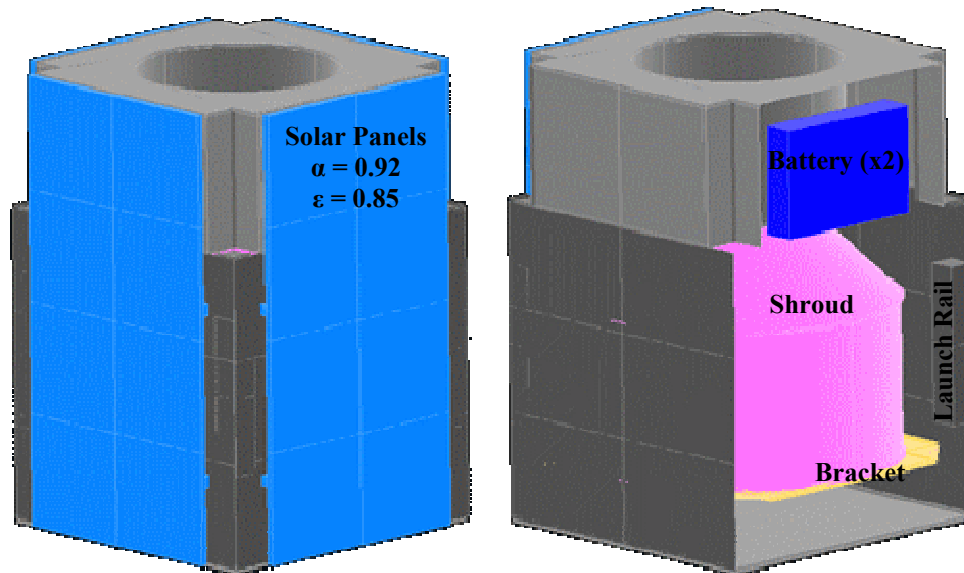


Figure 6-18: BSat SINDA Model

Parametric Orbits

Referring back to Figure 4-26 it becomes somewhat apparent that the change in altitude of BSat's orbit has little effect on the satellite's yearly-average thermal environment. However, to quantify this statement from a more direct thermal approach, the heating rates were first calculated at the altitude boundaries of 600 km and 800 km. The results of this study are presented in Appendix D.4. This analysis showed that the constricted altitude range has little effect on the overall thermal environment of BSat. The *optimal* altitude for this parametric study was selected to be 700 km. More importantly, this information revealed the dependence of the thermal environment on the beta angle. The incident heating shown below is defined as the total absorbed flux from the contributions of solar, albedo, and Earth emissions. These values were normalized in

a manner that reflected a passively spinning satellite at 1 rpo⁶⁶; allowing each surface perpendicular to the z-axis to experienced an equal opportunity of exposure. Figure 6-19 shows the total absorbed flux on each of BSat’s exterior surfaces with respect to a 0° beta angle.

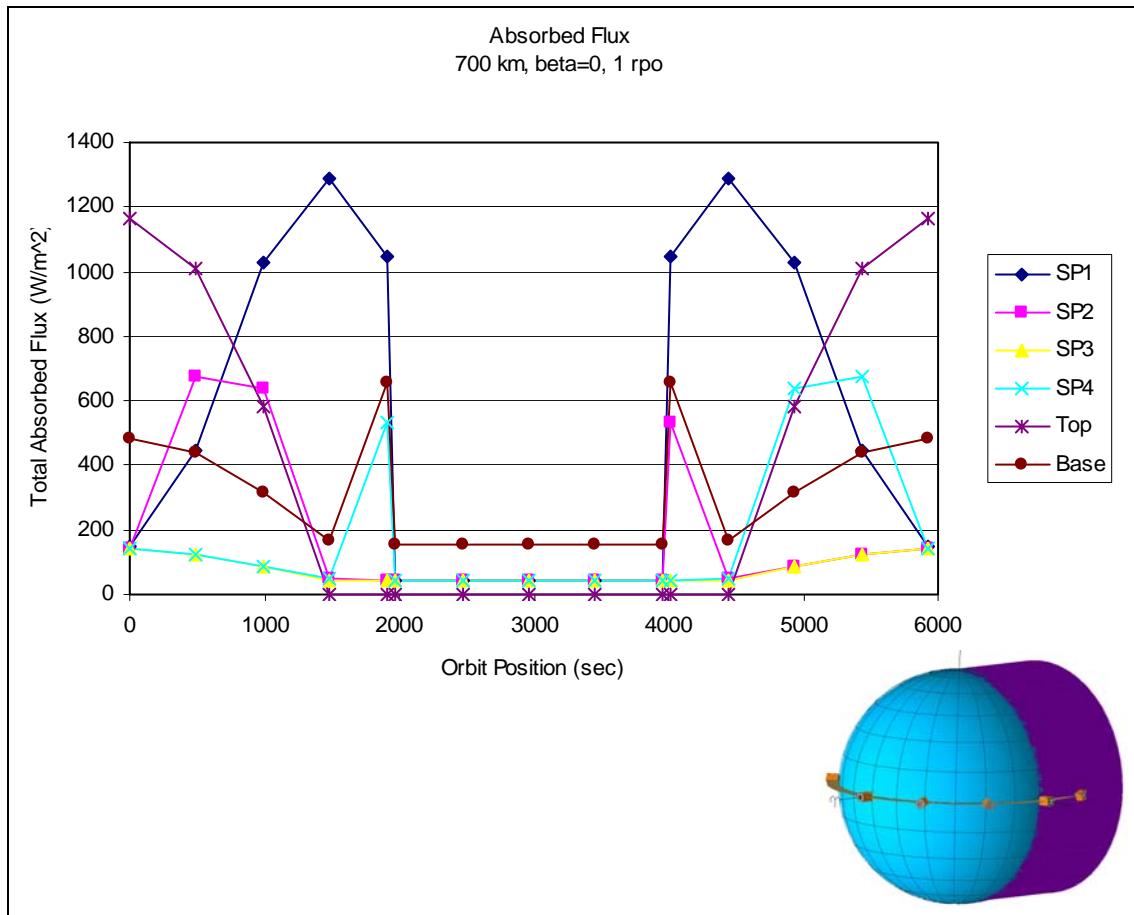


Figure 6-19: Total Absorbed Flux, $\beta=0^\circ$

With a beta angle equal to zero, BSat will orbit Earth at its coldest state, with eclipse times approaching 35 minutes. It is very clear in Figure 6-19 the effect of eclipse on

⁶⁶ Revolution Per Orbit

BSat's incident flux loads. The interval between 2000 and 4000 seconds signifies that BSat is shaded by Earth in which the only incident flux is the planet's infrared radiation. Also, the *attitude* of BSat can be inferred from Figure 6-19 by following the data corresponding to *Top*. During the eclipse period the top of BSat is facing the 4 °K temperature of space because the opposing *Base* is nadir pointed. In any case, it is quite clear the magnitude of the solar flux incident upon BSat. Figure 6-20 expresses the total absorbed flux of BSat at a beta angle of 68.4°. A beta angle of 68.4° signifies the maximum angle attainable with an orbit inclined to 45°.

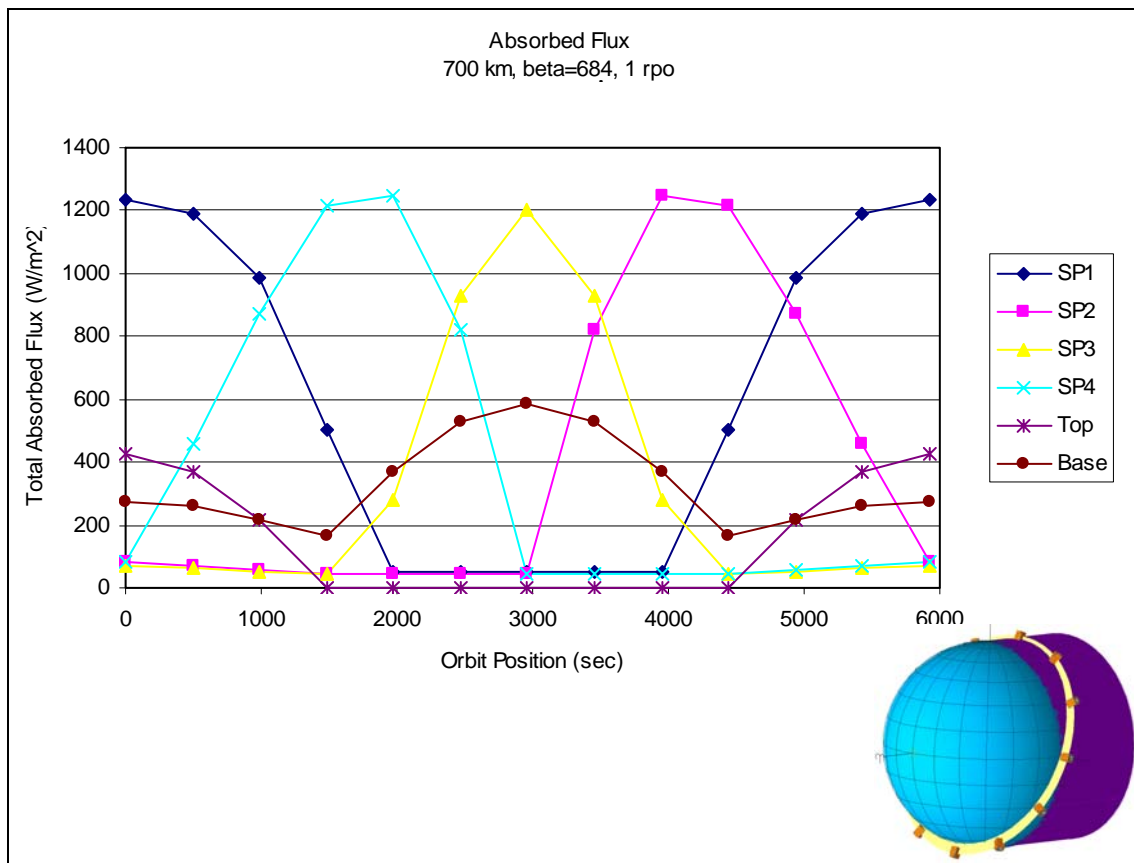


Figure 6-20: Total Absorbed Flux, $\beta=68.4^\circ$

Figure 6-20 reveals that each solar panel of BSat absorbs incident radiation of the same magnitude, but that the total absorbed energy is greatest on the surfaces which face the sun at the equatorial and sub-polar locations around Earth; side three is seen to face the sun for the shortest duration of time and is nearly on the backside of Earth in doing so. It is also clear that at this angle BSat is exposed to the Sun continuously throughout its orbit; a circumstance which is favorable from a power-generation perspective.

The greatest of beta angles is defined at 90° , when the satellite's orbit plane is perpendicular to the solar vector. A 90° beta angle is attainable by an inclination of 66° and typically induces the satellite into its warmest environment. However, given the unique nadir-pointing *attitude* of BSat, Figure 6-21 identifies some interesting characteristics.

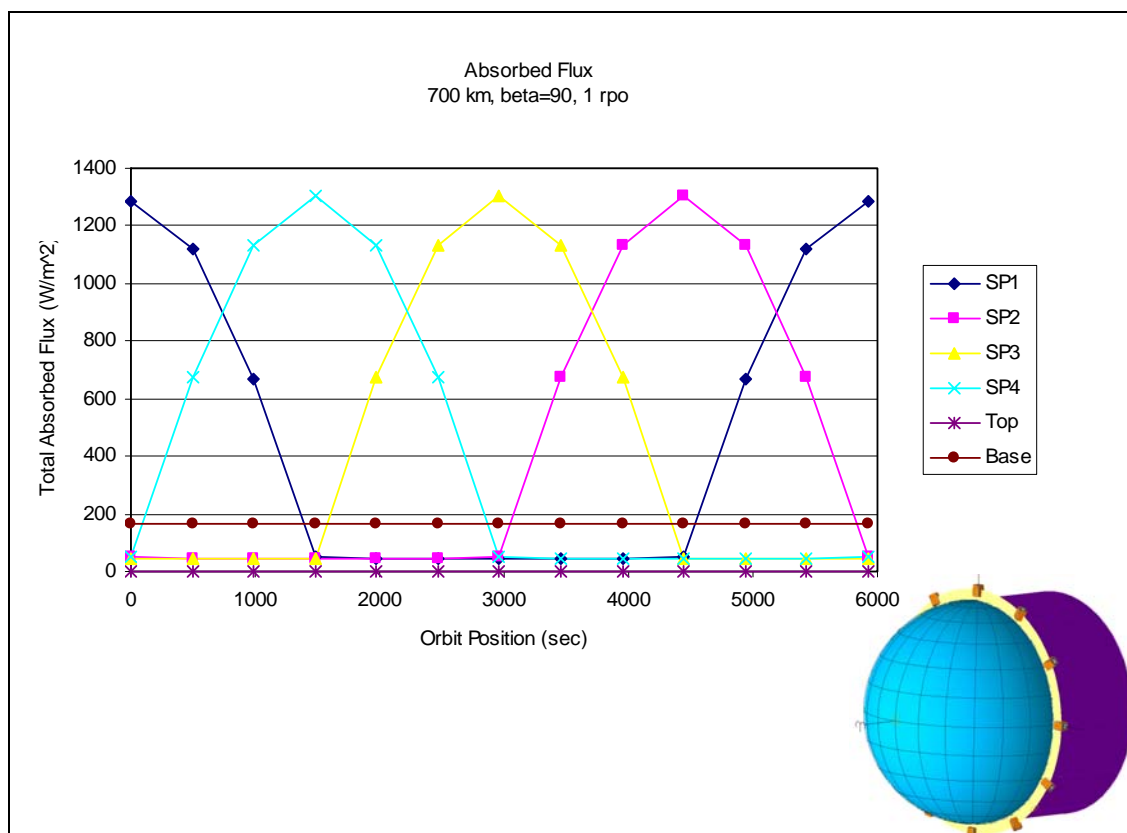


Figure 6-21: Total Absorbed Flux, $\beta=90^\circ$

While all the *solar panels* experience an equal amount of solar radiation, the *Base* and *Top* experience absolutely none. By carefully examining the discrepancies between Figures 6-20 and 6-21, it becomes clear that the total absorbed energy (the area under the curve) for the solar panels is comparable; the general bell-shape, the magnitude of absorbed flux, and the approximate 3000 second time duration suggest a thermal environment that is similar. The more noticeable difference is the total absorbed flux for the *Base* and *Top*. Figures 6-21 shows that the *Top* of BSat will consistently see the darkness of space while its nadir-pointing *Base* is only influenced by Earth's albedo and IR emissions. For a $\beta = 68.4^\circ$, Figures 6-20 expresses a more dynamic thermal environment by which surfaces are influenced more significantly by the characteristics of its orbit. Ultimately, the attitude of BSat along with the information provided in the above figures suggest that its worst-case hot environment occurs at beta angles leading up to, but not equal to 90° . Figure 6-22 is a superposition of the three angles investigated for BSat.

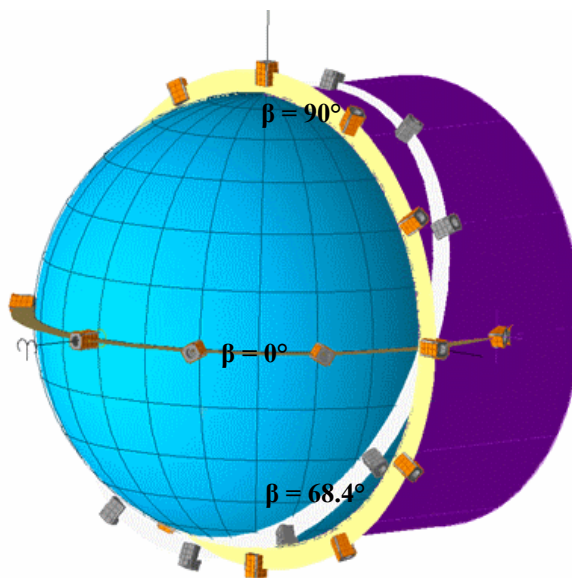


Figure 6-22: Parametric Beta Angles

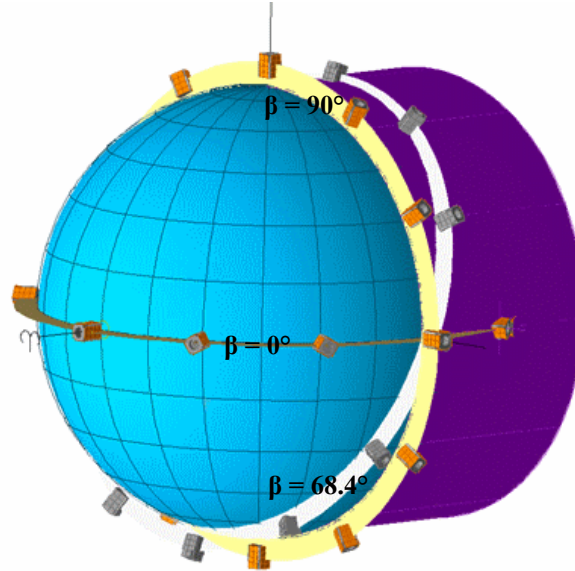


Figure 6-22: Parametric Beta Angles

Incident Flux

The parametric beta angles include the worst-case cold, $\beta = 0^\circ$, the angle at nominal inclination⁶⁷, $\beta_{\max} = 68.4^\circ$, and the worst-case hot where $\beta = 90^\circ$. These angles defined the incidences of the environmental radiation upon the exterior surfaces of BSat. The contributions of both solar and albedo shortwave radiation are of particular interest in terms of BSat's power-generation capabilities. Clearly the satellite's capabilities increase with an increase in inclination; the intent of the depictions below is to quantify the radiation sources responsible for power conversion: solar and albedo direct incidence. Figure 6-23 through Figure 6-26 depicts the direct incidence of the shortwave radiation on BSat's solar panels for beta angles of 0° , 68.4° , and 90° .

⁶⁷ nominal inclination is defined at 45° , the XSS-10 baseline; at this inclination the max beta angle is 68.4°

Direct Incidence
700 km, beta=0, 1 rpo

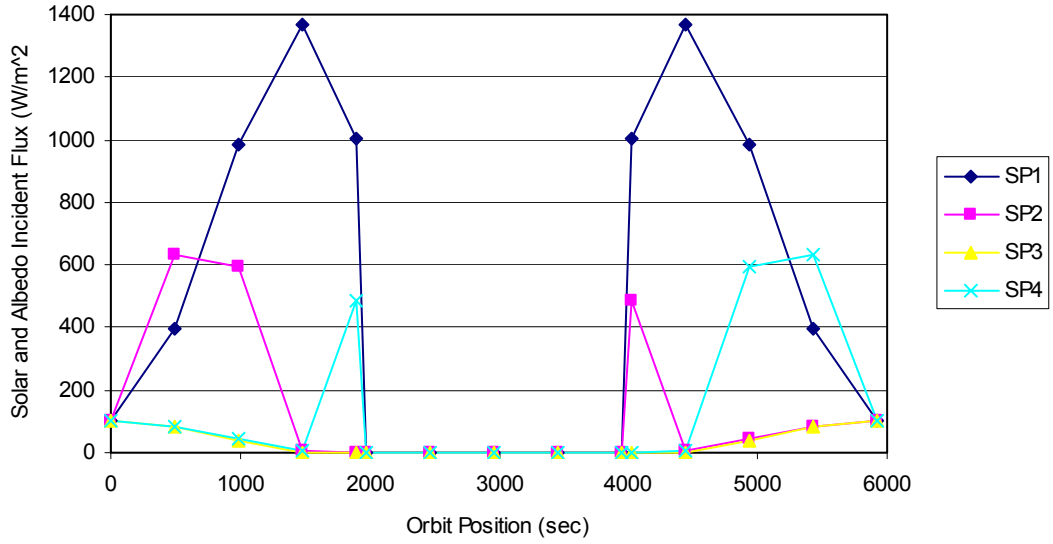


Figure 6-23: Direct Incidence, $\beta=0^\circ$

Direct Incidence
700 km, beta=68.4, 1 rpo

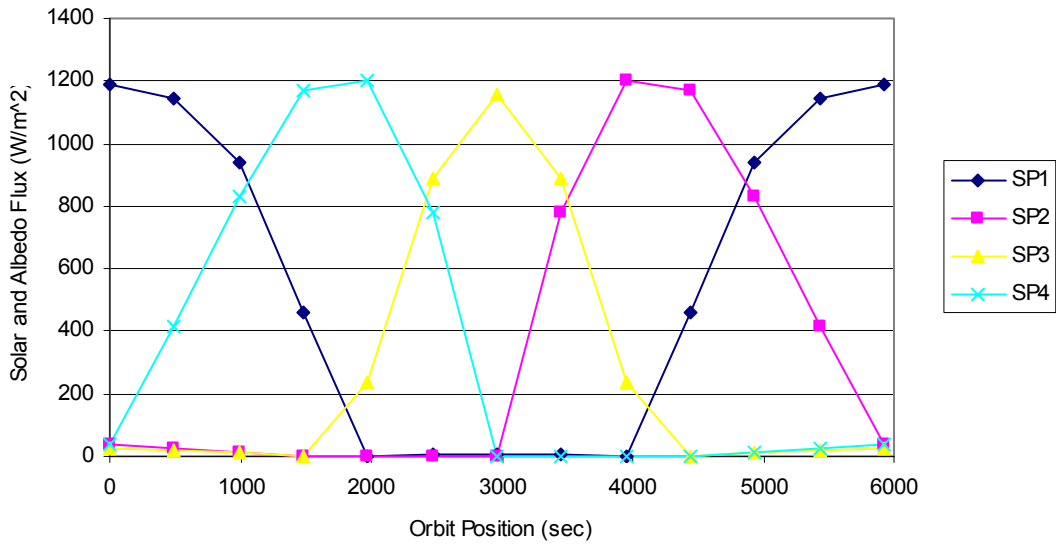


Figure 6-24: Direct Incidence, $\beta=68.4^\circ$

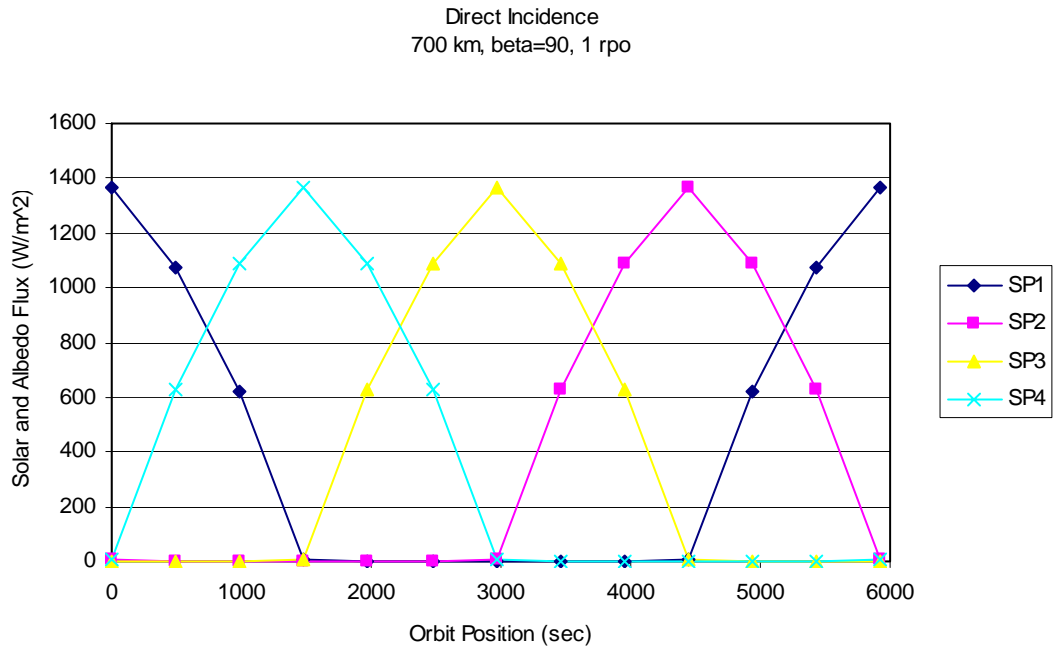


Figure 6-24: Direct Incidence, $\beta=90^\circ$

Figure 6-25 shows the effect on BSat spinning on its z-axis at a rate equal to 5 revolutions per orbit. Comparing this to the *slow-spinning* data of Figure 6-24 shows that the rate at which BSat will physically spin has little effect on BSat's power-generation capabilities; however, recognizing the possibility of BSat remaining stationary about its z-axis while in orbit is a concern that should be addressed when finalizing the power allocation budget and the duty cycles of the electronics. For the purposes of BSat's thermal analysis it is assumed that BSat will spin modestly at one revolution per orbit.

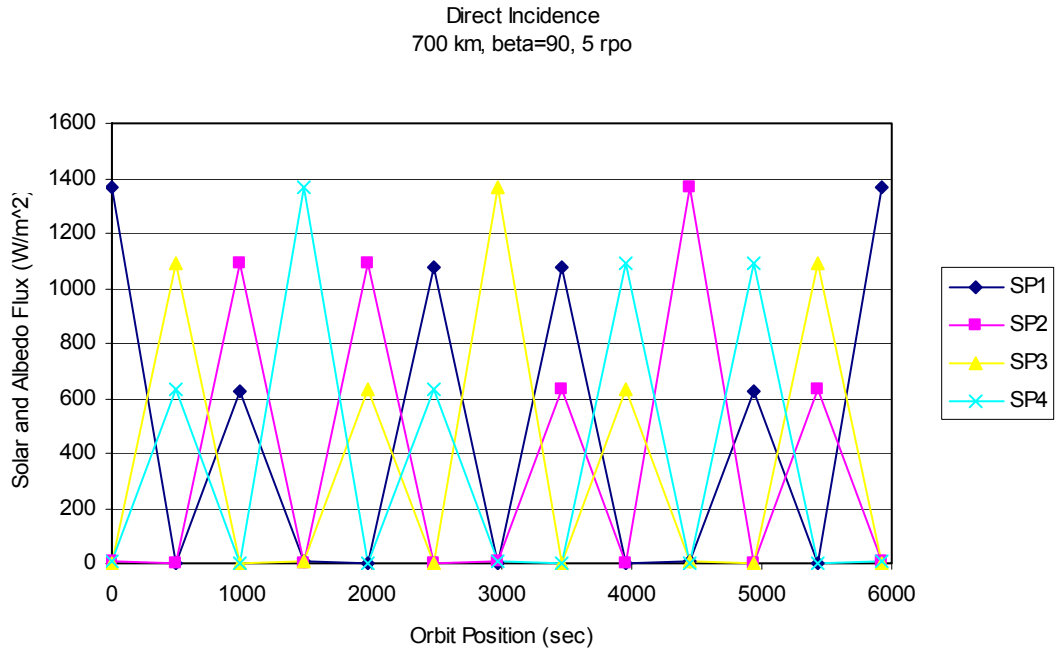


Figure 6-26: Direct Incidence, $\beta=90^\circ$, fast-spin

Transient Temperatures

The materials and properties presented earlier were used in creating the BSat SINDA model. The thermal capacitance was measured by applying the appropriate thermophysical and optical properties to the structure, and then by applying a series of orbital constraints. In the case of BSat, and by first understanding the variability with altitude, the thermal capacitance was measured by the applications of the beta angle: 0° , 68.4° , and 90° , and the variation in internal heat generation: minimum: 0 W, and maximum 3W. To compensate for the lack of temperature stability under a set of parameters, BSat was then scrutinized against the optical properties of clear-anodized and black-anodized. The environmental heating loads were taken as averages from the information in Table 6-1.

Due to the locations of electrical components within the satellite, it was important to allocate the internal heat generation to specific *cavities* of the satellite; areas above and below the tether shroud. In the model this was accomplished by defining a heat source measured absolute, [W], at a node; a load which was varied from 0 W to 3 W. The batteries were defined with 1 mm of Kapton insulation on their exterior surface and were allowed to radiatively interact with the interior surfaces of the satellite. For BSat's optical properties, both clear and black-anodized were investigated where the higher absorptivity for the black was found to increase the maximum temperatures in all the orbital cases. It is a requirement of the deployment device that at a minimum BSat's launch rails must be anodized, where clear and black are the bounds of this spectrum of surface finishes.

One of the capabilities within SINDA is the ability to visually check the thermal model to verify user-defined parameters. In regards to the BSat SINDA model, Figure 6-27 shows a visual inspection of the satellite's external optical properties.

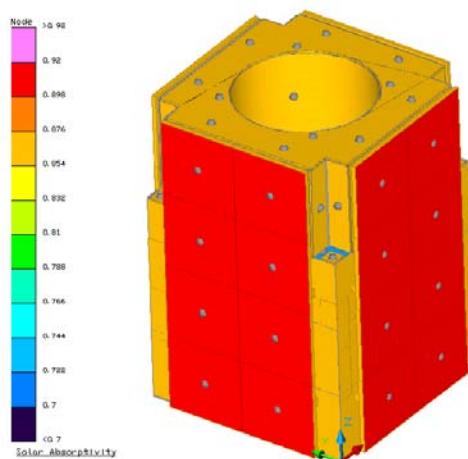


Figure 6-27: BSat Solar Absorptivity Verification

While the red surfaces in Figure 6-27 correspond to the solar cell real estate, the gold surfaces were manipulated to reflect both of the surface finishes in question. That is, the solar cells' optical properties go unchanged when redefining the surfaces of BSat. On a figure of merit, Figure 6-27 infers that each surface could be modeled independently to optimize the temperature state of the satellite; with more complicated architectures it is not uncommon to specify *checkered* surfaces in terms of emissive and absorptive capabilities. For BSat, it was decided that complicating the surface finishes would have an undesirable financial effect.

BSat's coldest environment occurs at a beta angle equal to zero, an environment that defines long eclipse periods and because of the satellite's *attitude*, minimum surface-exposure to solar radiation. During this time internal heat plays a significant role in the satellite's ability to provide a conforming environment in the absence of a physical heating system. Figure 6-28 through Figure 6-30 show BSat's distributed temperatures for $\beta = 0^\circ$. The first two show BSat in the absence of internal heat for both the clear and black-anodized cases.

It appears that two very distinct characteristics are highlighted with the change in BSat's surface optical properties; first, that the ability to absorb solar radiation with clear-anodized is 60% less than that with black anodized, and secondly that the tether-shroud has a significantly larger thermal capacity. To understand more clearly the distributions leading up to the steady-state temperatures, these first two figures show the transients which begin with the initial guess value. While in all cases the temperature profile of the batteries follow closely the profile of BSat's aluminum structure, the significant

difference is the *state of temperature* of the batteries relative to the structure. For the hot-case when BSat is black-anodized, the structure responds much more strongly to the exposure of the sun; therefore, the sinusoidal profile is of larger amplitude. Because the emissive qualities of the two finishes are nearly identical, the temperature response of the satellite during eclipse goes unaffected. Simultaneously, the temperature of the tether shroud reaches steady-state more quickly with the black-anodized; meaning that in return, the batteries also reach steady-state more quickly. With no internal heat generation the temperature of the batteries is then strongly influenced by the temperature of the shroud. In all the figures presented next (Figure 6-28 through Figure 6-38), the apparent time-lag of the temperatures associated with the shroud is also evident. This is a result of its increased heat capacity when compared to the other constituents of the satellite and a characteristic which brings validity to the results.

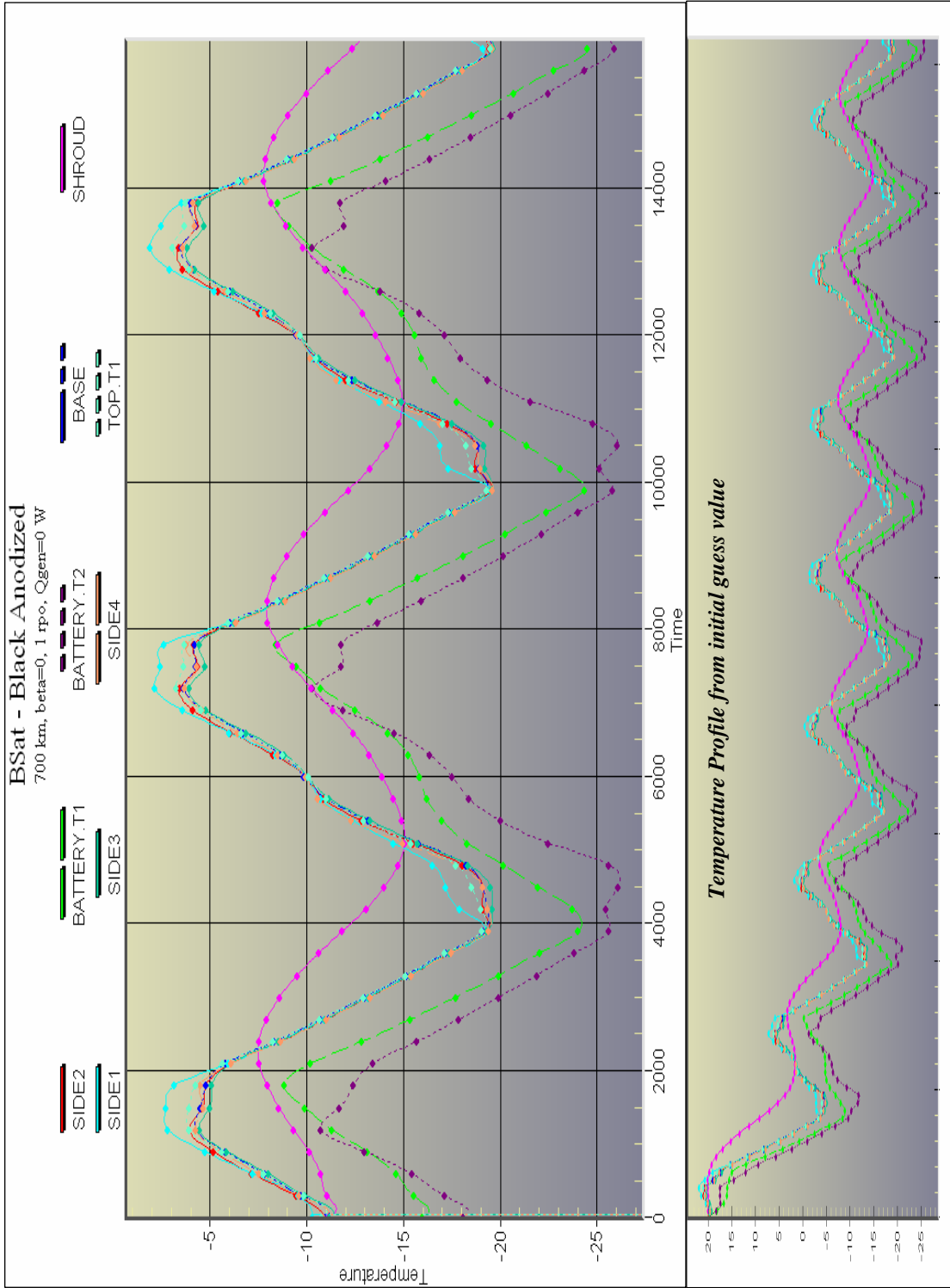


Figure 6-28: BSat (Black Anodized): 700 km, $\beta=0^\circ$, 1 rpo, $Q_{gen} = 0$ W

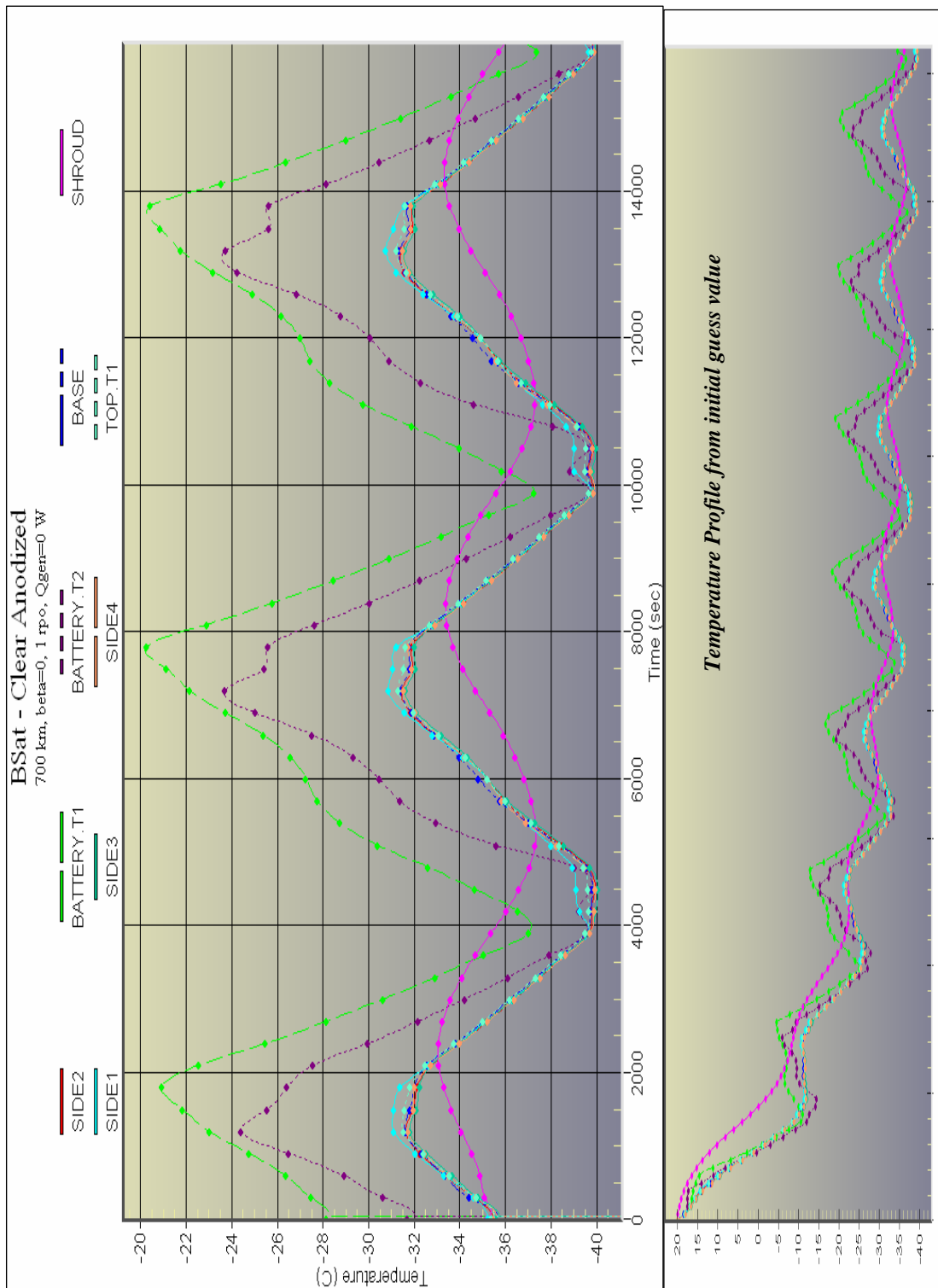


Figure 6-29: BSat (Clear Anodized): 700 km, $\beta=0^\circ$, 1 rpo, $Q_{gen} = 0W$

The conclusions drawn from Figures 6-28 and 6-29 are that with a beta angle of zero, a black-anodizing finish serves BSat's thermal requirements more appropriately than would a clear-anodizing. However, attention is addressed on the batteries which have an absolute minimum temperature limit (during discharge) of $-10\text{ }^{\circ}\text{C}$; this requirement alone suggests that the addition of internal heat dissipation is essential for BSat's thermal stability at $\beta = 0^{\circ}$. Presented below, Figure 6-29 and 6-30 is the case with 3W internal heat generation showing notable temperature improvements. This data is presented for both finishes with transient effects omitted.

While the amplitudes of cyclical temperatures remain relatively unchanged, the general increase in the average temperature is more favorable given the requirements of BSat. Naturally it is easy to assume that internal radiation is negligible in relation to the responsiveness of thermal conduction; however, to achieve thermal control of such narrow margins when it comes to BSat's batteries, internal radiation was included. [Hansman, 2003] Enclosure radiation, or internal heat, was applied to the inner walls of the tophat and sides to reflect the onboard operation of the satellite's electronics. This radiation was assumed diffuse, meaning that it is acting outward in all directions from the surface designated as the source. It is of common industry practice that many spacecraft utilize the high absorptivity, high emissivity properties of black paint on all inner surfaces of the satellite structure to enhance heat sharing through radiation. For BSat, these results show an overall increase in the state of temperature of the satellite in addition to the significance of the selected surface finish.

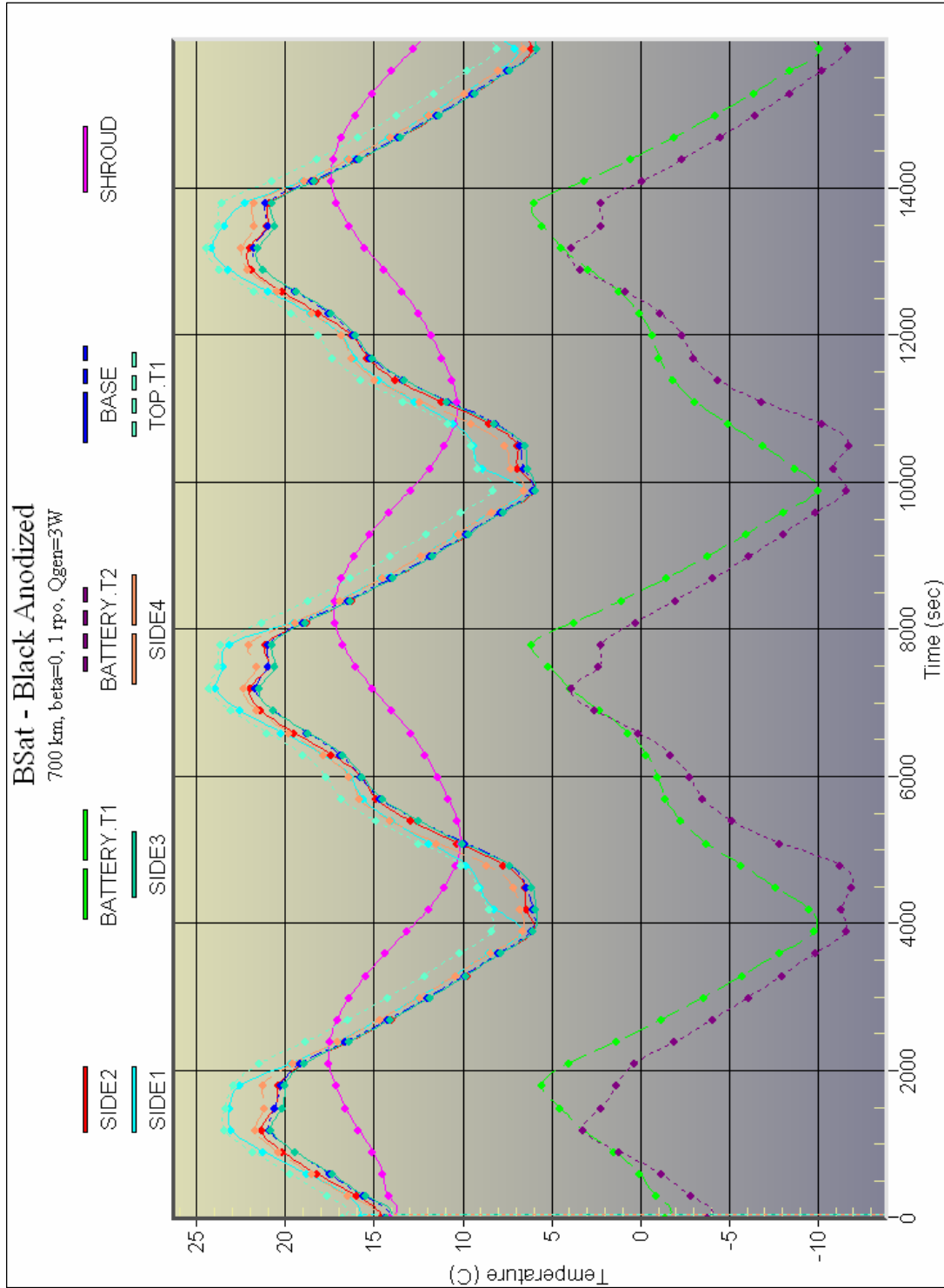


Figure 6-29: BSat (Black Anodized): 700 km, $\beta=0^\circ$, 1 rpo, $Q_{gen} = 3W$

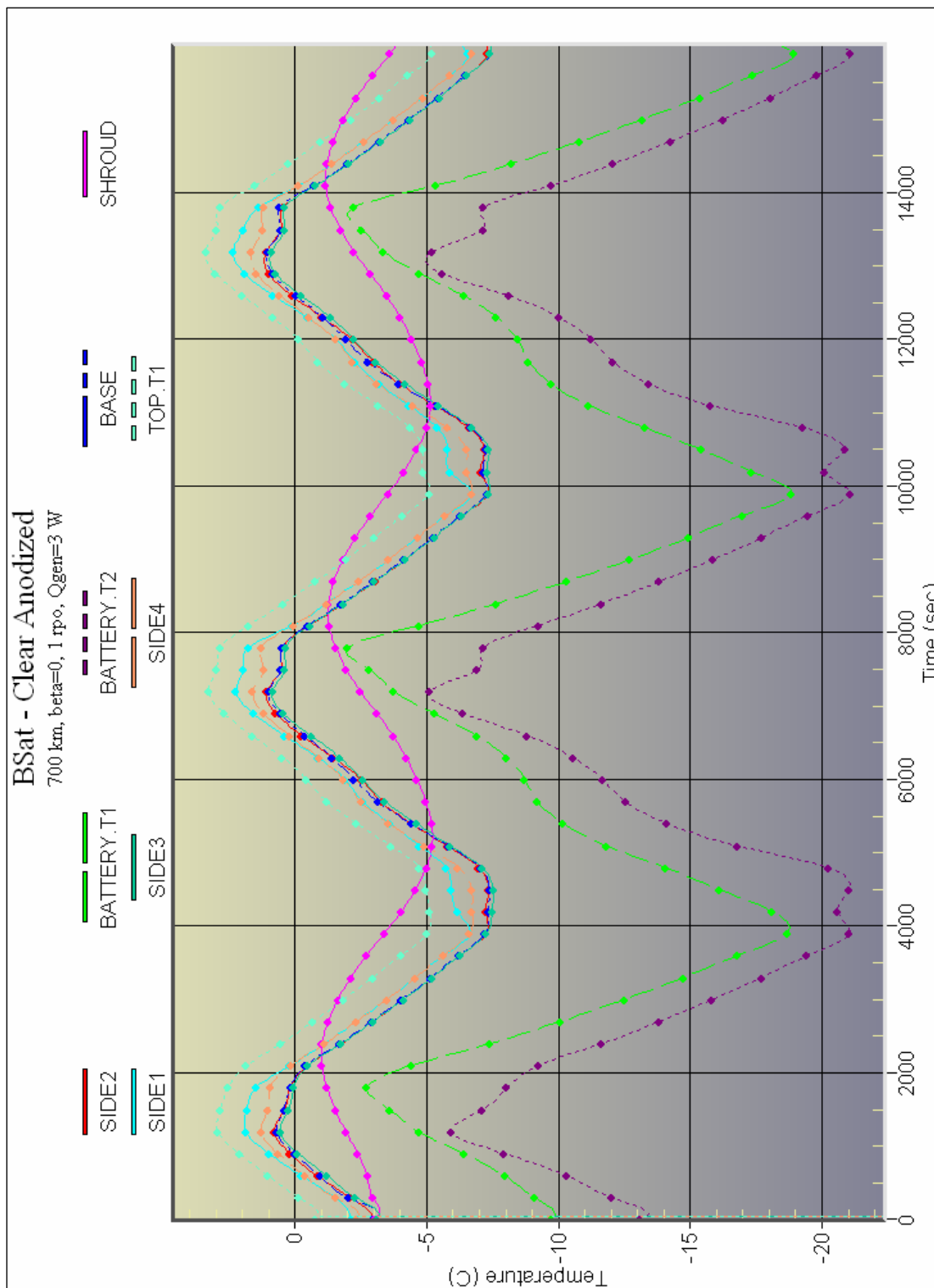


Figure 6-30: BSat (Clear Anodized): 700 km, $\beta=0^\circ$, 1 rpo, $Q_{gen} = 3W$

Figure 6-29 complements the direction by which thermal control should be implemented for BSat. The minimum temperatures associated with internal heat and black-anodized surfaces are nearly sufficient to meet the requirements of the satellite's batteries; however, these temperatures approach the threshold of the batteries' specification during discharge ($-10\text{ }^{\circ}\text{C}$). Because the batteries will heat up during discharge, it is recommended that this temperature increase be quantified further during environmental testing when the satellite is capable of functioning as a complete system. Parametrically, the self-heating characteristic of the battery is omitted, but is referred to here due to the suitability of black-anodized at $\beta = 0^{\circ}$.

For $\beta = 68.4^{\circ}$ the temperature distributions are much more dynamic because the attitude of the satellite is much more complicated. Due to the nadir-pointing baseplate, the external surfaces will see variable sources of radiation; whereas in the case of $\beta = 0^{\circ}$ and 90° , the surfaces remain relatively normal to a particular radiation source. Figures 6-31 through 6-34 show the temperature distributions for the two surface finishes imposed on BSat at a beta angle equal of 68.4° . It is clear that with a higher solar absorptivity the temperatures of the satellite are more favorable for the conditions specified by the battery. With an increase in the exposure to the Sun it also becomes apparent that the absorbed flux is dependent upon the angle of incidence. While the four adjacent surfaces of the satellite witness a maximum incidence independently, the overall temperature distributions are favorably similar; that is no appreciable difference in the temperature of one surface relative to another.

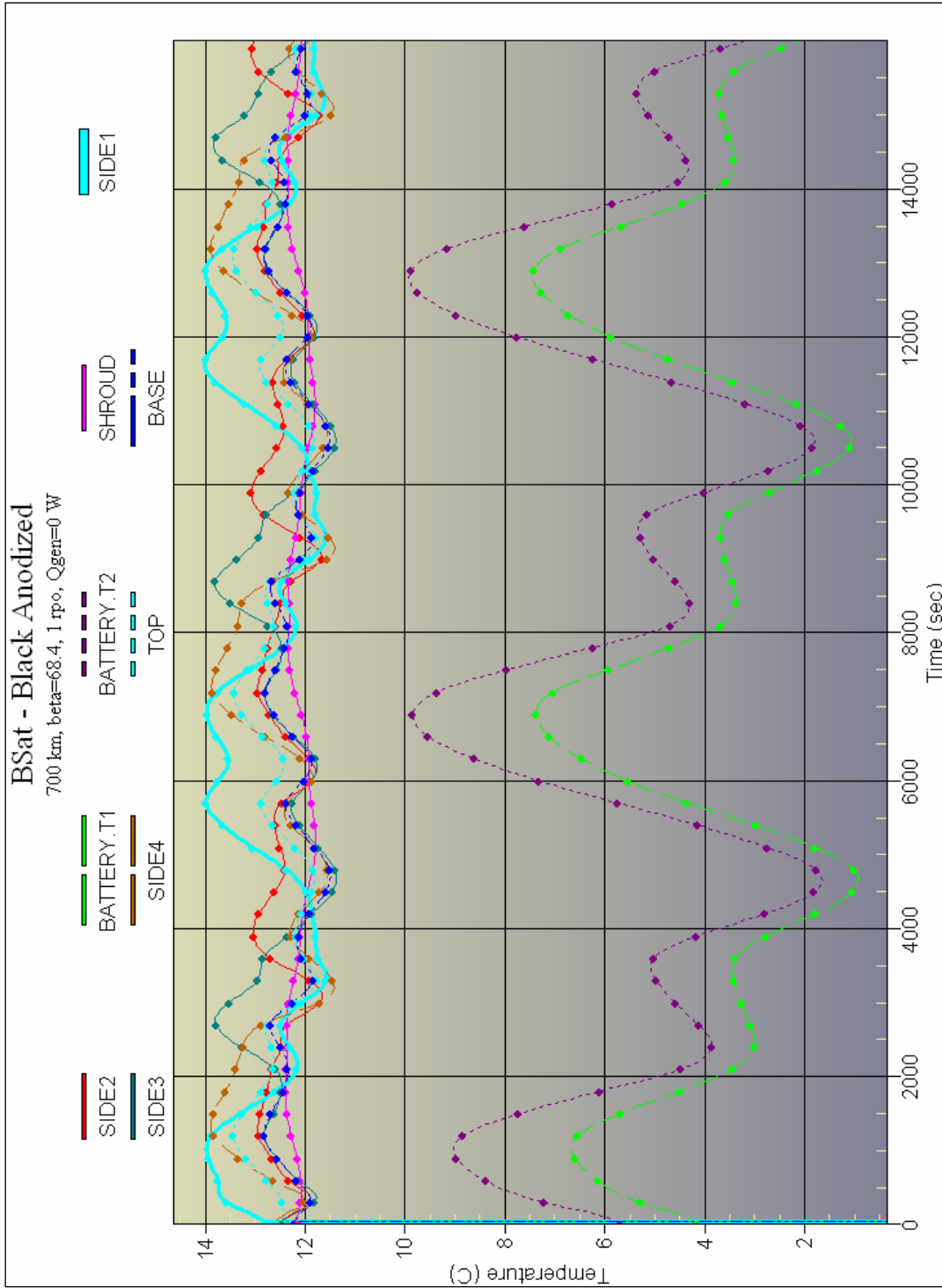


Figure 6-31: BSat (Black Anodized): 700 km, $\beta=68.4^\circ$, 1 rpo, $Q_{gen} = 0W$

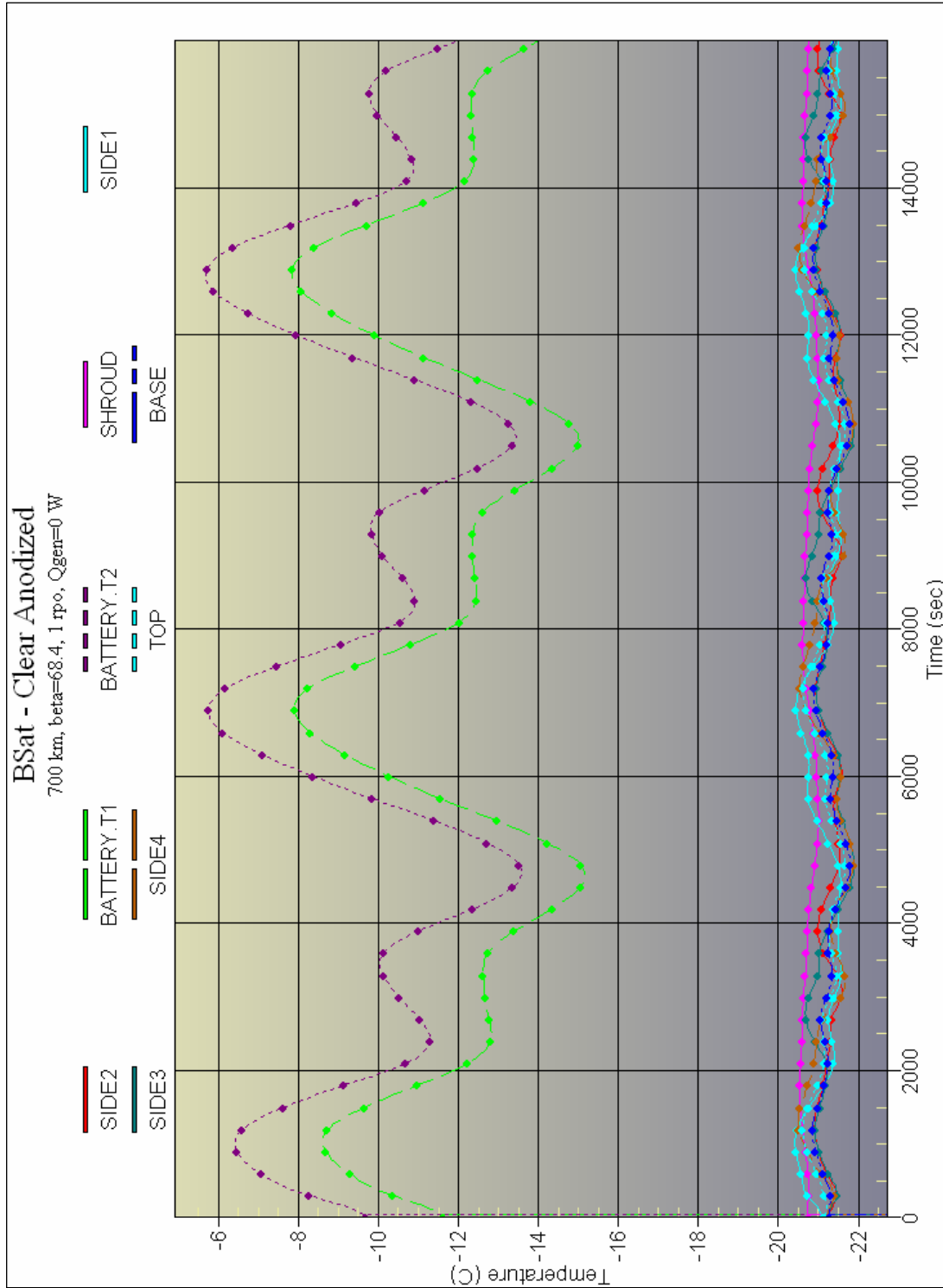


Figure 6-32: BSat (Clear Anodized): 700 km, $\beta=68.4^\circ$, 1 rpo, $Q_{gen} = 0W$

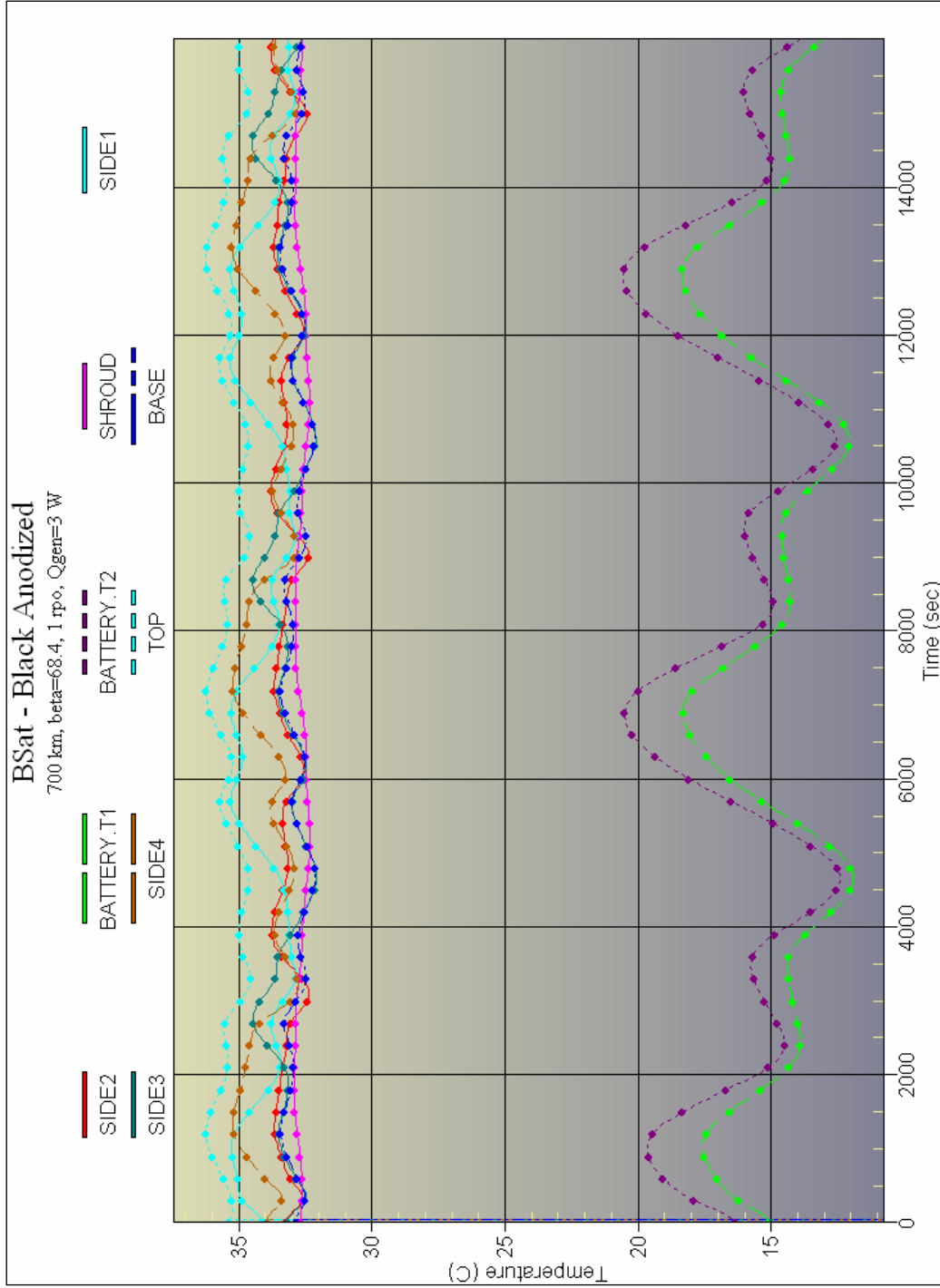


Figure 6-33: BSat (Black Anodized): 700 km, $\beta=68.4^\circ$, 1 rpo, $Q_{gen} = 3\text{ W}$

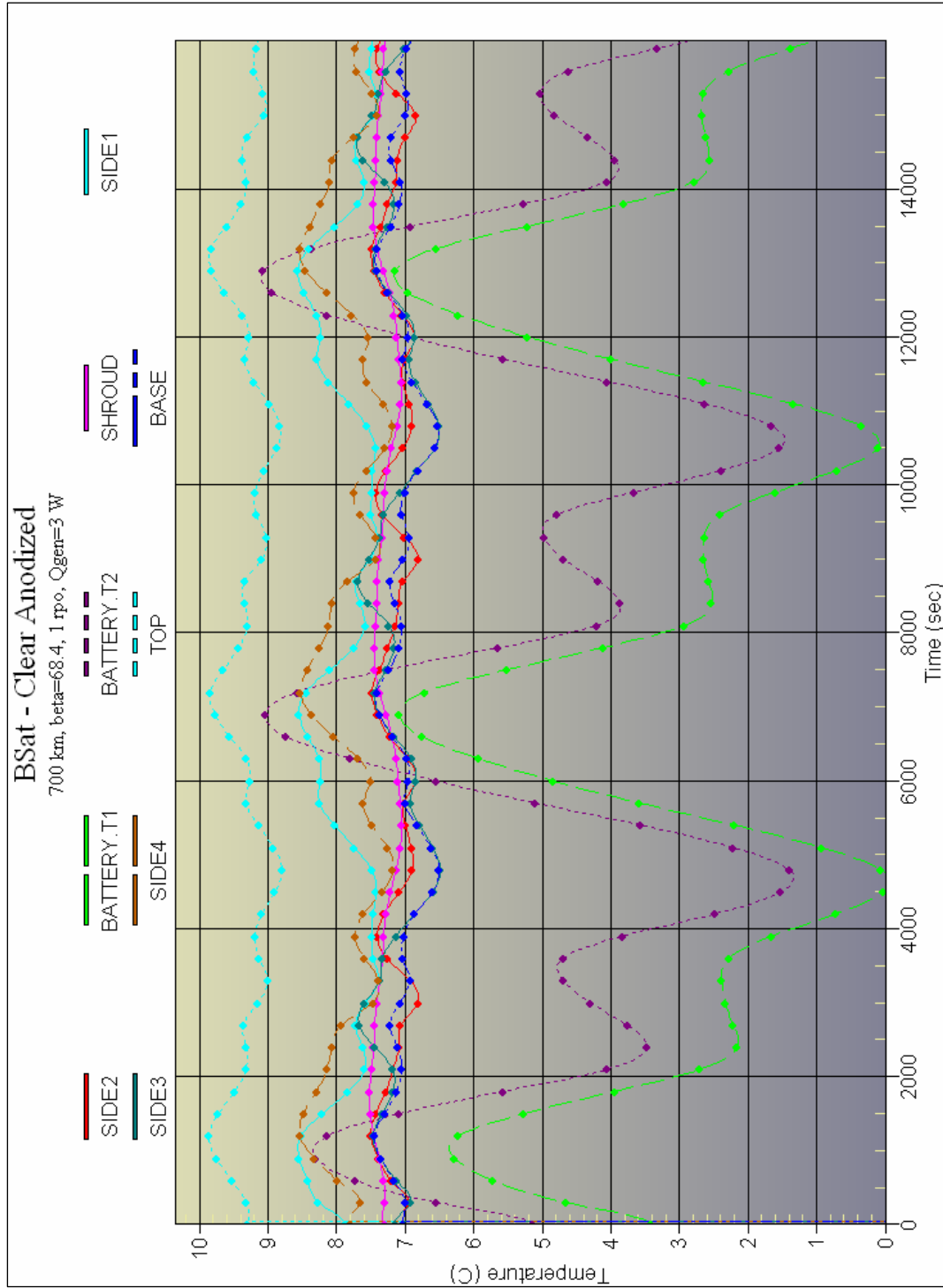


Figure 6-34: BSat (Clear Anodized): 700 km, $\beta=68.4^\circ$, 1 rpo, $Q_{gen} = 3W$

The results of the temperature analysis for $\beta = 68.4^\circ$ reveal that BSat will satisfy the thermal requirements of its electronics most appropriately by the implementation of a black-anodized surface finish. At this angle a clear-anodized satellite satisfies the requirements only when the satellite is dissipating internal heat equal to 3 W; any value less than this will result in temperatures encroaching the limits of the battery. In both cases, the extended exposure to the Sun produces temperature cycling less in amplitude as compared to $\beta = 0^\circ$. For an orbit inclination of 45° that produces a maximum beta angle equal of 68.4° , it is recommended that BSat have a black-anodized finish to satisfy the requirements of its batteries.

For the maximum beta angle, $\beta = 90^\circ$, and that corresponding to a full sunlit orbit, the temperature results are less in magnitude to those corresponding to $\beta = 68.4^\circ$. This is a result of the satellite's passive attitude characteristic; if the z-axis of the satellite was oriented parallel to Earth's magnetic field lines, the temperatures would be significantly greater for this particular orbit as more surfaces would be exposed to solar heating. From Figures 6-35 through 6-38 the correlation between the locations of the batteries is distinguishable within the satellite. While the temperatures of *Battery.T1* follow the profile of *Side1*, *Battery.T2* follows the profile of *Side4*; this was an encouraging result which again helped to verify the defining parameters of the physical SINDA model. For orbit inclinations ranging from 68.4° to 90° , it is advantageous to implement black-anodizing for BSat's exterior surfaces. Although the temperature of the batteries is unfavorably low for the 0 W case, this analysis should be considered as a conservative estimate with actual temperatures slightly greater than those presented here.

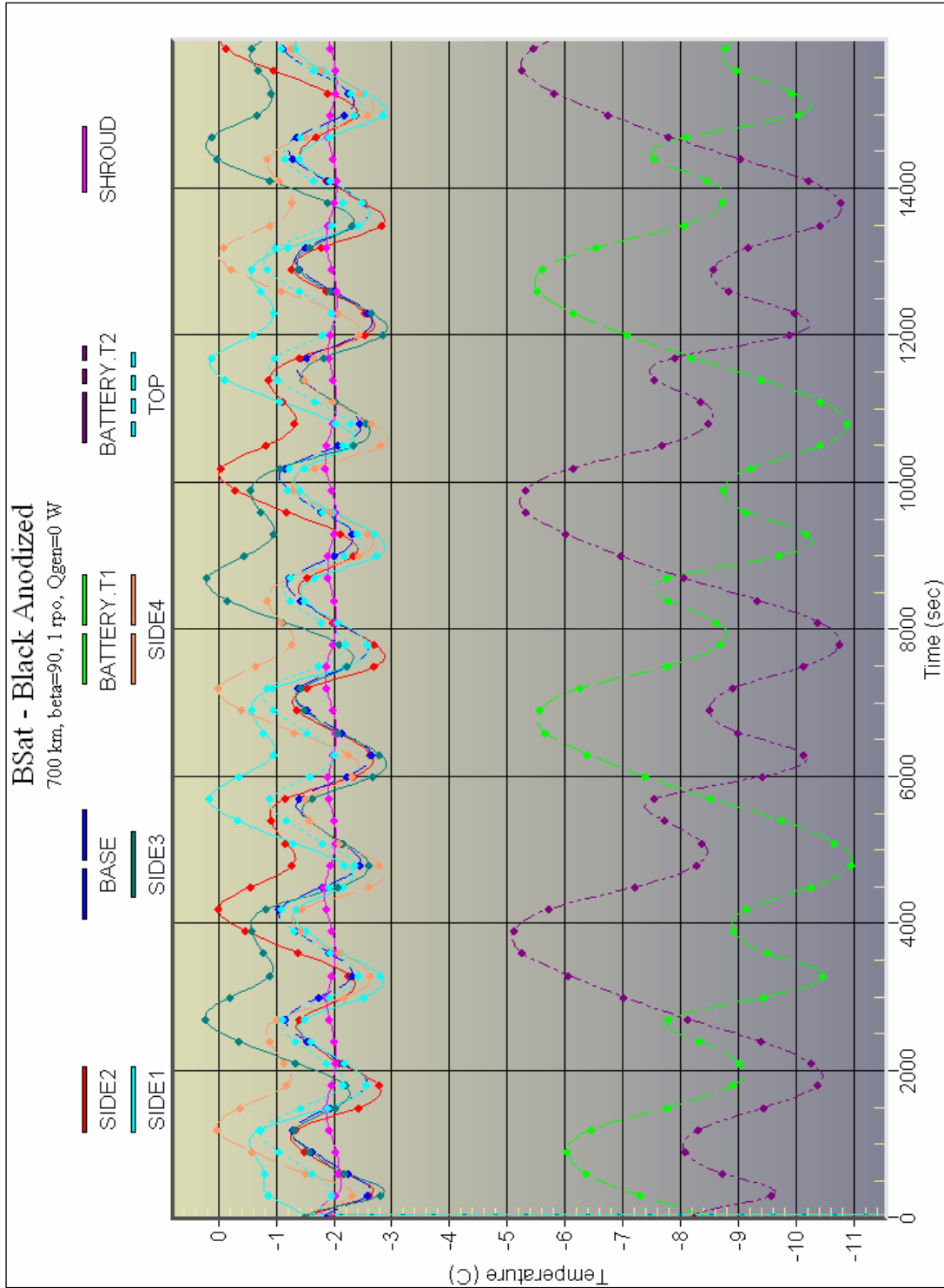


Figure 6-35: BSat (Black Anodized): 700 km, $\beta=90^\circ$, 1 rpo, $Q_{gen} = 0W$

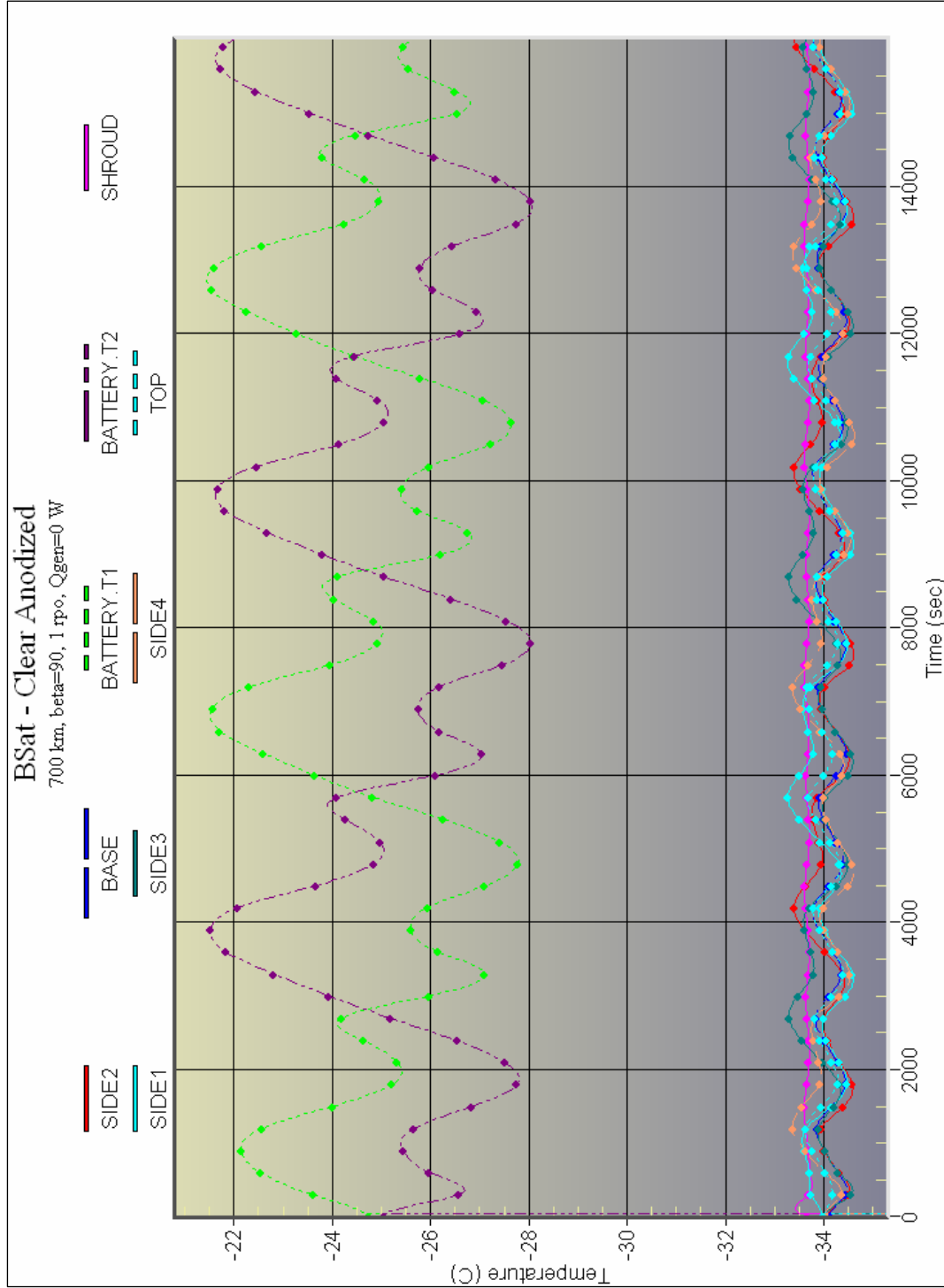


Figure 6-36: BSat (Clear Anodized): 700 km, $\beta=90^\circ$, 1 rpo, $Q_{gen} = 0W$

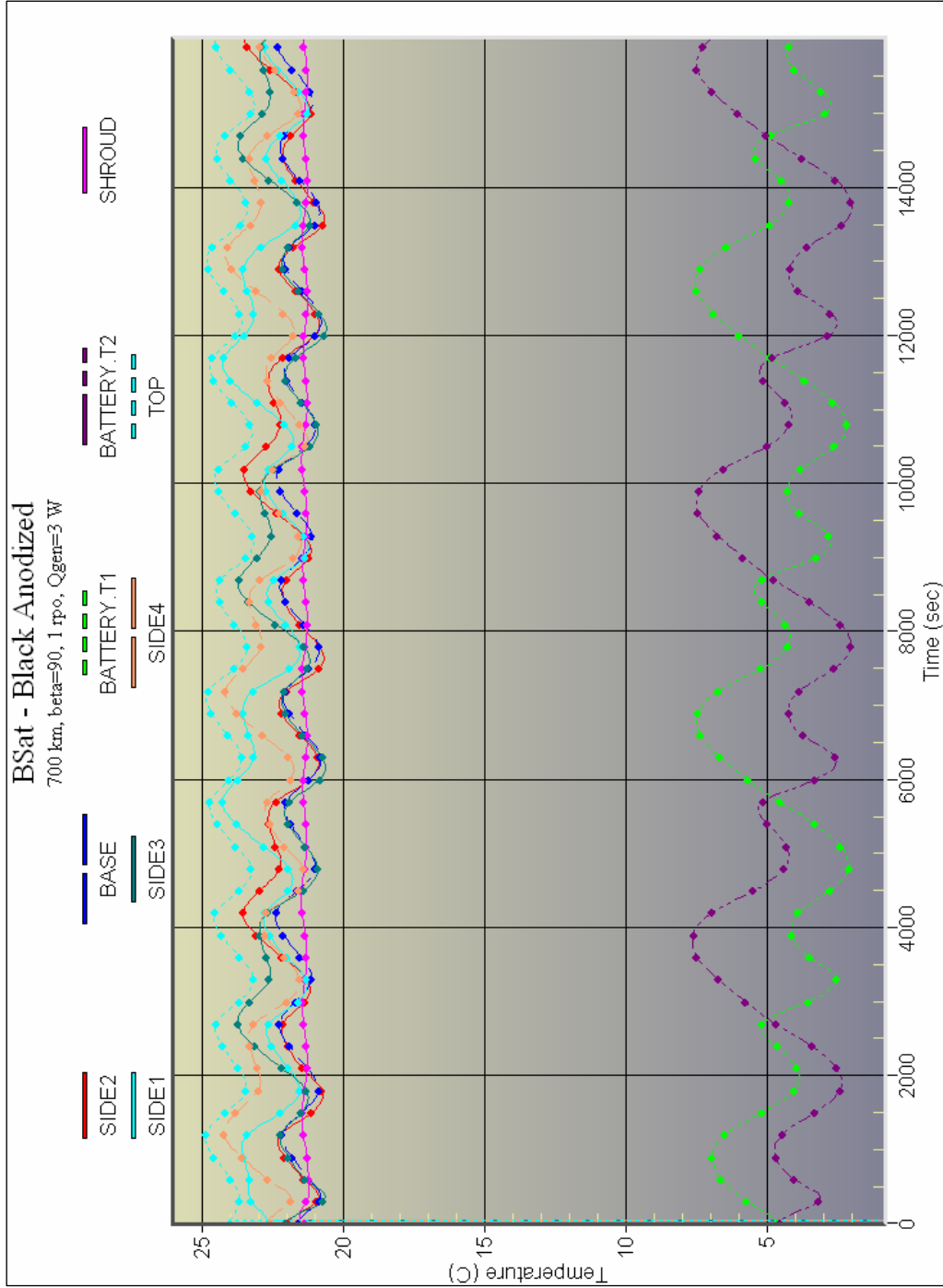


Figure 6-37: BSat (Black Anodized): 700 km, $\beta=90^\circ$, 1 rpo, $Q_{gen} = 3W$

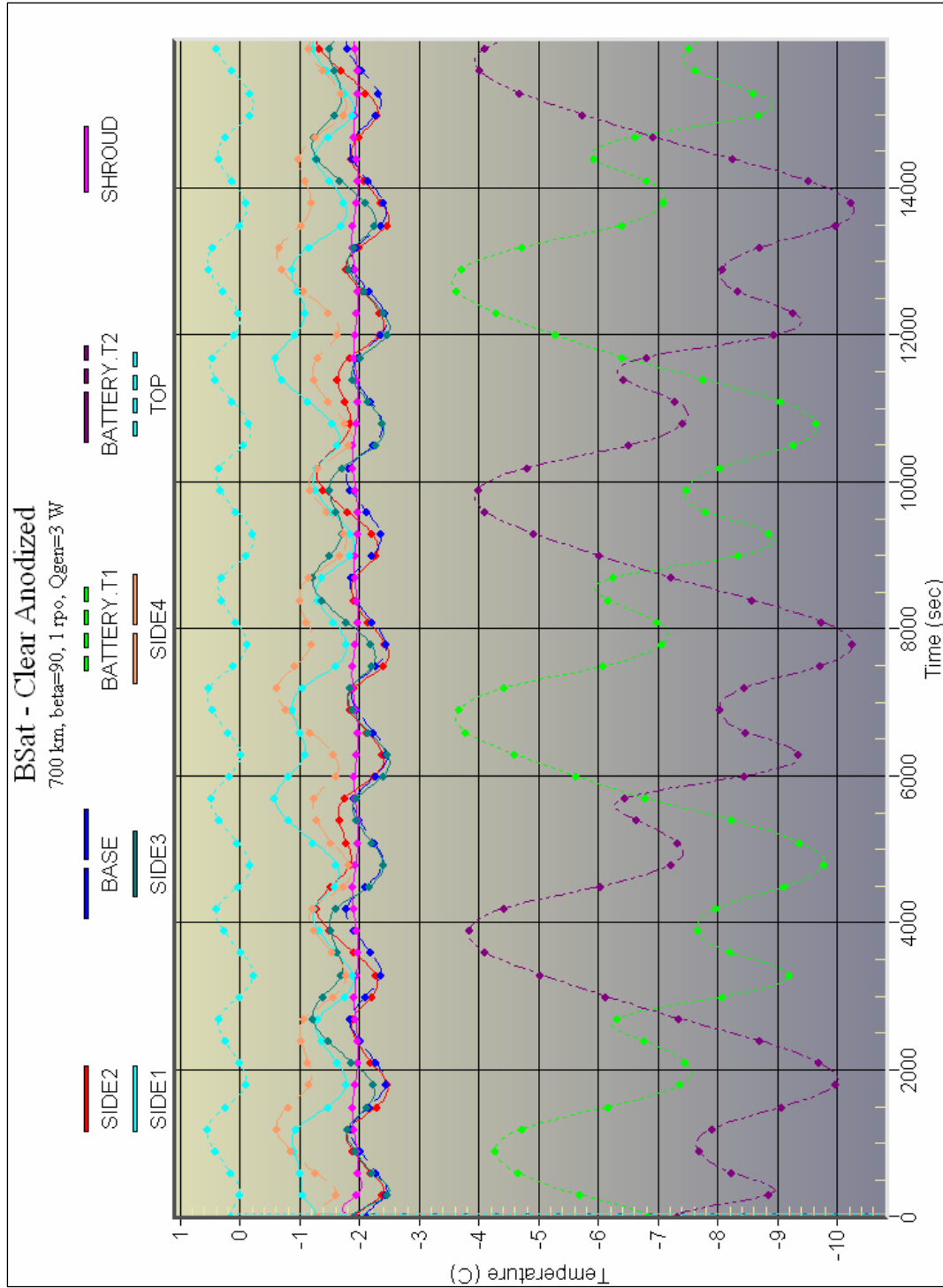


Figure 6-38: BSat (Clear Anodized): 700 km, $\beta=90^\circ$, 1 rpo, $Q_{gen} = 3W$

Thermal Stress

As the external surfaces of the satellite interact directly with environmental radiation, it is expected that these materials will expand when heated and contract when cooled. The various materials that make up a spacecraft expand and contract by different amounts as the temperatures change; thus, they develop stresses due to incompatible *coefficients of thermal expansion* (CTE). The CTE is a proportionality constant which relates thermal strain to a temperature change. The application of Hooke's law provides the following stress relations for a homogeneous, isotropic material:

$$\begin{aligned}
 f_x &= \frac{E\nu(\varepsilon_x + \varepsilon_y + \varepsilon_z)}{(1+\nu)(1-2\nu)} + \frac{E\varepsilon_x}{1+\nu} - \frac{E(\text{CTE})\Delta T}{1-2\nu} \\
 f_y &= \frac{E\nu(\varepsilon_x + \varepsilon_y + \varepsilon_z)}{(1+\nu)(1-2\nu)} + \frac{E\varepsilon_y}{1+\nu} - \frac{E(\text{CTE})\Delta T}{1-2\nu} \\
 f_z &= \frac{E\nu(\varepsilon_x + \varepsilon_y + \varepsilon_z)}{(1+\nu)(1-2\nu)} + \frac{E\varepsilon_z}{1+\nu} - \frac{E(\text{CTE})\Delta T}{1-2\nu}
 \end{aligned} \tag{6.2}$$

were f_i and ε_i are the strains and stresses in the i -th direction, respectively, ν is Poisson's ratio, E is Young's modulus, and ΔT is the change in temperature. Because of complex geometry and nonuniform temperatures, COSMOS was employed to solve these equations as they pertain to BSat's solar panels.

Since both types of aluminum encompassing BSat have an identical CTE, this analysis was limited to the exterior mounted solar panels. The simplification made here also assumes that the affected solar panels are isolated from the rest of the structure and

that worst-case temperatures are applied to the exterior of the panel relative to a reference temperature of 25°C. The worst-case temperatures as obtained from the SINDA analysis are presented in the Table 6-6.

Table 6-6: BSat Temperature Extremes

	Temperature [°C]	Orbit / Surface Finish
Hot Case	37	beta=68.4°/Black Anodized
Cold Case	-35	beta=0°/ Clear Anodized

When considering the behavioral response of the solar panel thru-holes under a temperature gradient, the fastener itself to prevent translation expansion and contraction of the panel surface opposing the exposed surface. On a figure of merit, the CTE of aluminum is rated with respect to a temperature range where the effect of thermal expansion becomes significant at temperatures exceeding the boundaries of 20°C and 100°C [Hansman, 2003]. The results from this analysis included determining the thermal stress, the displacements, and the margin of safety; all appear in Table 6-7 in relation to the temperature extremes provided above.

Table 6-7: Solar Panel Thermal Stress Results

	Max Thermal Stress [MPa]	Max Displacement [mm]	Minimum Margin of Safety
Solar Panel at 37.0°C	91	.036	3
Solar Panel at -35.0°C	250	.17	1.2

The results of this analysis reiterate the severity of exceeding the temperature limits stated above; thermal expansion remains minimal because the applied temperature of 37°C is within the limits, while thermal contraction reveals severe effects mostly likely a

result of the applied -35°C exceeding these empirical limits. However, there is no cause for concern here considering that ductile materials seldom rupture or buckle solely from a single application of thermal stress. Also the temperatures imposed for this analysis are conservative over-estimates for the true temperatures likely to exist on the exterior surfaces. Figure 6-39 depicts the conditions imposed on the solar panel. The green arrows represent fixed constraints imposed on the six mount holes, and the steady-state temperature of Table 6-6, marked with blue rods, was distributed on the external surface. The two pictures on the right are the thermal stress distribution and the corresponding deformation.

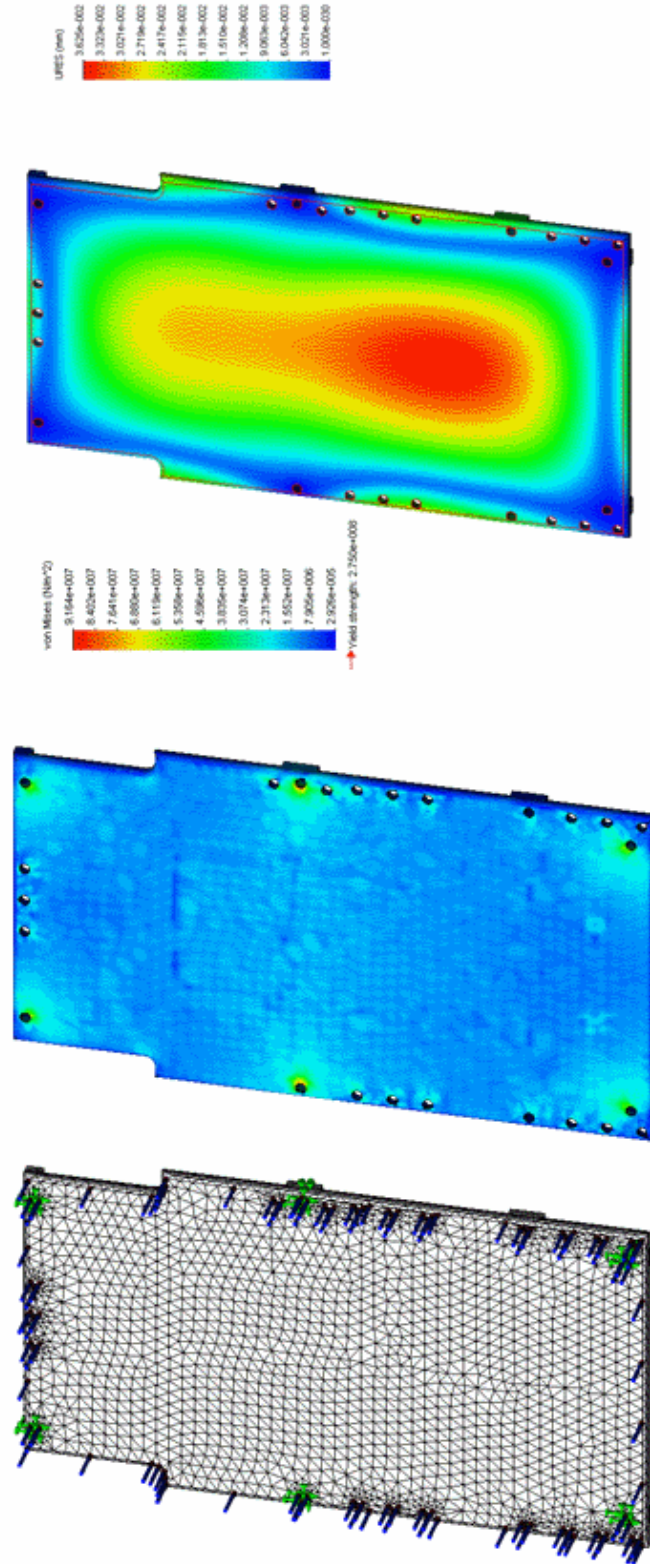


Figure 6-39: Solar Panel Thermal Stresses; Hot Case

Results and Conclusions

The objective of this analysis was to investigate the thermal environment of BSat for a variety of imposed conditions. Using the temperature data exported from SINDA the temperature distributions throughout the satellite were determined concurrently with complete orbit cycles. It was important to verify the numerical analysis with the construction of a simplified thermal model allowing for analytical solutions to verify the numerical results. A complete list of results follows:

1. Temperature profiles for the three beta angles investigated reveal that BSat is most suited for the application of a black-anodized finish.
2. For the nadir-pointing, passive attitude of the satellite, the maximum beta angle corresponding to a complete sunlit orbit produces lower satellite temperatures when compared with $\beta=68.4^\circ$; this is a result of the apparent *projected area* as seen by the Sun.
3. A nominal orbit for BSat has been selected with an inclination of 45° . At this inclination and with black anodize surface finish, the onboard batteries remain within a satisfactory temperature range.
4. The behavioral characteristics of the satellite were quantified by implementing the significant thermal masses of the satellite: the tether shroud and both secondary batteries. Including these entities in the thermal model helped to visually inspect the thermal simulations for errors and correlations. While the batteries responded

quite similar to the temperature profile of the satellite, the shroud exhibited a thermal time-lag; a result of utilizing the Halpin-Tsai approximation and the rule of mixtures to determine its thermophysical properties. With the shroud present within the satellite, the global temperatures tend to remain lower than in its absence. The absolute temperature difference when excluding BSat's tether payload results in temperatures which are approximately ten degrees higher, again a cause of the shroud's thermal capacity.

5. The SINDA plots show battery temperatures that are questionably lower than the temperature of the structure. Although the differences are small in terms of their values, it was expected that the magnitude of the batteries temperatures would lie amongst the temperatures of the structure. The possible cause of this could be a thermal modeling error in which internal radiation was neglected. However, the temperature profiles of the batteries follow the generic trend of the sides which it is next to; this is because the battery was linked to their sides by a contact conductor. While the ability to conduct heat remains small, including internal radiation is expected to bring the temperature of the batteries in closer vicinity of the structure.
6. To appropriately construct a SINDA model, a calorimeter experiment was performed on BSat's secondary batteries to determine their specific heat. The value obtained by this experiment was input manually into the SINDA thermal model.

7. The temperature response of the battery when enduring different charging and discharging currents was obtained by performing another experiment that allowed for user-defined rates. The results of this experiment show that while the increase in the battery's temperature increases slightly, it was omitted from the thermal analysis to provide a conservative estimate of the true temperatures expected during flight. It is highly likely that during in-situ telemetry monitoring that the temperatures of the batteries can be correlated to the data obtain empirically through further environmental testing.
8. As a last consideration the absolute extreme temperatures recorded from this analysis were applied to BSat's exterior mounted solar panels. Considering that these interact directly with the incident radiation it is understood that they would be most susceptible to thermal stresses. While the values for thermal expansion remained within the predefined threshold for aluminum, the thermal contractions did not and produced significantly lower margins of safety.
9. Further assessments were not possible at this time. Upon environmental testing new insights will be gained on the mechanical performance characteristics of the satellite.
10. The antenna housing was omitted from this assessment because it is still in development. When it has materialized, it is suggested that the antenna assembly be thermal cycled to ensure proper allowances for thermal contraction. These

results should not be surprising considering that the baseplate cavity was taken directly from the flight-qualified MEROPE design.

11. The self-heating of the battery has been quantified and determine insignificant to include in the thermal model.
12. However, under the presumed *natural* spin rate of 1 rpo, the cavities within the tophat have been determined to thermally cycle evenly. In the likelihood that BSat will not rotate while on-orbit, it is recommended that careful attention be addressed on the state-of-temperature of the battery in-situ.
13. It is recommended that SSEL obtain a thermal-vacuum chamber for readily testing space hardware in the expected thermal environments of space.

7. RESULTS, CONCLUSIONS, and FUTURE WORK

With the conclusion of this thesis comes an opportunity to summarize the iterative processes and analytic routines employed in the mechanical design of the picosatellite, BSat. Its procurement and problem statement are governed by the orbital debris concern and a technology demonstration mission to test two enabling technologies: the RocketPod™ and the EDT. As cost is a fundamental limitation to nearly all space missions, the CubeSat Plus architecture of BSat is marketed by the desire of smaller and more compact test platforms for operations in LEO. In the preceding sections the assessment of BSat's mechanical systems are summarized.

Structure

The structural design of BSat is fundamentally governed by the P-Pod and RocketPod™ ICDs, and then by the requirements which flowed down from the mission's top-level requirements. Structural analysis was systematically conducted by first simplifying the satellite's geometry for analytical computations and then by performing a series of FEM analyses utilizing the numerical computational package, COSMOS. BSat's structural response to acoustics, or random vibrations, was limited to geometries of flat plates while its response to quasi-static loading and harmonic vibrations was quantified in its physical geometry with COSMOS. The iterative history of BSat was omitted from this these; however, is available in SSEL's certification logs which document the design and analysis processes.⁶⁸

⁶⁸ i.e. *orange notebooks available in SSEL's SOC (Space Operations Center)*

Success iterations lead to a more detailed, better defined space mission concept. But we must still return regularly to the broad mission objectives and search for ways to achieve them at lower cost. [Wertz and Larson, 1999]

This statement is not taken lightly and is used philosophically as a foundation for work conducted on all aspects of a satellite's development. The following listed results have been taken directly from chapter five:

1. The harmonic vibrations of all structural members surpass the fundamental frequency requirement of 35 Hz in both the axial and lateral directions.
2. The simplified structure was analyzed dynamically for vibroacoustic response. Both the baseplate and FR4 board are sufficient in strength to accommodate the SPL levels of the Delta II LV. The dynamic analysis was simplified to that of the dynamics of a flat plate because of the highest surface area to mass ratio. This analysis was conducted under small-deflection theory in which both parts were verified not to deflect greater than half their thicknesses.
3. The acoustic vibrations appear to induce the most critical dynamic response. In this case, the maximum deflections at the center of the plate were observed to occur at the entities fundamental frequency. It is recommended that components mounted at the center of these plates be appropriately bonded and inspected after environmental testing.

4. Comparison of analytical and FEM solutions for the simplified geometry are within 10%, a value that is acceptable and builds confidence in the FEM solutions pertaining to the physical structure.
5. The physical structure was examined against a strain-energy convergence criterion that systemically calculated the elemental stress values and their deviation from the corresponding nodal stress value. Plotted results are available in Appendix C.4. In most cases there existed outlier elements with large error values; therefore, they were omitted and attention was instead addressed to the critical stress areas.
6. The critical members of the structure in a static sense are the battery brackets and tether bracket. These members are critical in bending and bearing, respectively. The high stress concentrations are relatively localized where effort was made to resolve mesh conflicts and error convergence. In both cases the margin of safety is acceptable and is a conservative estimate.
7. The structure will not experience a high enough load during any phase of the mission to experience linear buckling of any components.
8. The induced stress by both the dynamic and static loading are well within the yield strength of Al-6061-T6 with acceptable margins of safety. However, to

satisfy the RocketPod™ requirement the four sides which interface directly with the deployer must be fabricated from Al-7075-T6.

9. TUI has stated that a torsional spring will be incorporated into their deployment spool which is meant to gradually decrease the unwinding rate when the tether approaches its full length. For this reason, shock analysis was omitted from this investigation.
10. All structural parts are intended to be surface-treated upon fabrication. This process has been conducted by Sonju Inc. of Kalispell, MT. For masking instructions refer to the *orange notebook* documentation of the tether bracket.
11. BSat's manufacturing cost table is available in Appendix C.6 and was obtained from Montana Tech who was responsible for the fabrication. It is intended that this cost is retained with the fabrication of BSat's flight structure, and that the CNC code can be manipulated to reflect the specifications as outlined in Appendix A.
12. With final assembly it is recommended that the preload on all the satellite's fasteners be addressed to ensure proper tightening.

BSat's RF antenna cassettes are currently under development and it is recommend that its design be scrutinized with significant environmental testing as it pertains to the satellite as a whole. The deployment sequence has already been observed to *stick* within the confines of the tophat, and that the radii owing to the fishing-line groove are anticipated

to cause breakage problems during shake. These two issues must be resolved and should be effectively documented.

Thermal

There are many characteristics of the satellite that require the assessment of the in-situ thermal environment. Because the exact orbit is currently undefined and will ultimately depend on the primary payload, BSat's thermal environment was evaluated on a parametric basis which included the spectrum of beta angles and plausible surface finishes. Utilizing SINDA and Thermal Desktop, the assessment scheme systematically revealed a black-anodizing finish for all orbits. Environmental testing will further verify the conclusions made in chapter six and should be conducted with TUI's tether system installed. It has been observed that because of the high specific heat of the shroud, the satellite's temperature is approximately 10 °C lower with the tether shroud inside the satellite. Therefore, thermal testing the satellite in the absence of the shroud will result in values that are significantly higher than would actually occur. Due to the uncertainty in the exact orbit, it is recommended that chapter six be used as a guide in selecting the appropriate surface finish under the presumed tether payload. For this reason, surface treatment on the flight unit should be queued until testing is accomplished on the current EDU and a physical tether system. The conclusions of BSat's thermal characteristics are listed below:

14. Temperature profiles for the three beta angles investigated reveal that BSat is most suited for the application of a black-anodized finish.

15. For the nadir-pointing, passive attitude of the satellite, the maximum beta angle corresponding to a complete sunlit orbit produces lower satellite temperatures when compared with $\beta=68.4^\circ$; this is a result of the apparent *projected area* as seen by the Sun.
16. A nominal orbit for BSat has been selected with an inclination of 45° . At this inclination and with the black anodized surface finish, the onboard batteries remain within a satisfactory temperature range.
17. The behavioral characteristics of the satellite were quantified by implementing the significant thermal masses of the satellite: the tether shroud and both secondary batteries. Including these entities in the thermal model helped to visually inspect the thermal simulations for errors and correlations. While the batteries responded quite similar to the temperature profile of the satellite, the shroud exhibited a thermal time-lag; a result of utilizing the Halpin-Tsai approximation (see equations on page 91) and the rule of mixtures to determine its thermophysical properties. With the shroud present within the satellite, the global temperatures tend to remain lower than in its absence. The absolute temperature difference when excluding BSat's tether payload results in temperatures which are approximately ten degrees higher, again a cause of the shroud's thermal capacity.
18. The SINDA plots show battery temperatures that are questionably lower than the temperature of the structure. Although the differences are small in terms of their values, it was expected that the magnitude of the batteries temperatures would lie

amongst the temperatures of the structure. The possible cause of this could be a thermal modeling error in which internal radiation was neglected. However, the temperature profiles of the batteries follow the generic trend of the sides which it is next to; this is because the battery was linked to their sides by a contact conductor. While the ability to conduct heat remains small, including internal radiation is expected to bring the temperature of the batteries in closer vicinity of the structure.

19. To appropriately construct a SINDA model, a calorimeter experiment was performed on BSat's secondary batteries to determine their specific heat. The value obtained by this experiment was inputted manually into the SINDA thermal model.
20. The temperature response of the battery when enduring different charging and discharging currents was obtained by performing another experiment which allowed for user-defined rates. The results of this experiment show that while the increase in the battery's state of temperature increases slightly, it was omitted from the thermal analysis to provide a conservative estimate of the true temperatures expected during flight. It is highly likely that during in-situ telemetry monitoring that the temperatures of the batteries can be correlated to the data obtain empirically through further environmental testing.
21. As a last consideration the absolute extreme temperatures recorded from this analysis were applied to BSat's exterior mounted solar panels. Considering that

these interact directly with the incident radiation it is understood that they would be most susceptible to thermal stresses. While the values for thermal expansion remained within the predefined threshold for aluminum, the thermal contractions did not and produced significantly lower margins of safety.

22. Further assessments were not possible at this time. Upon environmental testing new insights will be gained on the mechanical performance characteristics of the satellite.
23. The antenna housing was omitted from this assessment because it is still in development. When it has materialized, it is suggested that the antenna assembly be thermal cycled to ensure proper allowances for thermal contraction. These results should not be surprising considering that the baseplate cavity was taken directly from the flight-qualified MEROPE design.
24. The self-heating of the battery has been quantified and determine insignificant to include in the thermal model.
25. However, under the presumed *natural* spin rate of 1 rpo, the cavities within the tophat have been determined to thermally cycle evenly. In the likelihood that BSat will not rotate while on-orbit, it is recommended that careful attention be addressed on the state-of-temperature of the battery in-situ.
26. It is recommended that SSEL obtain a thermal-vacuum chamber for readily testing space hardware in the expected thermal environments of space.

The documentation provided by this thesis in its entirety is expected to be used as a guide for further work in the area of BSat's mechanical systems. In the event that BSat is adapted for P-Pod deployment, the lingering question of the tether payload remains essential for predicting the satellite's thermal response. This possibility makes all of BSat's systems vulnerable for change and should be avoided in future BSat configuration management decisions. In conclusion, Wertz and Larson philosophically state:

Although we must maintain orderly progress, we must also review the mission design regularly for better ways to achieve the mission objectives...Methods may change as a result of evolving technology, a new understanding of the problem, or simply fresh ideas and approaches as more individuals become involved. [Wertz and Larson, 1999]

The design and analysis of BSat as outlined in this thesis are based upon requirements that have been defined and that were used throughout this assessment study. This documentation is a result of many agreements with the project's industry partners and the objectives as currently defined by BSat's interdisciplinary team. Any modifications should begin with these requirements and should be evaluated at the system level.

REFERENCES CITED

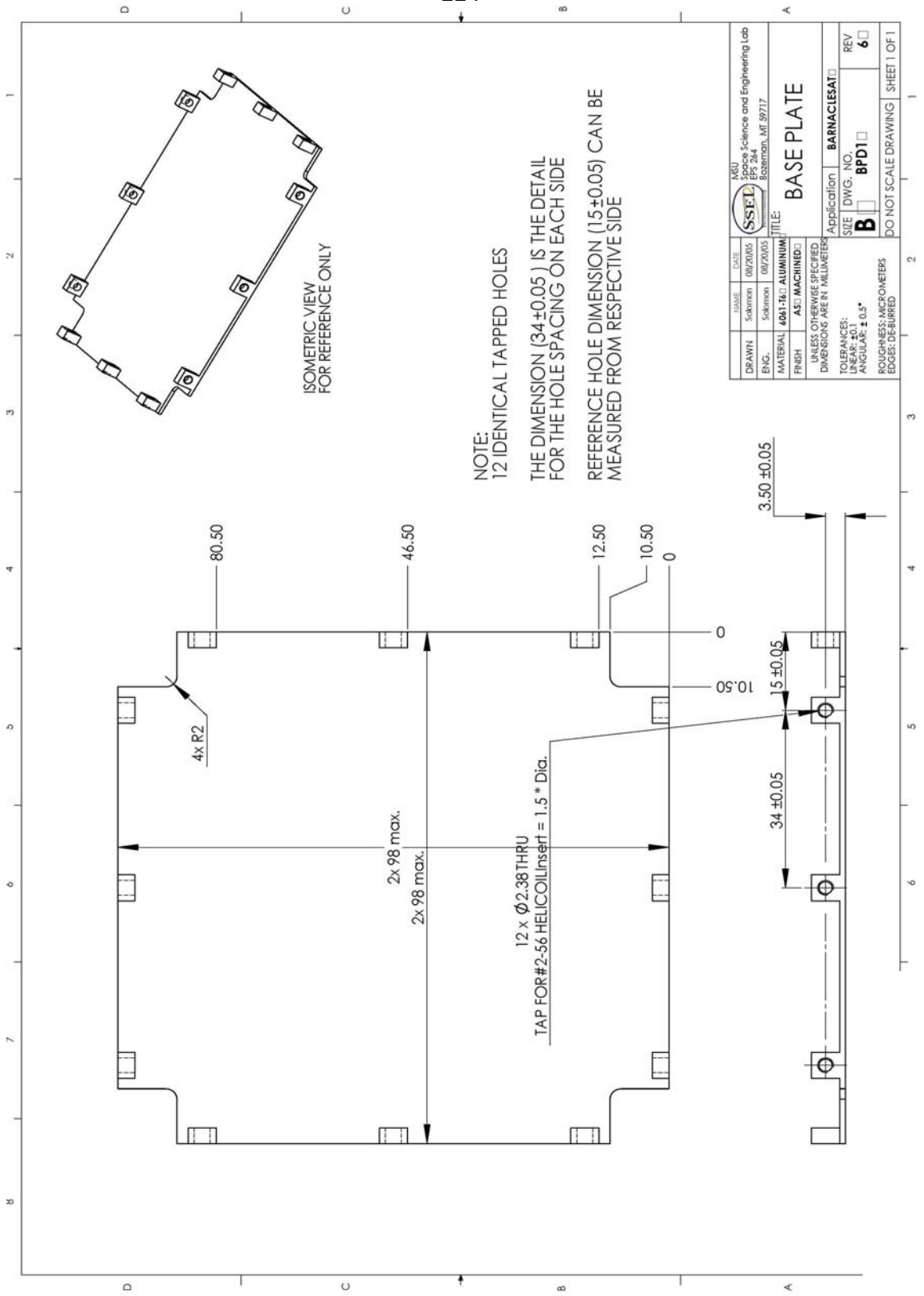
- Barbero, E., (1999). *Introduction to Composite Materials Design*. Taylor & Francis, Inc.
- Baumann, R., (1996). *Structural and Mechanical, Section 2.4. General Environmental Verification Specification for STS & ELV Payloads, Subsystems, and Components*. NASA Goddard Space Flight Center.
- Bleier, T., et al. (2004). *QuakeSat Lessons Learned: Notes from the Development of a Triple CubeSat*. Publication of QuakeFinder, LLC.
- CubeSat (2005). *CubeSat Introduction*. <http://cubesat.calpoly.edu/>
- Duran, D., (1999). *Thermal Final Design Review*. Spartnik Microsatellite Project.
- Forward, R., R. Hoyt, (1998). *Application of the Terminator Tether™ Electrodynamic Drag Technology to the Deorbit of Constellation Spacecraft*. AAIA publication.
- Futron Corporation, (2002). *Space Transportation Costs: Trends in Price Per Pound to Orbit 1990-2000*. In White Paper at <http://www.futron.com/>
- Gere, L., (2001). *Mechanics of Materials (5th ed)*. Brooks/Cole of Thomas Learning
- Gilmore, D., (2002). *Spacecraft Thermal Control Handbook, V.1: Fundamental Technologies*. The Aerospace Corporation.
- Hansman, S., (2003) *In-Orbit Thermal Analysis of BLUESat*. The University of New South Wales. School of Mechanical and Manufacturing Engineering.
- Heidt, H., J. Puig-Suari, A. S. Moore, S. Nakasuka, R. J. Twiggs, (2000). *CubeSat: A New Generation of Picosatellite for Education and Industry Low-Cost Space Experimentation*. In 14th Annual/USU Conference on Small Satellites.
- Motorola Data Sheet (2005). <http://www.motorola.com>.
- Incropera, F., Dewitt, D., (1996). *Introduction to Heat Transfer (3rd ed)*. John Wiley & Sons.
- JED Connector (2005). *JST website*. <http://www.jst.co.uk/index.php>
- Logan, D., (2000). *A First Course in the Finite Element Method (3rd ed)*. Wadsworth Group, Brooks/Cole.

- NASA, (1995). *NASA Safety Standard: Guidelines and Assessment Procedures for Limiting Orbital Debris*. NSS 1740.14
- Obland, M., Hunyadi G., et. al. (2001). *The Montana State University NASA Space Grant Explorer-1 Science Reflight Commemorative Mission*. In 15th Annual AIAA/USU Conference on Small Satellites Paper.
- Rao, S., (1995). *Mechanical Vibrations*. Addison-Wesley Publishing Company.
- Sarafin, T., (1995). *Spacecraft Structures and Mechanisms*. Space Technology Series. Microcosm Press.
- Spectrolab (2005). <http://www.spectrolab.com/DataSheets/DJCell/dj.pdf>
- The Boeing Company, (2000). *Payload Environments*. Delta II Payload Planners Guide. MDC 00H0016 Commercial Publication.
- Voronka, N., D. Solomon, D. Caldwell, et al. (2005). *Technology Demonstrator of Standardized Deorbit Module Designed for CubeSat and RocketPod Applications*. In 19th Annual/USU Conference on Small Satellites.
- Wertz, J., W. Larson, (1999). *Space Mission Analysis and Design (3rd ed)*. Space Technology Series. Microcosm Press.
- Young, W., (1989). *Roark's Formulas for Stress and Strain (6th ed)*. McGraw-Hill Inc.
- XSS-10 E-Publication, (2003). <http://www.globalsecurity.org/space/systems/xss.htm>

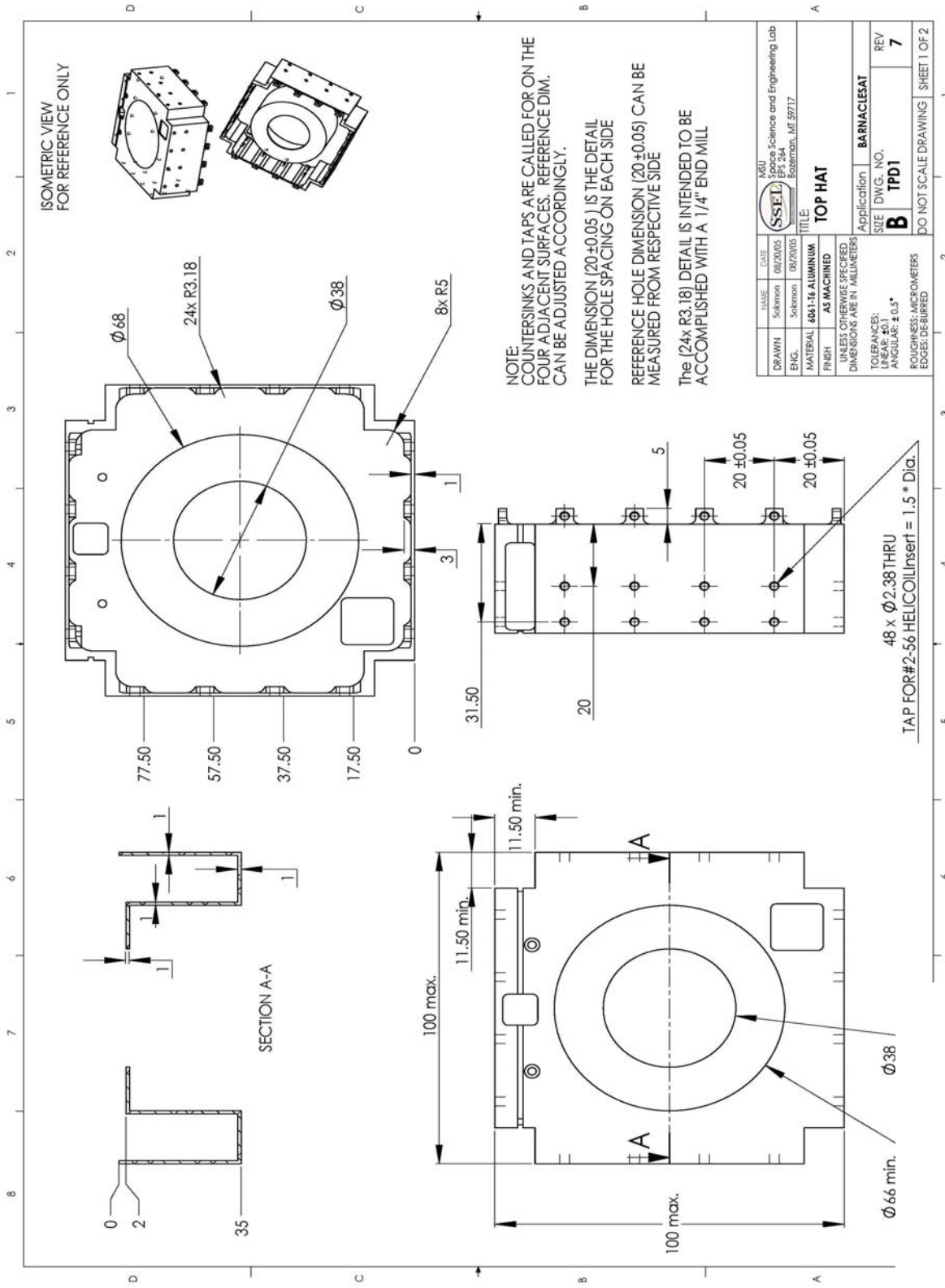
APPENDICES

APPENDIX A

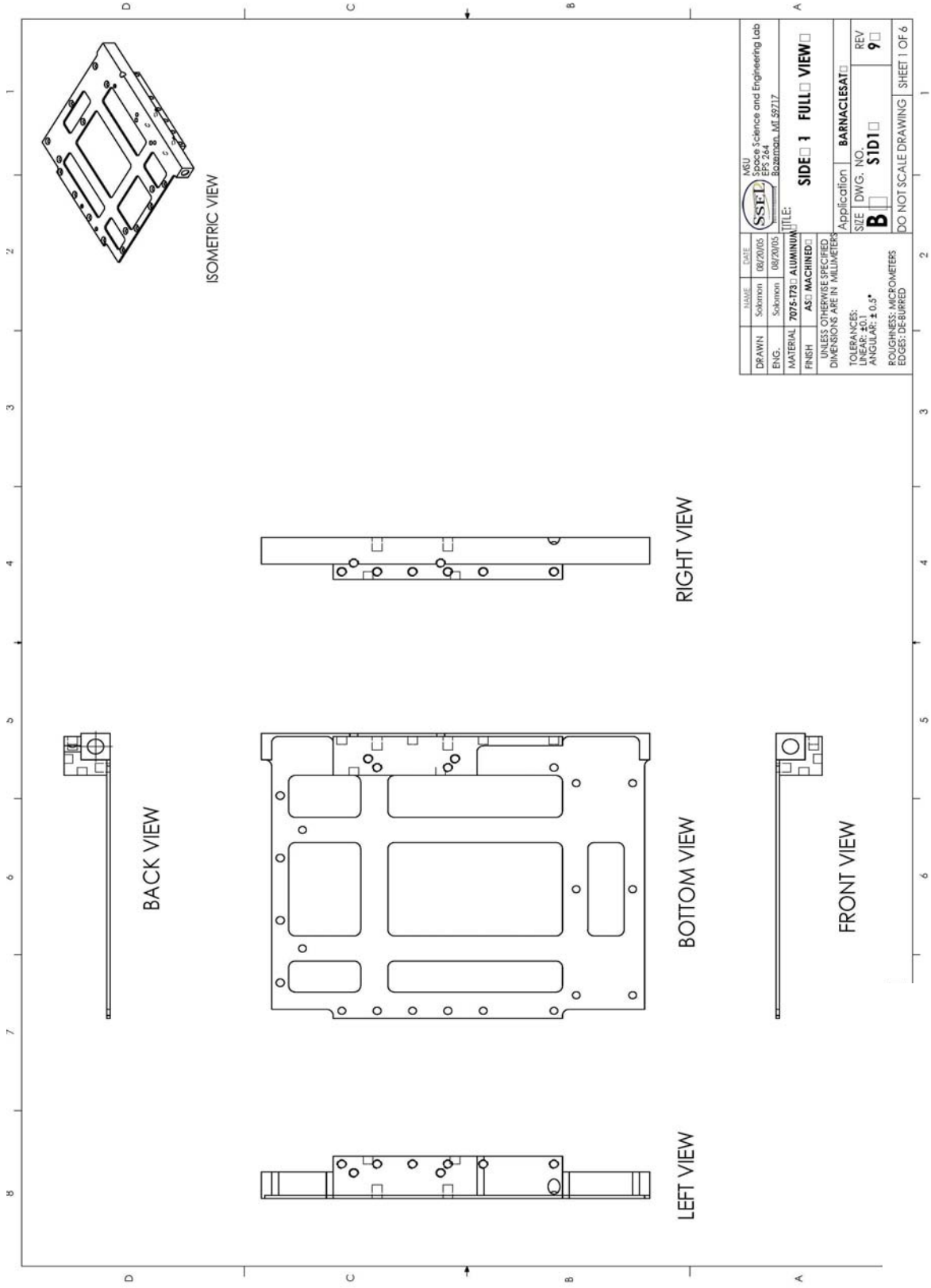
ENGINEERING DRAWINGS



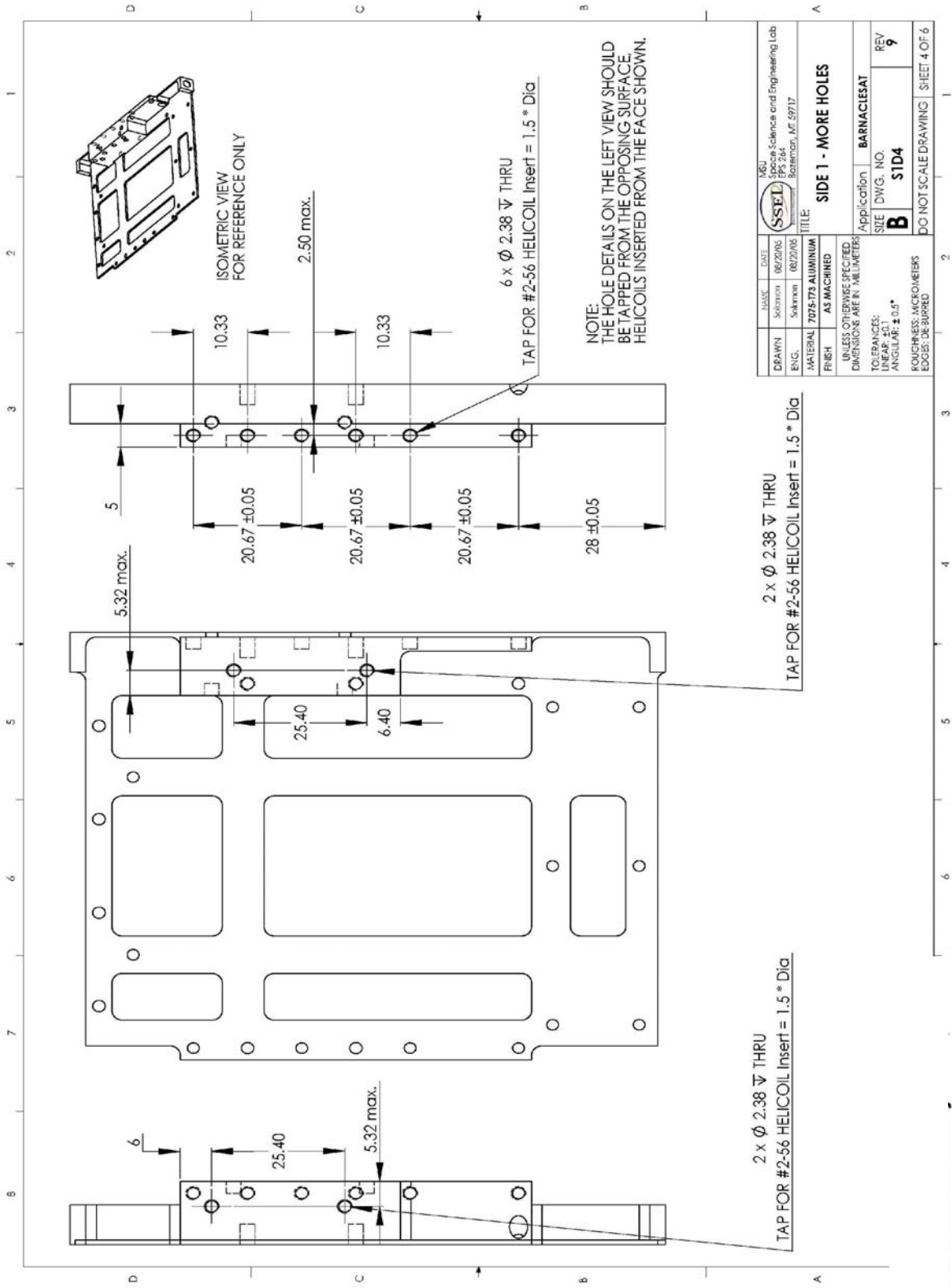
NAME	DATE	MSU	Space Science and Engineering Lab Department of Earth and Planetary Science Boston, MA 02139
DRAWN Sakman	08/20/05	SSFL	
ENG.	08/20/05		Application
MATERIAL	6061-T6 ALUMINUM	TITLE:	BASE PLATE
FINISH	AS: MACHINED	UNLESS OTHERWISE SPECIFIED DIMENSIONS ARE IN MILLIMETERS	BARNACLESAT
TOLERANCES:		LINEAR: ±0.1	SIZE DWG. NO.
ANGULAR: ±0.5°		ROUGHNESS: MICROMETERS	B BPD1
EDGES: DEBURRED		DO NOT SCALE DRAWING	REV 6
			SHEET 1 OF 1



NAME	DATE	 SSEL Science and Engineering Lab 855 244 Roseman, ME 99717
DRAWN	06/20/05	
ENG.	Salomon 06/20/05	
MATERIAL	6061-T6 ALUMINUM	TITLE
FINISH	AS MACHINED	TOP HAT
UNLESS OTHERWISE SPECIFIED DIMENSIONS ARE IN MILLIMETERS		Application
TOLERANCES:		BARNACLESAT
LINEAR: ±0.1		SIZE DWG. NO.
ANGULAR: ±0.5°		B TPD1
ROUGHNESS: MICROMETERS		REV
EDGES: DEBURRED		7
		DO NOT SCALE DRAWING
		SHEET 1 OF 2



MSU Michigan State University Department of Mechanical Engineering Bozeman, MI 49717	MSU Michigan State University Department of Mechanical Engineering Bozeman, MI 49717
NAME: Solomon DATE: 08/20/05 ENG: Solomon MATERIAL: 7075-T73 ALUMINUM FINISH: AS1 MACHINED	DATE: 08/20/05 TITLE: SIDE 1 FULL VIEW
Application: BARNACLESAT	SIZE: B DWG. NO.: STD1 REV: 9
UNLESS OTHERWISE SPECIFIED, DIMENSIONS ARE IN MILLIMETERS TOLERANCES: LINEAR: ±0.1 ANGULAR: ±0.5° ROUGHNESS: MICROMETERS EDGES: DE-BURRED	DO NOT SCALE DRAWING SHEET 1 OF 6



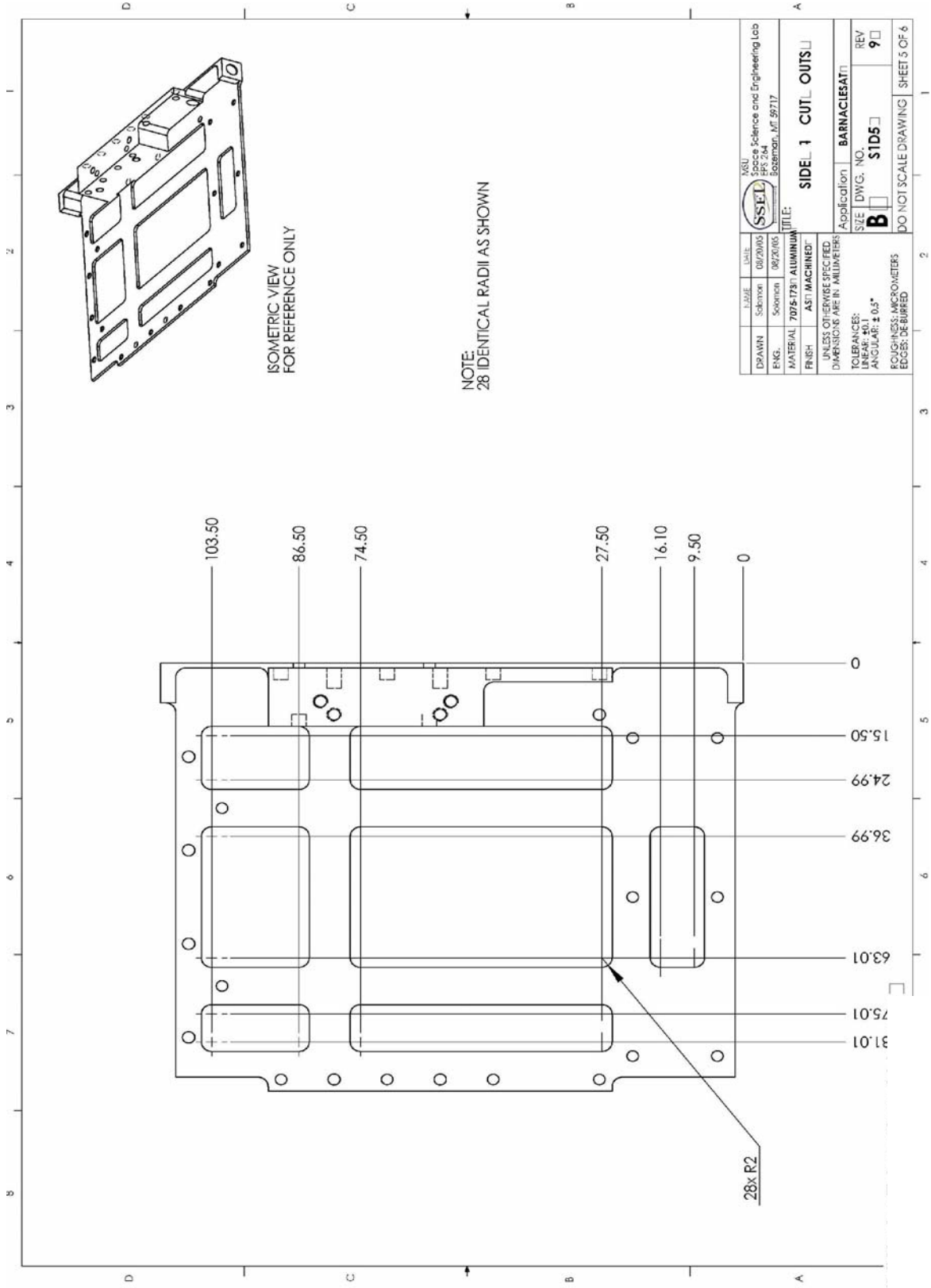
DATE	06/22/05	SCALE	AS MACHINED
DRAWN	Sullivan	MATERIAL	7075-T73 ALUMINUM
ENG.	Sullivan	FINISH	AS MACHINED
UNLESS OTHERWISE SPECIFIED DIMENSIONS ARE IN MILLIMETERS			
TOLERANCES:			
LINEAR: ±0.1			
ANGULAR: ±0.5°			
FINISHES: MICRO METERS			
EDGES: DEBURRED			

Application	BARNACLESAT
SIZE	STD4
REV	9
DO NOT SCALE DRAWING SHEET 4 OF 6	

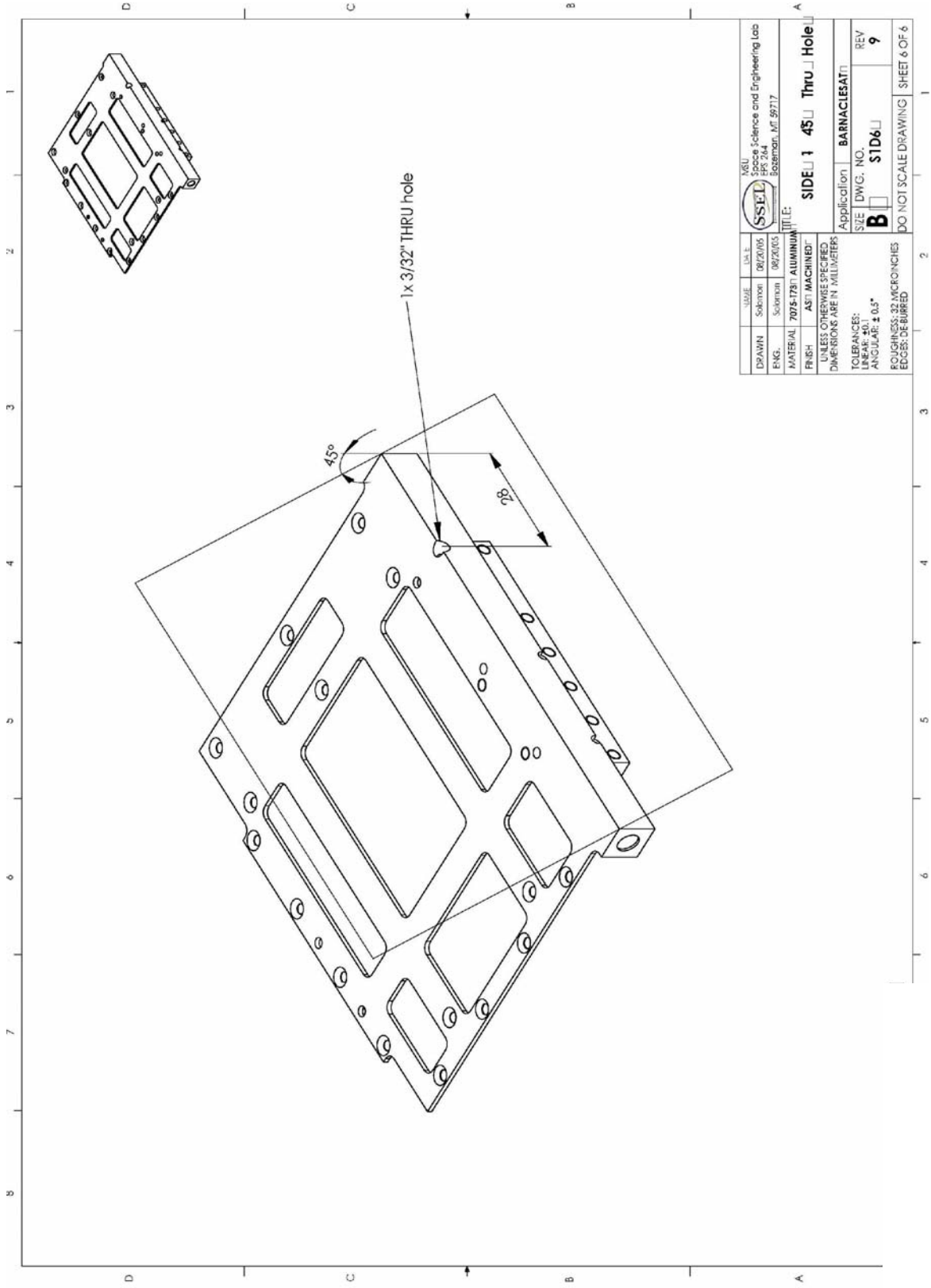
NGU, Science and Engineering Lab
 PK 264
 Boston, MA 02117

SSEL

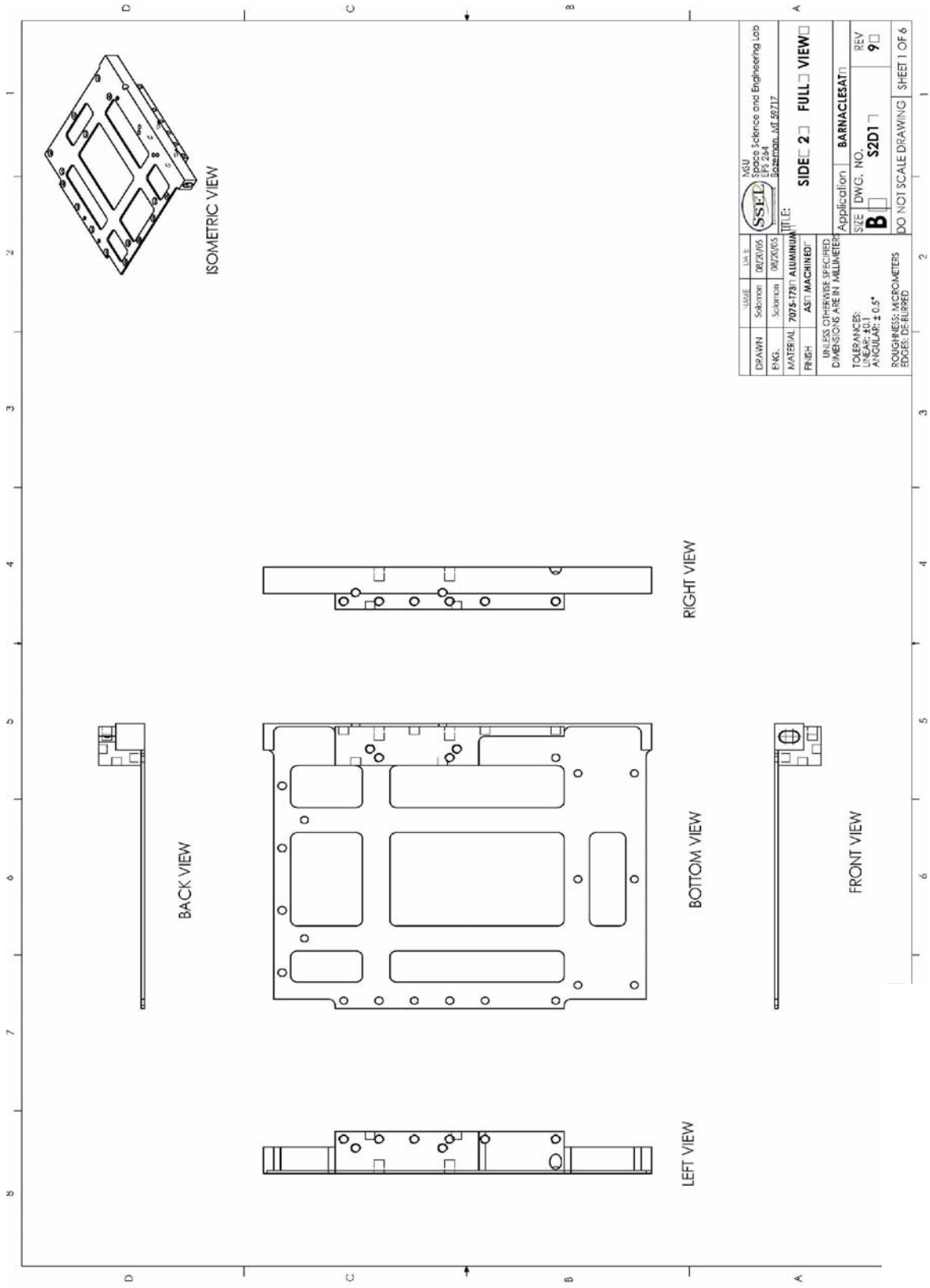
TITLE: **SIDE 1 - MORE HOLES**



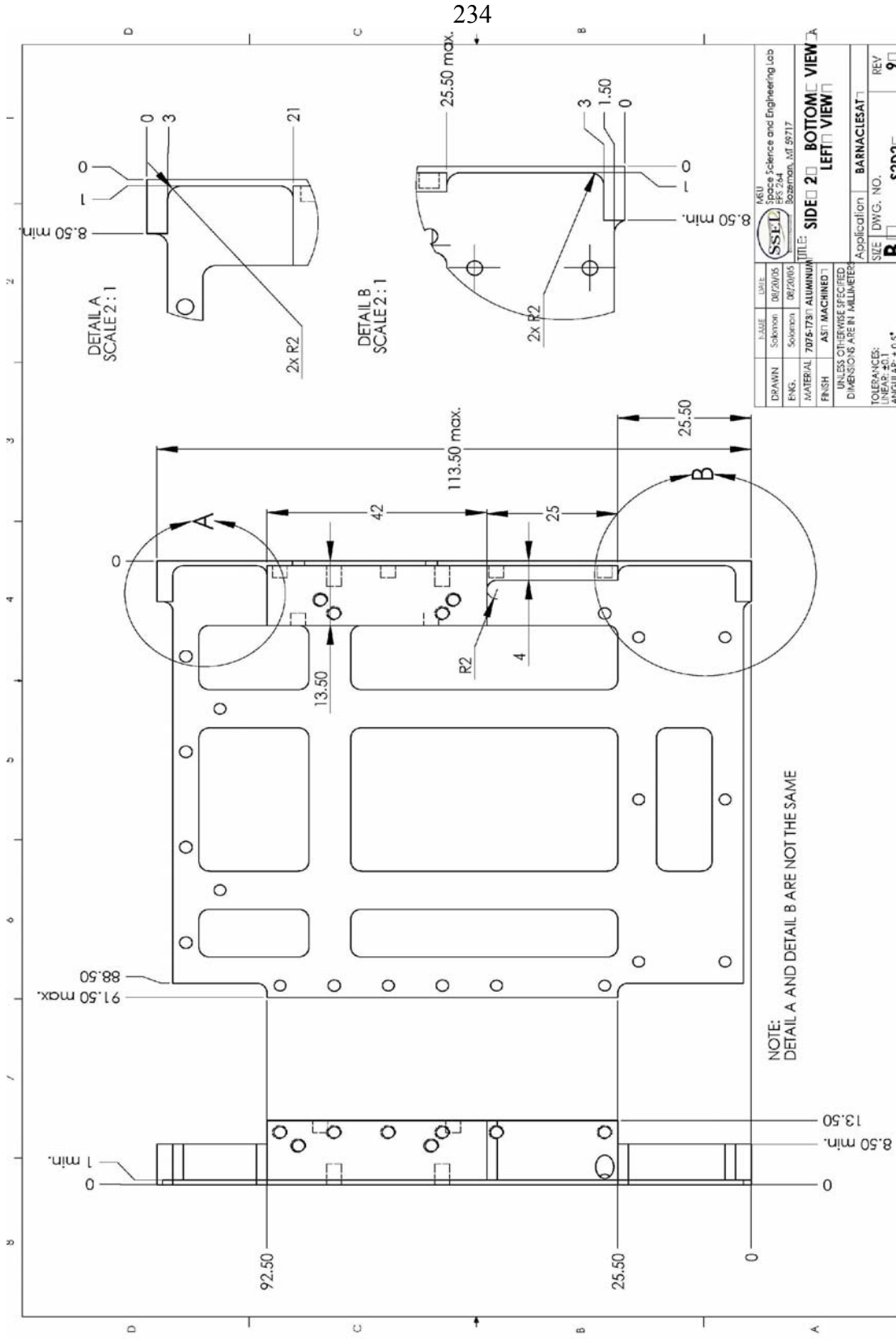
DATE:	08/20/05	SCALE:	1:1
DESIGNED BY:	Sullivan	DRAWN BY:	Sullivan
DATE:	08/20/05	DATE:	08/20/05
ENGINEER:	Sullivan	DATE:	08/20/05
MATERIAL:	7075-T73 ALUMINUM	TITLE:	SIDE_1 CUTL OUTS
FINISH:	AS1 MACHINED	Application:	BARNACLESAT
UNLESS OTHERWISE SPECIFIED DIMENSIONS ARE IN MILLIMETERS			
TOLERANCES:			
LINEAR: ±0.1			
ANGULAR: ±0.5°			
SURFACE FINISH: MICROMETERS			
EDGES: DEBURRED			
SIZE:	DWG. NO. B	REV:	9
SIZE:	S1D5	REV:	9
DO NOT SCALE DRAWING			SHEET 5 OF 6



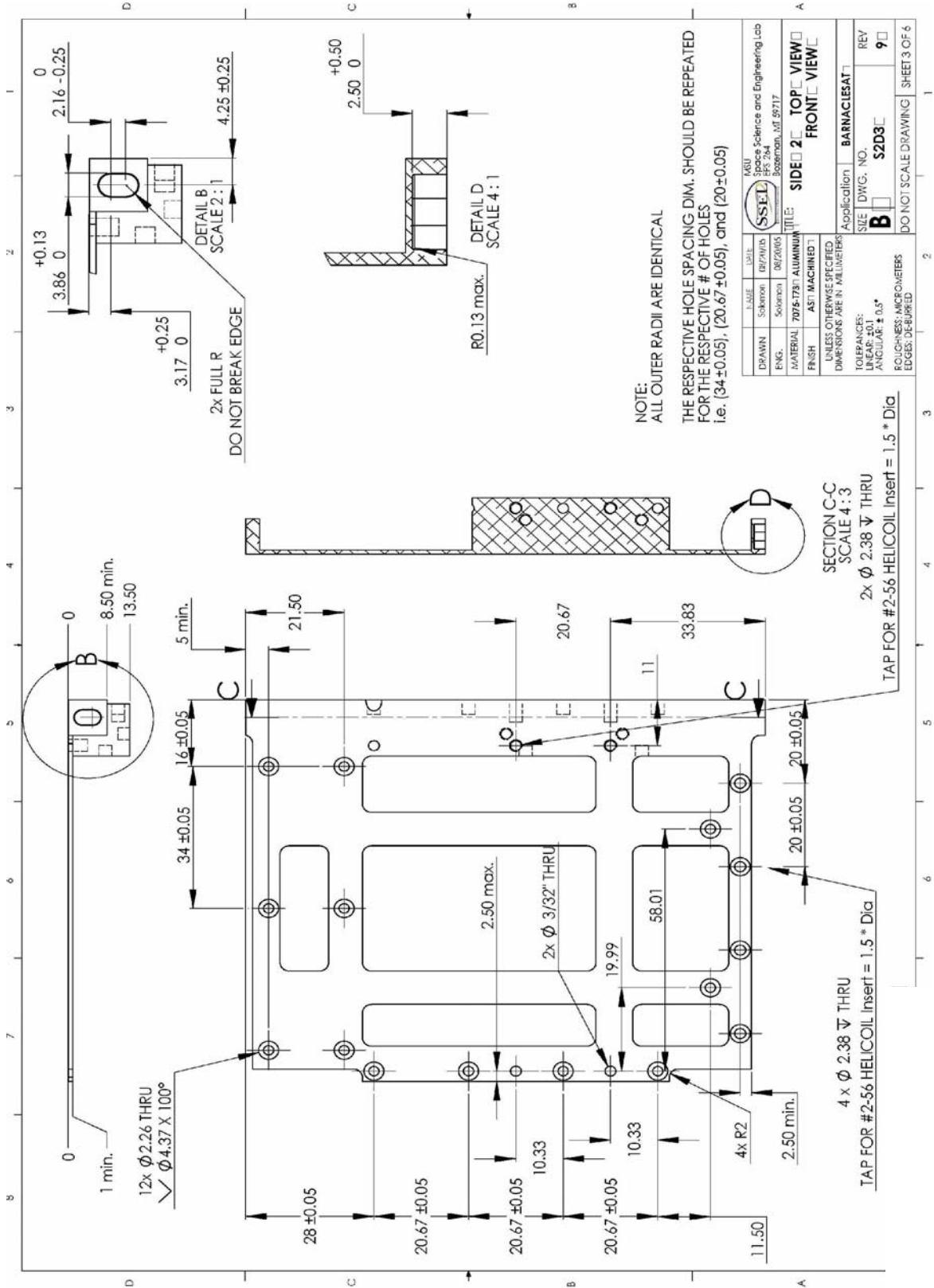
SCALE	DATE	SSEL School of Science and Engineering Lab 85C 264 Eastman, ME 59717	TITLE: SIDE 1 45 Thru Hole
DRAWN	DATE		
ENG.	DATE	Application	BARNACLESAT
MATERIAL	7075-T731 ALUMINUM	SIZE	DWG. NO. B STD6
FINISH	AS1 MACHINING	REV	9
UNLESS OTHERWISE SPECIFIED DIMENSIONS ARE IN MILLIMETERS		DO NOT SCALE DRAWING SHEET 6 OF 6	
TOLERANCES: LINEAR: ± 0.1 ANGULAR: $\pm 0.5^\circ$		ROUGHNESS: 32 MICRONS EDGES: DEBURR	



DATE	SCALE	DATE	SCALE
08/20/05	1:1	08/20/05	1:1
MSU Mechanical Engineering Lab 300 S. State St. East Lansing, MI 48824			
DRAWN: Sokomon		TITLE:	
ENG. Sokomon		Application: BARNACLESAT	
MATERIAL: 7075-T731 ALUMINUM		SIZE: DWG. NO. B S2D1	
FINISH: AS1 MACHINING		REV: 9	
UNLESS OTHERWISE SPECIFIED DIMENSIONS ARE IN MILLIMETERS TOLERANCES: LINEAR: ±0.1 ANGULAR: ±0.5° SURFINISH: MICROMETERS EDGES: DEBURRED			
DO NOT SCALE DRAWING			SHEET 1 OF 6



DATE:	08/20/05	REV:	1
DESIGNER:	Sokolov	DATE:	08/20/05
ENGINEER:	Sokolov	DATE:	08/20/05
MATERIAL:	7075-T731 ALUMINUM	TITLE:	SIDE 2 BOTTOM VIEW
FINISH:	AS1 MACHINING 1	TITLE:	LEFT VIEW
UNLESS OTHERWISE SPECIFIED DIMENSIONS ARE IN MILLIMETERS			
TOLERANCES: LINEAR: ±0.1 ANGULAR: ±0.5°			
ROUGHNESS: MICROMETERS EDGES: DEBURRED			
Application: BARNACLESAT		SIZE:	B
DWG. NO.:		REV:	9
DO NOT SCALE DRAWING		SHEET 2 OF 6	



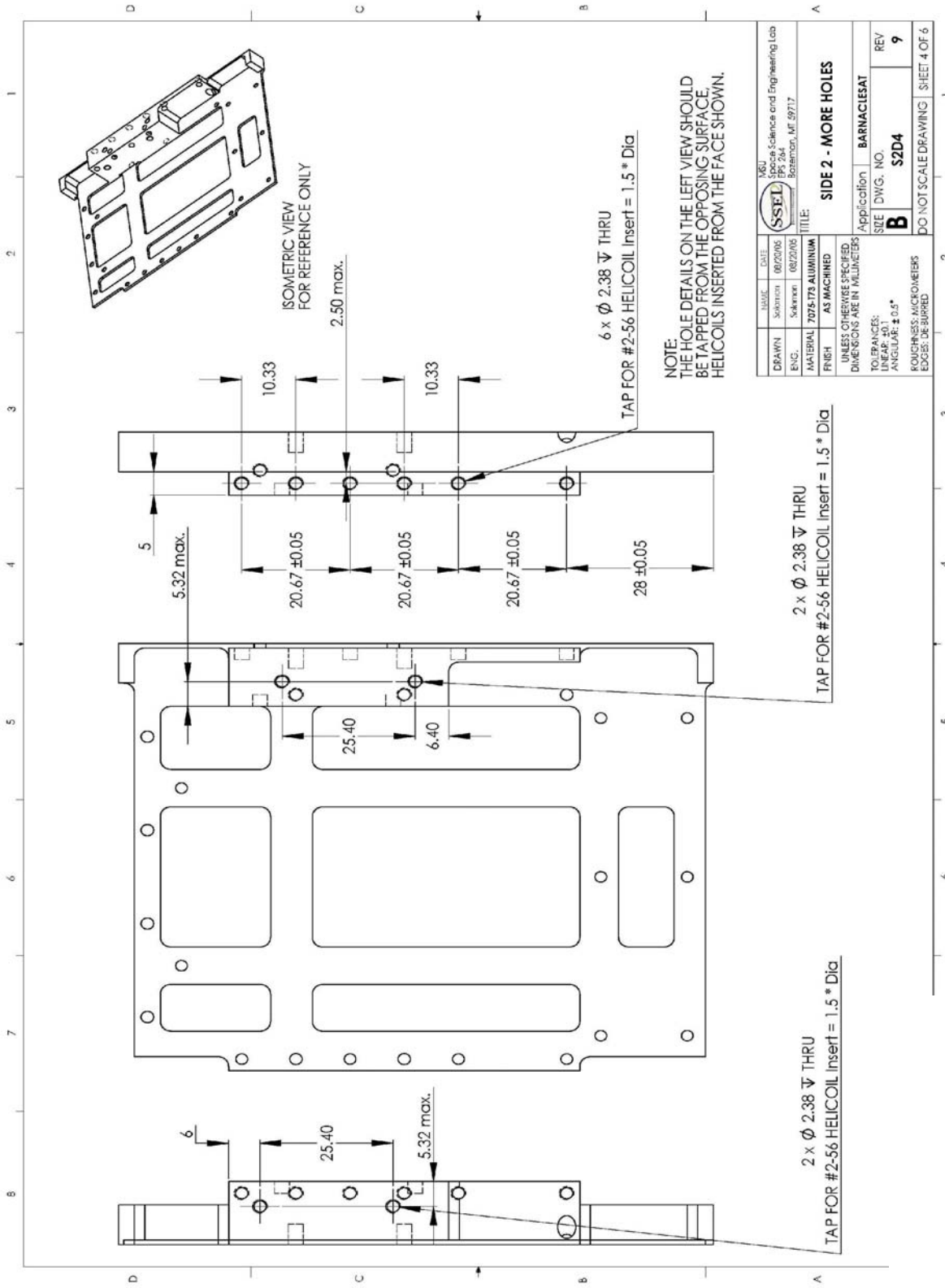
NOTE:
ALL OUTER RADII ARE IDENTICAL

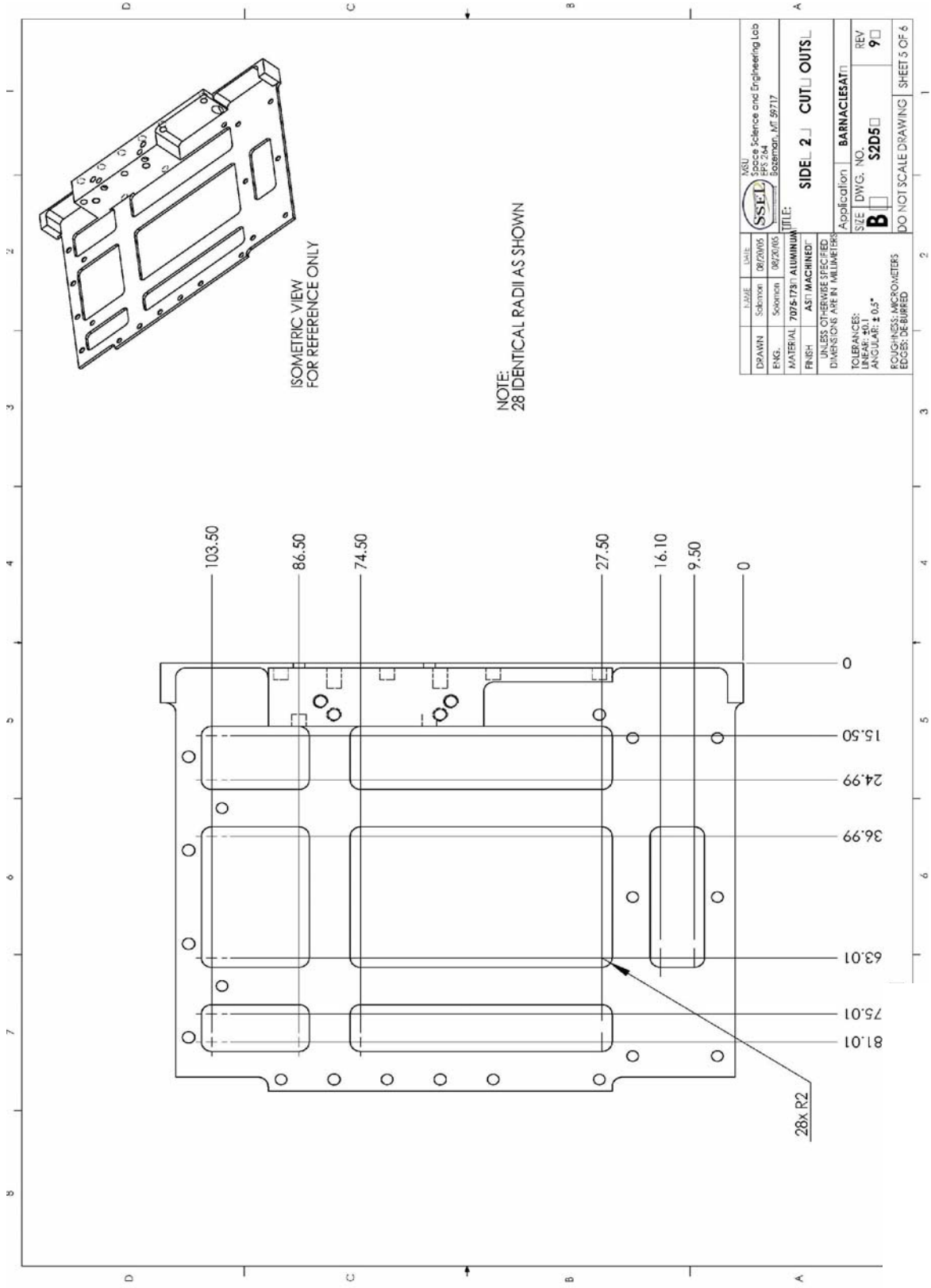
THE RESPECTIVE HOLE SPACING DIM. SHOULD BE REPEATED FOR THE RESPECTIVE # OF HOLES i.e. (34±0.05), (20.67±0.05), and (20±0.05)

DATE: 08/20/05	DESIGNER: S. Solomon	DATE: 08/20/05	DESIGNER: S. Solomon
DRAWN: S. Solomon		DRAWN: S. Solomon	
MATERIAL: 7075-T73 ALUMINUM		MATERIAL: 7075-T73 ALUMINUM	
FINISH: AS1 MACHINED 1		FINISH: AS1 MACHINED 1	
UNLESS OTHERWISE SPECIFIED DIMENSIONS ARE IN MILLIMETERS			
TOLERANCES: LINEAR: ±0.1 ANGULAR: ±0.5°			
EDGES: DEBURR			
TITLE: SIDE VIEW		TITLE: TOP VIEW	
Application: BARNACLESAT		Application: BARNACLESAT	
SIZE DWG. NO. B S2D3		SIZE DWG. NO. B S2D3	
REV 9		REV 9	
DO NOT SCALE DRAWING SHEET 3 OF 6			

SECTION C-C
SCALE 4:3
2x Ø 2.38 ∇ THRU
TAP FOR #2-56 HELICOIL Insert = 1.5 * Dia

4 x Ø 2.38 ∇ THRU
TAP FOR #2-56 HELICOIL Insert = 1.5 * Dia

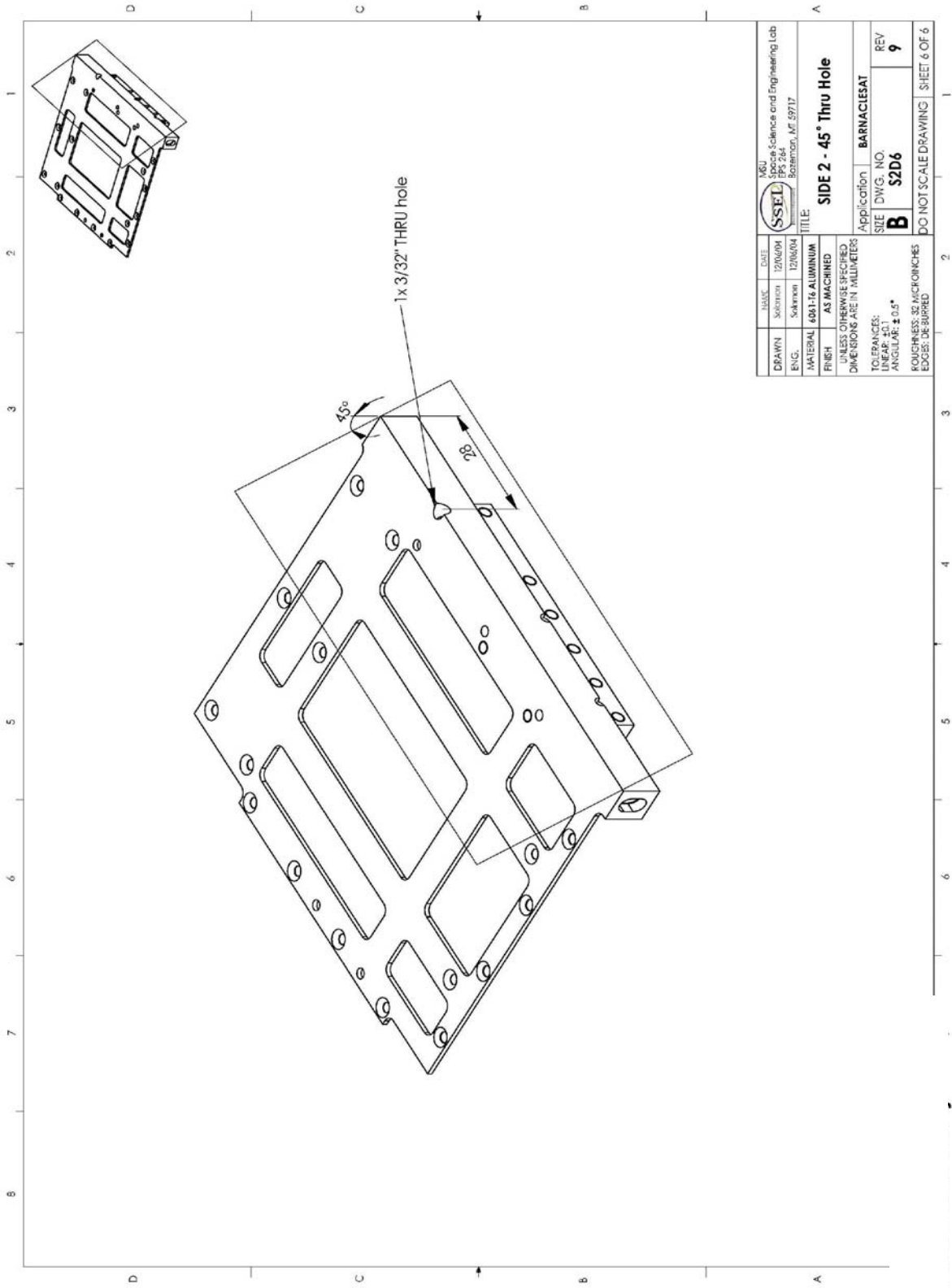




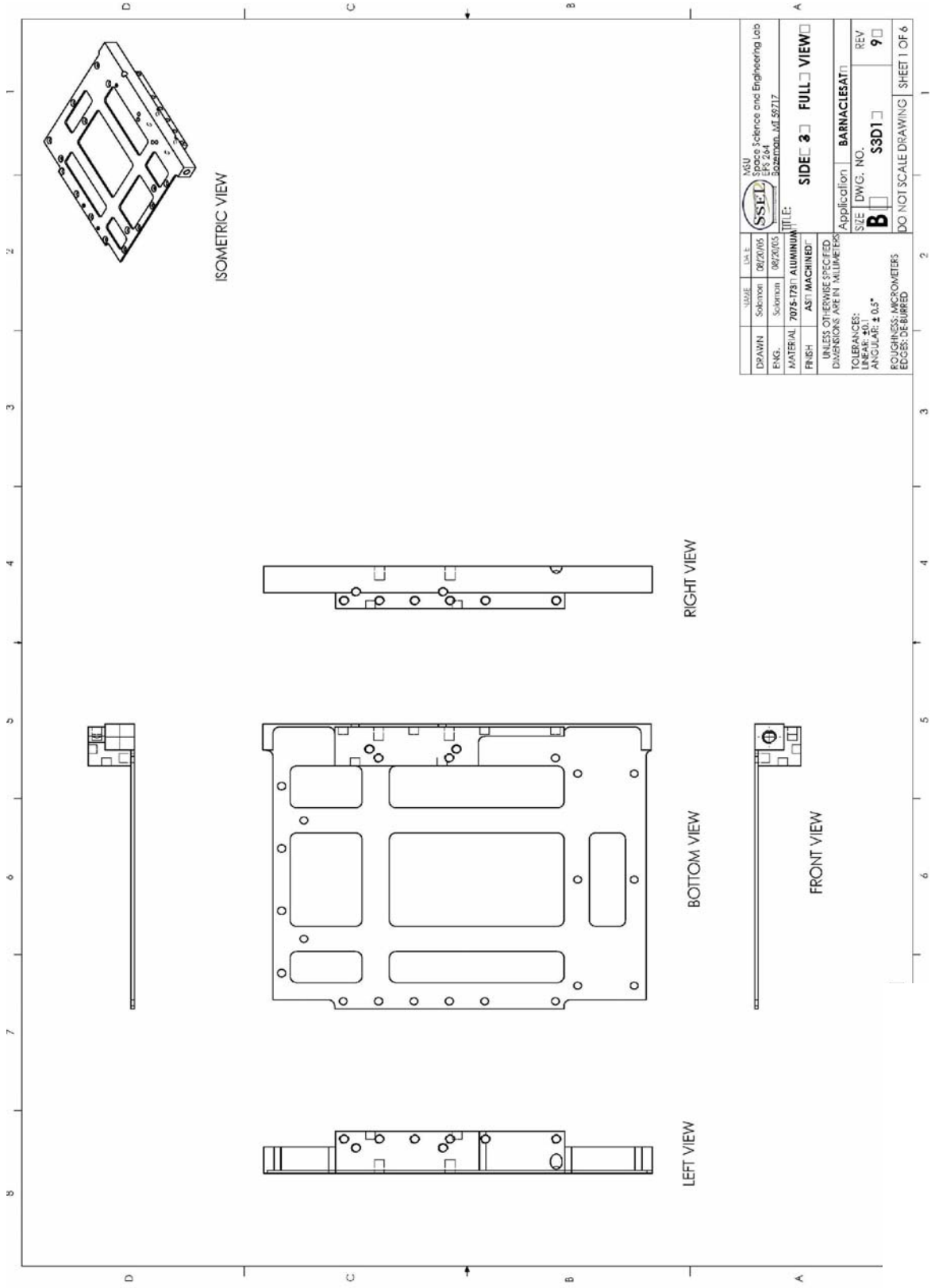
ISOMETRIC VIEW
FOR REFERENCE ONLY

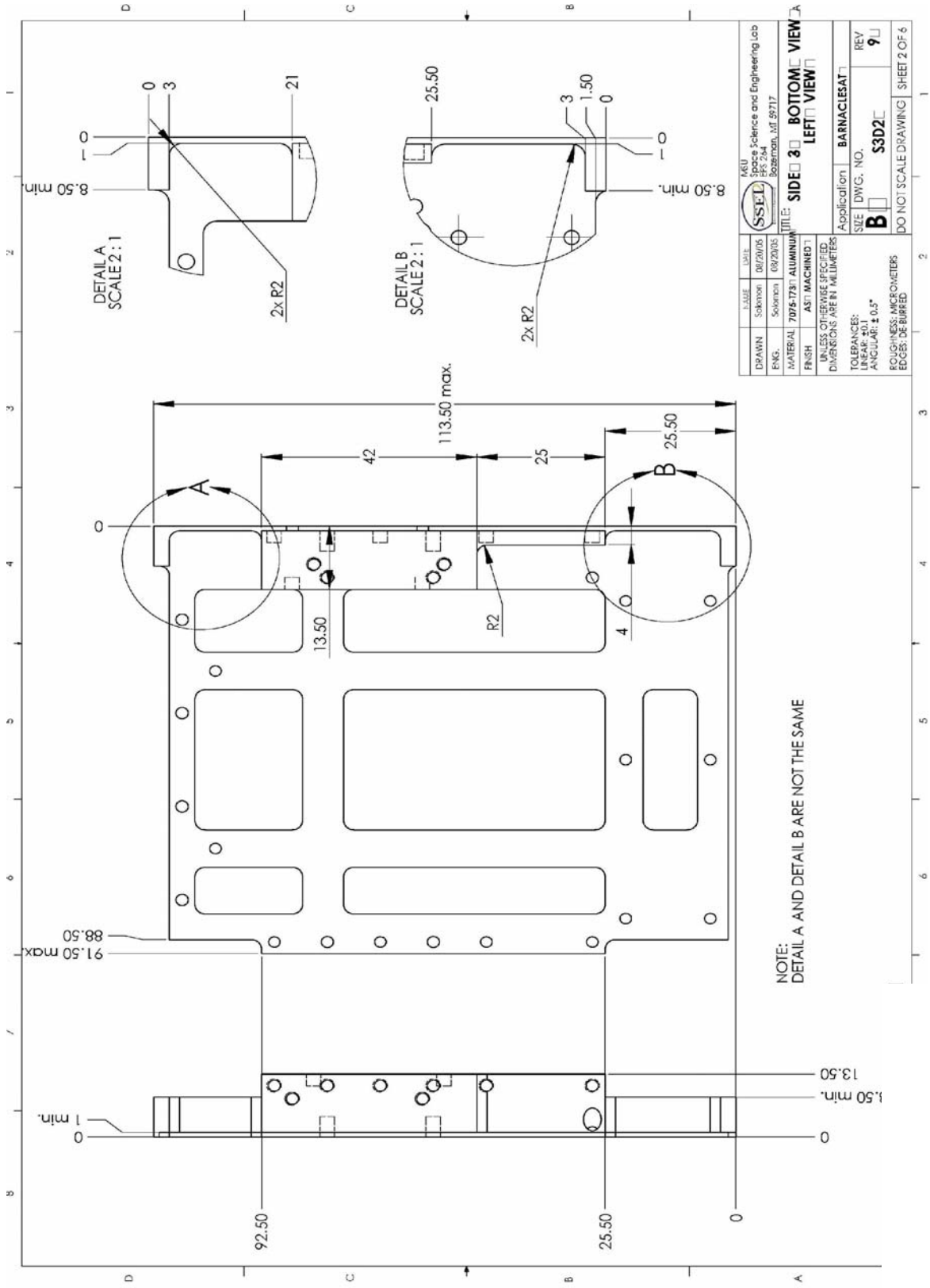
NOTE:
28 IDENTICAL RADII AS SHOWN

DATE:	08/20/05	SCALE:	1:1
DESIGNED BY:	Solomon	DRAWN BY:	Solomon
DATE:	08/20/05	SCALE:	1:1
DESIGNED BY:	Solomon	DRAWN BY:	Solomon
MATERIAL:	7075-T73 ALUMINUM	TITLE:	SIDE_2 CUT OUTS
FINISH:	AS1 MACHINED	Application:	BARNACLESAT
UNLESS OTHERWISE SPECIFIED DIMENSIONS ARE IN MILLIMETERS			
TOLERANCES: LINEAR: ±0.1 ANGULAR: ±0.5°			
ROUGHNESS: MICROMETERS EDGES: DEBURRED			
SIZE:	B	DWG. NO.:	S2D5
REV:	9	DO NOT SCALE DRAWING:	SHEET 5 OF 6



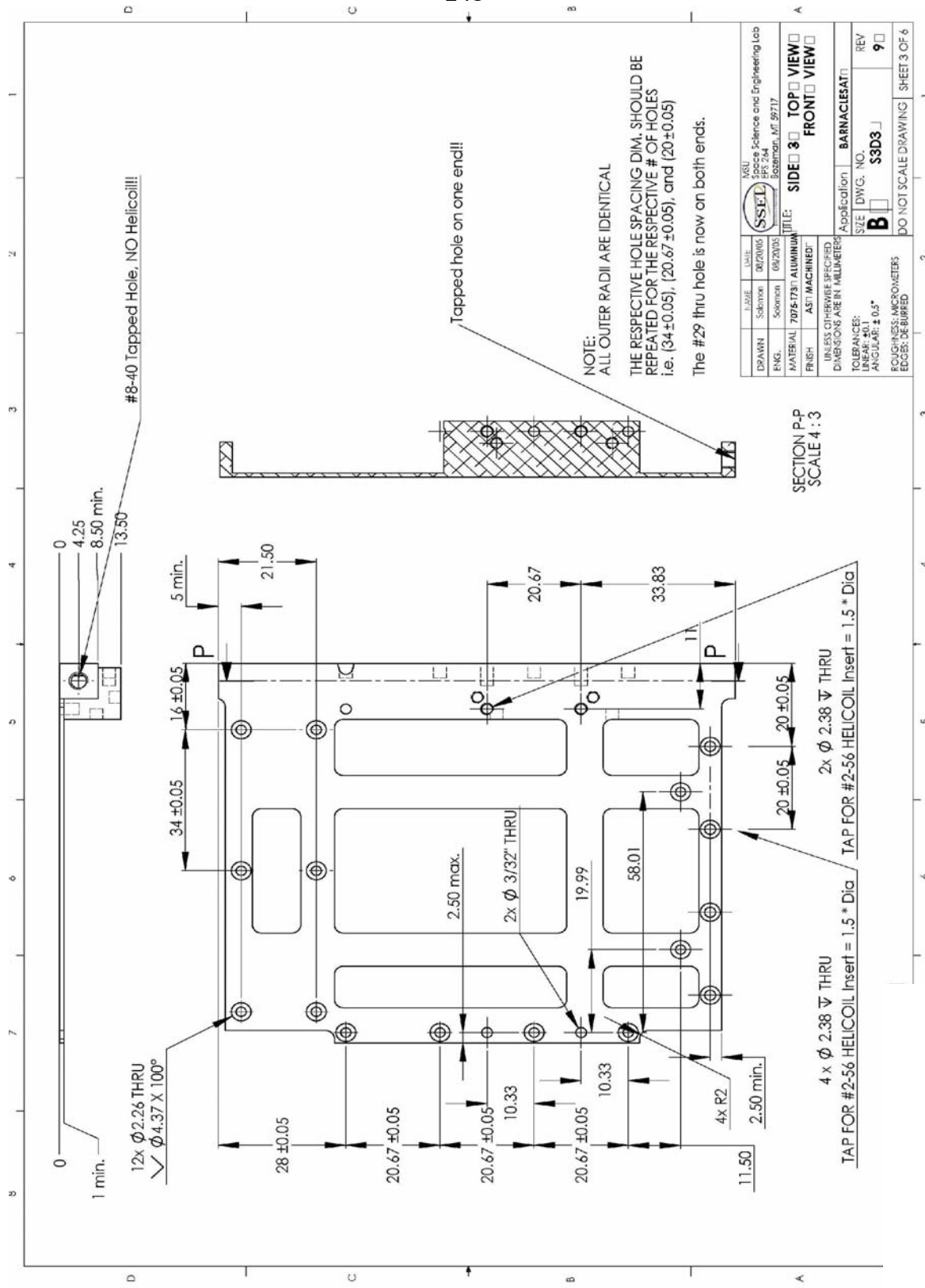
DATE	12/06/04
DESIGNER	S. S. S. S.
ENGINEER	S. S. S. S.
MATERIAL	6061-T6 ALUMINUM
FINISH	AS MACHINED
UNLESS OTHERWISE SPECIFIED DIMENSIONS ARE IN MILLIMETERS	
TOLERANCES:	
LINEAR: ±0.1	
ANGULAR: ±0.5°	
FINISH: 32 MICRONS	
EDGES: DEBURR	
SCALE	AS SHOWN
TITLE	SIDE 2 - 45° Thru Hole
Application	BARNACLESAT
SIZE	DWG. NO. B S2D6
REV	9
DO NOT SCALE DRAWING SHEET 6 OF 6	





DATE:	08/20/05	REV:	9
DESIGNER:	Sokolov	APP.:	
ENGINEER:	Sokolov	CHECKED:	
MATERIAL:	7075-T73 ALUMINUM	FINISH:	AS1 MACHINING 1
UNLESS OTHERWISE SPECIFIED: DIMENSIONS ARE IN MILLIMETERS			
TOLERANCES: LINEAR: ±0.1 ANGULAR: ±0.5°			
SURFACE FINISH: EDGES: DEBURRED			
Application: BARNACLESAT		DO NOT SCALE DRAWING	
SIZE DWG. NO. B S3D2		SHEET 2 OF 6	

SIDE VIEW
 BOTTOM VIEW
 LEFT VIEW



#8-40 Tapped Hole, NO Helicoid!!!

Tapped hole on one end!!

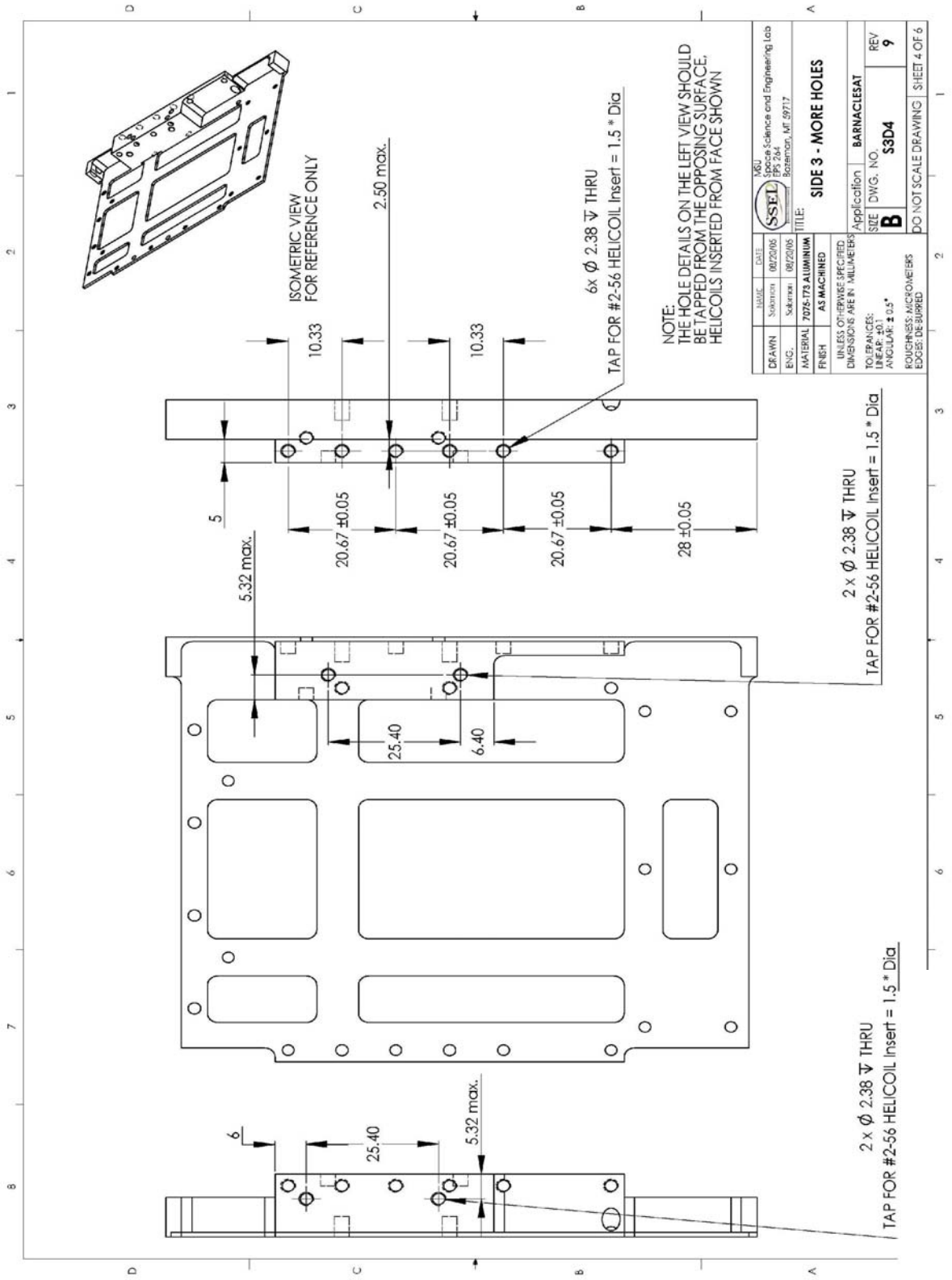
NOTE:
ALL OUTER RADII ARE IDENTICAL
THE RESPECTIVE HOLE SPACING DIM. SHOULD BE REPEATED FOR THE RESPECTIVE # OF HOLES i.e. (34±0.05), (20.67±0.05), and (20±0.05)
The #29 thru hole is now on both ends.

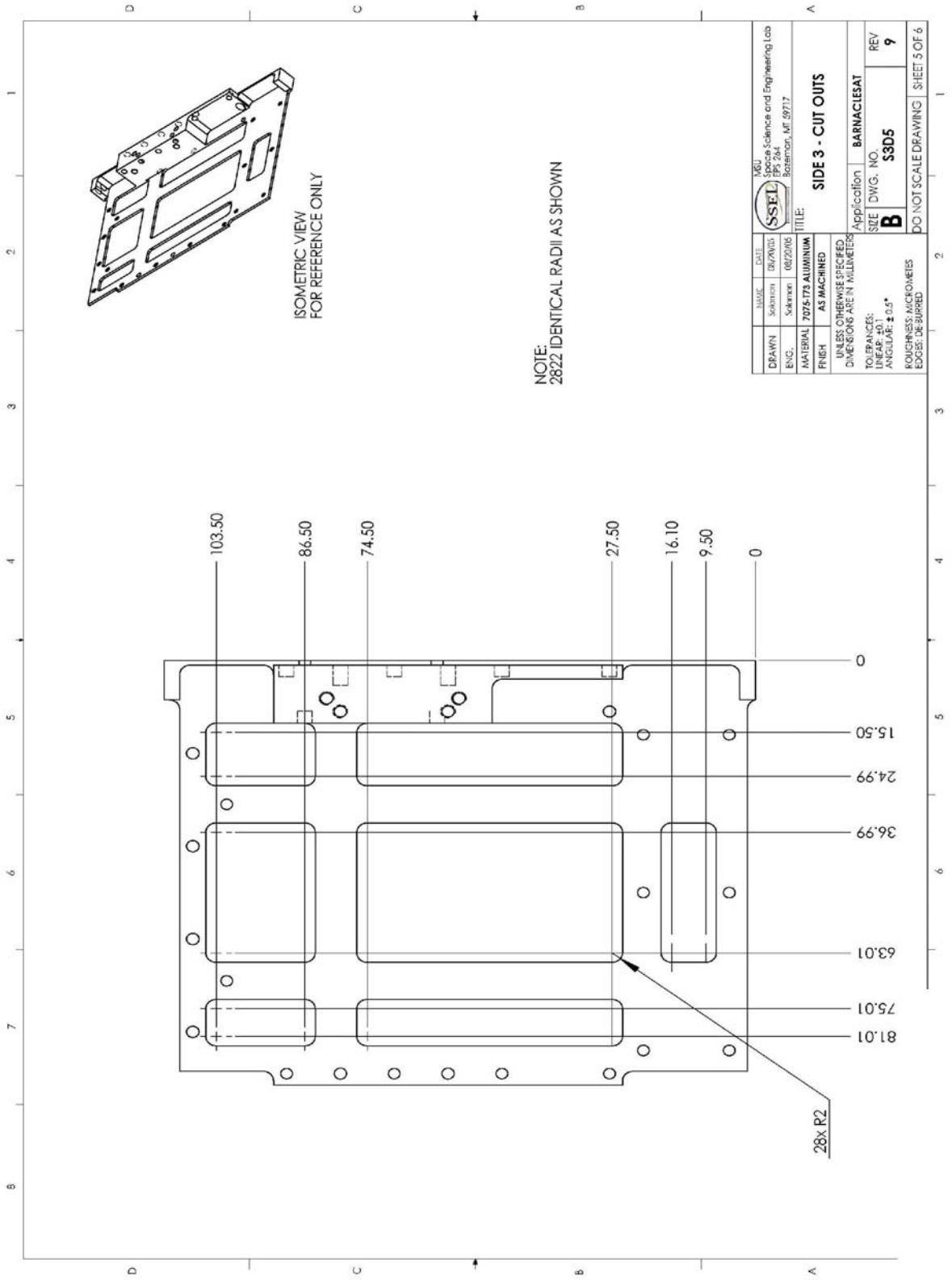
DATE:	08/20/05	SCALE:	AS SHOWN
DESIGNER:	Sullivan	DATE:	08/20/05
ENGINEER:	Sullivan	PROJECT NO.:	SPC 204
MATERIAL:	7075-T73 ALUMINUM	TITLE:	SIDE 3 TOP VIEW
FINISH:	AST MACHINED	Application:	BARNACLESAT
UNLESS OTHERWISE SPECIFIED DIMENSIONS ARE IN MILLIMETERS			
TOLERANCES:			
LINEAR: ±0.1			
ANGULAR: ±0.5°			
SURFACE FINISH: MICROMETERS			
EDGES: DEBURRED			
SIZE:	B	DWG. NO.:	S3D3
REV:	9	DO NOT SCALE DRAWING:	SHEET 3 OF 6

SECTION P-P
SCALE 4:3


4 x Ø 2.38 THRU
TAP FOR #2-56 HELICOIL Insert = 1.5 * Dia

2 x Ø 2.38 THRU
TAP FOR #2-56 HELICOIL Insert = 1.5 * Dia



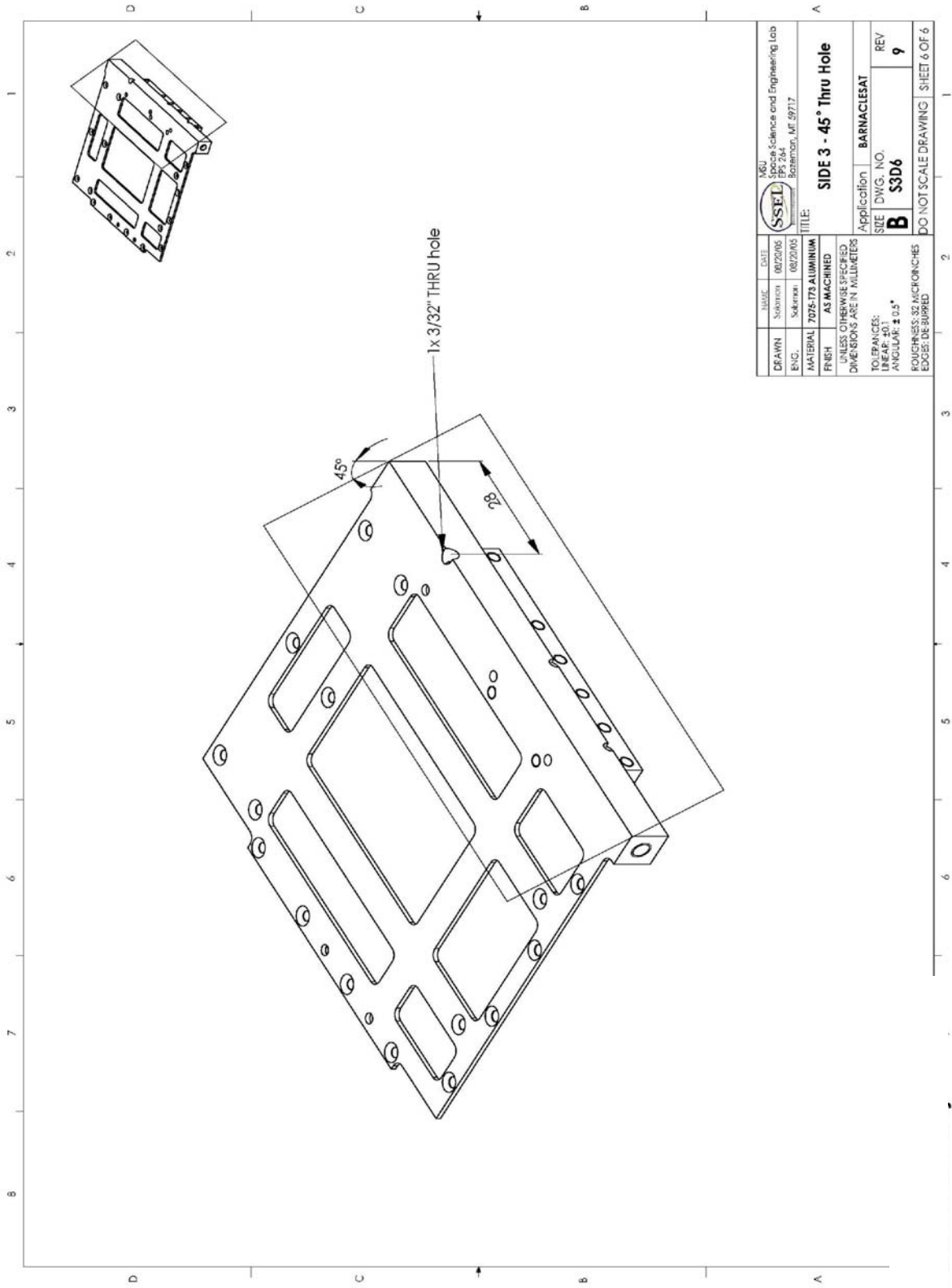


NAME	DATE	SCALE	REV
Sullivan	08/22/05		9
ENGINEER	DATE	SCALE	REV
Sullivan	08/22/05		9
MATERIAL: 7075-T73 ALUMINUM			
FINISH: AS MACHINED			
UNLESS OTHERWISE SPECIFIED DIMENSIONS ARE IN MILLIMETERS			
TOLERANCES:			
LINEAR: ±0.1			
ANGULAR: ±0.5°			
FINISHES: MICROMETERS			
EDGES: DEBURRED			
DRAWN		DATE	
Sullivan		08/22/05	
ENGINEER		DATE	
Sullivan		08/22/05	
MATERIAL: 7075-T73 ALUMINUM			
FINISH: AS MACHINED			
UNLESS OTHERWISE SPECIFIED DIMENSIONS ARE IN MILLIMETERS			
TOLERANCES:			
LINEAR: ±0.1			
ANGULAR: ±0.5°			
FINISHES: MICROMETERS			
EDGES: DEBURRED			
DRAWN		DATE	
Sullivan		08/22/05	
ENGINEER		DATE	
Sullivan		08/22/05	
MATERIAL: 7075-T73 ALUMINUM			
FINISH: AS MACHINED			
UNLESS OTHERWISE SPECIFIED DIMENSIONS ARE IN MILLIMETERS			
TOLERANCES:			
LINEAR: ±0.1			
ANGULAR: ±0.5°			
FINISHES: MICROMETERS			
EDGES: DEBURRED			

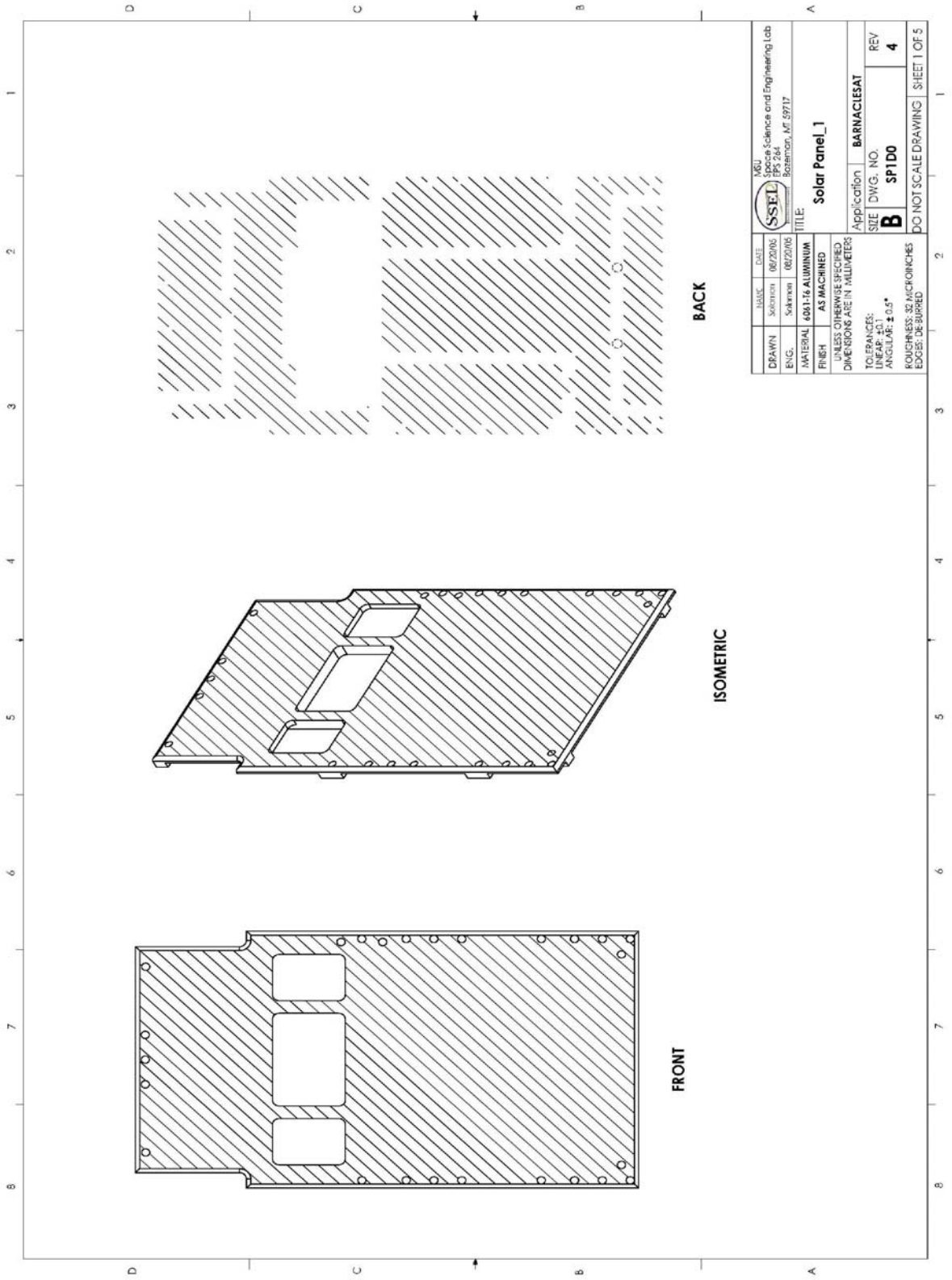

 SSEL
 Science and Engineering Lab
 PK 264
 Boston, MA 02177

TITLE: **SIDE 3 - CUT OUTS**
 Application: **BARNACLESAT**
 SIZE: **B**
 DWG. NO.: **S3D5**
 REV: **9**

DO NOT SCALE DRAWING SHEET 5 OF 6



NAME	DATE	 SSEL Science and Engineering Lab PK 264 Bateman, ME 99717
Drawn Sakran	08/20/05	
ENG.	Sakran	08/22/05
MATERIAL	7051T3 ALUMINUM	
FINISH	AS MACHINED	
UNLESS OTHERWISE SPECIFIED DIMENSIONS ARE IN MILLIMETER		
TOLERANCES: LINEAR: ±0.1 ANGULAR: ±0.5°		
FINISHES: 32 MICRONS/CHES EDGES: DEBURR		
Application	BARNACLESAT	
SIZE	DWG. NO.	REV
B	S3D6	9
DO NOT SCALE DRAWING		
SHEET 6 OF 6		



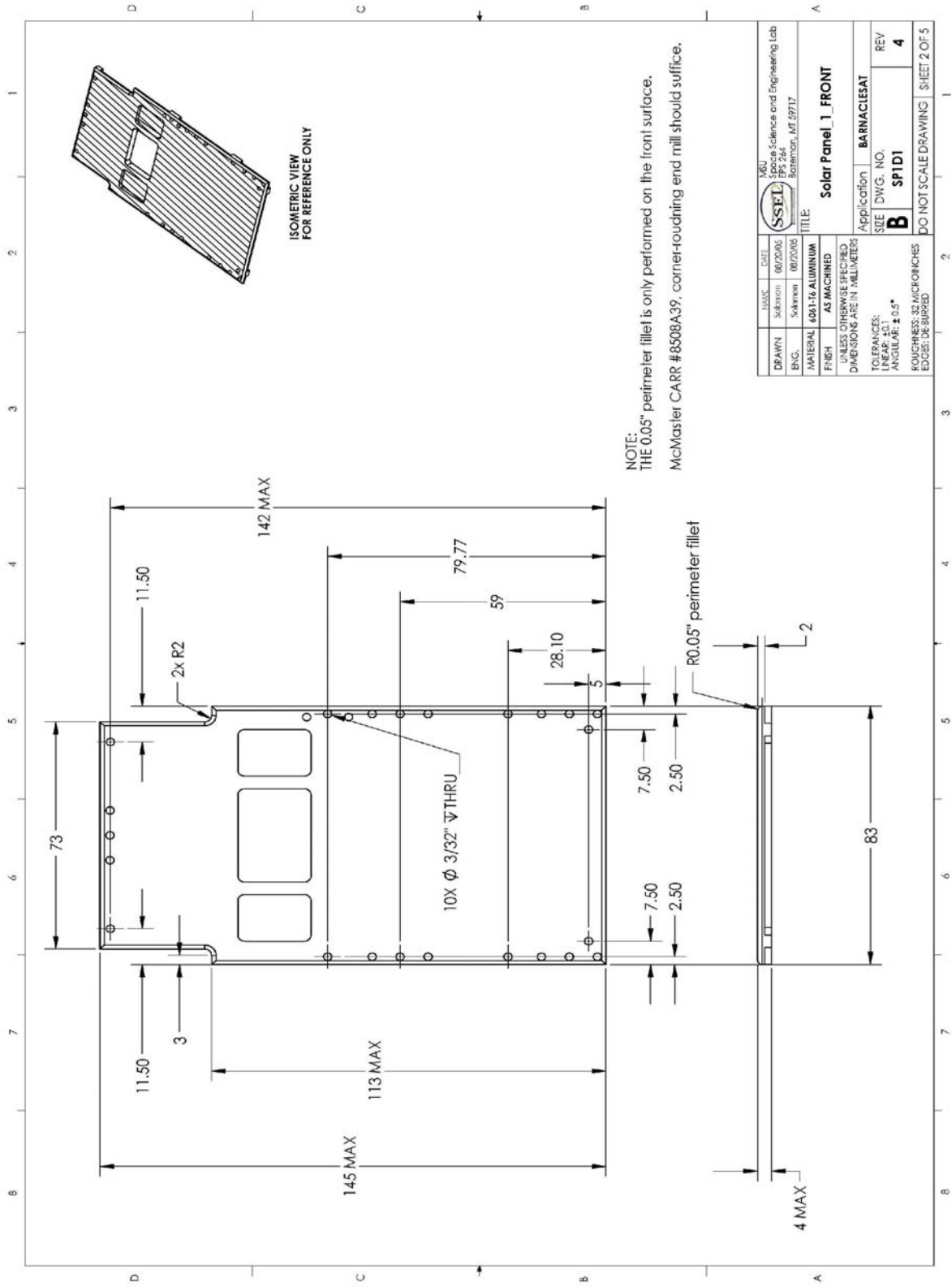
BACK

ISOMETRIC

FRONT

NGU Noble Science and Engineering Lab PK 284 Baton Rouge, LA 70717	SSEL	DATE: 06/22/05	ENGINEER: Sakirwan
TITLE: Solar Panel_1		DATE: 06/22/05	ENGINEER: Sakirwan
Application: BARNACLESAT		SIZE: B	DWG. NO: SP100
MATERIAL: 6061-T6 ALUMINUM		FINISH: AS MACHINED	REV: 4
TOLERANCES: UNLESS OTHERWISE SPECIFIED		DIMENSIONS ARE IN MILLIMETER	
LINEAR: ±0.1		ANGULAR: ±0.5°	
EDGES: DEBURRED		DO NOT SCALE DRAWING	

SHEET 1 OF 5



NOTE:
THE 0.05" perimeter fillet is only performed on the front surface.
McMaster CARR #8508A39, corner-rounding end mill should suffice.

DATE	06/22/05
DESIGNER	Sullivan
DRAWN	Sullivan
DATE	06/22/05
DESIGNER	Sullivan
DRAWN	Sullivan
MATERIAL	6061-T6 ALUMINUM
FINISH	AS MACHINED
UNLESS OTHERWISE SPECIFIED DIMENSIONS ARE IN MILLIMETERS	
TOLERANCES:	
LINEAR: ±0.1	
ANGULAR: ±0.5°	
FINISHNESS: 32 MICRONS	
EDGES: DEBURR	
SCALE	1:1
REV	4
SP1D1	
DO NOT SCALE DRAWING	
SHEET 2 OF 5	

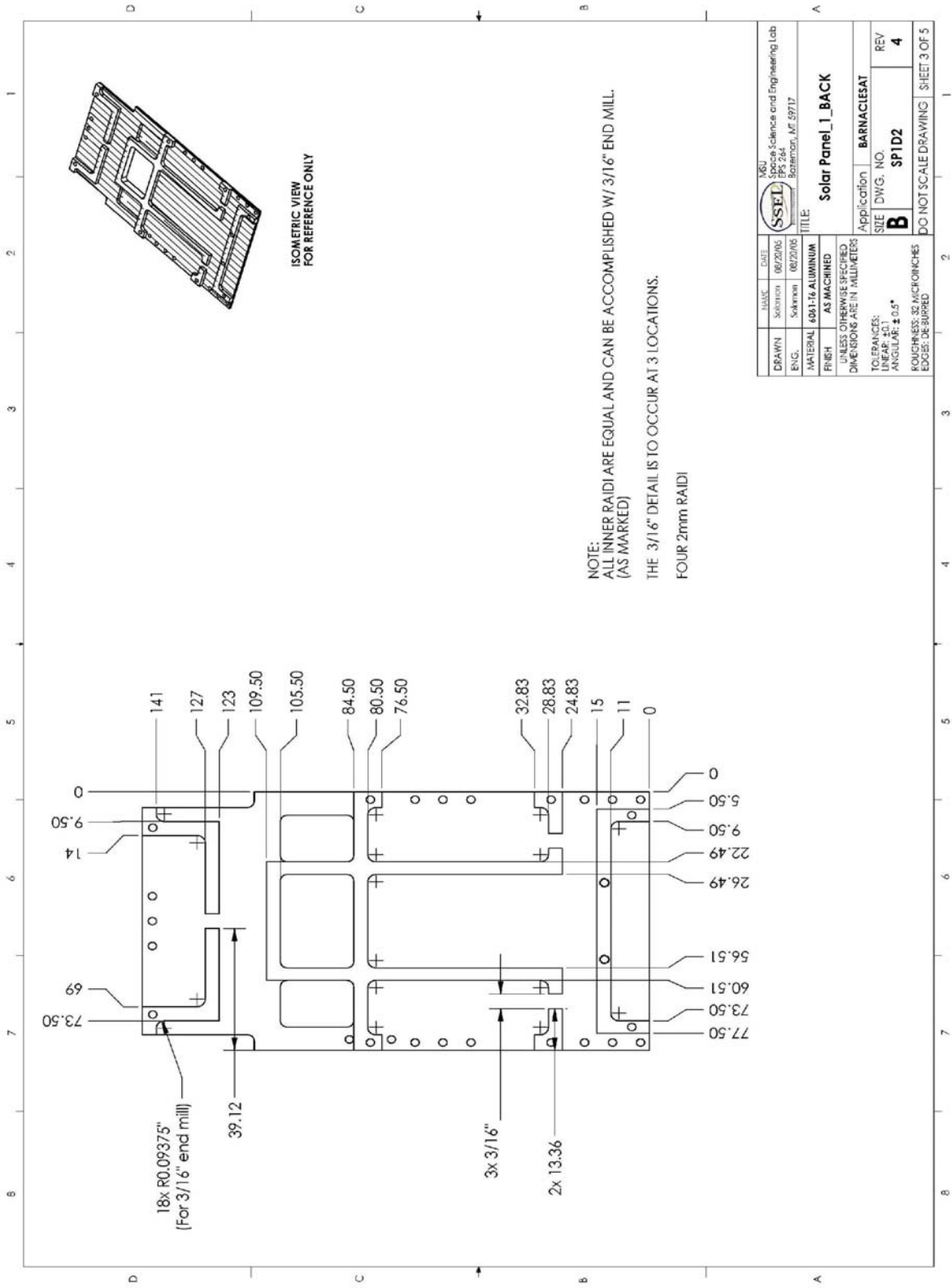
Solar Panel 1 FRONT

Application: BARNACLESAT

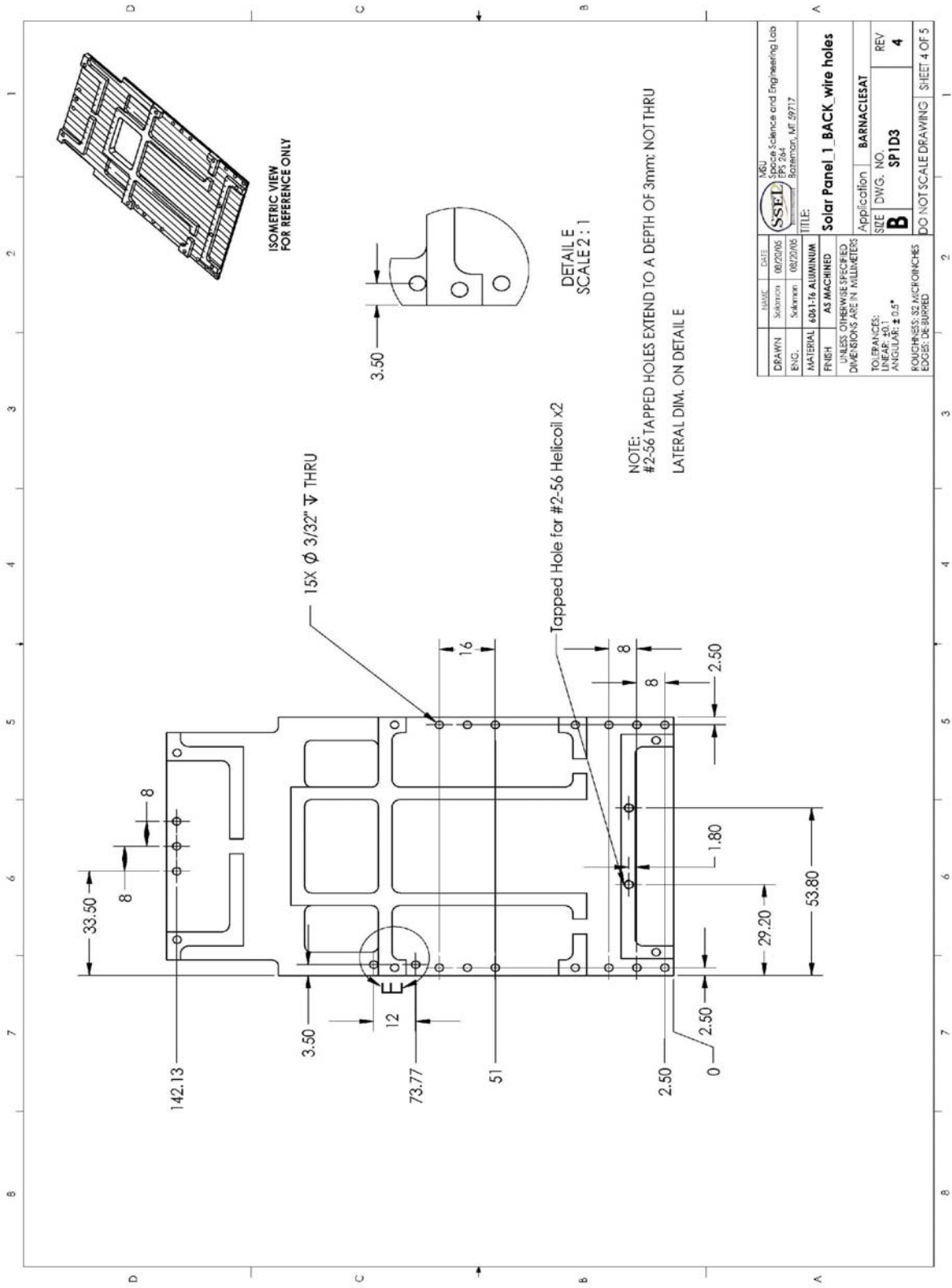
SIZE: DWG. NO. SP1D1

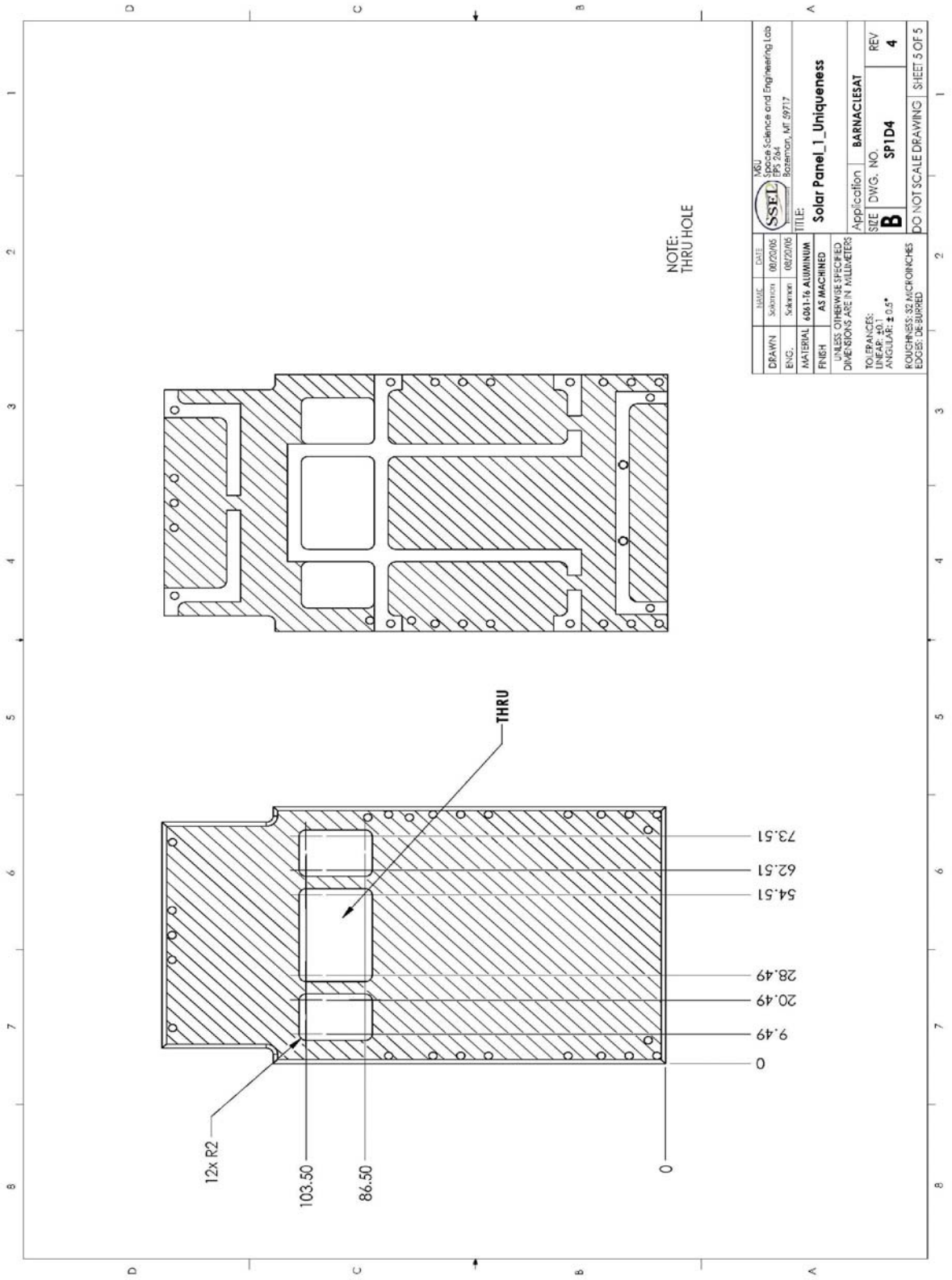
REV: 4

SSEL
SSEL Science and Engineering Lab
PK 264
Bateson, MI 49717



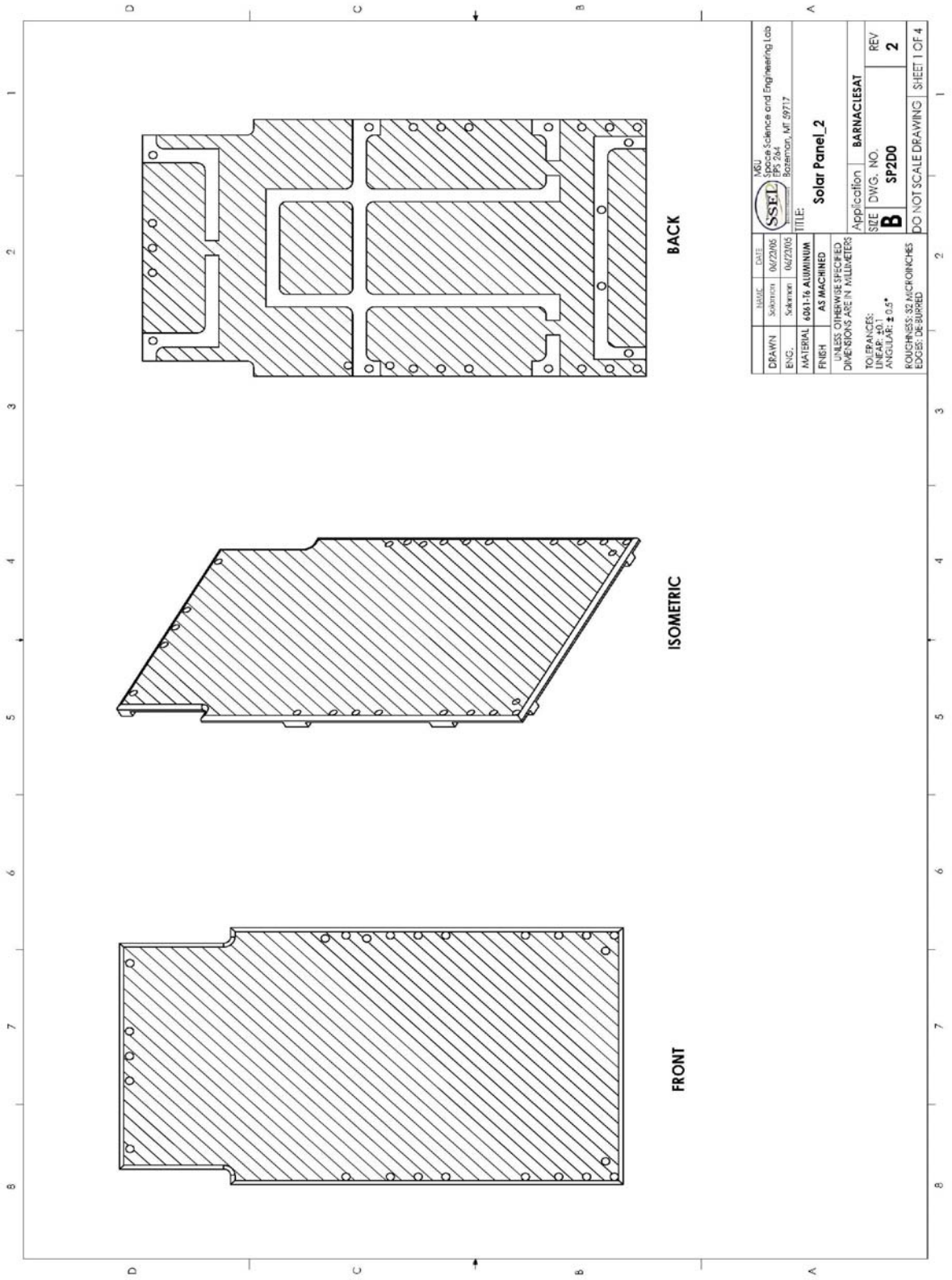
DATE	06/22/05
DESIGNER	Sullivan
DATE	06/22/05
ENGINEER	Sullivan
MATERIAL	6061-T6 ALUMINUM
FINISH	AS MACHINED
UNLESS OTHERWISE SPECIFIED DIMENSIONS ARE IN MILLIMETERS	
TOLERANCES:	
LINEAR: ±0.1	
ANGULAR: ±0.5°	
ROUGHNESS: 32 MICRONS	
EDGES: DEBURRED	
SCALE	AS SHOWN
PROJECT	0601-16
DESCRIPTION	Solar Panel_1_BACK
APPLICATION	BARNACLESAT
SIZE	B
DWG. NO.	SP1D2
REV	4
DO NOT SCALE DRAWING SHEET 3 OF 5	





NOTE:
THRU HOLE

DATE	08/22/05	NO.	08/22/05
DESIGNED BY	Sakrison	DRAWN BY	Sakrison
CHECKED BY		DATE	08/22/05
<p>SSEL Science and Engineering Lab 100 PK 264 Bateman, ME 09717</p>			
<p>Solar Panel_L_ Uniqueness</p>			
Application	BARNACLESAT		
SIZE	DWG. NO.	REV	
B	SP1D4	4	
<p>UNLESS OTHERWISE SPECIFIED DIMENSIONS ARE IN MILLIMETER TOLERANCES: LINEAR: ±0.1 ANGULAR: ±0.5° FINISH: 32 MICRONS EDGES: DEBURRED</p>			
<p>DO NOT SCALE DRAWING SHEET 5 OF 5</p>			

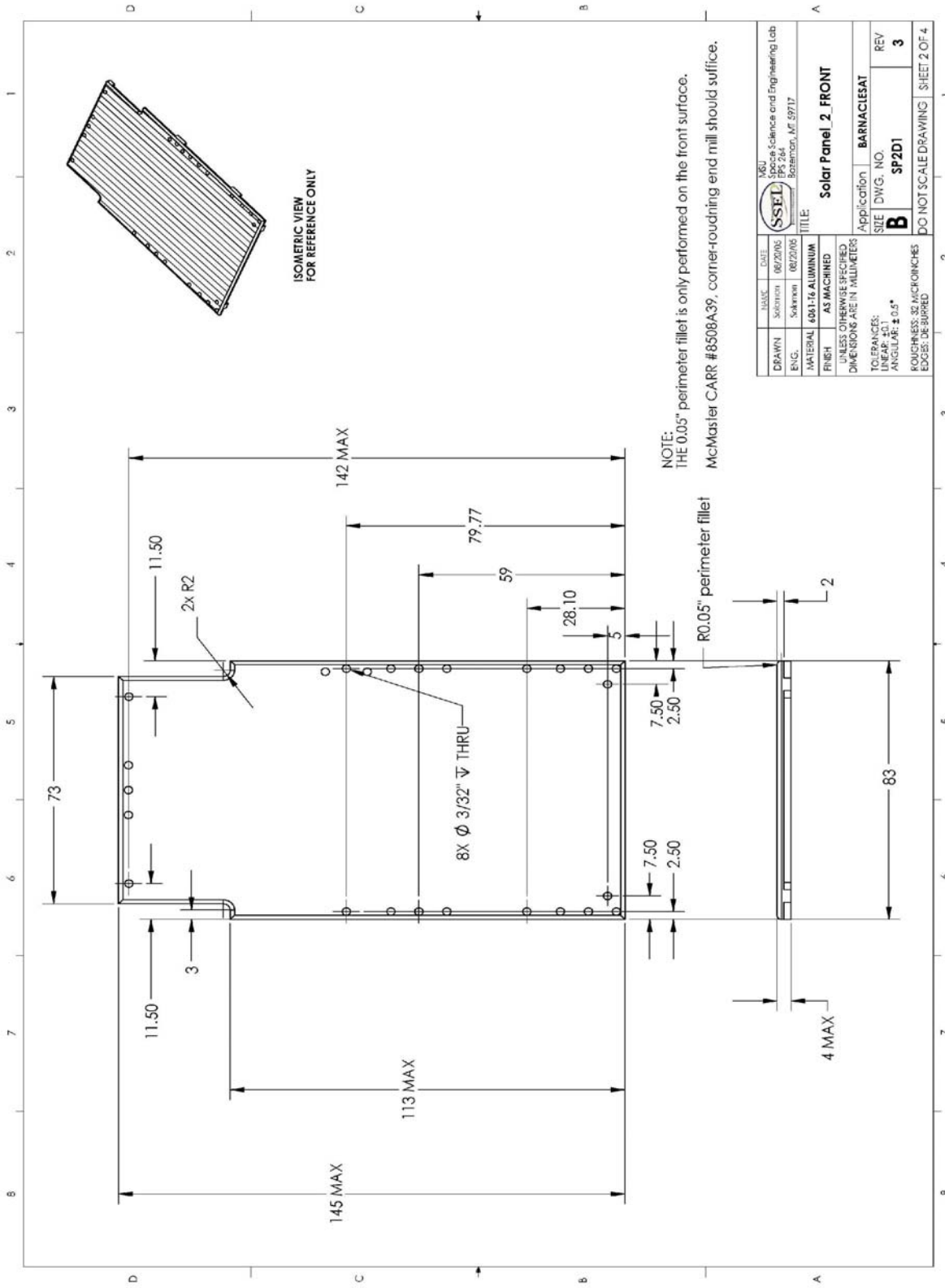


DATE	06/22/05
DESIGNER	Sakrwan
DATE	06/22/05
ENGINEER	Sakrwan
MATERIAL	6061-T6 ALUMINUM
FINISH	AS MACHINED
UNLESS OTHERWISE SPECIFIED DIMENSIONS ARE IN MILLIMETER	
TOLERANCES:	
LINEAR: ±0.1	
ANGULAR: ±0.5°	
FINISHNESS: 32 MICRONS	
EDGES: DEBURRED	

 SSEL Science and Engineering Lab PK 264 Bateman, ME 99717	TITLE: Solar Panel_2
--	--------------------------------

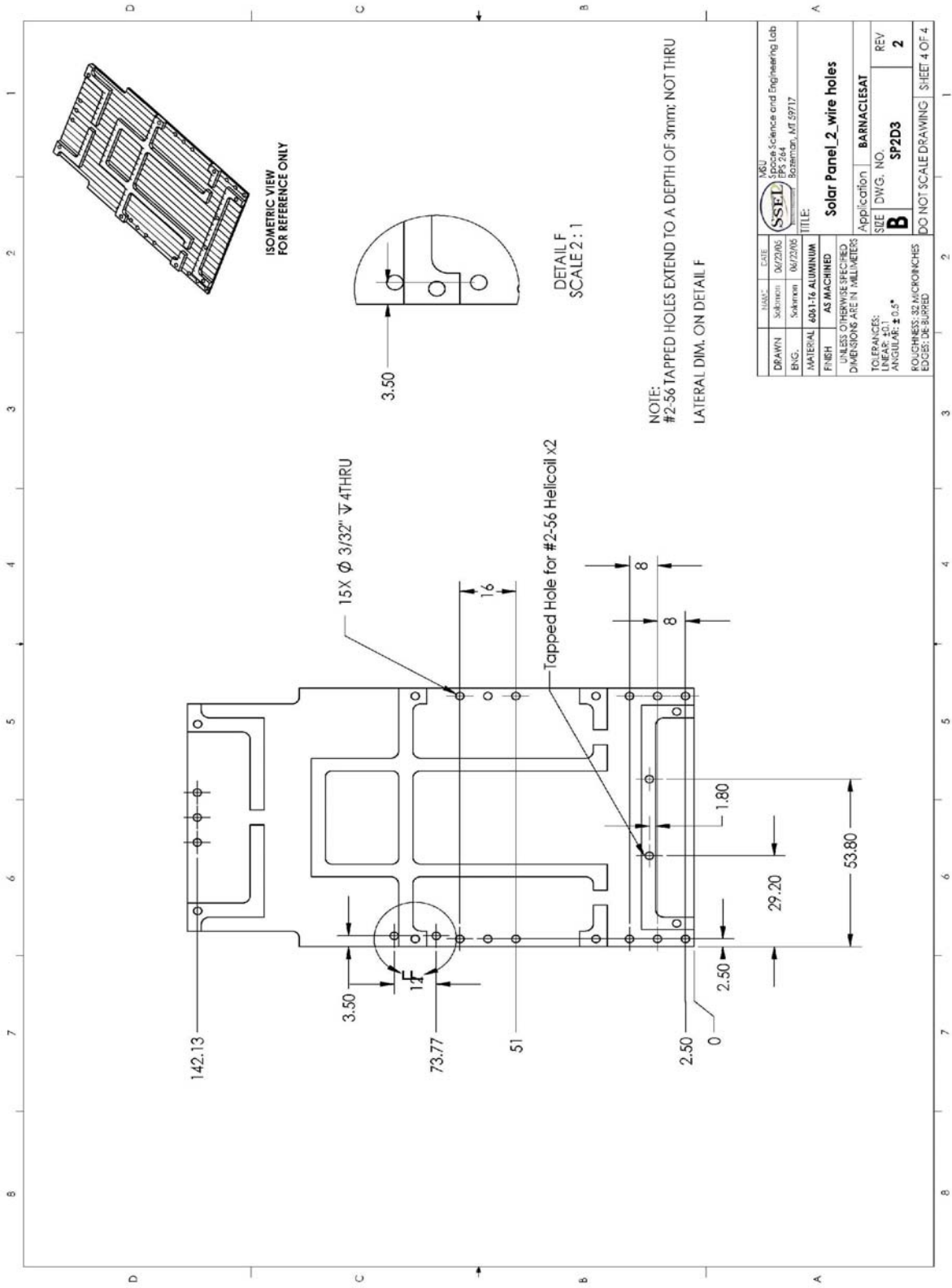
Application	BARNACLESAT
SIZE	B
DWG. NO.	SP2D0
REV	2

DO NOT SCALE DRAWING SHEET 1 OF 4

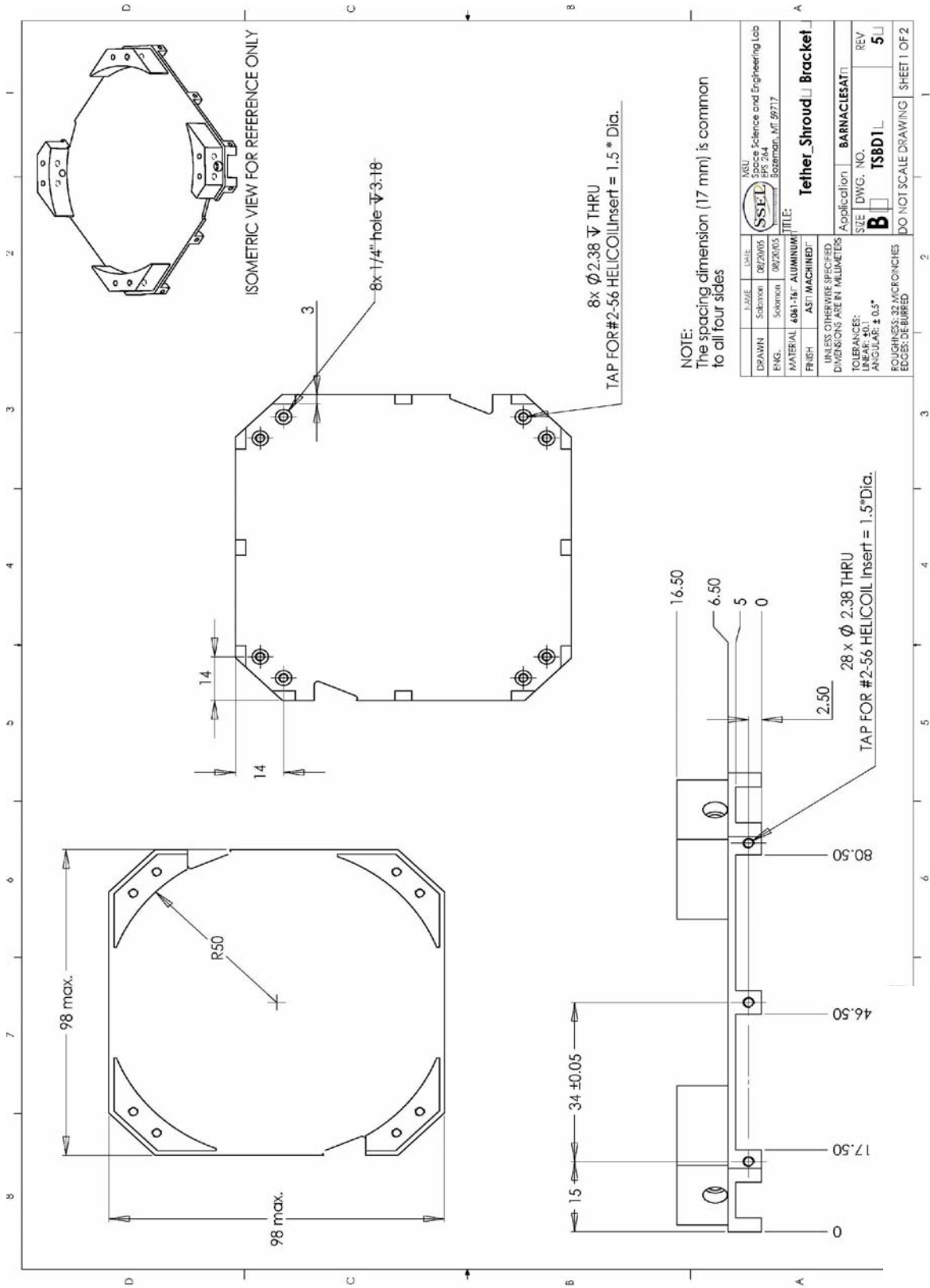


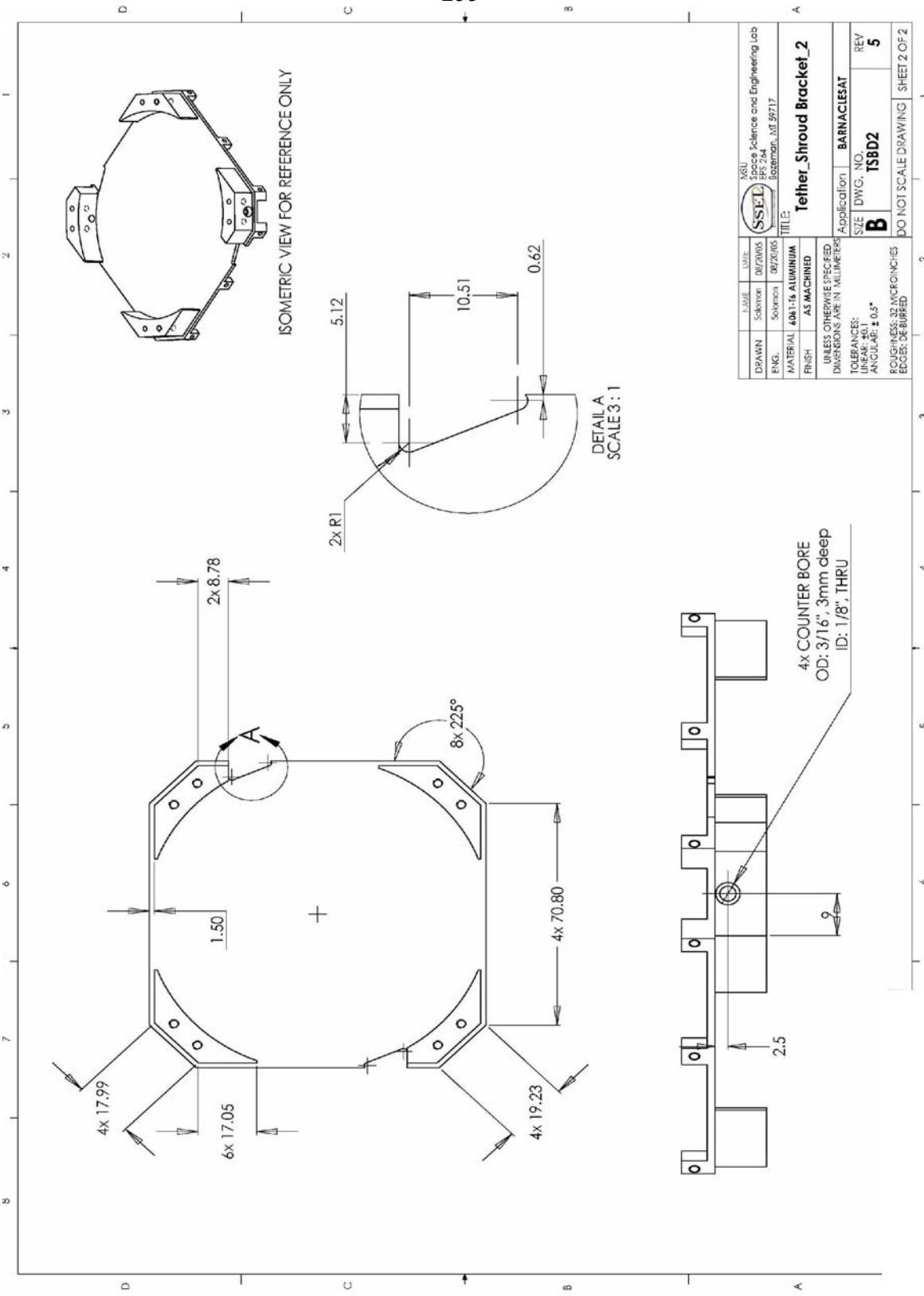
NOTE:
THE 0.05" perimeter fillet is only performed on the front surface.
McMaster CARR #8508A39, corner-rounding end mill should suffice.

DATE	06/22/05	SCALE	AS MACHINED
DESIGNED BY	Sullivan	DRAWN BY	Sullivan
CHECKED BY		DATE	06/22/05
SSEL Science and Engineering Lab PK 264 Boston, MA 02117			
TITLE: Solar Panel 2 FRONT			
Application: BARNACLESAT		SIZE: DWG. NO. SP2D1	
UNLESS OTHERWISE SPECIFIED DIMENSIONS ARE IN MILLIMETERS		DO NOT SCALE DRAWING SHEET 2 OF 4	
TOLERANCES: LINEAR: ± 0.1 ANGULAR: $\pm 0.5^\circ$		REV: 3	
FINISH: 6061-T6 ALUMINUM		EDGE: DEBURRED	



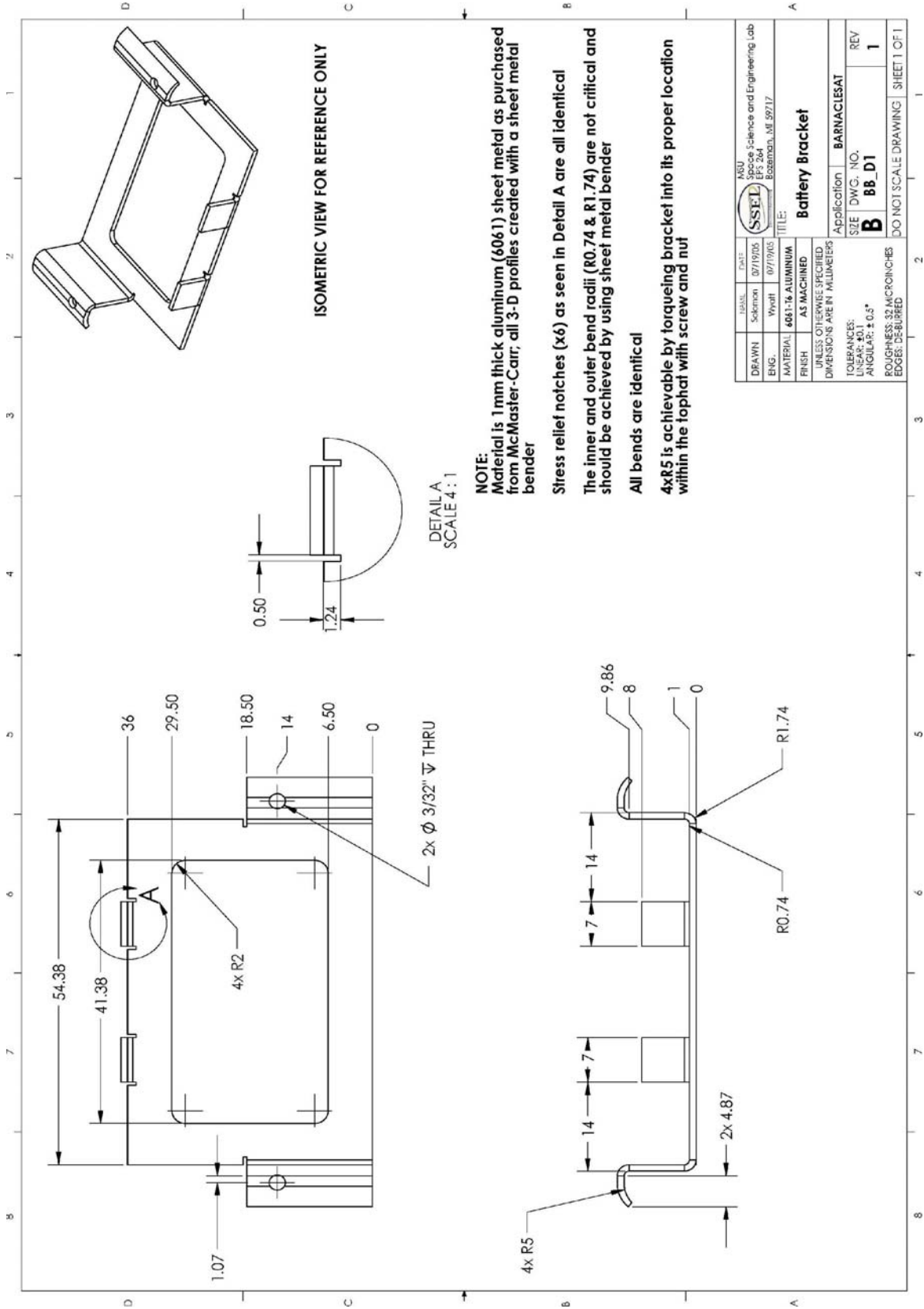
NOV-11	DATE	04/22/05
Sakrison	DRAWN	04/22/05
Sakrison	ENG.	04/22/05
6031-16 ALUMINUM	MATERIAL	
AS MACHINED	FINISH	
UNLESS OTHERWISE SPECIFIED DIMENSIONS ARE IN MILLIMETERS		
TOLERANCES:		
LINEAR: ± 0.1		
ANGULAR: $\pm 0.5^\circ$		
ROUGHNESS: 3.2 MICROMETERS		
EDGES: DE BURRED		
SSEL		SGS Science and Engineering Lab PK 284 Baton Rouge, LA 70803
TITLE: Solar Panel_2_wire holes		
Application: BARNACLESAT		REV
SIZE DWG. NO.	SP2D3	2
DO NOT SCALE DRAWING SHEET 4 OF 4		





DATE:	08/20/05	SCALE:	AS MACHINED
DESIGNED BY:	Solomon	DRAWN BY:	Solomon
CHECKED BY:	Solomon	DATE:	08/20/05
MATERIAL:	6061-T6 ALUMINIUM	TITLE:	Tether_Shroud Bracket_2
FINISH:	AS MACHINED	Application:	BARNACLESAT
UNLESS OTHERWISE SPECIFIED DIMENSIONS ARE IN MILLIMETERS			
TOLERANCES:			
LINEAR: ±0.1			
ANGULAR: ±0.5°			
SURFACE FINISH: 32 MICRONS			
EDGES: DEBURRED			
SIZE:	B	DWG. NO.:	TSBD2
REV:	5	DO NOT SCALE DRAWING	
			SHEET 2 OF 2

LOGO:	SSEL	Department:	Science and Engineering Lab
ADDRESS:	1000 E. 24th St.	City:	Eastman, MI 49717



NOTE:
 Material is 1mm thick aluminum (6061) sheet metal as purchased from McMaster-Carr; all 3-D profiles created with a sheet metal bender

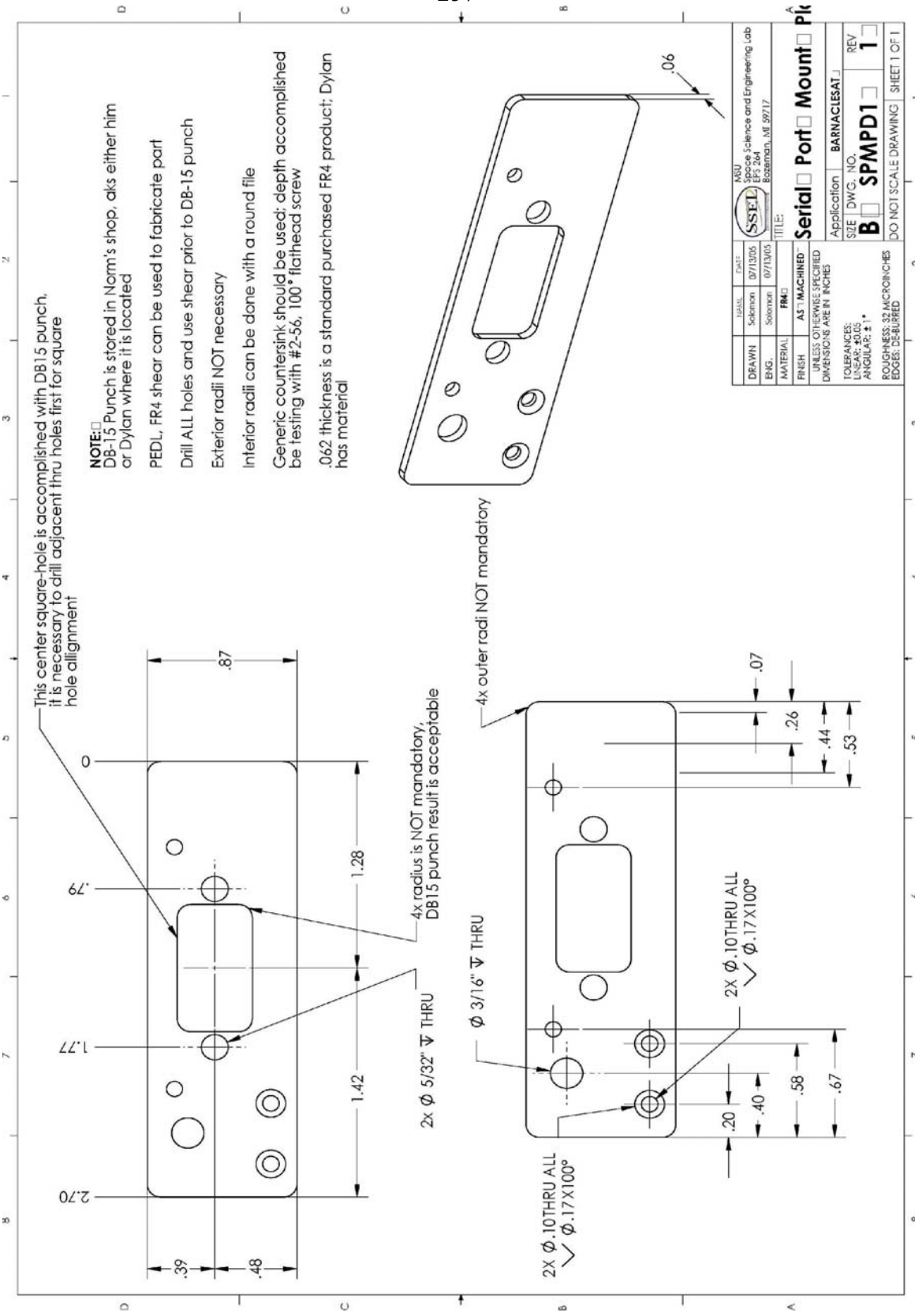
Stress relief notches (x6) as seen in Detail A are all identical

The inner and outer bend radii (R0.74 & R1.74) are not critical and should be achieved by using sheet metal bender

All bends are identical

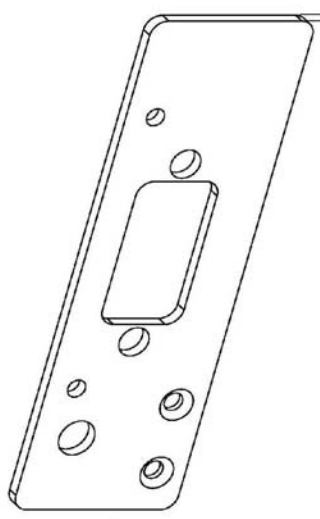
4xR5 is achievable by torquing bracket into its proper location within the top hat with screw and nut

DATE:	07/19/05	DESIGNER:	Science and Engineering Lab
DRAWN:	Solomon	ENG.:	Wright
MATERIAL:	6061-T6 ALUMINUM	TITLE:	Battery Bracket
FINISH:	AS MACHINED	Application:	BARNACLESAT
UNLESS OTHERWISE SPECIFIED DIMENSIONS ARE IN MILLIMETERS			
TOLERANCES:			
LINEAR: ± 0.1			
ANGULAR: $\pm 0.5^\circ$			
ROUGHNESS: 32 MICRONS			
EDGES: DEBURRED			
SIZE:	DWG. NO. B_BB_D1	REV:	1
DO NOT SCALE DRAWING SHEET 1 OF 1			



This center square-hole is accomplished with DB15 punch. it is necessary to drill adjacent thru holes first for square hole alignment

- NOTE:**
- DB-15 Punch is stored in Norm's shop, aks either him or Dylan where it is located
 - PEDL, FR4 shear can be used to fabricate part
 - Drill ALL holes and use shear prior to DB-15 punch
 - Exterior radii NOT necessary
 - Interior radii can be done with a round file
 - Generic countersink should be used; depth accomplished be testing with #2-56, 100° flathead screw
 - .062 thickness is a standard purchased FR4 product; Dylan has material



DESIGN	DATE	BY	APP
Solomon	07/13/05	Solomon	07/13/05
ENG.			
MATERIAL	FR4		
FINISH	AS MACHINED		
UNLESS OTHERWISE SPECIFIED DIMENSIONS ARE IN INCHES			
TOLERANCES: LINEAR: $\pm .005$ ANGULAR: $\pm 1^\circ$			
ROUGHNESS: 32 MICROINCHES EDGES: REQUIRED			
SERIAL <input type="checkbox"/> PORT <input type="checkbox"/> MOUNT <input type="checkbox"/> Pk <input type="checkbox"/>		Application: BARNACLESAT J SIZE: DWG. NO. B SPMPD1 REV: 1	
TITLE:		DO NOT SCALE DRAWING SHEET 1 OF 1	

APPENDIX B
MASS BUDGET

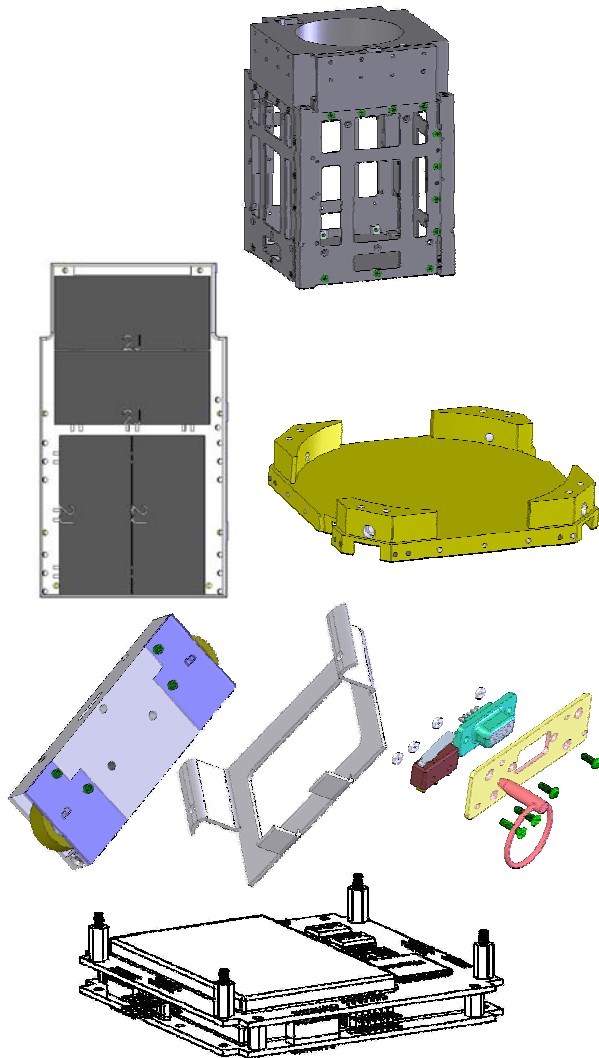
Bsat Mass Budget

	Component	Quantity	Mass/unit (g)	Total (g)	Comments
Structure	Baseplate	1	27	27	per SW
	Tophat	1	118	118	per SW
	Sides	4	39	156	per SW
	Solar Panels	4	74	296	per scale
	Ser. Prt. Mnt. Plt	1	4	4	per SW
	Battery Bracket	2	5	10	per scale
	Total			611	
Hardware	m/f standoffs	4	1.5	6	per SW
	f/f standoffs	4	1	4	per SW
	fasteners	70	0.25	17.5	per SW, 1/4" L
	Total			27.5	
Payload	Tether Assem.	1	280	280	per TUI mass model
	Tether Bracket	1	67	67	per SW
	GPS	1	20	20	per Surrey SGR-05U data sheet
	GPS Ant.	1	9	9	per Nestor, TUI, MAST
	Total			376	
Comm.	Board	1		0	TBD
	Antennas	1	27	27	per SW
	Total			27	
C&DH	Board	1		0	TBD
		Total			0
Power	Solar Cells	12	3.6	43.2	per scale
	Silicon	12	3	36	per scale
	Battery	2	40	80	per CGA103450A data sheet
	Board	1		0	TBD
	Kill Switches	2	2	4	per scale
	Total			163.2	
Misc.	RBF Pin & Swtich	1	8	8	per scale
	DB Connector	1	4	4	per scale
	Total			12	

Grand Total 1216.7
5% misc. 60.835
= 1277.535
Remaining 722.465

APPENDIX C

FASTENER DIAGRAM



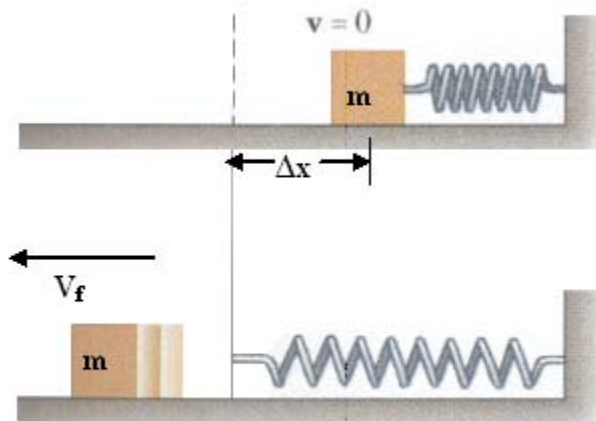
	Component	Fasteners	Quantity	Comments
Primary	Sides (x4)	#2-56, 100°, flathead	16	3/16 L
		#2-56 Helicoil Inserts	16	1.5*dia
	Baseplate	#2-56, 100°, flathead	12	3/16 L
		#2-56 Helicoil Inserts	12	1.5*dia
	Tophat	#2-56, 100°, flathead	16	3/16 L
		#2-56 Helicoil Inserts	48	1.5*dia
Secondary	Solar Panels (x4)	#2-56, 100°, socketcap	24	≥ 1/4 L
	Tether Bracket	#2-56, 100°, flathead	12	3/16 L
		#2-56 Helicoil Inserts	12	1.5*dia
		M2.5 x 0.45 socketcap	4	supplied by TUI
Tertiary	Antenna Housing	#2-56, 100°, flathead	4	1/4 L
		#0-80 socketcap	4	1/2 L
	Acculam™ Plate	#2-56, 100°, flathead	2	3/16 L
		#2-56 nut	2	
	Battery Bracket (x2)	#2-56, 100°, flathead	4	3/16 L
	Electronics Module	#2-56 male/female standoff	4	3/16 HEX x 1/4L
#2-56 female/female standoff		4	1/4 HEX 3/8 L	
#2-56 screws		8	3/4 L	

APPENDIX D

ROCKETPOD™ SPRING FORCE

Calculation of Spring Force

First examine spring/mass system seen below. The figure on the right is information provided by Ecliptic at the SmallSat conference.



The objective of this analytical exercise is to gain insight into the loading environment experience by the tophat and its interface with the spring plunger.

Relevant Equations

$$F = -k \cdot x$$

Hooke's Law

$$\frac{d^2}{dt^2}x + \frac{k}{m} \cdot x = 0$$

O.D.E. of a spring's motion

$$K_m = \frac{1}{2} \cdot m \cdot v^2$$

K.E. of mass moving at constant velocity

$$U_s = \frac{1}{2} \cdot k \cdot x^2$$

P.E. of energy stored in spring while compressed

From information provided by Ecliptic during SmallSat it is possible to determine the exact ejection velocity once a final satellite mass has been determined.

Work Energy Theorem suggests that in the absence of nonconservative forces (i.e. friction), the conservation of energy equation takes on the following form. This equation shows that the kinetic energy of the mass traveling at a known velocity was created exclusively by the stored energy within the spring prior to separation.

$$K_m = U_s$$

$$\text{mass} := 1 \cdot \text{kg}$$

$$\text{vel} := 2 \cdot \frac{\text{m}}{\text{s}}$$

$$\frac{1}{2} \cdot m \cdot v^2 = \frac{1}{2} \cdot k \cdot x^2$$

$$v = \frac{C}{\sqrt{m}}$$

where C is a constant

$$C = \sqrt{k} \cdot x$$

By knowing v and m we can find C

$$C := \text{vel} \cdot \sqrt{\text{mass}}$$

$$C = 2 \frac{\text{kg}^{0.5} \cdot \text{m}}{\text{s}}$$

To check:

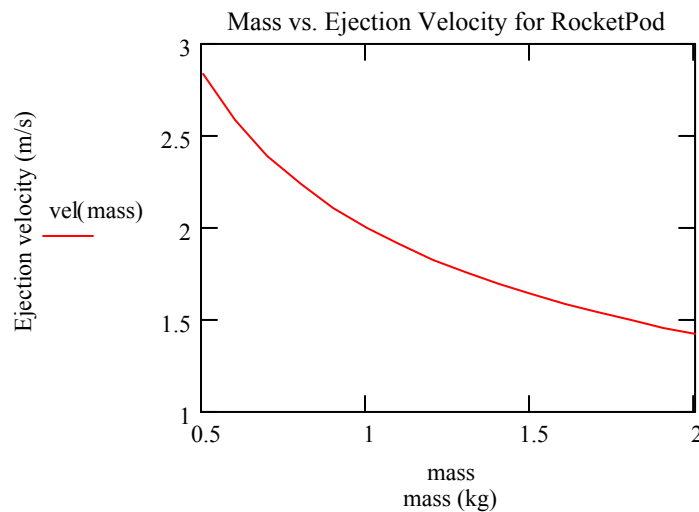
$$m_2 := 2 \cdot \text{kg}$$

$$v_2 := \frac{C}{\sqrt{m_2}}$$

$$v_2 = 1.414 \frac{\text{m}}{\text{s}}$$

$$\text{mass} := .5 \cdot \text{kg}, .6 \text{kg}.. 2 \text{kg}$$

$$\text{vel}(\text{mass}) := \frac{C}{\sqrt{\text{mass}}}$$



The next step is to determine the force acting upon the tophat while stored within the RocketPod. Doug Caldwell from Ecliptic has confirmed that the spring is being compressed to approximately 100 mm. A 100 mm Δ_x will be assumed.

$$\frac{1}{2} \cdot m \cdot v^2 = \frac{1}{2} \cdot k \cdot x^2$$

Conservation of Energy

By knowing $x = 100$ mm, we can find the spring stiffness, k

$$x := 100 \text{ mm}$$

$$k := \frac{m_2 \cdot v_2^2}{x^2}$$

$$k = 0.4 \frac{\text{N}}{\text{mm}}$$

Spring stiffness

$$F_s := k \cdot x$$

$$F_s = 40 \text{ N}$$

Spring force exerted on tophat

APPENDIX E

STRUCTURE ANALYTICAL
WORKSHEETS

Simplified Static Analysis
Material Properties (via MatWeb)

Young's Modulus:

Yield Strength

Density:

$$E_{6061} := 68.9 \cdot 10^9 \cdot \text{Pa}$$

$$\sigma_{y_6061} := 276 \cdot 10^6 \cdot \text{Pa}$$

$$\rho_{6061} := 2700 \frac{\text{kg}}{\text{m}^3}$$

$$E_{7075} := 71.7 \cdot 10^9 \cdot \text{Pa}$$

$$\sigma_{y_7075} := 503 \cdot 10^6 \cdot \text{Pa}$$

$$\rho_{7075} := 2810 \frac{\text{kg}}{\text{m}^3}$$

Poisson's Ratio:

$$\nu := .33$$

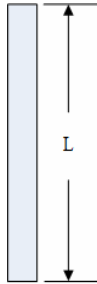
$$E := \begin{pmatrix} E_{6061} \\ E_{7075} \end{pmatrix}$$

$$\sigma_y := \begin{pmatrix} \sigma_{y_6061} \\ \sigma_{y_7075} \end{pmatrix}$$

$$\rho := \begin{pmatrix} \rho_{6061} \\ \rho_{7075} \end{pmatrix}$$

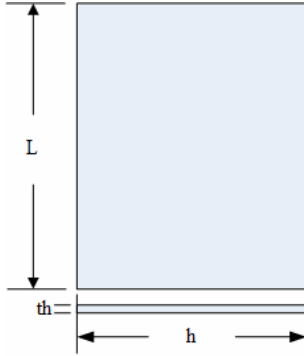
Areas of Interest: Buckling and Bending

Columns



 w

w



Plates

BSat Parameters

$$L := 113.5 \text{ mm}$$

$$w := 8.5 \text{ mm}$$

$$th := 1 \text{ mm}$$

$$h := 83 \text{ mm}$$

$$\text{mass} := 2 \text{ kg}$$

$$L_e := L$$

load factor:

$$lf := 8 \cdot g$$

factor of safety

$$FS := 1.25$$

$$\text{MPa} := 10^6 \cdot \text{Pa}$$

$$P_{\text{load}} := \frac{\text{mass} \cdot FS \cdot lf}{4}$$

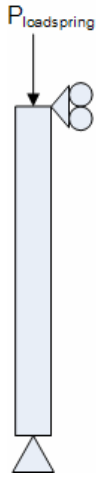
$$P_{\text{load}} = 49.033 \text{ N}$$

$$P_{\text{spring}} := 40 \cdot \text{N}$$

$$I := \frac{w^3 \cdot w}{12}$$

$$I = 435.005 \text{ mm}^4$$

Compression and Buckling Analysis for BSat's launch Rails



Max Axial Compression Load:

$$P_{\text{loadspring}} := P_{\text{load}} + P_{\text{spring}}$$

$$P_{\text{loadspring}} = 89.033\text{N}$$

$$\sigma_{\text{axial_comp_max}} := \frac{P_{\text{loadspring}}}{w \cdot w}$$

$$\sigma_{\text{axial_comp_max}} = 1.232\text{MPa}$$

$$MOS_{\text{axial_comp_max}} := \frac{\sigma_y}{\sigma_{\text{axial_comp_max}}} - 1$$

$$MOS_{\text{axial_comp_max}} = \begin{pmatrix} 222.973 \\ 407.182 \end{pmatrix}$$

For Euler Buckling, the critical buckling stress for a fixed-pinned column is (Gere, 748):

$$\sigma_{\text{buck_cr}} := \frac{\pi^2 \cdot E \cdot I}{L_e^2 \cdot (w \cdot w)}$$

$$\sigma_{\text{buck_cr}} = \begin{pmatrix} 317.822 \\ 330.738 \end{pmatrix} \text{MPa}$$

$$P_{\text{buck_cr}} := \sigma_{\text{buck_cr}} \cdot w \cdot w$$

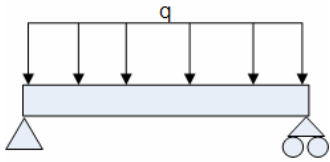
$$P_{\text{buck_cr}} = \begin{pmatrix} 2.296 \times 10^4 \\ 2.39 \times 10^4 \end{pmatrix} \text{N}$$

safety factor:

$$\eta_{\text{clmn}} := \frac{\sigma_{\text{buck_cr}}}{\sigma_{\text{axial_comp_max}}}$$

$$\eta_{\text{clmn}} = \begin{pmatrix} 257.911 \\ 268.392 \end{pmatrix}$$

For Beam Bending (simply-supported)



$$q := \frac{P_{\text{load}}}{L}$$

$$q = 432.011 \frac{\text{N}}{\text{m}}$$

$$x := 0 \cdot \text{mm}, .5 \cdot \text{mm}, 113.5 \text{mm}$$

$$\delta_{\text{beam_mx}} := \frac{5 \cdot q \cdot L^4}{384 \cdot E \cdot I}$$

$$\delta_{\text{beam_mx}} = \begin{pmatrix} 0.031 \\ 0.03 \end{pmatrix} \text{mm}$$

deflection curve:

$$y(x) := \frac{-q \cdot x}{24 \cdot E \cdot 6061 \cdot I} \cdot (L^3 - 2 \cdot L \cdot x^2 + x^3)$$

maximum moment:

$$M_{\text{beam_mx}} := \frac{q \cdot L^2}{8}$$

$$M_{\text{beam_mx}} = 0.696 \text{N} \cdot \text{m}$$

maximum stress:

$$\sigma_{\text{beam_mx}} := \frac{M_{\text{beam_mx}} \cdot \frac{w}{2}}{I}$$

$$\sigma_{\text{beam_mx}} = 6.797 \text{MPa}$$

margin of safety:

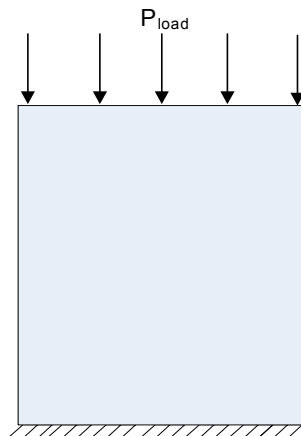
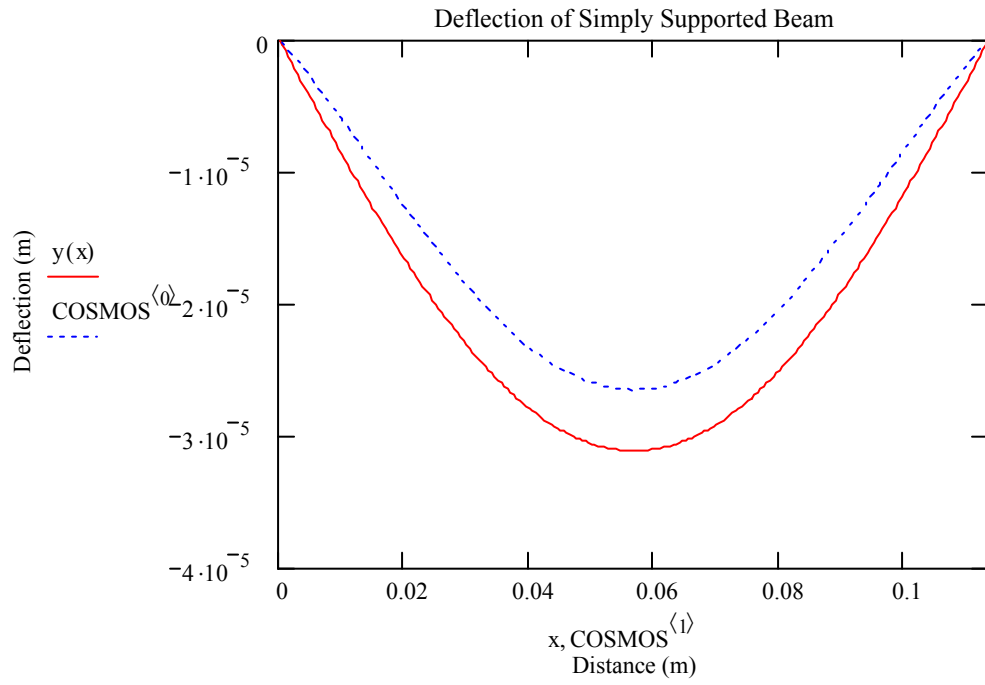
$$\text{MOS}_{\text{beam_mx}} := \frac{\sigma_y}{\sigma_{\text{beam_mx}}}$$

$$\text{MOS}_{\text{beam_mx}} = \begin{pmatrix} 40.609 \\ 74.008 \end{pmatrix}$$

COSMOS BEAM DEFLECTION RESULTS:

COSMOS :=

	0	1
0	0	0.1135
1	$-8.461 \cdot 10^{-7}$	0.1119
2	$-1.758 \cdot 10^{-6}$	0.1103
3	$-2.729 \cdot 10^{-6}$	0.1086
4	$-3.746 \cdot 10^{-6}$	0.107
5	$-4.767 \cdot 10^{-6}$	0.1054
6	$-5.809 \cdot 10^{-6}$	0.1038
7	$-6.868 \cdot 10^{-6}$	0.1022
8	$-7.936 \cdot 10^{-6}$	0.1005
9	$-9.007 \cdot 10^{-6}$	0.0989



Max Compressive Stress in Plate:

$$\sigma_{\text{comp_plate}} := \frac{P_{\text{load}} + P_{\text{spring}}}{t \cdot h}$$

$$\sigma_{\text{comp_plate}} = 1.073 \text{ MPa}$$

$$\text{MOS}_{\text{comp_plate}} := \frac{\sigma_y}{\sigma_{\text{comp_plate}}} - 1$$

$$\text{MOS}_{\text{comp_plate}} = \begin{pmatrix} 256.297 \\ 467.915 \end{pmatrix}$$

For Flat Plate Buckling, the critical buckling stress for a fixed-fixed plate is (Roark & Young, 684):

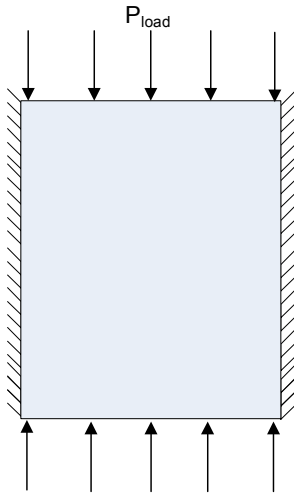


plate buckling coefficient (fixed-fixed):

$$\frac{L}{h} = 1.367$$

$$k_{\text{coeff}} := 3.68$$

$$\sigma_{\text{buck_pl}} := \frac{k_{\text{coeff}} \cdot E}{(1 - \nu^2)} \cdot \left(\frac{t}{h} \right)^2$$

$$\sigma_{\text{buck_pl}} = \begin{pmatrix} 41.303 \\ 42.982 \end{pmatrix} \text{ MPa}$$

$$P_{\text{buck_pl}} := \sigma_{\text{buck_pl}} \cdot h \cdot t$$

$$P_{\text{buck_pl}} = \begin{pmatrix} 3.428 \times 10^3 \\ 3.567 \times 10^3 \end{pmatrix} \text{ N}$$

safety factor:

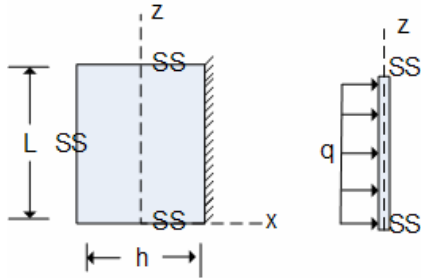
$$\eta_{\text{fltplt}} := \frac{\sigma_{\text{buck_pl}}}{\sigma_{\text{comp_plate}}}$$

$$\eta_{\text{fltplt}} = \begin{pmatrix} 38.504 \\ 40.069 \end{pmatrix}$$

Bending of a uniformly loaded flat plate over its surface:

(Roark and Young, 462)

Three edges simply supported (SS), long edge fixed:



For side plates:

$$L = 113.5 \text{ mm}$$

$$h = 83 \text{ mm}$$

Mass of side plate:

$$m_{\text{sp}} := L \cdot h \cdot t \cdot \rho \quad 707 \text{ kg/m}^3$$

$$m_{\text{sp}} = 0.026 \text{ kg}$$

Load:

$$q := \frac{FS \cdot l_f \cdot m_{\text{sp}}}{L \cdot h}$$

$$q = 275.567 \text{ Pa}$$

bending coefficient:

$$\frac{L}{h} = 1.367$$

$$\beta := .617$$

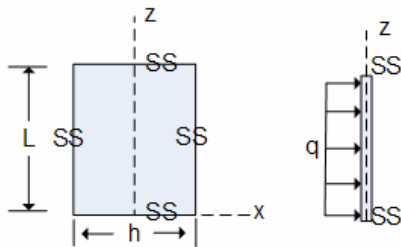
$$\sigma_{\text{bending}} := \frac{\beta \cdot q \cdot h^2}{t^2}$$

$$\sigma_{\text{bending}} = 1.171 \text{ MPa}$$

$$MOS_{\text{fltp}|\text{bending}} := \frac{\sigma_y}{\sigma_{\text{bending}}}$$

$$MOS_{\text{fltp}|\text{bending}} = \begin{pmatrix} 235.636 \\ 429.437 \end{pmatrix}$$

Four edges simply supported:



For baseplate:

$$L := 100 \text{ mm}$$

$$h := 100 \text{ mm}$$

Mass of baseplate:

$$m_{bp} := L \cdot h \cdot th \cdot \rho \quad 6061$$

Load:

$$q := \frac{FS \cdot lf \cdot m_{bp}}{L \cdot h}$$

$$q = 264.78 \text{ Pa}$$

bending coefficient:

$$\frac{L}{h} = 1$$

$$\beta := .2874$$

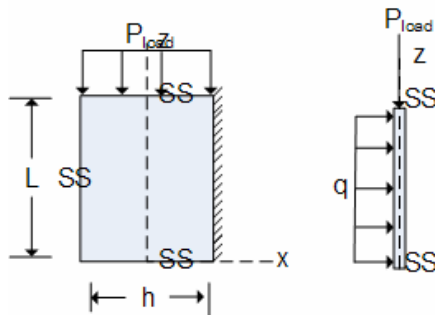
$$\sigma_{\text{bending}} := \frac{\beta \cdot q \cdot h^2}{th^2}$$

$$\sigma_{\text{bending}} = 0.761 \text{ MPa}$$

$$MOS_{\text{baseplate}} := \frac{\sigma_y}{\sigma_{\text{bending}}}$$

$$MOS_{\text{baseplate}} = \begin{pmatrix} 362.692 \\ 660.993 \end{pmatrix}$$

Bending of a simply supported flat plate with uniform loading over entire plate plus uniform compression applied to short edges.
(Roark and Young, 460)



For side plates:

$$L := 113.5 \text{ mm}$$

$$h := 83 \text{ mm}$$

Mass of side plate:

$$m_{sp} := L \cdot h \cdot th \cdot \rho \quad 7075$$

Stress due to mass of plate:

$$\sigma_{\text{plate}} := \frac{FS \cdot lf \cdot m_{sp}}{th \cdot h}$$

$$\sigma_{\text{plate}} = 3.128 \times 10^4 \text{ Pa}$$

load:

$$q := \frac{FS \cdot lf \cdot m_{sp}}{L \cdot h}$$

$$q = 275.567 \text{ Pa}$$

bending coefficients for x and z directions:

$$\frac{L}{h} = 1.367$$

$$\beta_z := .3$$

$$\beta_x := .43$$

bending stress

$$\sigma_h := \frac{\beta_z \cdot q \cdot h^2}{th^2} + \frac{P_{\text{spring}}}{4 \cdot h \cdot th}$$

$$\sigma_h = 6.9 \times 10^5 \text{ Pa}$$

$$\sigma_L := \frac{\beta_x \cdot q \cdot h^2}{th^2}$$

$$\sigma_L = 8.163 \times 10^5 \text{ Pa}$$

By taking the maximum of these two stress values:

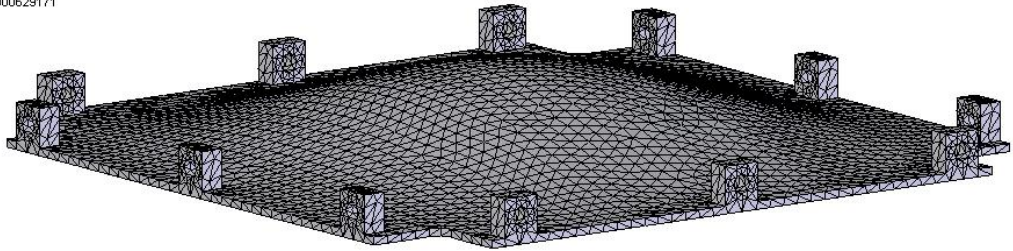
$$MOS_{\text{compression_normal}} := \frac{\sigma_y}{\sigma_L}$$

$$MOS_{\text{compression_normal}} = \begin{pmatrix} 338.11 \\ 616.192 \end{pmatrix}$$

APPENDIX F

STRUCTURAL HARMONIC
RESPONSE FIGURES

Model name: baseplate_rev6_flight
 Study name: frequency
 Plot type: Frequency Plot1
 Mode Shape : 1 Value = 962.79 Hz
 Deformation scale: 0.000629171

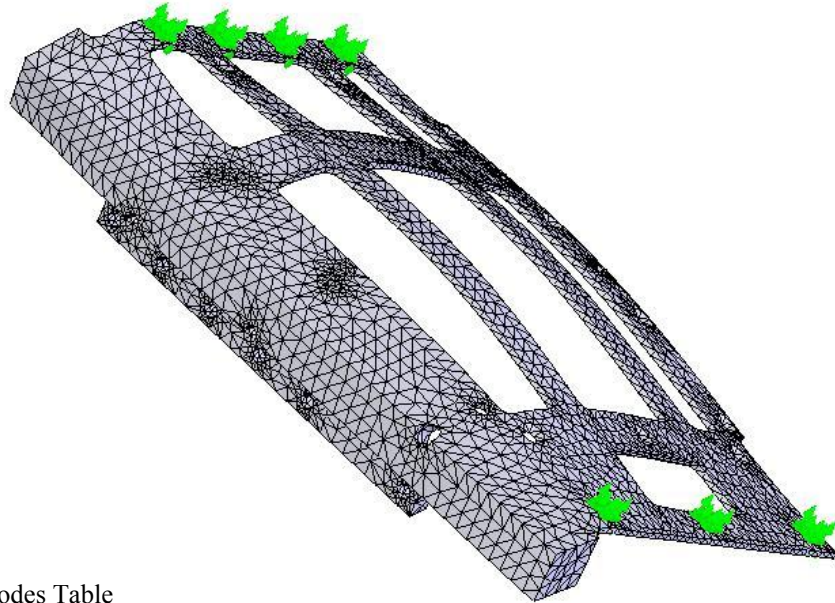


Baseplate Natural Frequency

BaseplateVibration ModesTable

Study name: frequency Baseplate Flight			
Mode No.	Frequency(Rad/sec)	Frequency(Hertz)	Period (Sec)
1	6049.4	962.79	0.001039
2	12216	1944.3	0.000514
3	12255	1950.5	0.000513
4	17768	2827.8	0.000354
5	21920	3488.7	0.000287

Model name: sides_flight
 Study name: natural frequency
 Plot type: Frequency Plot1
 Mode Shape : 1 Value = 388.18 Hz
 Deformation scale: 0.00119071

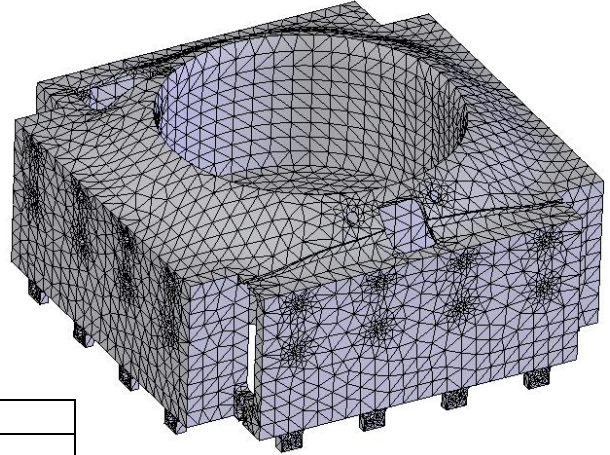


BSat Side Vibration Modes Table

Study name: natural frequency Individual Side			
Mode No.	Frequency(Rad/sec)	Frequency(Hertz)	Period(Sec)
1	2439	388.18	0.0025761
2	3127.1	497.69	0.0020093
3	4190.8	666.98	0.0014993
4	5866.1	933.61	0.0010711

Fundamental Frequency of Individual Side

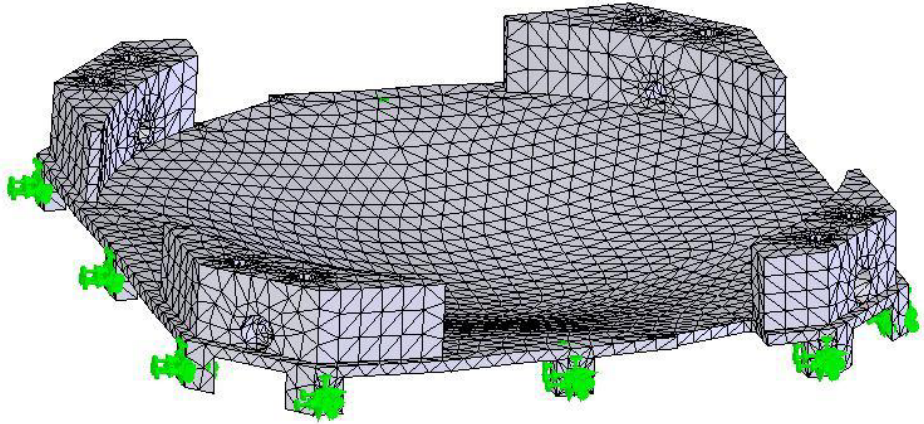
Model name: tophat_antennas_rev7_flight
 Study name: frequency
 Plot type: Frequency Plot1
 Mode Shape: 1 Value = 1594.6 Hz
 Deformation scale: 0.00147945



Tophat Natural Frequency Modes

Study name: frequency Tophat Flight			
Mode No.	Frequency(Rad/sec)	Frequency(Hertz)	Period(Sec)
1	10019	1594.6	0.00062713
2	27569	4387.7	0.00022791
3	30227	4810.7	0.00020787
4	32189	5123	0.0001952
5	34245	5450.2	0.00018348

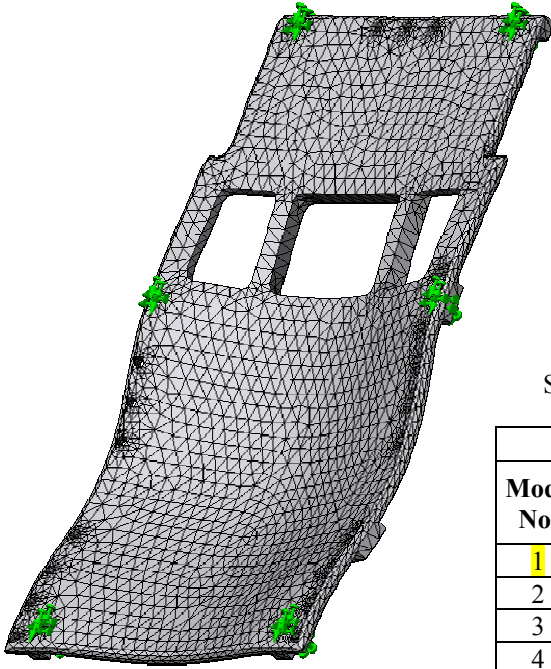
Tophat Natural Frequency



Tether Bracket Natural Frequency

Tether Bracket Natural Frequency Modes

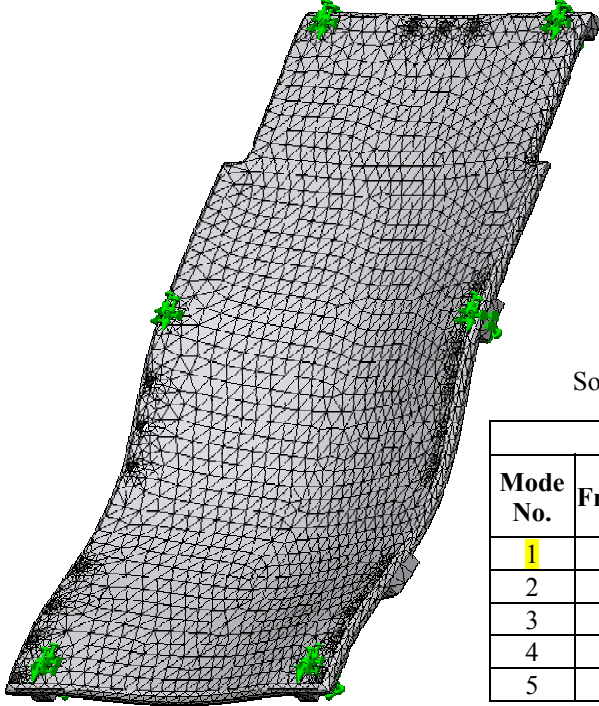
Study name: frequency Tether Bracket Flight			
Mode No.	Frequency(Rad/sec)	Frequency(Hertz)	Period(Sec)
1	8793.4	1399.5	0.00071453
2	17173	2733.1	0.00036588
3	17350	2761.4	0.00036214
4	23402	3724.6	0.00026849
5	27717	4411.3	0.00022669



Solar Panel_1 Nатура Frequency Modes

Study name: frequency Solar Panel 1			
Mode No.	Frequency(Rad/sec)	Frequency(Hertz)	Period(Sec)
1	16512	2628	0.000381
2	22108	3518.6	0.000284
3	28919	4602.6	0.000217
4	32710	5205.9	0.000192
5	35795	5697	0.000176

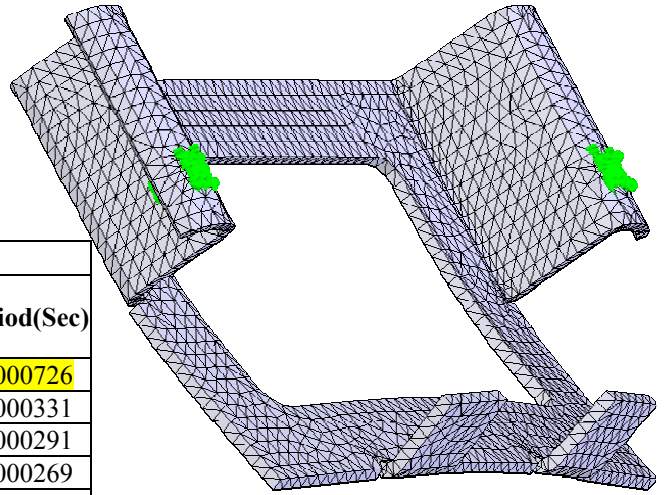
FSolar Panel 1 Natural Frequency



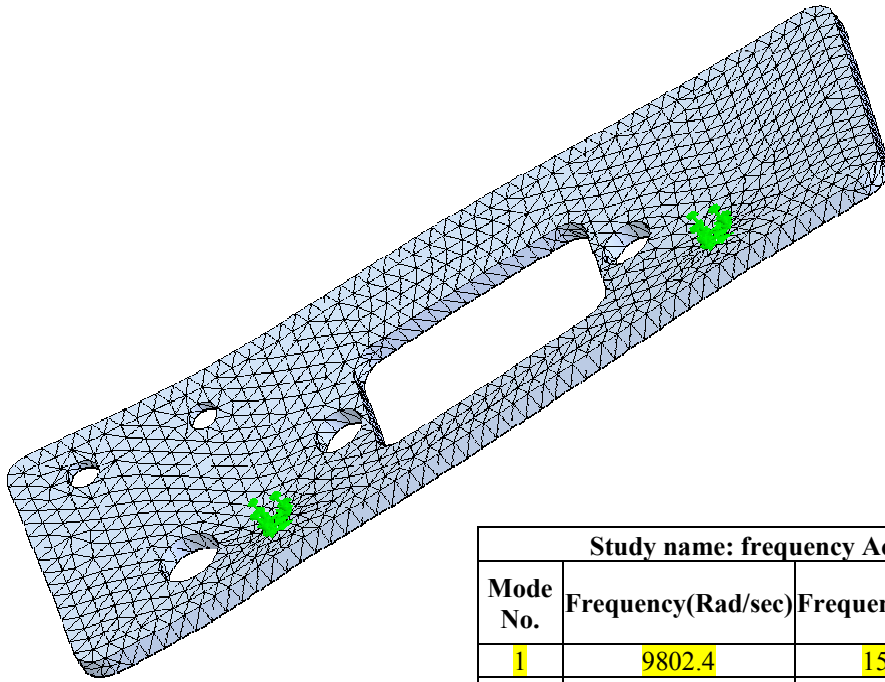
Solar Panel_2 Na Frequency Modes

Study name: frequency Solar Panel 2			
Mode No.	Frequency(Rad/sec)	Frequency(Hertz)	Period(Sec)
1	16518	2628.9	0.00038
2	21043	3349	0.000299
3	28812	4585.5	0.000218
4	32933	5241.5	0.000191
5	36745	5848.1	0.000171

Solar Panel_2 Natural Frequency



Study name: frequency Battery Bracket			
Mode No.	Frequency(Rad/sec)	Frequency(Hertz)	Period(Sec)
1	8653.2	1377.2	0.000726
2	18986	3021.8	0.000331
3	21586	3435.5	0.000291
4	23344	3715.3	0.000269
5	32118	5111.7	0.000196



Study name: frequency Acculam Plate			
Mode No.	Frequency(Rad/sec)	Frequency(Hertz)	Period(Sec)
1	9802.4	1560.1	0.000641
2	11167	1777.3	0.000563
3	14171	2255.5	0.000443
4	20810	3312	0.000302
5	27547	4384.2	0.000228

APPENDIX G

VIBROACOUSTIC RESPONSE
MATLAB CODE

One-Third Octave Center Frequency (Hz)	7900 Three-Stage Mission	7900 Two-Stage Mission	7400 Three-Stage Mission	7400 Two-Stage Mission
31.5	121.5	121.5	119.9	119.9
40	124	124	122.5	122.5
50	127	127	127	127
63	127.5	127.5	126.1	126.1
80	128.5	128.5	127.2	127.2
100	129	129.5	127.8	128.3
125	129.5	130.5	128.3	129.3
160	129.5	131	128.4	129.9
200	130	132	129	131
250	130	133	129.1	132.1
315	130	135	129.1	134.1
400	129	139	128.2	138.2
500	126.5	140.5	126.5	140.5
630	124	138	124	138
800	121	133	121	133
1000	117	131	117	131
1250	114.5	130.5	114.5	130.5
1600	112	128.5	112	130.5
2000	109.5	127	109.5	128.5
2500	108	127	108	127
3150	106.5	125	106.5	127
4000	104.5	124	104.5	125
5000	104	120.5	104	124
6300	103	119.5	103	120.5
8000	102.5	118.5	102.5	119.5
10000	102.5	146.6	102.5	118.5

Delta II Acoustic Data

%this MATLAB code is intended to solve for the response of a flatplate to the
 %acoustic environment. this code is the product of a methodology outlined by Sarafin
 %and MATLAB code generate by a group at Cornell University.
 function out = flatplate(a, b, th, E, v, rho);

disp('a (meters)='), disp(a)
 disp('b (meters)='), disp(b)
 disp('plate thickness(meters)='), disp(th)
 disp('Youngs Modulus (Pa=)'), disp(E)
 disp('Poisons Ratio='), disp(v)
 disp('Desnity (kg/m^3)='), disp(rho)

%assumed damping ratio
 dr=.01;

%%%%%%%%Determining Natural Frequencies
 %bending stiffness or bending constant of a flat plate
 D=E*th^3/(12*(1-v^2));
 %number of mode shapes for this analysis

```

p=5;

natural_f=zeros(p,p);
for (i=1:p)
    for (j=1:p)
        natural_f(i,j)=(pi/2)*((i/a)^2 + (j/b)^2)*sqrt(D/(rho*th));
    end
end
natural_f; %(Hz)
wn=2*pi*natural_f %(rad/sec)
disp('natural frequency (Hz)='), disp(natural_f)

%%%%%%%%Vibration mode shapes for a uniform, simply supported plate
%incrementing the (x,y) coordinates of plate
x=0:a/100:a;
y=0:b/100:b;

q=size(x);
for(i=1:q(2))
    for(j=1:q(2))
        mode_shapes1(i,j)=sin(pi*x(i)/a)*(sin(pi*y(j)/b));
    end
end
for(i=1:q(2))
    for(j=1:q(2))
        mode_shapes2(i,j)=sin(2*pi*x(i)/a)*(sin(pi*y(j)/b));
    end
end

subplot (3,2,1);
contour3(x,y,mode_shapes1)
title('Modal Displacement Amplitude of Plate at Fundamental Frequency')
xlabel('Distance along Width of Plate')
ylabel('Distance along Length of Plate')
xlabel('Displacement Amplitude')
subplot (3,2,2);
contour3(x,y,mode_shapes2)
title('Modal Displacement Amplitude of Plate at 2nd Natural Frequency')
xlabel('Distance along Width of Plate')
ylabel('Distance along Length of Plate')
xlabel('Displacement Amplitude')

```

```

%%%%%%%%Modal displacement amplitude at the plate's center (a/2,b/2)
for (i=1:p)
    for(j=1:p)
        disp_amp(i,j)=sin(i*pi/2)*sin(j*pi/2);
    end
end
disp_amp

%%%%%%%%Need to mass-normalize the mode shapes
%generalized mass (kg)
gm=rho*th*a*b/4;
phi_center_norm=disp_amp/(sqrt(gm));
phi_center_norm;

%%%%%%%%Need to compute the net volume swept by the vibration mode shape
%This value is called the generalized force coefficient
%Multiplying by pressure results in the generalized force
%Two methods will be deployed here bc of the difference between low and
%high frequency pressure
%First step is to assume a pressure distribution function on the surface of
%the plate; this is satisfied by dividing the speed of sound by the plate's
%width (a)
%"a" in this case is assumed to be the acoustic wavelength; the frequency
%of sound that has a wavelength as long as the plate's width

%speed of sound (m/s)
sos=335;
%transition frequency (Hz)
trf=sos/a;
disp('transition frequency (Hz)=', disp(trf))

%%%%%%%%For Low-frequency band
%For the low-frequency band, pressure is assumed correlated over the entire
%panel surface
for (i=1:p)
    for (j=1:p)
        coeff_low(i,j)=(a*b/(i*j*(pi^2)*sqrt(gm)))*((1-cos(i*pi))*(1-cos(j*pi)));
    end
end

%%%%%%%%For High-frequency band
%We assume pressure is correlated over each quarter-panel region; thus for
%the entire panel the generalized force coef. are as follows
for (i=1:p)

```

```

for (j=1:p)
    coeff_high(i,j)=(sqrt(4)*a*b/(i*j*(pi^2)*sqrt(gm)))*((1-cos(i*pi/2)*(1-
cos(j*pi/2)))));
end
end

%%%%%%%%%Next we need to convert the SPL curve to a pressure spectral density curve
%The information below is provide in the DeltaII Payload Planners Guide
freq_spl=[31.5 40 50 63 80 100 125 160 200 250 315 400 500 630 800 1000 1250 1600
2000 2500 3150 4000 5000 6300 8000];
dB_spl=[121.5 124 127 127.5 128.5 129.5 130.5 131 132 133 135 139 140.5 138 133 131
130.5 128.5 127 127 125 124 120.5 119.5 118.5];
%vibracoustic=[freq_spl;dB_spl]';
subplot(3,2,3);
plot(freq_spl,dB_spl)
title('Delta II Acoustic SPL Data')
xlabel('Frequency (Hz)')
ylabel('SPL (dB)')

%The acoustic environment is described by a plot of sound pressure level
%(SPL) or simply pressure spectral density
%This requires finding the root mean-square pressuar at the frequencies

%reference pressure (Pa)
pressure_ref=2e-5;

q=size(freq_spl);

for (i=1:q(2));
    deltaf(i)=.2316*freq_spl(i); %frequency bandwidth
    rms_p(i)=pressure_ref*(10^(dB_spl(i)/20)); %rms pressure
    PSD(i)=(rms_p(i)^2)/deltaf(i); %pressure spectral density (PSD)
end
subplot(3,2,4);
loglog(freq_spl,PSD)
title('Acoustic Pressure Spectral Density (PSD)')
xlabel('Mean Geometric Frequency (Hz)')
ylabel('Pressure Spectral Density (Pa^2/Hz)')
grid

%%%%%%%%%Next step is to compute the response spectral density for the plate
%We are going to calculate the acceleration response spectral desnity
%This is done by; taking the transfer function that relates the acceleratoin
%response at the plate's center to the applied pressure

```

```

%This is done by taking the Fourier transform of the equation of the
%equations of motion

num=cell(p);
den=cell(p);

for (i=1:p)
    for (j=1:p)
        if(natural_f(i,j)<trf)
            num(i,j)={[-1 0 0]*phi_center_norm(i,j)*coeff_low(i,j)};
            den(i,j)={[-1 (2*dr*wn(i,j)) wn(i,j)^2]};
        else
            num(i,j)={[-1 0 0]*phi_center_norm(i,j)*coeff_high(i,j)};
            den(i,j)={[-1 (2*dr*wn(i,j)) wn(i,j)^2]};
        end
    end
end

%%%%%%%%Need to sum the transfer functions
Hlow=tf(num,den);
Hf=tf([0],[1]);
for (i=1:p)
    for(j=1:p)
        Hf=Hlow(i,j)+Hf;
    end
end

%%%%%%%%Need to calculate the magnitude of the transfer function at the SPL frequencies
w_spl=freq_spl*2*pi;
deltaw=deltaf*2*pi;
[mag,phase]=bode(Hf,w_spl);

%%%%%%%%Computing the response acceleration spectral density
g=9.81 %gravity (m/s^2)
for (i=1:q(2))
    H(i)=mag(i);
    PSD_squared(i)=PSD(i)*PSD(i);
    Wz(i)=((H(i))^2)*PSD_squared(i)/(g^2);
end

subplot(3,2,5);
loglog(freq_spl,Wz)
title('Response Acceleration Spectral Density')
xlabel('Frequency (Hz)')

```

```

ylabel('g^2/Hz')
grid

%%%%%%%%%Need to numerically integrate the response acceleration SD to find the area
under
%%%%%%%%%the curve

r=0
for (i=1:q(2))
    r=r+Wz(i)*deltaf(i);
end
rms_acceleration=sqrt(r) %g's

%%%%%%%%%Need to check that the peak displacement of this plate is not more
%%%%%%%%%that about half the plate's thickness to ensure the small-delfection
%%%%%%%%%method usded is applicable.
    %need to convert the acceleration PSD to displacement PSD

for (i=1:q(2))
    Dz(i)=Wz(i)/((2*pi*freq_spl(i))^4);
end

subplot(3,2,6);
loglog(freq_spl,Dz)
title('Response Displacement Spectral Density')
xlabel('Frequency (Hz)')
ylabel('m^2/Hz')
grid

s=0;
for (i=1:q(2))
    s=s+Dz(i)*deltaf(i);
end
rms_displacement=sqrt(s) %m

% %%%%%%%%%%Random Vibration for the same
%
% %%%%%%%%%%plate%%%%%%%%%
%
%
% rf_spl=[20 300 700 2000]; %Hz
% rf_asd=[.0016 .06 .06 .021]; %g^2/Hz

```

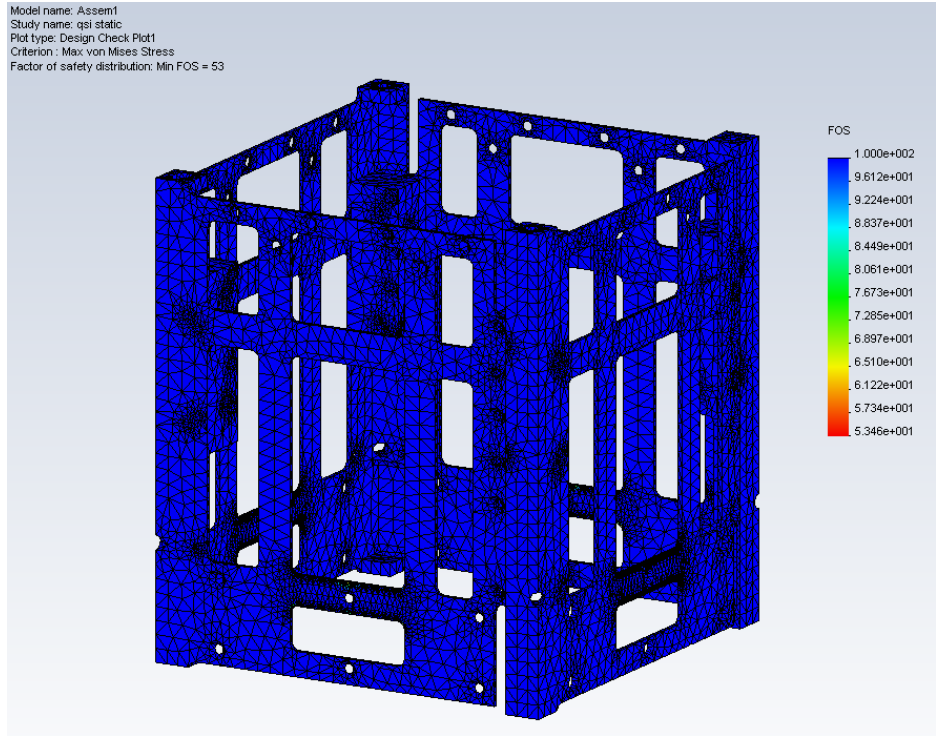


```

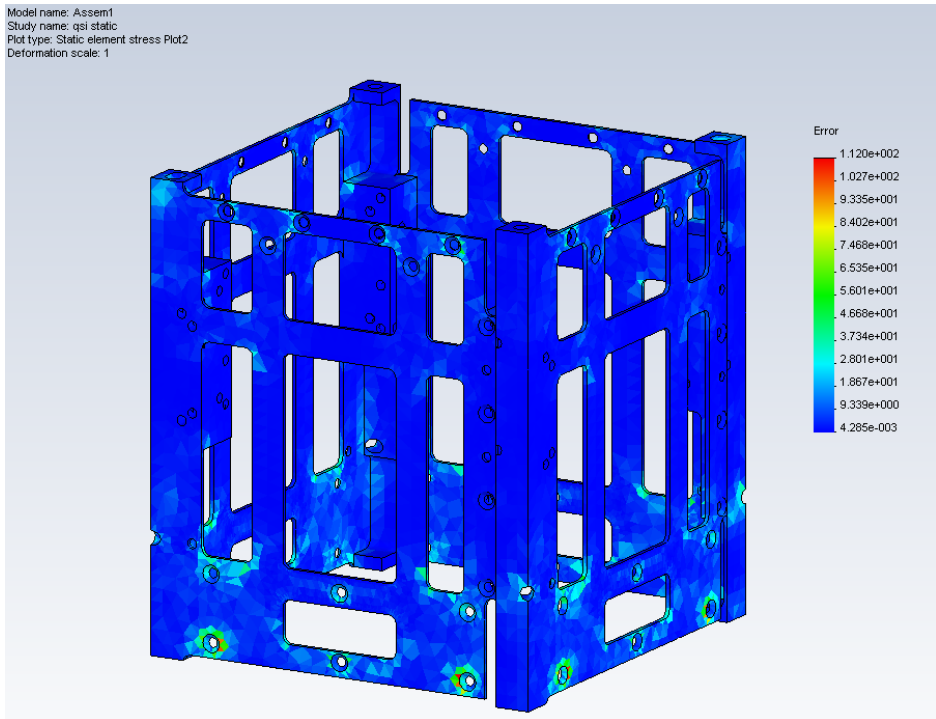
% fmin=min(rf_spl);
% fmax=max(rf_spl);
% fdelta=(fmax-fmin)/100;
% W=2*pi*rf_spl
%
% %First five modes of vibration from previous results (rad/sec)
% wn_rad=[3012.7,7549.2,2403,4085.1,6247.8];
%
% subplot(4,2,7);
% loglog(rf_spl,rf_asd);
% title('Random Acceleratoin Spectral Density')
% xlabel('Mean Geometric Frequency (Hz)')
% ylabel('Random Acceleration Spectral Density g^2/Hz')
% grid
%
% for (i=1:2)
%   H_mag=((1-(W/wn_rad(i)).^2)+(2*dr*(W/wn_rad(i))).^2).^(-.5);
%   H_mag_square=H_mag.^2;
%   y=H_mag_square.*rf_asd
%   figure
%   title(j)
%   loglog(W,y)
%   xlabel('Frequency (Hz)')
%

```

APPENDIX H
SAFETY FACTORS
AND
ERROR CONVERGENCE

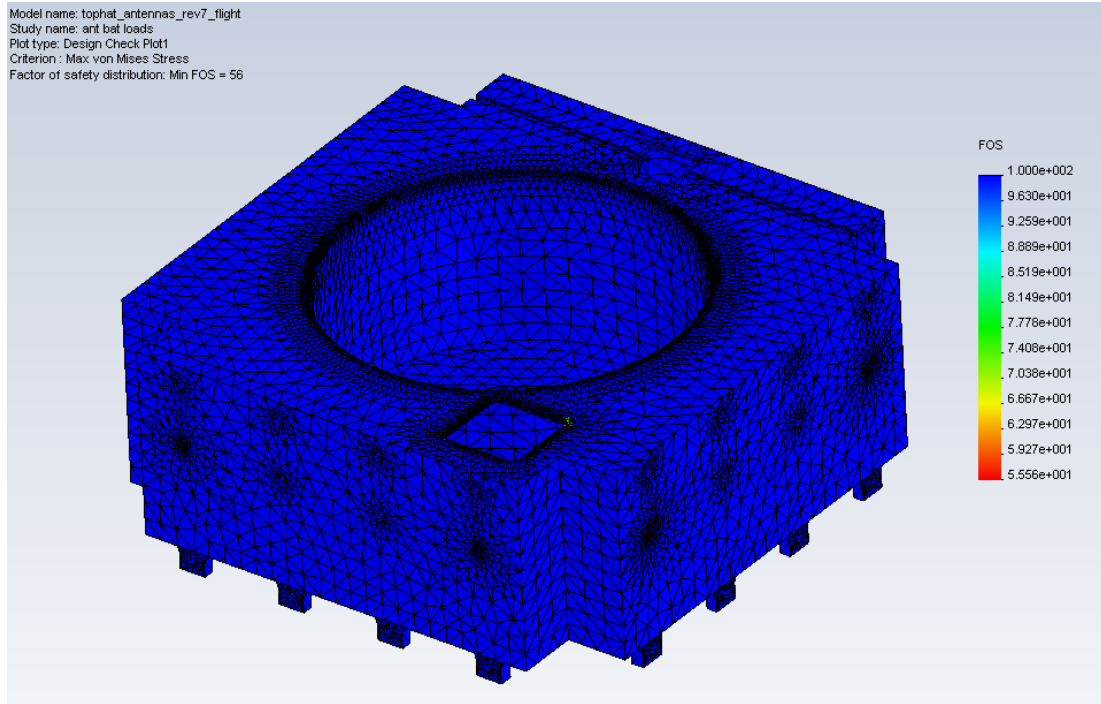


Margin of Safety, Sides

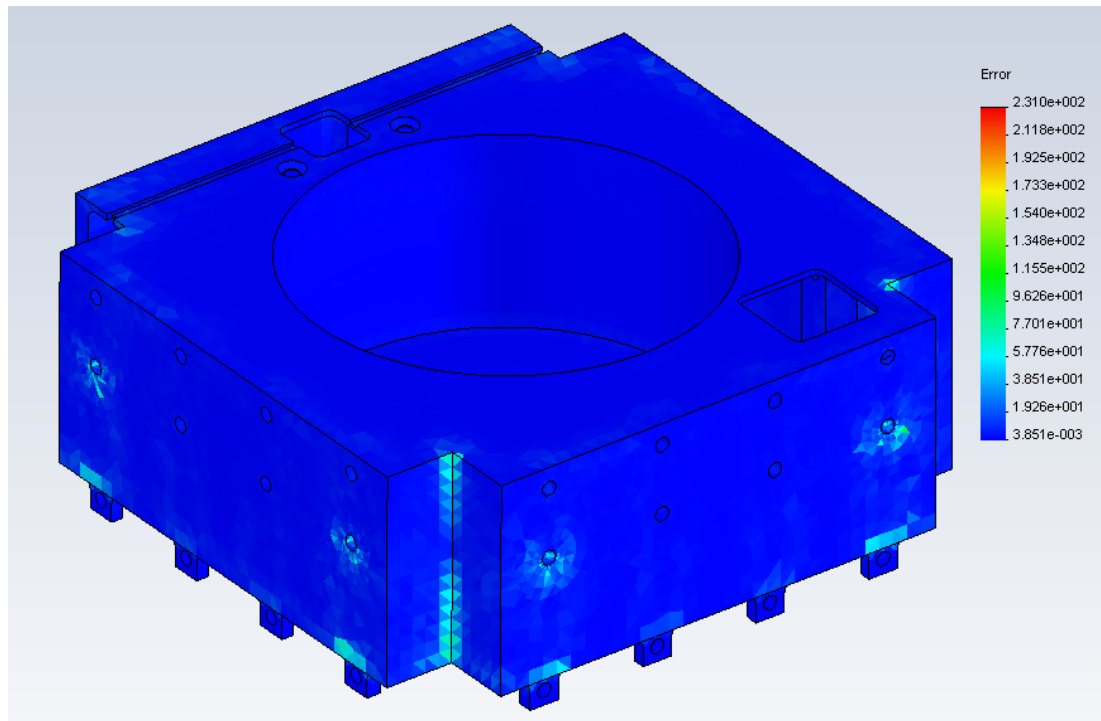


Error Plot, Sides

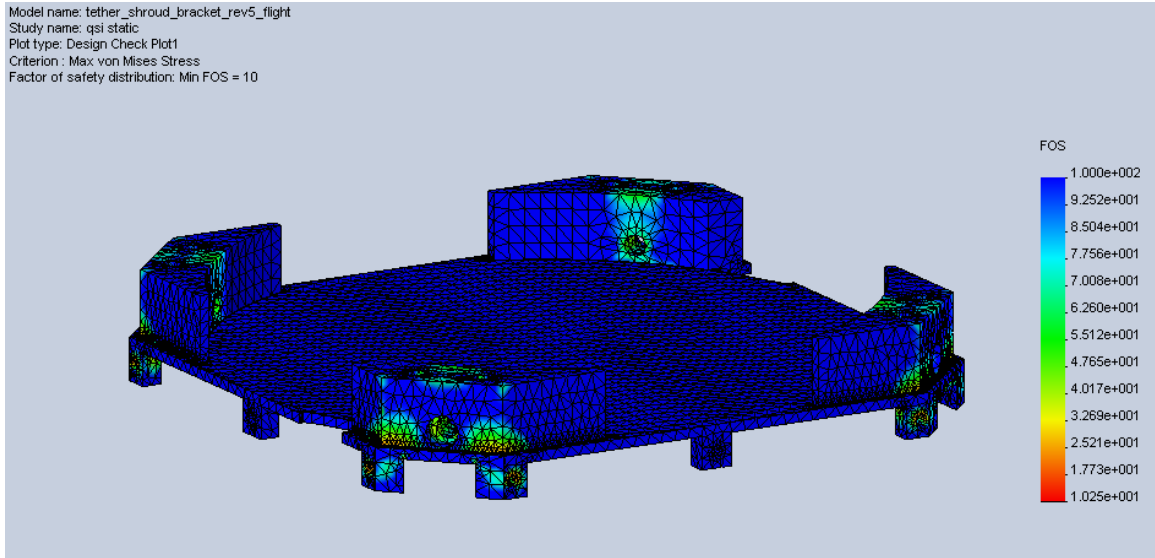
Model name: tophat_antennas_rev7_flight
Study name: ant bat loads
Plot type: Design Check Plot1
Criterion : Max von Mises Stress
Factor of safety distribution: Min FOS = 56



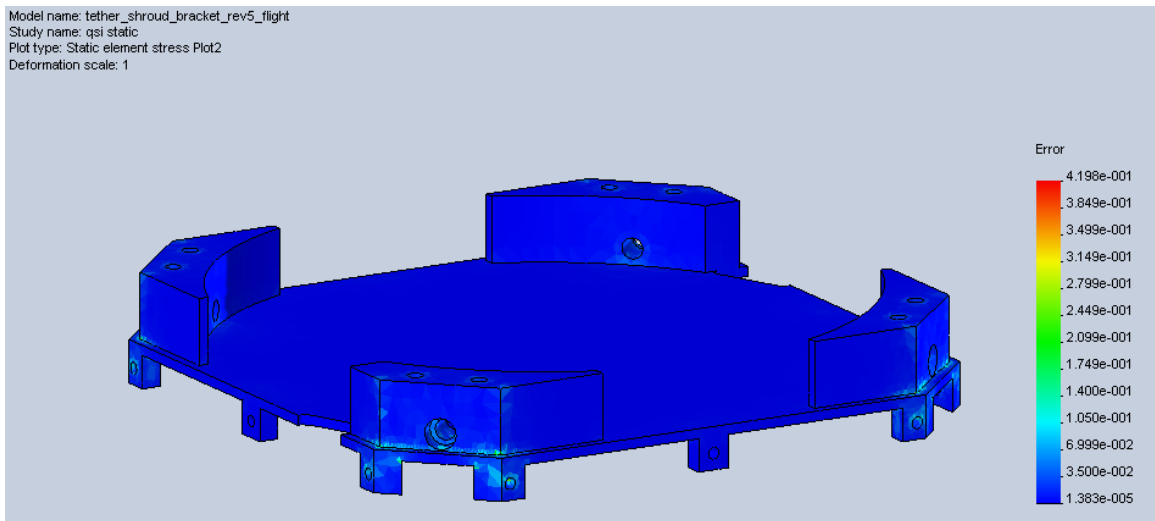
Margin of Safety, Tophat



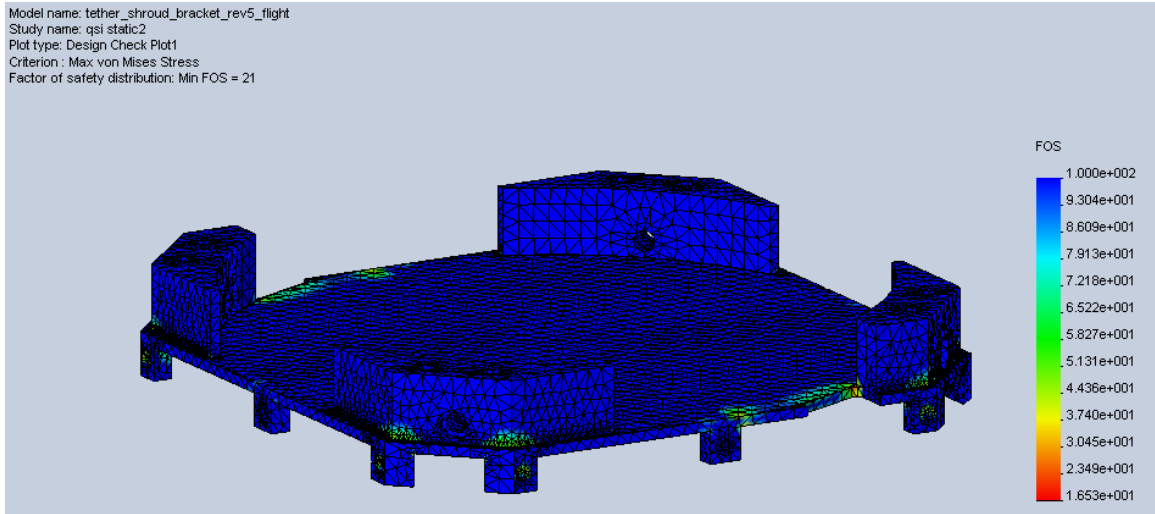
Error Plot, Tophat



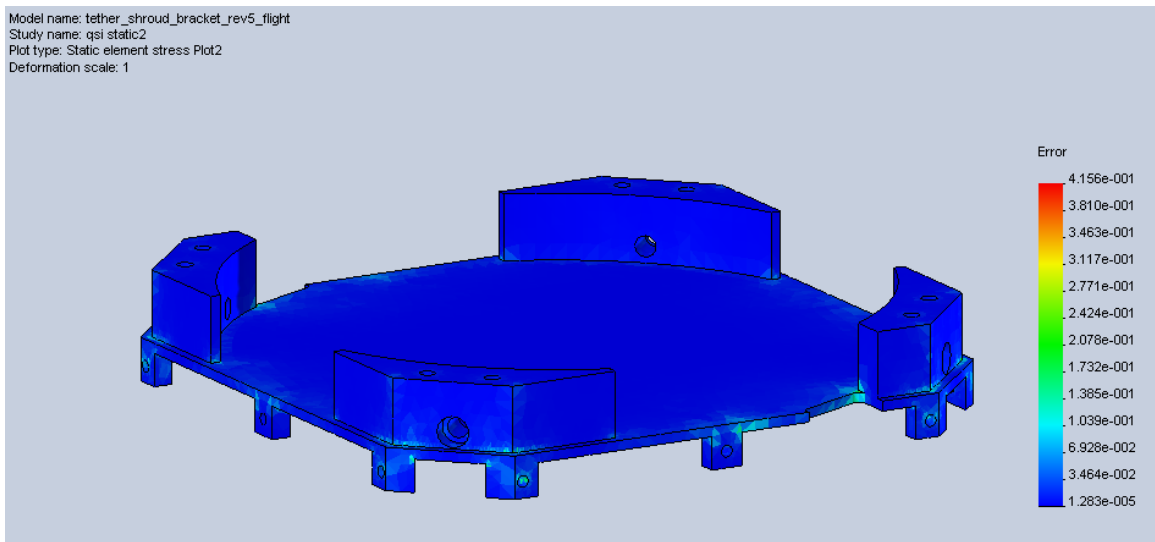
Margin of Safety for Bearing, Tether Bracket



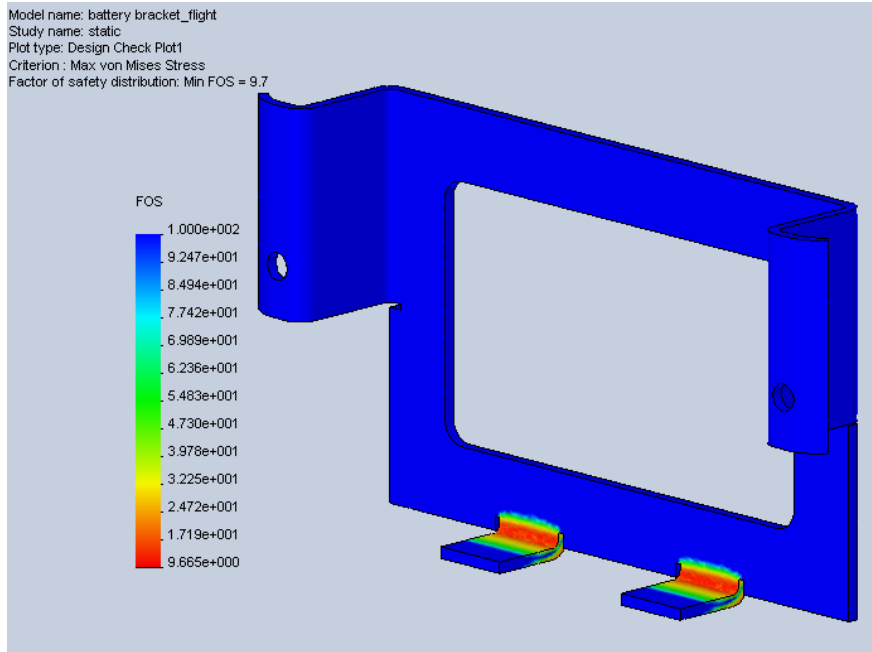
Error Plot for Bearing, Tether Bracket



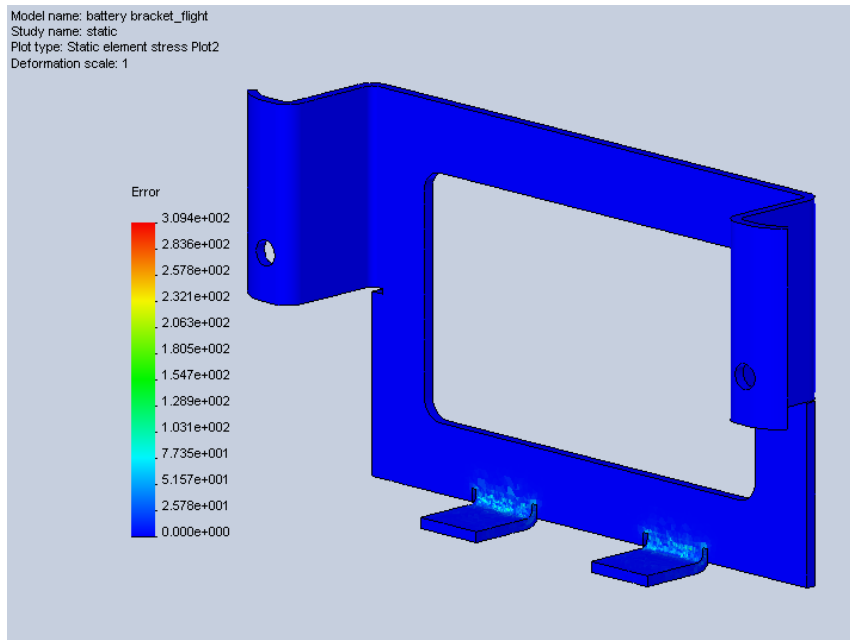
Margin of Safety for Quasi-Static Loading, Tether Bracket



Error Plot for Quasi-Static Loading, Tether Bracket



Margin of Safety, Battery Bracket



Error Plot, Battery Bracket

APPENDIX I

FABRICATION COSTS

Materials: 7075-T73 Aluminum

Quantity	length	width	height	cost	total
4	6"	6"	1-1/2"	70.97\$	283.88\$
12	6"	5"	5/8"	21.75\$	261.00\$
				total	544.88\$

Materials: 6061-T651 Aluminum

Quantity	length	width	height	cost	total
4	6"	6"	1-1/2"		
12	6"	5"	5/8"		
				total	\$0.00

Would like to know where material was ordered from

Tooling

	Quantity	Price/per	Total
3/4"	4	\$24.99	\$99.96
1/2"	4	\$14.38	\$57.52
3/8"	4	\$9.37	\$37.48
1/4"	4	\$9.37	\$37.48
1/8"	8	\$18.98	\$151.84
3/16" BEM	2	\$17.38	\$34.76
100 ° chmr tool	2	\$13.83	\$27.66
2-56 tap	6	\$6.85	\$41.10
3/32 drill	12	\$0.77	\$9.24
5/64 drill	12	\$0.77	\$9.24
#3 drill	12	\$1.34	\$16.08
#29 drill	12	\$0.87	\$10.44
helicoil	100	\$0.45	\$45.00
helicoil insert tool	2	\$18.56	\$37.12
		total	\$614.92

Fabrication

Part	Setups	RT (Hrs)
baseplate	5	1
Side 1	5	3
Side 2	5	3
Side 3	5	3
Side 4	5	3
Tophat	6	4
SP_1	2	2
SP_2	2	2
SP_3	2	2
SP_4	2	2
Teth. Brack		
total		25

Total cost estimation in Dollars

Materials	\$544.88
Tooling	\$614.92
Cycle time	\$1,250.00
Total	\$2,409.80

APPENDIX J

SIMPLIFIED GEOMETRY

Steady-State Energy Balance and Thermal Analysis

Satellite Configuration: External Dimensions

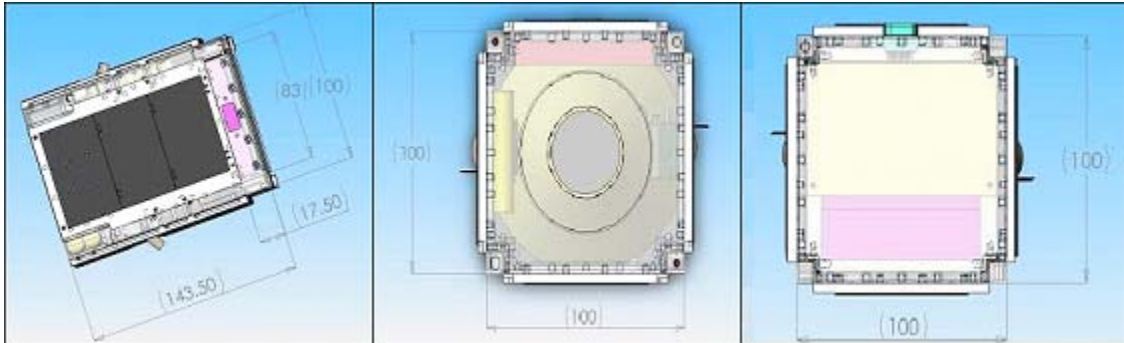


Figure I.1

Figure I.2

Figure I.3

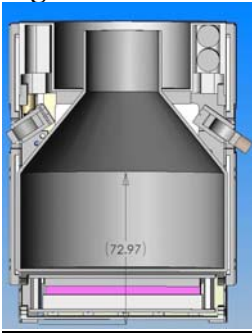
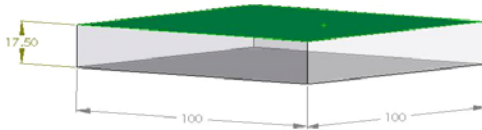


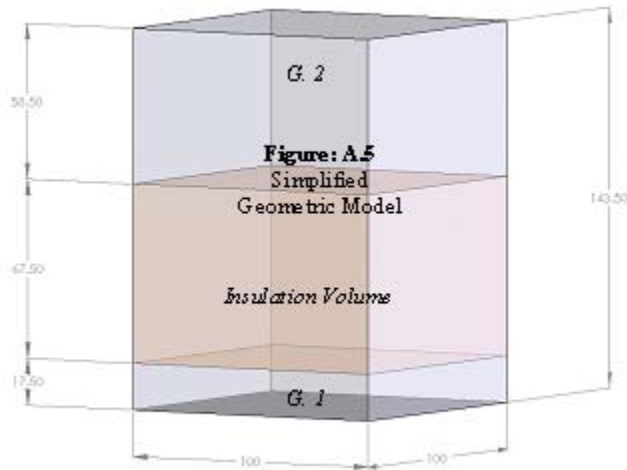
Figure A.4 is a cross-section view of BSat's interior. As depicted the tether shroud consumes a larger portion of the interior volume. As currently identified this shroud is composed of a fiberglass-type material. For thermal analysis it is **assumed** that this fiberglass barrier is an adiabatic, insulated surface that prohibits heat transfer.

This assumption allows the steady-state thermal analysis to divide the satellite into **two analytical groups**: The electronics consuming the volume below the tether shroud, and the electronics that occupy the space above the tether shroud.

Figure I.4

The geometry of the shroud's conical section was normalized against the overall volume and added, resulting in the simplified, yet effective model as seen in Figure A.5. Figures A.6 and A.7 were then analyzed wrt to their respective electronic groups.



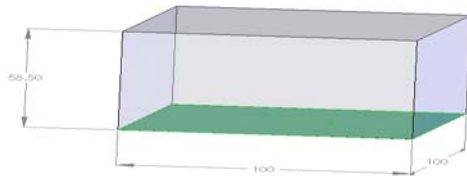


46.5

Figure: I.6

Group 1: Below Shroud

131.5



67.5

46.5

Figure: I.7

Group 2: Above Shroud

Simplified Tophat to account for the cylindrical extrusion as seen in Figure A.4. It is assumed

that significant amount of shading occurs within this recess such that a geometric simplification

can be made that reduces the overall height of BSat.

radius := 33·mm

depth := 35·mm

volume := $\pi \cdot \text{radius}^2 \cdot \text{depth}$

volume = 119.742cm³

volume := 120·cm³

height_corr := 143.5mm - $\frac{\text{volume}}{(100\text{·cm}^2)}$

height_corr = 131.5mm

Simplify geometry of the conical section of the shroud such that an effective increase in the insulation height is achieved.

Figure: I.8

Frustrum of a

Right Circular Cone

$$R_1 := 19 \cdot \text{mm}$$

$$R_2 := 50 \cdot \text{mm}$$

$$\text{height} := 58.5 \cdot \text{mm}$$



$$\text{volume}_{\text{cone}} := \frac{\pi \cdot (R_2^2 - R_1 \cdot R_2 + R_1^2) \cdot \text{height}}{3}$$

$$\text{volume}_{\text{cone}} = 117.07 \text{cm}^3$$

$$\text{volume}_{\text{cone}} := 117 \cdot \text{cm}^3$$

$$\text{insulation_height_corr} := 73 \cdot \text{mm} + \frac{\text{volume}_{\text{cone}}}{100 \text{cm}^2}$$

$$\text{insulation_height_corr} = 84.7 \text{mm}$$

Orbital Parameters for determining the extreme-energy inputs anticipated for BSat
Radius of Earth:

$$R_{\text{earth}} := 6378.14 \text{km}$$

Spacecraft Altitude:

$$\text{altitude} := 800 \cdot \text{km}$$

Angular Radius:

$$R_{\text{angular}} := \text{asin} \left(\frac{R_{\text{earth}}}{R_{\text{earth}} + \text{altitude}} \right)$$

$$R_{\text{angular}} = 62.692 \text{deg}$$

Orbital Environment

Solar Flux

$$q_{\text{solar_hot}} := 1420 \frac{\text{W}}{\text{m}^2}$$

$$q_{\text{solar_cold}} := 1360 \frac{\text{W}}{\text{m}^2}$$

Earth IR

$$q_{\text{ir_hot}} := 244 \frac{\text{W}}{\text{m}^2}$$

$$q_{\text{ir_cold}} := 218 \frac{\text{W}}{\text{m}^2}$$

*AlbedoCorrection**Factor*

$$\alpha_{\text{hot}} := .3$$

$$\alpha_{\text{cold}} := .23$$

Albedo

$$q_{\text{albedo_hot}} := q_{\text{solar_hot}} \cdot \alpha_{\text{hot}}$$

$$q_{\text{albedo_cold}} := q_{\text{solar_cold}} \cdot \alpha_{\text{cold}}$$

$$q_{\text{albedo_hot}} = 426 \frac{\text{W}}{\text{m}^2}$$

$$q_{\text{albedo_cold}} = 312.8 \frac{\text{W}}{\text{m}^2}$$

Internal Spacecraft Heat is assumed to be the max electrical energy input into each component

$$Q_{\text{cdh}} := .3 \cdot W$$

$$Q_{\text{power}} := .6 \cdot W$$

$$Q_{\text{GPS}} := .2 \cdot W$$

$$Q_{\text{batt_discharge}} := 0 \cdot W$$

$$Q_{\text{comm_tx}} := 2 \cdot W$$

$$Q_{\text{comm_rx}} := .1 \cdot W$$

$$Q_{\text{int_maxG1}} := Q_{\text{power}} + Q_{\text{comm_tx}} + Q_{\text{cdh}}$$

$$Q_{\text{int_maxG1}} = 2.9 \text{ W}$$

$$Q_{\text{int_minG1}} := Q_{\text{power}} + Q_{\text{cdh}}$$

$$Q_{\text{int_minG1}} = 0.9 \text{ W}$$

*For **Group 2** components (GPS and Battery) the following information has been provided by a representative at Rose Electronics, the supplier of BSat's battery.*

$$\text{length}_{\text{batt}} := 59 \cdot \text{mm}$$

$$\text{width}_{\text{batt}} := 38 \cdot \text{mm}$$

$$\text{th}_{\text{batt}} := 12 \cdot \text{mm}$$

$$SA_{\text{batt}} := (2 \cdot \text{length}_{\text{batt}} \cdot \text{width}_{\text{batt}}) + (2 \cdot \text{length}_{\text{batt}} \cdot \text{th}_{\text{batt}}) + 2 \cdot \text{width}_{\text{batt}} \cdot \text{th}_{\text{batt}}$$

$$SA_{\text{batt}} = 68.12 \text{ cm}^2$$

$$\Delta T_{\text{increase_batt_charging}} := 15 \cdot \text{K}$$

This value will be added to the max. obtainable temperature value from the steady-state results.

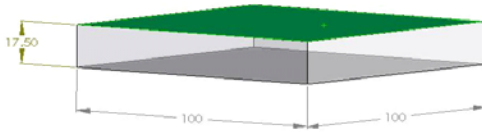
$$Q_{\text{int_maxG2}} := Q_{\text{GPS}}$$

$$Q_{\text{int_maxG2}} = 0.2 \text{ W}$$

$$Q_{\text{int_minG2}} := Q_{\text{batt_discharge}}$$

$$Q_{\text{int_minG2}} = 0 \text{ W}$$

*For **Group 1** Electronics (those below the shroud) the dimensional arguments were made (Figure A.6):*



$$SA_{\text{baseplateG1}} := 100 \text{ mm} \cdot 100 \text{ mm}$$

$$SA_{\text{topplateG1}} := 100 \text{ mm} \cdot 100 \text{ mm}$$

Figure: I.6

Group 1: Below Shroud

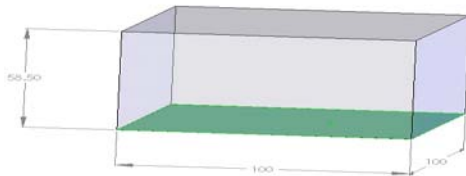
$$SA_{\text{sideG1}} := 17.5 \text{ mm} \cdot 100 \text{ mm}$$

The insulated surface (green) was omitted!

$$SA_{\text{totalG1}} := SA_{\text{baseplateG1}} + 4 \cdot SA_{\text{sideG1}}$$

$$SA_{\text{totalG1}} = 170 \text{ cm}^2$$

For **Group 2 Electronics** (those above shroud) the dimensional arguments were made (Figure A.7):



$$SA_{\text{baseplateG2}} := 100 \text{ mm} \cdot 100 \text{ mm}$$

46.5

$$SA_{\text{topplateG2}} := 100 \text{ mm} \cdot 100 \text{ mm}$$

Figure: I.7

Group 2: Above Shroud

$$SA_{\text{sideG2}} := 46.5 \text{ mm} \cdot 100 \text{ mm}$$

The insulated surface (green) was omitted!

$$SA_{\text{totalG2}} := SA_{\text{topplateG2}} + 4 \cdot SA_{\text{sideG2}}$$

$$SA_{\text{totalG2}} = 286 \text{ cm}^2$$

Determining the **projected-area** takes into account a baseplate pointing towards nadir that is 45 deg. out of plane, and rotated 45 deg.

$$FA_{G1} := (\cos(45) \cdot SA_{\text{baseplateG1}} + \cos(45) \cdot SA_{\text{sideG1}}) \cdot \cos(45) + \cos(45) \cdot SA_{\text{sideG1}}$$

$$FA_{G1} = 41.619 \text{ cm}^2$$

$$FA_{G2} := (\cos(45) \cdot SA_{\text{topplateG2}} + \cos(45) \cdot SA_{\text{sideG2}}) \cdot \cos(45) + \cos(45) \cdot SA_{\text{sideG2}}$$

$$FA_{G2} = 64.856 \text{ cm}^2$$

The following equation was used to determine the surface temperature of the two enclosures for steady-state conditions.

(Eq't. 1)

$$T_s = \left[\frac{\left(FA \cdot q_{\text{solar}} \cdot \alpha + FA \cdot q_{\text{ir}} \cdot \varepsilon + FA \cdot q_{\text{albedo}} \cdot \alpha + q_{\text{int_max}} + T_{\text{boundary}}^4 \cdot \sigma \cdot \varepsilon \cdot SA_{\text{boundary}} \right)}{SA_{\text{total}} \cdot \sigma \cdot \varepsilon} \right]^{\frac{1}{4}}$$

Optical Properties (From Excel Spreadsheets, APP. B)

The Excel spreadsheet takes in the surface area quantities from above and calculates an effective absorptivity and emissivity based upon the presence of other materials (e.g solar cells) that occupy space on respective surfaces. The results of APP.B are defined below.

Bare Aluminum

Silver Teflon

Anodized AL

White Paint

Black Anodized

Bare Aluminum

Silver Teflon

Anodized AL

White Paint

Black Anodized

$$\alpha_{G1} := \begin{pmatrix} .1706 \\ .0934 \\ .3541 \\ .2093 \\ .9432 \end{pmatrix}$$

$$\varepsilon_{G1} := \begin{pmatrix} .0338 \\ .7870 \\ .816 \\ .8933 \\ .8257 \end{pmatrix}$$

Bare Aluminum

Silver Teflon

Anodized AL

White Paint

Black Anodized

Bare Aluminum

Silver Teflon

Anodized AL

White Paint

Black Anodized

$$\alpha_{G2} := \begin{pmatrix} .5341 \\ .4947 \\ .6277 \\ .5538 \\ .9281 \\ .4278 \\ .8120 \\ .8268 \\ .8662 \\ .8317 \end{pmatrix}$$

$$i := 0, 1..4$$

Stefan-Boltzmann Constant

$$\sigma := 5.67051 \cdot 10^{-8} \cdot \frac{\text{W}}{\text{m}^2 \cdot \text{K}^4}$$

$$T_{\max G1_i} := \left[\frac{\left(FA_{G1} \cdot q_{\text{solar hot}} \cdot \alpha_{G1_i} + FA_{G1} \cdot q_{\text{ir hot}} \cdot \epsilon_{G1_i} + FA_{G1} \cdot q_{\text{albedo hot}} \cdot \alpha_{G1_i} + q_{\text{int max G1}} \right)}{SA_{\text{total G1}} \cdot \sigma \cdot \epsilon_{G1_i}} \right]^{\frac{1}{4}}$$

Bare Aluminum

Silver Teflon

Anodized AL

White Paint

Black Paint

$$\alpha_{G1} = \begin{pmatrix} 0.171 \\ 0.093 \\ 0.354 \\ 0.209 \\ 0.943 \end{pmatrix}$$

$$T_{\max G1} = \begin{pmatrix} 600.79 \\ 276.226 \\ 300.909 \\ 281.602 \\ 342.749 \end{pmatrix} \text{ K}$$

$$T_{\max G1} \left(\frac{1}{\text{K}} \right) - 273 = \begin{pmatrix} 327.79 \\ 3.226 \\ 27.909 \\ 8.602 \\ 69.749 \end{pmatrix}$$

$$\alpha_{G1_2} = 0.354$$

50

$$T_{\min G1} := \left[\frac{\left(FA_{G1} \cdot q_{\text{ir_cold}} \cdot \epsilon_{G1} + q_{\text{int_minG1}} \right)}{SA_{\text{totalG1}} \cdot \sigma \cdot \epsilon_{G1}} \right]^{\frac{1}{4}}$$

*Bare Aluminum**Silver Teflon**Anodized AL**White Paint**Black Paint*

$$T_{\min G1} \left(\frac{1}{K} \right) - 273 = \begin{pmatrix} 138.104 \\ -58.233 \\ -59.305 \\ -61.888 \\ -59.65 \end{pmatrix}$$

$$T_{\min G1} = \begin{pmatrix} 411.104 \\ 214.767 \\ 213.695 \\ 211.112 \\ 213.35 \end{pmatrix} K$$

$$T_{\max G2} := \left[\frac{\left(FA_{G2} \cdot q_{\text{solar_hot}} \cdot \alpha_{G2} + FA_{G2} \cdot q_{\text{ir_hot}} \cdot \epsilon_{G2} + FA_{G2} \cdot q_{\text{albedo_hot}} \cdot \alpha_{G2} + q_{\text{int_maxG2}} \right)}{SA_{\text{totalG2}} \cdot \sigma \cdot \epsilon_{G2}} \right]^{\frac{1}{4}}$$

$$T_{\max G2} = \begin{pmatrix} 319.962 \\ 273.864 \\ 286.416 \\ 276.418 \\ 311.059 \end{pmatrix} K$$

*Bare Aluminum**Silver Teflon**Anodized AL**White Paint**Black Anodized*

$$\left(T_{\max G2} + \Delta T_{\text{increase_batt_charging}} \right) \cdot \left(\frac{1}{K} \right) - 273 = \begin{pmatrix} 61.962 \\ 15.864 \\ 28.416 \\ 18.418 \\ 53.059 \end{pmatrix}$$

$$q_{\text{int_minG2}} := 0 \cdot W$$

$$T_{\min G2_1} := \left[\frac{\left(FA_{G2} q_{ir_cold} \cdot \epsilon_{G2_1} + q_{int_minG2} \right)}{SA_{totalG2} \cdot \sigma \cdot \epsilon_{G2_1}} \right]^{\frac{1}{4}}$$

Bare Aluminum

Silver Teflon

Anodized AL

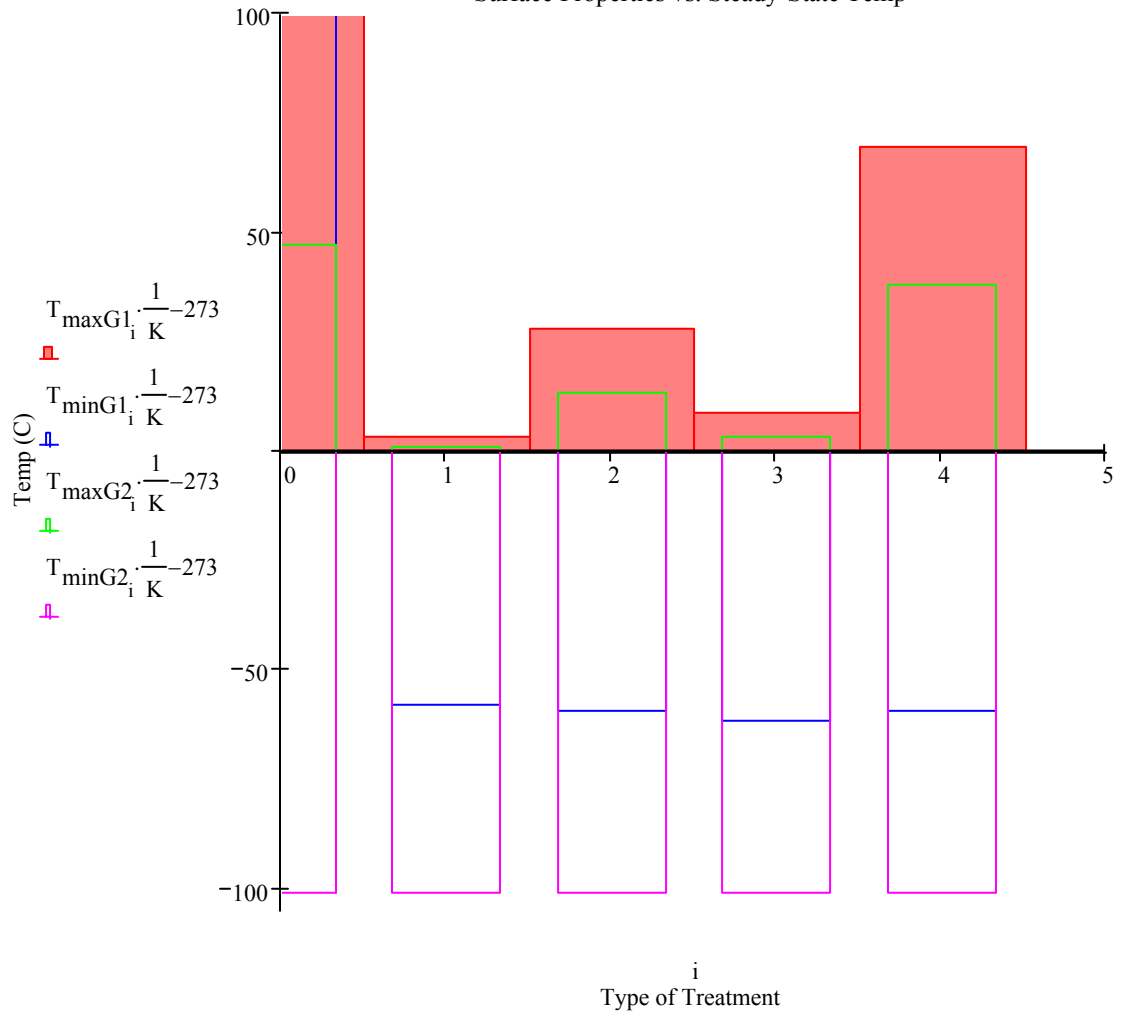
White Paint

Black Anodized

$$T_{\min G2} = \begin{pmatrix} 171.832 \\ 171.832 \\ 171.832 \\ 171.832 \\ 171.832 \end{pmatrix} \text{K}$$

$$T_{\min G2} \left(\frac{1}{\text{K}} \right) - 273 = \begin{pmatrix} -101.168 \\ -101.168 \\ -101.168 \\ -101.168 \\ -101.168 \end{pmatrix}$$

Surface Properties vs. Steady-State Temp



APPENDIX K

EFFECTIVE OPTICAL
PROPERTIES

Appendix J.1: Bare Aluminum, Sub Shroud Group

		Area (cm ²)	Absorptivity (α)	Emissivity (ε)	Area (α) (cm ²)	Area (ε) (cm ²)
Top Hat	Solar Cell	0.0000	0.9200	0.8500	0.0000	0.0000
	Screws	0.0000	0.4700	0.1400	0.0000	0.0000
	Antenna	0.0000	0.9600	0.8700	0.0000	0.0000
	Exposed Top Plate	100.0000	0.1600	0.0300	16.0000	3.0000
	Total Area	100.0000	0.1600	0.0300	16.0000	3.0000

Sides	Solar Cell	0.0000	0.9200	0.8500	0.0000	0.0000
	Screws	0.7500	0.4700	0.1400	0.3525	0.1050
	Antenna	0.0000	0.9600	0.8700	0.0000	0.0000
	Exposed Side	16.7500	0.1600	0.0300	2.6800	0.5025
	Total Area	17.5	0.1733	0.0347	3.0325	0.6075

BasePlate	Solar Cell	0.0000	0.9200	0.8500	0	0
	Screws	0.0000	0.4700	0.1400	0	0
	Antenna	0.0000	0.9600	0.8700	0	0
	Exposed Bottom Plate	100.0000	0.1600	0.0300	16	3
	Total Area	100.0000	0.1600	0.0300	16	3

"=SUM(4*D17,D23)/5"

Total SC AVG 170.0000 0.1706 0.0338

	Absorptivity (α)	Emissivity (ε)
Bare Aluminum	0.1600	0.0300
5 mil Silver Teflon	0.0800	0.8100
Anodized Aluminum	0.3500	0.8400
White Paint	0.2000	0.9200
Black Paint	0.9600	0.8500

Appendix J.1: Silver Teflon, Sub Shroud Group

		Area (cm ²)	Absorptivity (α)	Emissivity (ε)	Area (α) (cm ²)	Area (ε) (cm ²)
Top Hat	Solar Cell	0.0000	0.9200	0.8500	0.0000	0.0000
	Screws	0.0000	0.4700	0.1400	0.0000	0.0000

	Antenna	0.0000	0.9600	0.8700	0.0000	0.0000
	Exposed Top Plate	100.0000	0.0800	0.8100	8.0000	81.0000
	Total Area	100.0000	0.0800	0.8100	8.0000	81.0000

Sides	Solar Cell	0.0000	0.9200	0.8500	0.0000	0.0000
	Screws	0.7500	0.4700	0.1400	0.3525	0.1050
	Antenna	0.0000	0.9600	0.8700	0.0000	0.0000
	Exposed Side	16.7500	0.0800	0.8100	1.3400	13.5675
	Total Area	17.5	0.0967	0.7813	1.6925	13.6725

BasePlate	Solar Cell	0.0000	0.9200	0.8500	0	0
	Screws	0.0000	0.4700	0.1400	0	0
	Antenna	0.0000	0.9600	0.8700	0	0
	Exposed Bottom Plate	100.0000	0.0800	0.8100	8	81
	Total Area	100.0000	0.0800	0.8100	8	81

"=SUM(4*D17,D23)/5"

Total SC AVG 170.0000 0.0934 0.7870

	Absorptivity (α)	Emissivity (ϵ)
Bare Aluminum	0.1600	0.0300
5 mil Silver Teflon	0.0800	0.8100
Anodized Aluminum	0.3500	0.8400
White Paint	0.2000	0.9200
Black Paint	0.9600	0.8500

Appendix J.1: Anodized Aluminum, Sub Shroud Group

		Area (cm ²)	Absorptivity (α)	Emissivity (ϵ)	Area (α) (cm ²)	Area (ϵ) (cm ²)
Top Hat	Solar Cell	0.0000	0.9200	0.8500	0.0000	0.0000
	Screws	0.0000	0.4700	0.1400	0.0000	0.0000
	Antenna	0.0000	0.9600	0.8700	0.0000	0.0000
	Exposed Top Plate	100.0000	0.3500	0.8400	35.0000	84.0000
	Total Area	100.0000	0.3500	0.8400	35.0000	84.0000

Sides	Solar Cell	0.0000	0.9200	0.8500	0.0000	0.0000
	Screws	0.7500	0.4700	0.1400	0.3525	0.1050
	Antenna	0.0000	0.9600	0.8700	0.0000	0.0000
	Exposed Side	16.7500	0.3500	0.8400	5.8625	14.0700

	Total Area	17.5	0.3551	0.8100	6.2150	14.1750
--	-------------------	------	--------	--------	--------	---------

BasePlate	Solar Cell	0.0000	0.9200	0.8500	0	0
	Screws	0.0000	0.4700	0.1400	0	0
	Antenna	0.0000	0.9600	0.8700	0	0
	Exposed Bottom Plate	100.0000	0.3500	0.8400	35	84
	Total Area	100.0000	0.3500	0.8400	35	84

"=SUM(4*D17,D23)/5"

Total SC AVG **170.0000** **0.3541** **0.8160**

	Absorptivity (α)	Emissivity (ε)
Bare Aluminum	0.1600	0.0300
5 mil Silver Teflon	0.0800	0.8100
Anodized Aluminum	0.3500	0.8400
White Paint	0.2000	0.9200
Black Paint	0.9600	0.8500

Appendix J.1: White Paint, Sub Shroud Group

		Area (cm²)	Absorptivity (α)	Emissivity (ε)	Area (α) (cm²)	Area (ε) (cm²)
Top Hat	Solar Cell	0.0000	0.9200	0.8500	0.0000	0.0000
	Screws	0.0000	0.4700	0.1400	0.0000	0.0000
	Antenna	0.0000	0.9600	0.8700	0.0000	0.0000
	Exposed Top Plate	100.0000	0.2000	0.9200	20.0000	92.0000
	Total Area	100.0000	0.2000	0.9200	20.0000	92.0000

Sides	Solar Cell	0.0000	0.9200	0.8500	0.0000	0.0000
	Screws	0.7500	0.4700	0.1400	0.3525	0.1050
	Antenna	0.0000	0.9600	0.8700	0.0000	0.0000
	Exposed Side	16.7500	0.2000	0.9200	3.3500	15.4100
	Total Area	17.5	0.2116	0.8866	3.7025	15.5150

BasePlate	Solar Cell	0.0000	0.9200	0.8500	0	0
	Screws	0.0000	0.4700	0.1400	0	0
	Antenna	0.0000	0.9600	0.8700	0	0
	Exposed Bottom Plate	100.0000	0.2000	0.9200	20	92
	Total Area	100.0000	0.2000	0.9200	20	92

"=SUM(4*D17,D23)/5"

Total SC AVG 170.0000 0.2093 0.8933

	Absorptivity (α)	Emissivity (ϵ)
Bare Aluminum	0.1600	0.0300
5 mil Silver Teflon	0.0800	0.8100
Anodized Aluminum	0.3500	0.8400
White Paint	0.2000	0.9200
Black Paint	0.9600	0.8500

Appendix J.1: Black Paint, Sub Shroud Group

		Area (cm ²)	Absorptivity (α)	Emissivity (ϵ)	Area (α) (cm ²)	Area (ϵ) (cm ²)
Top Hat	Solar Cell	0.0000	0.9200	0.8500	0.0000	0.0000
	Screws	0.0000	0.4700	0.1400	0.0000	0.0000
	Antenna	0.0000	0.9600	0.8700	0.0000	0.0000
	Exposed Top Plate	100.0000	0.9600	0.8500	96.0000	85.0000
	Total Area	100.0000	0.9600	0.8500	96.0000	85.0000

Sides	Solar Cell	0.0000	0.9200	0.8500	0.0000	0.0000
	Screws	0.7500	0.4700	0.1400	0.3525	0.1050
	Antenna	0.0000	0.9600	0.8700	0.0000	0.0000
	Exposed Side	16.7500	0.9600	0.8500	16.0800	14.2375
	Total Area	17.5	0.9390	0.8196	16.4325	14.3425

BasePlate	Solar Cell	0.0000	0.9200	0.8500	0	0
	Screws	0.0000	0.4700	0.1400	0	0
	Antenna	0.0000	0.9600	0.8700	0	0
	Exposed Bottom Plate	100.0000	0.9600	0.8500	96	85
	Total Area	100.0000	0.9600	0.8500	96	85

"=SUM(4*D17,D23)/5"

Total SC AVG 170.0000 0.9432 0.8257

	Absorptivity (α)	Emissivity (ϵ)
Bare Aluminum	0.1600	0.0300

5 mil Silver Teflon	0.0800	0.8100
Anodized Aluminum	0.3500	0.8400
White Paint	0.2000	0.9200
Black Paint	0.9600	0.8500

Appendix J.2: Bare Aluminm, Upper Shroud Group

		Area (cm²)	Absorptivity (α)	Emissivity (ϵ)	Area (α) (cm²)	Area (ϵ) (cm²)
Top Hat	Solar Cell	0.0000	0.9200	0.8500	0.0000	0.0000
	Screws	0.0000	0.4700	0.1400	0.0000	0.0000
	Antenna	0.0000	0.9600	0.8700	0.0000	0.0000
	Exposed Top Plate	100.0000	0.1600	0.0300	16.0000	3.0000
	Total Area	100.0000	0.1600	0.0300	16.0000	3.0000

Sides	Solar Cell	28.0000	0.9200	0.8500	25.7600	23.8000
	Screws	1.5000	0.4700	0.1400	0.7050	0.2100
	Antenna	0.0000	0.9600	0.8700	0.0000	0.0000
	Exposed Side	17.0000	0.1600	0.0300	2.7200	0.5100
	Total Area	46.5	0.6276	0.5273	29.1850	24.5200

BasePlate	Solar Cell	0.0000	0.9200	0.8500	0	0
	Screws	0.0000	0.4700	0.1400	0	0
	Antenna	0.0000	0.9600	0.8700	0	0
	Exposed Bottom Plate	100.0000	0.1600	0.0300	16	3
	Total Area	100.0000	0.1600	0.0300	16	3

"=SUM(D11,4*D17)/5"

Total SC AVG 286.0000 0.5341 0.4278

	Absorptivity (α)	Emissivity (ϵ)
Bare Aluminum	0.1600	0.0300
5 mil Silver Teflon	0.0800	0.8100
Anodized Aluminum	0.3500	0.8400
White Paint	0.2000	0.9200
Black Paint	0.9600	0.8500

Appendix J.2: Silver Teflon, Upper Shroud Group

		Area (cm ²)	Absorptivity (α)	Emissivity (ϵ)	Area (α) (cm ²)	Area (ϵ) (cm ²)
Top Hat	Solar Cell	0.0000	0.9200	0.8500	0.0000	0.0000
	Screws	0.0000	0.4700	0.1400	0.0000	0.0000
	Antenna	0.0000	0.9600	0.8700	0.0000	0.0000
	Exposed Top Plate	100.0000	0.0800	0.8100	8.0000	81.0000
	Total Area	100.0000	0.0800	0.8100	8.0000	81.0000

Sides	Solar Cell	28.0000	0.9200	0.8500	25.7600	23.8000
	Screws	1.5000	0.4700	0.1400	0.7050	0.2100
	Antenna	0.0000	0.9600	0.8700	0.0000	0.0000
	Exposed Side	17.0000	0.0800	0.8100	1.3600	13.7700
	Total Area	46.5	0.5984	0.8125	27.8250	37.7800

BasePlate	Solar Cell	0.0000	0.9200	0.8500	0	0
	Screws	0.0000	0.4700	0.1400	0	0
	Antenna	0.0000	0.9600	0.8700	0	0
	Exposed Bottom Plate	100.0000	0.0800	0.8100	8	81
	Total Area	100.0000	0.0800	0.8100	8	81

"=SUM(D11,4*D17)/5"

Total SC AVG 286.0000 0.4947 0.8120

	Absorptivity (α)	Emissivity (ϵ)
Bare Aluminum	0.1600	0.0300
5 mil Silver Teflon	0.0800	0.8100
Anodized Aluminum	0.3500	0.8400
White Paint	0.2000	0.9200
Black Paint	0.9600	0.8500

Appendix J.2: Anodized Aluminm, Upper Shroud Group

		Area (cm ²)	Absorptivity (α)	Emissivity (ϵ)	Area (α) (cm ²)	Area (ϵ) (cm ²)
Top Hat	Solar Cell	0.0000	0.9200	0.8500	0.0000	0.0000
	Screws	0.0000	0.4700	0.1400	0.0000	0.0000
	Antenna	0.0000	0.9600	0.8700	0.0000	0.0000
	Exposed Top Plate	100.0000	0.3500	0.8400	35.0000	84.0000

BasePlate	Solar Cell	0.0000	0.9200	0.8500	0	0
	Screws	0.0000	0.4700	0.1400	0	0
	Antenna	0.0000	0.9600	0.8700	0	0
	Exposed Bottom Plate	100.0000	0.2000	0.9200	20	92
	Total Area	100.0000	0.2000	0.9200	20	92

"=SUM(D11,4*D17)/5"

Total SC AVG 286.0000 0.5538 0.8662

	Absorptivity (α)	Emissivity (ϵ)
Bare Aluminum	0.1600	0.0300
5 mil Silver Teflon	0.0800	0.8100
Anodized Aluminum	0.3500	0.8400
Appendix B.2: White Paint	0.2000	0.9200
Black Paint	0.9600	0.8500

Appendix J.2: Black Paint, Upper Shroud Group

		Area (cm²)	Absorptivity (α)	Emissivity (ϵ)	Area (α) (cm²)	Area (ϵ) (cm²)
Top Hat	Solar Cell	0.00	0.92	0.85	0.00	0.00
	Screws	0.00	0.47	0.14	0.00	0.00
	Antenna	0.00	0.96	0.87	0.00	0.00
	Exposed Top Plate	100.00	0.96	0.85	96.00	85.00
	Total Area	100.00	0.96	0.85	96.00	85.00

Sides	Solar Cell	28.00	0.92	0.85	25.76	23.80
	Screws	1.50	0.47	0.14	0.71	0.21
	Antenna	0.00	0.96	0.87	0.00	0.00
	Exposed Side	17.00	0.96	0.85	16.32	14.45
	Total Area	46.50	0.92	0.83	42.79	38.46

BasePlate	Solar Cell	0.00	0.92	0.85	0.00	0.00
	Screws	0.00	0.47	0.14	0.00	0.00
	Antenna	0.00	0.96	0.87	0.00	0.00
	Exposed Bottom Plate	100.00	0.96	0.85	96.00	85.00
	Total Area	100.00	0.96	0.85	96.00	85.00

"=SUM(D11,4*D17)/5"

Total SC AVG 386.0000 0.9281 0.8317

	Absorptivity (α)	Emissivity (ϵ)
Bare Aluminum	0.1600	0.0300
5 mil Silver Teflon	0.0800	0.8100
Anodized Aluminum	0.3500	0.8400
White Paint	0.2000	0.9200
Black Paint	0.9600	0.8500

Appendix J Summary: Upper and Sub Shroud Optc. And Temp. Properties	
---	--

Summary of Optical Props and Temps for Sub Shroud Group

	α	E	Tmax	Tmin
Bare Aluminum	0.1706	0.0338	433	320
Silver Teflon	0.0934	0.7870	50	8
Anodized AL	0.3541	0.8160	65	6
White Paint	0.2093	0.8933	49	1
Black Paint	0.9432	0.8257	96	5

Total Satellite Area (cm ²)
170

Summary of Optical Props and Temps for Upper Shroud Group

	α	E	Tmax	Tmin
Bare Aluminum	0.5341	0.4278	68	-101
Silver Teflon	0.4947	0.8120	21	-101
Anodized AL	0.6277	0.8268	33	-101
White Paint	0.5538	0.8662	23	-101
Black Paint	0.9281	0.8317	57	-101

Total Satellite Area (cm ²)
286

APPENDIX L

MATLAB
LUMPED CAPACITANCE
CODE

```

%Dylan Solomon
%BSat Thermal Analysis
%Lumped Capacitance Transient Heat Analysis

function out = lumped(dt, epsilon, alpha, Qgen, FA, SA,
Tstart,Qcold,Qhot,hotcold,orbit,N,mass,Cp);

format short g

disp ('timestep(min)='), disp(dt)
disp ('emmissivity='), disp (epsilon)
disp ('absorptivity='), disp(alpha)
disp ('projected area (m^2)'), disp (FA)
disp ('total surface area (m^2)'), disp (SA)
disp ('initial temp (K)'), disp (Tstart)
%%%%%%%%%%
%%%%%%%%%%
%%

% Qalbedo_cold = 312.8;    Qalbedo_hot = 428.4;
% Qsolar_cold = 1360;    Qsolar_hot = 1428;
% Qir_cold = 218;        Qir_hot = 240;

% Qcold=[Qalbedo_cold;Qsolar_cold;Qir_cold]
% Qhot=[Qalbedo_hot;Qsolar_hot; Qir_hot]

%hotcold = 1%input('for accurate environmental energy loads, input 1 for hot and 2 for
cold:');

if hotcold == 1
    Qenvironment = Qhot;
else
    Qenvironment = Qcold;
end
disp ('Qenvironment='), disp (Qenvironment)

%%%%%%%%%%
%%%%%%%%%%
%%

%disp ('From backcover of SMAD, enter the following orbit parameters in matrix form:
orbit = [alt (km);period (min);eclipse (min)] ')
%orbit = [800,90,35.13]%input ('orbit=');

```



```

%%%%%%%%%%%%%%%%%%%%%%%%%%%%%%%%%%%%%%%%%%%%%%%%%%%%%%%%%%%%%%%%%%%%%%%%
%%%%%%%%%%%%%%%%%%%%%%%%%%%%%%%%%%%%%%%%%%%%%%%%%%%%%%%%%%%%%%%%%%%%%%%%
%%%%%%%%%%%%%%%%%%%%%%%%%%%%%%%%%%%%%%%%%%%%%%%%%%%%%%%%%%%%%%%%%%%%%%%%
%
```

```

time_per_deg = (orbit(2)/360);
degree_per_time = dt/time_per_deg;
disp ('min/deg='), disp (time_per_deg)
disp ('deg/min='), disp (degree_per_time)

```

```

%%%%%%%%%%%%%%%%%%%%%%%%%%%%%%%%%%%%%%%%%%%%%%%%%%%%%%%%%%%%%%%%%%%%%%%%
%%%%%%%%%%%%%%%%%%%%%%%%%%%%%%%%%%%%%%%%%%%%%%%%%%%%%%%%%%%%%%%%%%%%%%%%
%%%%%%%%%%%%%%%%%%%%%%%%%%%%%%%%%%%%%%%%%%%%%%%%%%%%%%%%%%%%%%%%%%%%%%%%
%
```

```

SB=5.67*10^-8;
Tspace=4;
% N=1000;
% time=[0:N];
% deg=[0:N];
% Qout=[0:N];
% %
% Tinitial=[0:N];
Tinitial(1)=Tstart;
% Tfinal=[0:N];
% %
% Qout=[0:N];
% Qin=[0:N];
% Qnet=[0:N];

```

```

% Cp = 16.02;      % [W*min/kg*C]
% mass = 25;      % [kg]

```

```

degi=0;
ti=0;
iter=0;
count=0;

```

```

for i=1:N

```

```

time(i)=ti + dt*i;
deg(i)=degi + time(i)*degree_per_time;

iter=iter+dt;

if deg(i)>=360
    factor=floor(deg(i)/360);
    deg(i)=deg(i)-360*factor;
end

if iter>=orbit(2)
    iter=0;
end

period(i)=iter;

Qout(i)=SA*epsilon*SB*(Tinitial(i)^4-Tspace^4);

if period(i)<=(orbit(2)-orbit(3))
    Qin(i)=FA*Qenvironment(2)*alpha + SA*.27*Qenvironment(3)*epsilon +
SA*.27*.784*Qenvironment(1)*alpha + Qgen;
else
    Qin(i)=SA*.27*Qenvironment(3)*epsilon + Qgen;
end

Qnet(i)=Qin(i)-Qout(i);

deltaT(i)=(Qnet(i)*dt)/(mass*Cp);
Tfinal(i)=Tinitial(i)+ deltaT(i);

%[test(i+1),Tinitial(i+1),Qout(i+1),Qin(i+1),Qnet(i+1),deltaT(i+1),Tfinal(i+1)]
if i<N
%    break;
%    else
    Tinitial(i+1)=Tfinal(i);
end
end

format compact

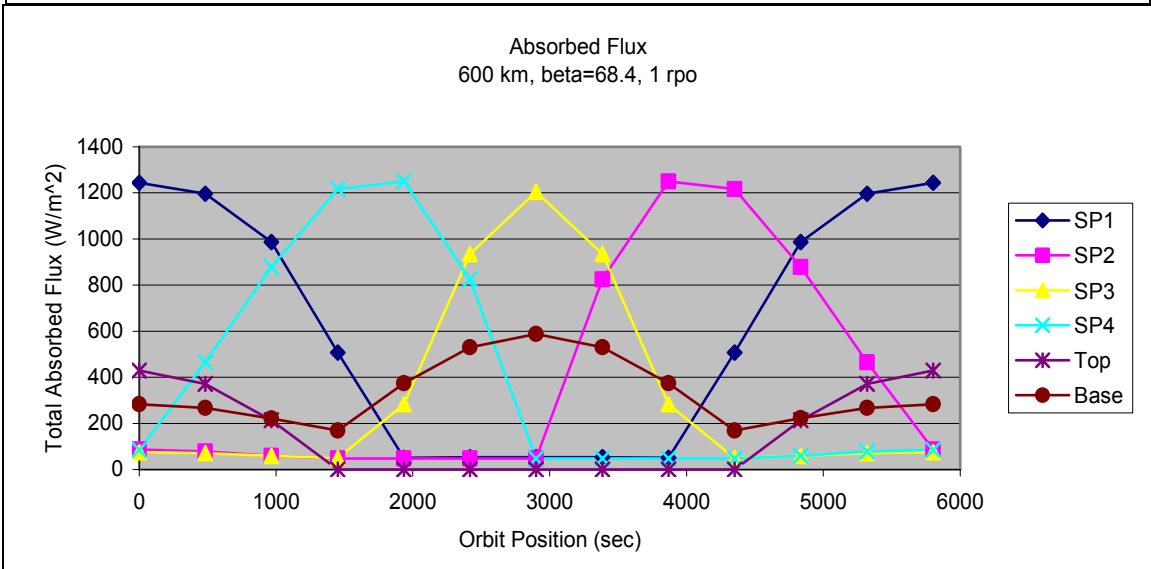
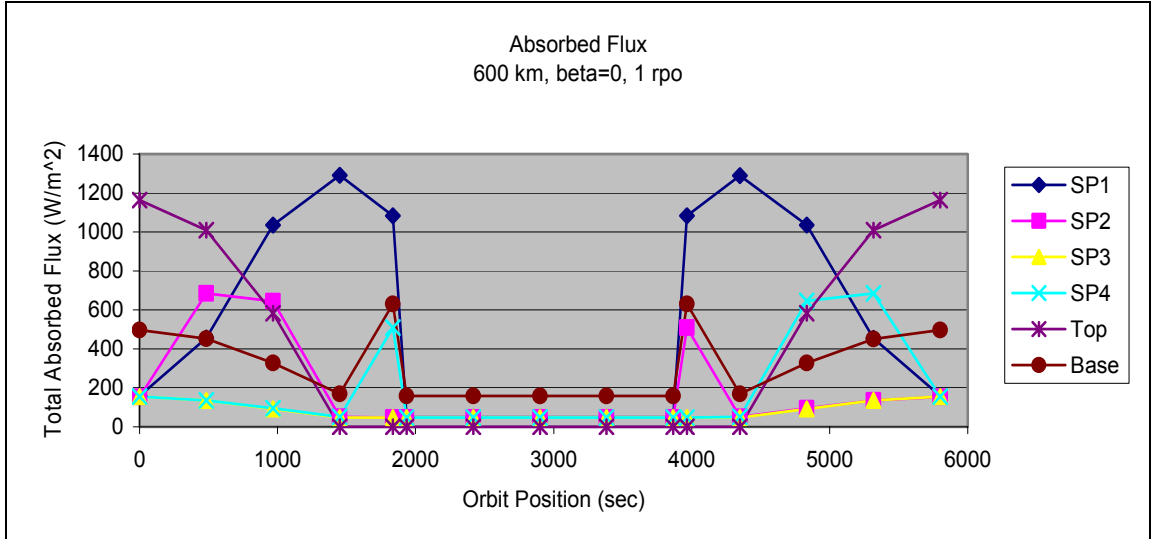
[time',period',deg',Tinitial',Qout',Qin',Qnet',deltaT',Tfinal']
figure(2)
plot(time,Tfinal);
title('Lumped Capacitance Temperature of Spherical Satellite')

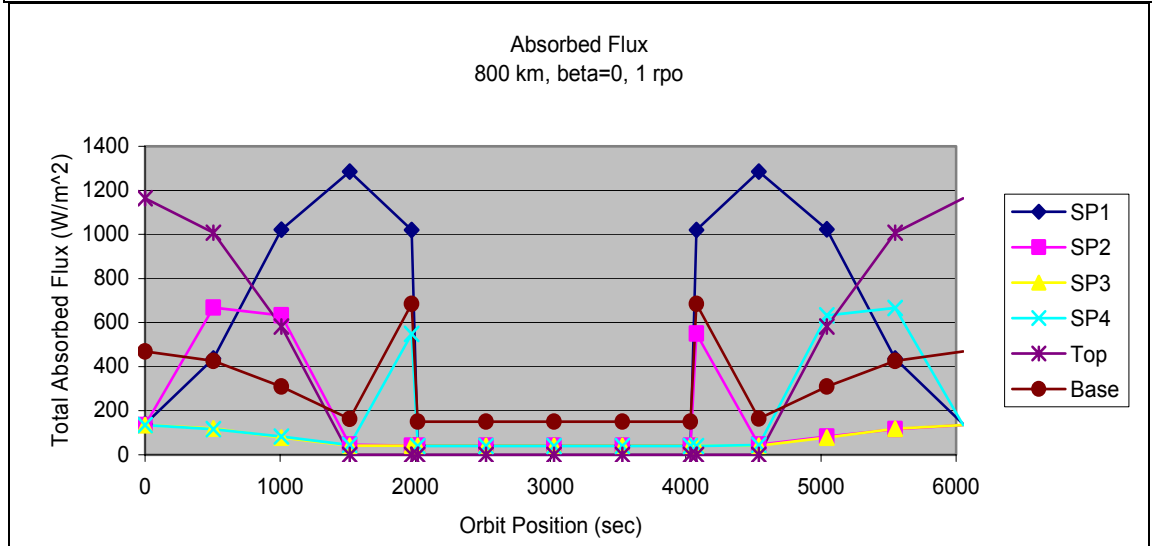
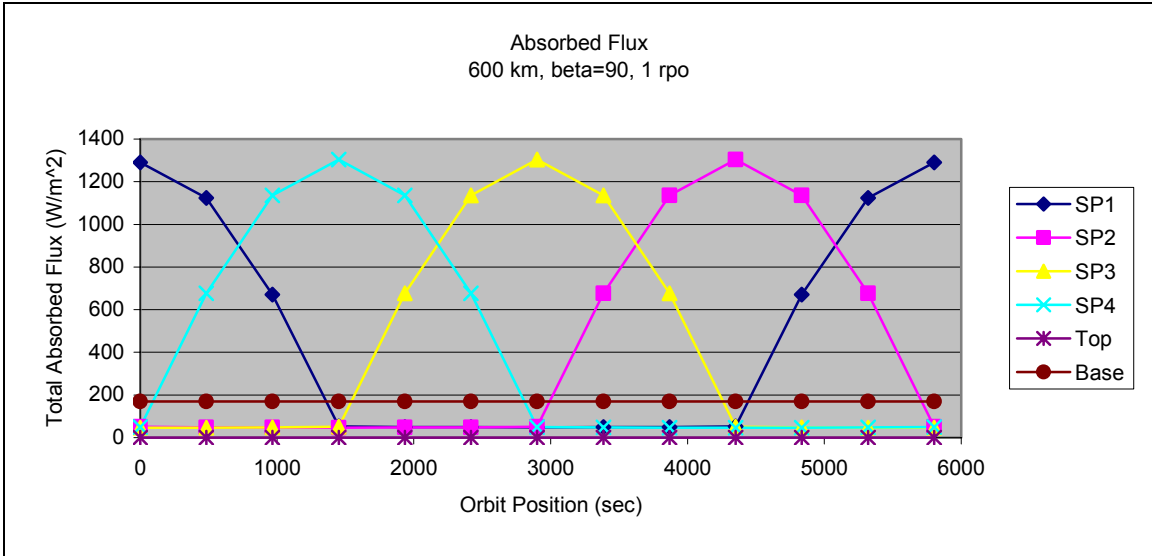
```

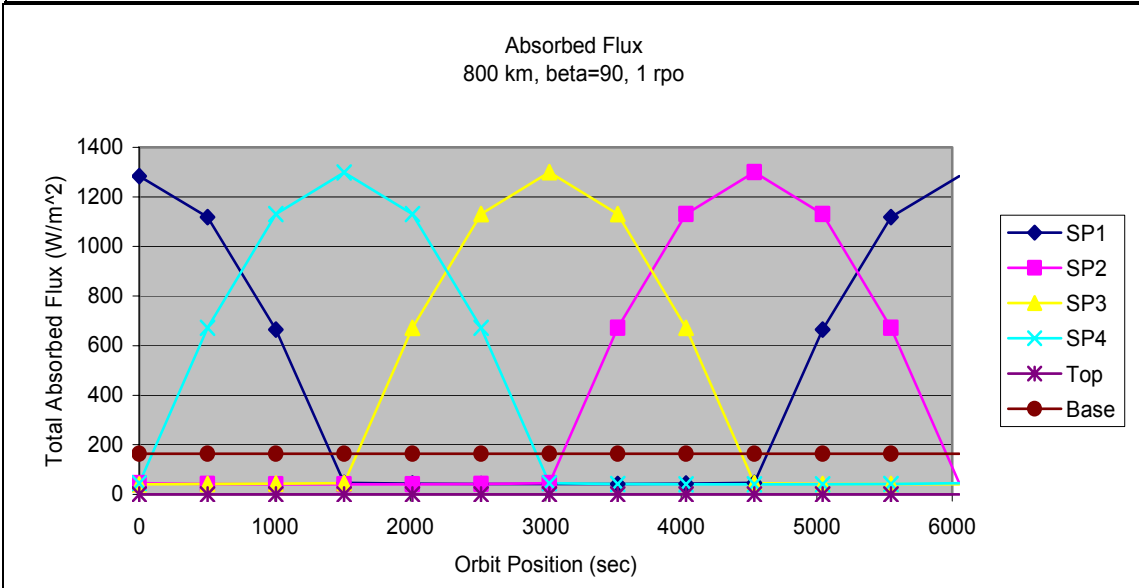
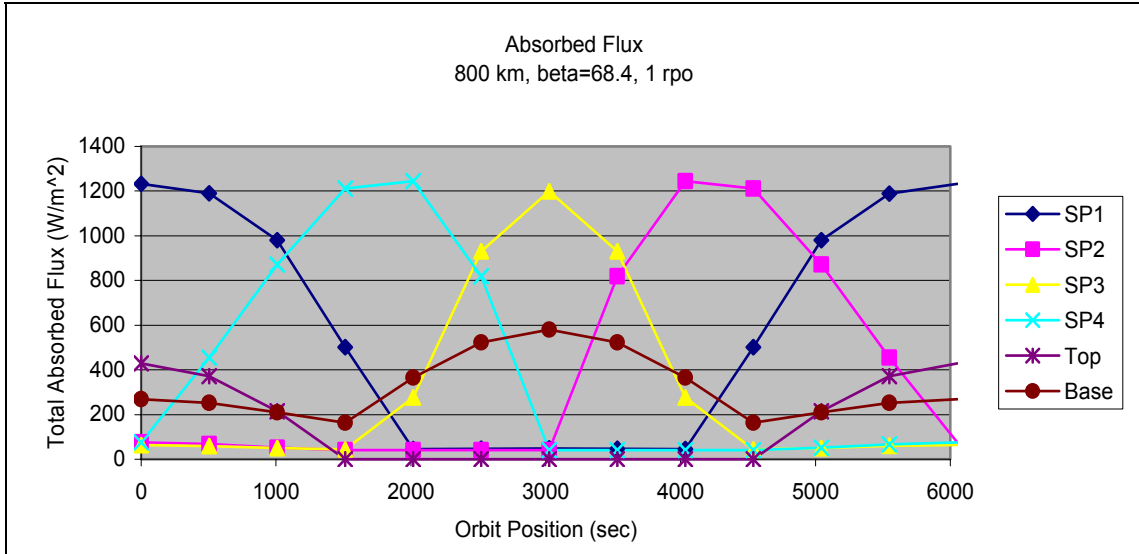
```
xlabel('Time (min)')  
ylabel('Temperature (K)')  
hold on;  
grid on;  
  
%abs(Tfinal(i)-Tinitial(i))<=.5 && i>1
```

APPENDIX M

ABSORBED FLUX







APPENDIX N

Calorimeter Experiment

Determining Thermal Capacitance
SSEL, MSU-Bozeman

- Objective:** To experimentally determine the heat capacity (C_p) of BarnacleSat's secondary battery. To calibrate and validate a calorimeter-type apparatus by experimentally obtaining a material's heat capacity, and then comparing that value against the material's tabulated value.
- Motivation:** To accurately model the thermal stability of a satellite in its space environment particular attention is required on the aforementioned energy storage technique. Obtaining a well understood thermal capacity of the battery will provide insight into what thermal control techniques are necessary for maintaining the battery within its appropriate temperature limits. It has been defined by the thermal designer that a thermal environment by which the temperature exceeds this predefined range is unacceptable; thus, requiring a thermal control technique.
- Background:** Heat capacity (thermal capacity) is defined as the ability of an object to store heat. The heat capacity of a certain amount of matter is the quantity of heat required to raise its temperature by one degree. In other words, when heat is transferred to an object the temperature of the object increases; when the heat is removed from an object the temperature of the object decreases. This phenomenon is the very essence of thermal capacity.

$$Q = m \cdot C_p \cdot \Delta T$$

$$Q [=] \text{ J}$$

$$m [=] \text{ kg}$$

$$C_p [=] \text{ J/(kg} \cdot \text{K)}$$

$$T [=] \text{ K}$$

$$\text{Specific Heat} \rightarrow C_p [=] \text{ J/(kg} \cdot \text{K)}$$

$$\text{Heat Capacity} \rightarrow C [=] \text{ J/K}$$

- Method:** The calorimeter method is a standardized technique often employed for the experimental determination of an object's specific heat (thermal capacity). Calorimetry is a branch of thermodynamics which is the study of energy and heat flow. The apparatus is well insulated so that no heat is allowed to enter or escape the test chamber to the surroundings, and is defined as an experimental device in which a chemical reaction (i.e. heat exchange) takes place.

Experiment: The calorimetry experiment consists of the following equipment:

Equipment List

Insulated Calorimeter
Styrofoam Cup
Digital Scale
Heating Device
Thermometer
Stop Watch
Mt'l samples
Battery

Procedure: The practice of calorimetry assumes a perfectly insulated apparatus; one in which no heat enters or leavings from its surroundings. To validate this claim a material sample of known specific heat will be investigated prior to testing the battery. **To minimize heat loss to the surroundings the water bath inside the calorimeter will initially be at room temperature.**

- 1) Place 300g of distilled water into Styrofoam cup and place into calorimeter.
- 2) Weigh material sample
- 3) Place sample into an ice-water bath for 10 minutes and record temp.
OR
Place sample into boiling water for 10 minutes and record temp. (if using battery, make sure it is fully discharged).
- 4) Record initial temperature of water inside calorimeter, leave temp. measuring device in cup
- 5) Remove sample from ice bath and place into calorimeter bath
- 6) Place insulated lid on apparatus
- 7) Record temperature for 10 minutes on 1 minute intervals
- 8) Repeat procedure for different starting temps and time steps if necessary.

To verify apparatus one should repeat experiment with different initial temperatures and time durations. Scientists Dulong and Petit (1818) collaborated to discover that the quantity of thermal capacity is constant in a given object; therefore, changing the temperature and time parameters should not reveal a different specific heat value for the same material.

9) Repeat procedure now using the battery as the test sample.

Calculations:

$$q_{\text{sample}} = m_{\text{sample}} * C_{p_{\text{sample}}} * (T_f - T_{\text{sample}_i})$$

$$q_{\text{water}} = m_{\text{water}} * C_{p_{\text{water}}} * (T_f - T_i)$$

$$q_{\text{calorimeter}} = C_{\text{cal}} * (T_f - T_i)$$

The calorimeter method utilizes the conservation of energy approach:

$$q_{\text{net}} = 0 = q_{\text{sample}} + q_{\text{water}} + q_{\text{calorimeter}}$$

C_{cal} is determined by experiment

Solving the above equation for $C_{p_{\text{sample}}}$:

$$C_{p_{\text{sample}}} = -(C_{\text{cal}} + m_{\text{water}} * C_{p_{\text{water}}}) * (T_f - T_i) / (m_{\text{sample}} * (T_f - T_{\text{sample}_i}))$$

References:

<http://www.chm.davidson.edu/ChemistryApplets/calorimetry/SpecificHeatCapacityOfCopper.html>

<http://core.ecu.edu/chem/chemlab/exper7/determination.htm>

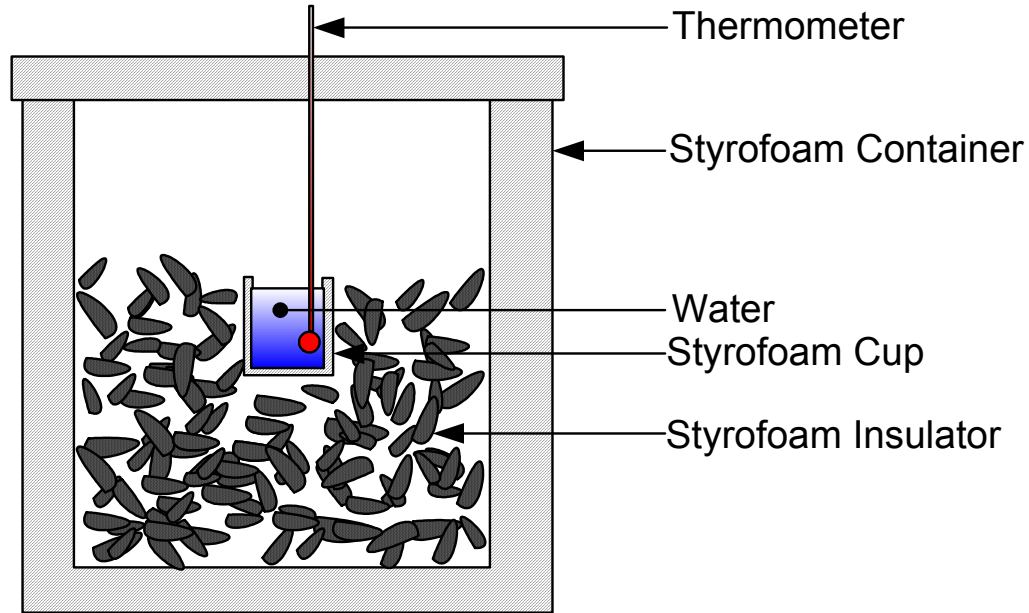
http://gorams.wssu.edu/physcilabs/Finished%20Pages/EXP_H-6.htm

http://www.chem.latech.edu/~deddy/chem104/L5Calorie_Summer2004.html

<http://core.ecu.edu/chem/chemlab/exper7/setups.htm>

<http://gorams.wssu.edu/physcilabs/Finished%20Pages/..%5CPhyscial%20Lab%20Web%5CH6.html>

http://www.brainyencyclopedia.com/encyclopedia/h/he/heat_capacity.html



Calorimeter Apparatus

Thermal Capacitance Determination of BSat Battery

Calorimeter Calibration

$$C_{p_water} := 4184 \frac{\text{J}}{\text{kg} \cdot \text{K}}$$

$$m_{water} := .1235 \text{ kg}$$

$$C_{p_sample} := 896 \frac{\text{J}}{\text{kg} \cdot \text{K}}$$

$$m_{sample} := .087 \text{ kg}$$

$$T_{cal_i} := 298 \text{ K}$$

$$T_f := 342 \text{ K}$$

$$T_{sample_i} := 273 \text{ K}$$

$$T_{w_i} := 358 \text{ K}$$

$$C_{cal} := \left[\frac{m_{sample} \cdot C_{p_sample} \cdot (T_f - T_{sample_i}) + m_{water} \cdot C_{p_water} \cdot (T_f - T_{w_i})}{(T_f - T_{cal_i})} \right]$$

$$C_{cal} = 65.657 \frac{\text{J}}{\text{K}}$$

Battery Specific Heat Determination

$$m_{batt} := 0.05 \text{ kg}$$

$$m_w := .129 \text{ kg}$$

$$T_{final} := 351 \text{ K}$$

$$T_{batt_i} := 273 \text{ K}$$

$$T_{\text{water}_i} := 359 \text{ K}$$

$$T_{\text{cal}_i} := 359 \text{ K}$$

$$C_{p_batt} := \left[\frac{m_w \cdot C_{p_water} \cdot (T_{\text{final}} - T_{\text{water}_i}) - C_{\text{cal}} \cdot (T_{\text{final}} - T_{\text{cal}_i})}{m_{\text{batt}} \cdot (T_{\text{final}} - T_{\text{batt}_i})} \right]$$

$$C_{p_batt} = 972.47 \frac{\text{J}}{\text{kg} \cdot \text{K}}$$